Dottorato di ricerca in Fisica
XXXII ciclo

# Study of the Mu2e sensitivity to the $\mu^- \to e^+$ conversion process

Eleonora Diociaiuti

Tutor
*Prof. Roberto Messi*
*Prof. Annalisa D'Angelo*
*Dott. Stefano Miscetti*
Coordinatore
*Prof. Roberto Benzi*

ii

## Introduction

The Mu2e experiment at Fermilab (Batavia, IL) will search for the coherent neutrinoless conversion of a muon into an electron in the electric field of an aluminum atom. The conversion process results in a monochromatic electron with energy slightly below the muon rest mass ($E_e$ = 104.97 MeV). The experiment goal is to improve the previous measurement by four orders of magnitude and reach a single event sensitivity of $3 \times 10^{-17}$ on the conversion rate with respect to the muon capture rate.

The experiment will deliver a very intense pulsed negative muon beam to an aluminum target to achieve a total number of $10^{18}$ stopped muons in three years of running. Production and transport of the muons are accomplished with a sophisticated magnetic system comprised of a Production, a Transport and a Detector solenoid, with the last one hosting a Straw-tube Tracker and a Crystal Calorimeter. The entire detector region is surrounded by a Cosmic Ray Veto system. Mu2e is under construction at the Muon Campus of Fermilab.

The INFN italian group is responsible for the design and construction of the crystal calorimeter, which plays a crucial role in the Mu2e measurement, providing particle identification capabilities fundamental for the rejection of the different background sources that can mimic a conversion electron. The calorimeter information allows also to improve the tracking performances it provides a fast standalone trigger for the experiment.

After a long R&D phase, the final drawings see a calorimeter comprised of 1348 pure CsI crystals arranged in two annular disks. Each crystal is

readout by two custom UV-extended Silicon Photomultipliers (SiPMs). Performances of the selected components were verified with an electron beam test, carried out in 2017 at the Beam Test Facility (BTF) at the National Laboratories of Frascati, on a large size prototype of 51 crystals and 102 SiPMs, confirming excellent energy ($\sigma_E/E = \mathcal{O}(10\%)$) and timing ($\sigma_T < 500$ ps) resolutions in agreement with the Mu2e specifications. In the first chapters of this thesis, I describe my involvement in the calorimeter activities, with particular emphasis on the data analysis of the prototype energy response and resolution, that I was personally leading. Moreover, a description of the tuning of the simulation and the careful data-MC comparison is also reported.

An auxiliary measurement that can be performed with Mu2e is the search for a Lepton Number Violation (LNV) process where the negatively charged muon converts, without neutrinos, into a positron, $\mu^- + N(A, Z) \rightarrow e^+ + N(A, Z - 2)$. At the moment of writing, Neutrinoless Double Beta Decay ($0\nu\beta\beta$) has set the most stringent limit on the LNV processes ($T^{0\nu\beta\beta}_{1/2} > 1.1 \times 10^{26}$ yr at 90% CL) with the GERDA experiment. In $0\nu\beta\beta$ a pair of free electrons is created in the transformation from a nucleus $(A, Z)$ into its daughter $(A, Z + 2)$, namely: $(A, Z) \rightarrow (A, Z + 2) = 2e^-$. Similar transitions could proceed through the emission of a pair of positrons, double electron capture (EC), or EC and single emission of a positron, with the nucleus changing from $(A, Z)$ to $(A, Z - 2)$. All these variations are equally interesting when discussing of new Physics, since they all manifest a non-conservation of the number of leptons.

Moreover, recent studies show that, because of flavor effect, off-diagonal processes, such as the $\mu^- - e^+$ conversion, can have their rate enhanced with respect to processes occurring in the $e - e$ sector.

Mu2e will search for $\mu^- + Al(27, 13) \rightarrow e^+ + Na(27, 11)$, only considering ground state transition, producing a conversion positron with energy $E_{e^+} = 92.32$ MeV.

This thesis is focused on this search. In particular, I developed an algorithm to account for the radiative corrections to be applied to the

conversion positrons that resulted in a few percent reduction in signal acceptance.

One of the most prominent background to this search is the Radiative Muon Capture (RMC) $\mu + N(Z, A) \rightarrow \gamma + \nu_\mu + N(Z - 1, A)$. The produced photon can convert, virtually or in the detector materials (in the following referred as internal or external conversion respectively) in an electron-positron pair, producing positrons with energies approaching the expected conversion energy. Experimental results from previous experiments indicate the RMC endpoint ($k_{\max}$) to be of $\sim 90$ MeV. A precise modeling of this background is relevant due to the proximity of the photon spectrum endpoint to the positron conversion energy. The calorimeter group is obviously interested to reconstruct the RMC distribution having also the opportunity to improve the current knowledge of the process.

A toy MC has been developed to evaluate the number of $e^+$ from external RMC background in the signal window. Knowing this value and evaluating the other primary sources of background (internal RMC and cosmic rays) an upper limit to the LNV conversion process is extracted showing an improving of the limit by four orders of magnitude.

# Contents

# Chapter 1

# Lepton Flavor Violation and Lepton Number Violation

## 1.1 Theoretical introduction

The Standard Model (SM) [1] is a well-defined gauge theory, that provides the "nowadays" best description of the elementary particle physics and their interactions. It is a non-abelian gauge theory incorporating quantum electrodynamics, Glashow-Weinberg-Salam theory of electroweak processes and quantum chromodynamics. The SM is based on the gauge symmetry group $SU(3)_C \times SU(2)_L \times U(1)_Y$, where the index $C$ stands for color charge, $L$ refers to the fact that $SU(2)_L$ only acts on the left handed components of the fields and $Y$ refers to the hypercharge. The two building blocks of the matter are quarks and leptons. These sub-atomic particles are 1/2-spin fermions, arranged into three families.

Each family contains three color replicas of the weakly charged doublets of quarks and a colorless weakly charged doublet containing a neutrino and a charged lepton. The 1-spin force carriers are the photon $\gamma$, which mediates the electromagnetic force, the $W^+$,$W^-$ and $Z^0$ gauge bosons of the weak interactions and eight gluons $g$, which mediate the strong interactions. In order to explain the spontaneous breaking of the $SU(2)_L \times U(1)_Y$ electroweak sector, which give origin to the $U(1)_{EM}$, the Higgs mechanism is introduced.

Starting from the '70s until now, the SM explained most of the known phenom-

ena in particle physics, including the discovery of the Higgs Boson at the LHC at CERN in 2012 [2] [3]. However, it incorporates only three out of four fundamental forces (gravity is not included). This means that the Standard Model is not yet a complete theory. Moreover, it lacks of explanations for the flavour structure, the neutrino mass, the dark matter or dark energy and it does not provide a mechanism which could explain the observed baryon asymmetry in the Universe. Nowadays, the SM is regarded as a low-energy approximation of a more general theory.

### 1.1.1 Charged Lepton Flavour Violation (CLFV)

In the SM, the lepton flavour conservation is accidental: it is not related to the gauge structure of the theory, instead arises from its particle content, in particular from the absence of right-handed neutrinos. It is an automatic consequence of the gauge invariance and the renormalisability of the SM Lagrangian. Before the discovery of neutrino oscillations, lepton flavor changing processes were considered forbidden in the Standard Model and lepton flavor numbers $L_e$, $L_\mu$ and $L_\tau$ conserved. In the SM the lepton flavor has a value of $+1$ for the leptons and $-1$ for the antileptons, i.e. the muons has $L_\mu = 1$ and $L_e$, $L_\tau = 0$. In this scenario the unitary matrix Pontecorvo-Maki-Nakagawa-Sakata (PMNS), which relates weak eigenstates with mass eigenstates, is diagonal:

$$\begin{pmatrix} \nu_e \\ \nu_\mu \\ \nu_\tau \end{pmatrix} = V_{PMNS} \begin{pmatrix} \nu_1 \\ \nu_2 \\ \nu_3 \end{pmatrix} \tag{1.1}$$

In 1998 the Super Kamiokande experiment [4] showed for the first time the existence of $\nu_\mu \to \nu_\tau$ oscillations in the sector of the atmospheric neutrinos. Combining these results with those from solar, beam and reactor experiments, a clear evidence of the existence of oscillations in flight between neutrinos (and antineutrinos) of different flavors was proved. In the Standard Model neutrinos and antineutrinos are described respectively by chiral left-handed and right-handed eigenstates; allowing the possibility of flavor oscillation ($P(\nu_\mu \to \nu_\tau) \neq 0$) a super-position of mass eigenstates is produced. Hence, neutrino oscillations represent an evidence of Lepton Flavor Violation (LFV), whose rate is obtained from the PMNS matrix.

The rate of Charged Lepton Flavor Violation (CLFV) processes is model dependent. An example is provided by the minimal extension to the Standard Model (SME), where neutrino masses are generated by introducing three right-handed SU(2) singlet fields and three new Yukawa couplings. As an example, the BR the the CLFV $\mu \to e\gamma$ process,reported in Figure 1.1 (left), has been evaluated in SME. It BR is negligible, being the amplitude proportional to the neutrinos mass-squared differences:

$$BR(\mu \to e\gamma) = \frac{3\alpha}{32\pi} \left| \sum_{i=2,3} U^*_{\mu i} U_{ei} \frac{\Delta m^2_{1i}}{M^2_W} \right| < 10^{-54} \tag{1.2}$$

where $U^*_{\mu i}$ and $U_{ei}$ are elements of the PMNS matrix, $\Delta m^2_{1i}$ are the neutrino mass-squared and $M_W$ the W-boson mass. In this extension similar results are obtained
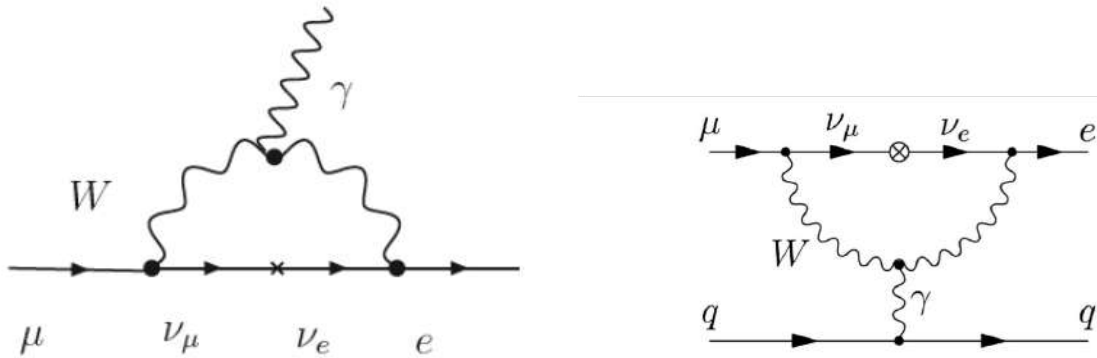


**Figure 1.1:** Feynman diagrams for the $\mu \to e\gamma$(left) and $\mu - e$ (right) conversions in the minimal extended Standard Model.

for the $\mu^- N \to e^- N$ conversion process (see Figure 1.1 (right)). However, in several alternative New Physics scenarios, much higher rates are expected for CLFV processes, with values that could be accessible by current and next generation experiments.

## 1.1.2 CLFV in muon decays

Even if there is still no evidence of CLFV, the search for this kind of processes has been pursued both at dedicated and general purpose experiments.
A collection of the current upper limits of various CLFV processes is reported in

Table 1.1.

| Process | Upper limit | references |
|---------|-------------|-----------|
| $\mu^+ \to e^+\gamma$ | $< 5.7 \times 10^{-13}$ | [5] |
| $\mu^+ \to e^+e^+e^-$ | $< 1.0 \times 10^{-12}$ | [6] |
| $\mu^- Ti \to e^- Ti$ | $< 1.7 \times 10^{-12}$ | [6] |
| $\mu^- Au \to e^- Au$ | $< 7 \times 10^{-13}$ | [7] |
| $\mu^+ e^- \to \mu^- e^+$ | $< 8.3 \times 10^{-11}$ | [8] |
| $\tau^\pm \to e^\pm\gamma$ | $< 3.3 \times 10^{-8}$ | [9] |
| $\tau^\pm \to \mu^\pm\gamma$ | $< 4.4 \times 10^{-8}$ | [9] |
| $\tau^- \to e^- e^+ e^-$ | $< 2.7 \times 10^{-8}$ | [10] |
| $\tau^- \to \mu^- \mu^+ \mu^-$ | $< 2.1 \times 10^{-8}$ | [10] |
| $\tau^- \to e^- \mu^+ \mu^-$ | $< 2.7 \times 10^{-8}$ | [10] |
| $\tau^- \to \mu^- e^+ e^-$ | $< 1.8 \times 10^{-8}$ | [10] |
| $\tau^- \to e^+ \mu^- \mu^-$ | $< 1.7 \times 10^{-8}$ | [10] |
| $\tau^- \to \mu^+ e^- e^-$ | $< 1.5 \times 10^{-8}$ | [10] |
| $\pi^0 \to \mu e$ | $< 3.6 \times 10^{-10}$ | [11] |
| $K_L^0 \to \mu e$ | $< 4.7 \times 10^{-12}$ | [12] |
| $K^+ \to \pi^+ \mu^+ e^-$ | $< 1.3 \times 10^{-11}$ | [13] |
| $K_L^0 \to \pi^0 \mu^+ e^-$ | $< 4.4 \times 10^{-10}$ | [11] |
| $Z^0 \to \mu e$ | $< 7.5 \times 10^{-7}$ | [14] |
| $Z^0 \to \tau e$ | $< 9.8 \times 10^{-6}$ | [15] |
| $Z^0 \to \tau \mu$ | $< 1.2 \times 10^{-6}$ | [15] |

**Table 1.1:** Sample of various CLFV processes reported with their latest upper limit measurement.

CLFV has been studied via a large variety of processes:

- muon decays: $\mu^+ \to e^+\gamma$, $\mu^+ \to e^+e^-e^+$ and muon conversion;

- tau decays: $\tau^+ \to e^+\gamma$, $\tau^\pm \to e^\pm e^-e^+$, etc;

- meson decay: $\pi^0 \to \mu e$, $K_L^0 \to \mu e$, $K^+ \to \pi^+\mu^+e^-$

- $Z^0$ decays: $Z^0 \to \mu e$, etc.

Muon processes have been intensely studied because they are the most sensitive probes to CLFV processes; low energy muon beams can be produced at high-intensity proton accelerator facilities and the final states can be precisely measured. In Figure 1.2 the experimental limits of the most studied processes, that is $\mu \to e\gamma$, $\mu \to eee$ and $\mu N \to eN$ are reported. The experimental sensitivity improved with time as long as new experiments were conducted. In the same figure the expected sensitivity for next generation experiments is also shown.
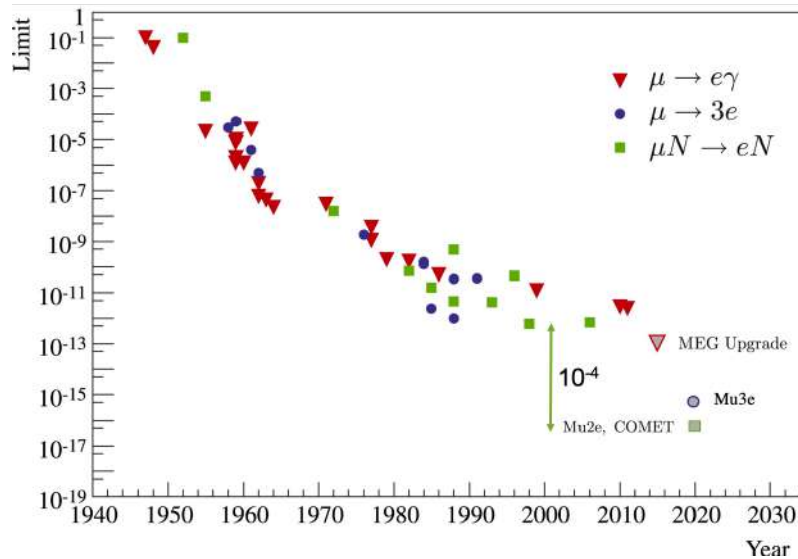


**Figure 1.2:** CLFV processes search with muons.

## 1.2 CLFV Independent Lagrangian and New Physics models

It is possible to estimate the sensitivity of CLFV processes to new physics in a model-indipendent way adding to the Standard Model Lagrangian effective operators, which violate lepton flavor conservation [16]:

$$\mathcal{L}_{CLFV} = \frac{m_\mu}{(1+\kappa)\Lambda^2}\overline{\mu}_R\sigma_{\mu\nu}e_L F^{\mu\nu} + \frac{\kappa}{(1+k)\Lambda^2}\overline{\mu}_L\gamma_\mu e_L \left(\sum_{q=u,d}\overline{q}_L\gamma^\mu q_L\right) \qquad (1.3)$$

this effective Lagrangian is a sum of "loop" and "contact" terms. L, R indicate the chirality of the different Standard Model fermion fields, $F_{\mu\nu}$ is the photon field strength and $m_\mu$ is the muon mass.

The coefficients of the two types of operators are parameterised by two independent constants: the $\Lambda$ parameter, with dimension of mass, which is meant to represent the effective mass scale of the new degrees of freedom, and the dimensionless parameter $\kappa$, which governs the relative size of the two different types of operators. The first term (Loop term) is the magnetic field operator, which mediates directly process such as $\mu \to e\gamma$ and, at order $\alpha$, $\mu \to eee$, and $\mu N \to eN$; the second one (contact term) one is the four-fermions operator, which mediates at the leading order muon into electron conversion and $\mu \to eee$ (Figure 1.3).

Supposing the photonic contribution is dominant ( $\kappa << 1$), the BR of the muon
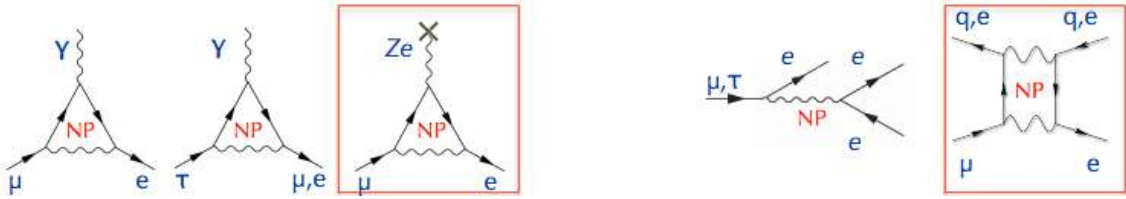


**Figure 1.3:** Representation of the vertices and interactions of some CLFV processes, where NP contribution could be measurable. The first four diagrams are mediated by magnetic field operators while the latter two by four-fermions operator. The diagrams in the red box are those describing the $\mu - e$ conversion.

conversion process is expected to be smaller than the other process by a factor $\alpha$ due to electromagnetic interaction of a virtual photon. This implies that the search for muon conversion at the level of $10^{-16}$ is comparable to that for $\mu \to e\gamma$ at the level of

$10^{-14}$. The second term includes contact terms and a variety of other processes not resulting in an on-mass-shell photon. Therefore, $\mu N \to eN$ and $\mu \to eee$ processes are sensitive to New Physics in a broad range of $\kappa$ parameters.

If a $\mu \to e\gamma$ signal is found, also a conversion signal should be observed. The ratio of the branching ratios between $\mu \to e\gamma$ decay and muon to electron conversion carries vital information on the intrinsic physics process. If no $\mu \to e\gamma$ signal is found, there will still be an opportunity to find a $\mu$-e conversion signal, because of the potential existence of non-photonic contributions.

Figure 1.4 shows the relation between the BRs of $\mu \to e\gamma$ and $\mu$-e conversion process (left) and $\mu \to eee$ (right) as a function of the parameter $\kappa$. The parameter space for muon CLFV that has been excluded by previous experiments and the region that future experiments will be able to probe are also reported. The upper limits expected at 90% C.L. for the future experiments MEG upgrade, Mu2e and Mu2e at PIP II (Proton Improvement Plan-II [17]) are also shown with dashed lines. It is
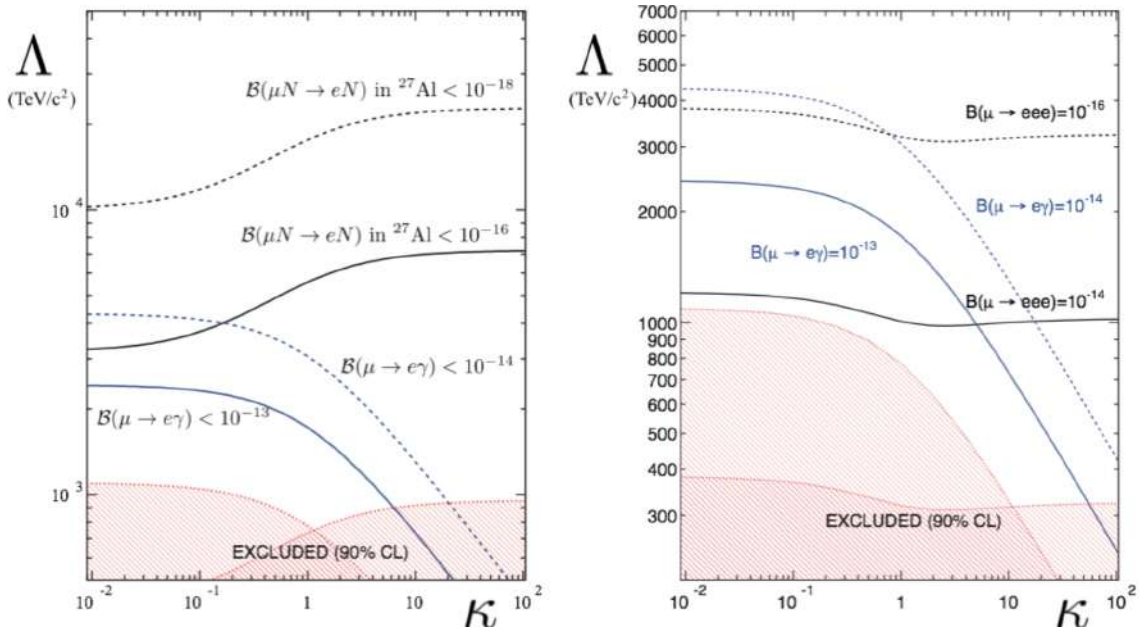


**Figure 1.4:** Current and future limits expected for $\mu N \to eN$ (left) and $\mu \to e\gamma$ (right) as a function of $\Lambda$ and $\kappa$.

also important to note that CLFV searches can probe energy scales of $\mathcal{O}\left(10^{4}\right)$ TeV, which are much higher than what can currently, or in the next future, be directly probed at colliders. Moreover, an observation in a single channel would not give any

indication to the form of the new interaction. For example, if a signal is seen in muon conversion alone with a branching ratio of $10^{-16}$ then the value of $\kappa$ would not be known until a signal is observed or excluded in $\mu \to e\gamma$ at a sensitivity greater than $10^{-14}$. However, a non-observation of CLFV would also restrict the large parameter space of these theories and possibly exclude most of them. The discovery of a lepton number violating process, but also a better constraint on the Branching Ratio, could give strong indications on which New Physics model is preferred. Some examples of NP models and their effect on CLFV process are reported in the following.

### 1.2.0.1 SO(10) SUSY Grand Unified Model

The supersymmetric version of the Standard Model with weak-scale supersymmetry (SUSY)-breaking parameters leads to large rates for CLFV processes. For example it is possible to relate the $\mu^- N \to e^- N$ rate in titanium as a function of SO(10) SUSY GUT breaking parameter [18], taking into account $\theta_{13}$ value and Higgs mass with different hypothesis of the neutrino Yukawa couplings, as shown in Figure 1.5. SUSY, in fact, predicts a $\mu - e$ conversion through a penguin diagram with two sleptons in the loop, as reported in Figure 1.6. In particular in the SUSY model, a slepton is in the loop and a chargino exchanges a photon with the nucleus, while in heavy neutrino model an heavy neutrino is in the loop and a W boson exchanges a photon with the nucleus.

### 1.2.0.2 Higgs-induced flavor violation

Some New Physics models includes LFV processes induced by Higgs exchange. Compared to $\mu \to e\gamma$ and $\mu \to eee$, muon conversion is more sensitive because of the Yukawa couplings result smaller in the first two cases [19]. As shown in the right side of the Figure 1.7 a tree-contribution involving light quark or a loop-induced effect of heavy quarks to the gluons can induce the conversion.

The muon conversion in nucleus is also the most sensitive channel for the study of Yukawa couplings $|Y_{\mu e}|$ and $|Y_{e\mu}|$. In the left side of the Figure 1.7 the thin blue
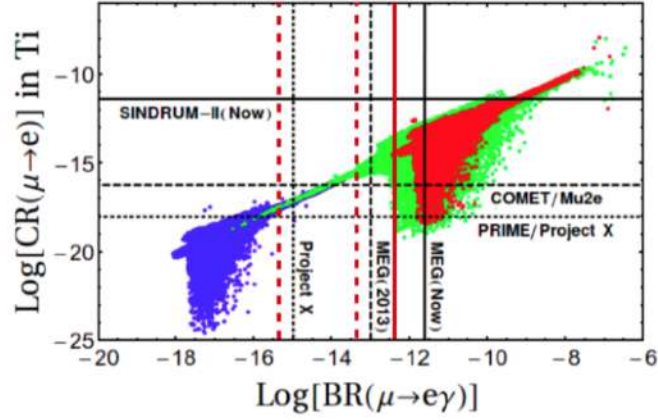
**Figure 1.5:** Muon Conversion Rate CR($\mu \to e$) in titanium as a function of the BR($\mu \to e\gamma$) for the PMNS-like neutrino Yukawa coupling in mSUGRA (red), Non Universal Higgs Mass (green) and for CKM-like neutrino Yukawa coupling (blue) for $\tan\beta = 10$. The red vertical lines represent the present limit given by MEG, the expected result for the MEG upgrade (dashed) and the expected result for a conceptual $\mu \to e\gamma$ experiment Project X ( PIP-II). Horizontal black lines, instead, represent limit on $\mu - e$ conversion rate from SINDRUM II result and Mu2e/COMET planned results. PIP-II is a set of still conceptual experiments working with a beam improved by a factor 10 in intensity currently under study at Fermilab.
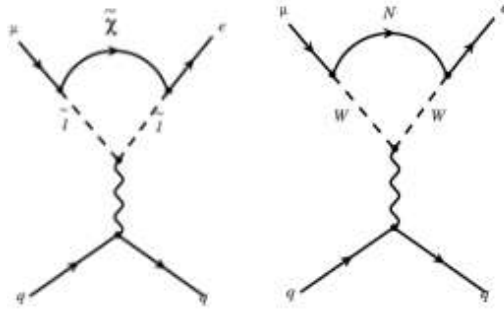


**Figure 1.6:** Feynman diagram for the $\mu N \to eN$ process in the SUSY (left) and heavy neutrino (right) model.

dashed lines are contours of constant BR($h \to \mu e$), while the thick red line is the projected Mu2e limit.
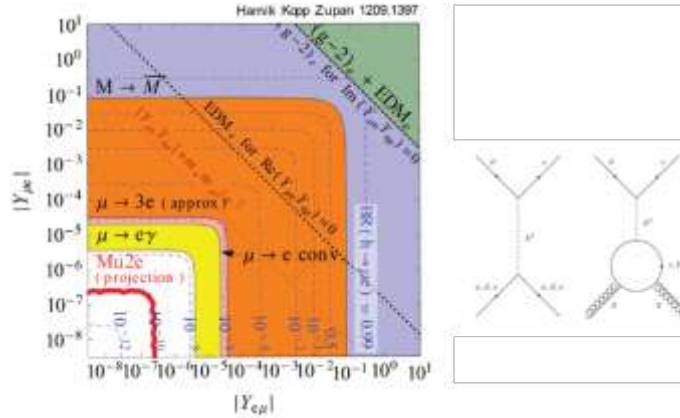
**Figure 1.7:** Left: constraints on the flavor-violating Yukawa couplings a 125 GeV Higgs boson. Right: Higgs-induced LFV for a muon conversion.

### 1.2.0.3   Littlest Higgs model with T-parity (LHT)

In the Littlest Higgs model with T-parity (LHT), the Higgs boson is considered an exact Goldstone boson under several symmetries. Only if the symmetries are all broken (collective symmetry breaking, CSB), the Higgs pick up a contribution to its mass. To avoid fine tuning from electroweak precision data, a discrete symmetry (analogous to SUSY) and called T-parity, is introduced. The scanning of the parameters of this model provides measurable BR both for $\mu \to e\gamma$ and for $\mu N \to eN$ [20]. In Figure 1.8 the blue line represents the MSSM dipole contribution, the solid green lines are the present (solid) and expected (dashed) upper limits by MEG and the yellow solid line is the SINDRUM II upper limit. Mu2e would cover all the parameters of this scan aand fully exclude the validity of this model.

### 1.2.0.4   Scalar Leptoquark model

Models with scalar leptoquarks at the TeV scale can [21], through top mass enhancement, modify the $\mu \to$ e conversion rate and BR ($\mu \to e\gamma$) while satisfying all known experimental constraints from collider and quark flavor physics. In Figure 1.9 the reaches in the new coupling $\lambda$ for a range of scalar leptoquark masses are compared for the $\mu \to e$ conversion rate with the sensitivity of Mu2e and BR($\mu \to e$ ) at the sensivity of the MEG upgrade.

**Figure 1.8:** Correlation between $\mu \rightarrow e\gamma$ and $\mu \rightarrow e$ conversion in titanium obtained from a general scan over the LHT parameters.
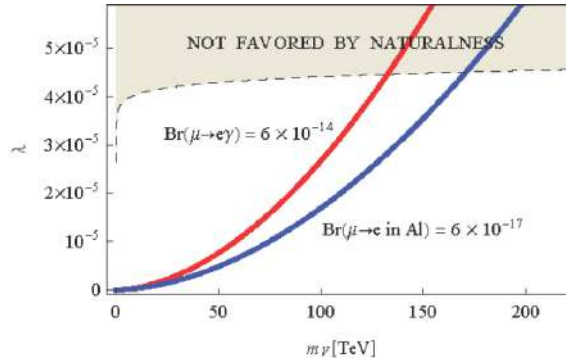


**Figure 1.9:** the new coupling $\lambda$ as a function of the scalar leptoquark mass for the $\mu \rightarrow e$ conversion rate (blue line) in Al at the sensitivity of Mu2e and BR($\mu \rightarrow e\gamma$) at the sensitivity of the MEG upgrade (red line).

### 1.2.0.5 Heavy neutrinos

Neutrino oscillation provides the first proof of CLFV interactions. However, rates for CLFV processes are not immediately related to neutrino masses, because they strongly depends on the undergoing mechanism. The presence of new heavy neutrino mass states, different from mass eigenstates $\nu_1, \nu_2, \nu_3$ [22], is related to a muon conversion process through the neutrino oscillation in Feynman loop reported in Figure 1.6.

## 1.3   Experimental Searches for CLFV

In 1937, when the muon was discovered, it was believed to be the Yukawa meson for the strong interactions. Soon afterwards, however, the leptonic nature of the muon was proved since its lifetime was too long and its interaction cross section too weak. Moreover, it was believed that the muon was an excited state of the electron and therefore could become de-excited by emitting photons. If these hypothesis were correct, the muon would decay into an electron and a photon. Experimental searches by Hincks and Pontecorvo (1948) [23] did not observe the process $\mu \to e\gamma$ but set an upper limit on the $\mathcal{BR} < 10\%$. The search for the neutrinoless muon to electron conversion process in the field of a nucleus, $\mu N(A, Z) \to eN(A, Z)$, where N(A,Z) is a nucleus capturing the muon, was also carried out. These searches were significantly improved when muons became artificially produced at accelerators, stopping pion beams in a first phase (until the 1970s) and starting directly with muon beams afterwards. In the following of this chapter the principal channels for search of CLFV processes are presented.

### $\mu^+ \to e^+\gamma$

It is a two body decay with a clear signature: a positron and a photon, emitted back to back in the rest frame of the decaying muon, with energy $E_{e^+} = E_\gamma = E_{\mu^+}/2$ = 52.8 MeV. Variation in the expected energy spectrum can occur in case of muon decays in flight, where a boost needs to be taken into account for re-evaluating both the energy spectra and the emission distributions. Only positive muons are used since negative ones would be efficiently captured by nuclei undergoing a subsequent nuclear capture. The $\mu^+ \to e^+\gamma$ process is sensitive to new physics mass scales around $10^3$ TeV/c$^2$ and primarily tests CLFV dipole couplings where new physics appears in loops [16]. The main backgrounds of this process are:

- Radiative Muon Decays (RMD) $\mu^+ \to e^+\gamma\nu_e\overline{\nu_\mu}$ represents an irreducible background in proximity of the kinematics endpoint when neutrinos carry off small

momentum. This process is proportional to the muons stopping rate ($\mathcal{R}_\mu$);

- accidental background produced by the coincidence of a positron from the muon decay and a photon coming from a RMD. Because the accidental background increases quadratically with the muon rate (the two background particles are uncorrelated produced by the beam particles), a continuous muon beam with a low instantaneous rate is preferable for the $\mu^+ \to e^+\gamma$ search.

The current best limit on $\mu^+ \to e^+\gamma$ search is $\mathcal{BR}(\mu^+ \to e^+\gamma) < 4.2 \times 10^{-13}$ at 90% C.L. [5] obtained by the MEG experiment. An upgrade of the detector system is underway for improving the detector performance. The goal is to increase the sensitivity by another order of magnitude [24] improving energy resolution and acceptance of the liquid Xenon Calorimeter (obtained substituting PMTs with SiPMs) as well as the time resolution on the timing counters and replacing the wire chambers with an ultra-light drift chamber.

## $\mu^+ \to e^+ e^+ e^-$

The signature is characterised by the coincidence of two positrons and one electron from a common vertex. As muons are stopped in the detector and decay at rest, the momenta of the three decay products vanish whereas the invariant mass equals the muon rest mass. The maximum energy that can be carried away by a positron or electron is equal to half the muon mass energy. The phase space distribution of the decay particles depends on the new physics inducing CLFV and therefore, it is not known a priori.

The search for this decay requires a detector system characterised by a large acceptance for low momentum electrons and positrons, and the consequent capability to tolerate the positron flux from the Michel muon decay. This process is sensitive to new physics at mass scales beyond $10^3$ TeV/c$^2$ and probes CLFV couplings that arise from dipole interactions where new physics appears in loop diagrams and from $\mu eee$ contact interactions [16].

The main source of background is represented by accidental coincidences of positrons from the Michel decay with $e^-e^+$ pairs either from gamma ray conversions, or from Bhabha scattering of Michael positrons with atomic electrons. The current best

limit, set by the SINDRUM experiment, is $BR(\mu^\pm \to e^\pm e^+ e^-) < 1 \times 10^{-12}$ [6]. A new experiment, named Mu3e, has been approved at PSI with the goal to reach a sensitivity of $5 \times 10^{-15}$[25] at 90 % CL in a first phase aiming to improve in a proposed second phase the limit or additional two order of magnitude

$$\mu^- N(A, Z) \to e^- N(A, Z)$$

The $\mu$ - e conversion may well exploit the new high intensity accelerators since, differently from the other CLFV processes previously listed, this conversion is in principle non-rate limited. The signal corresponds to a monoenergetic electron to be separated by a fast falling spectrum background. The current best limit, set by the SINDRUM II experiment using different targets [7], [26], [27], is $BR(\mu^- Au \to e^- Au) < 7 \times 10^{-13}$at 90% C.L. The COMET Phase-I experiment is currently under construction and aims to improve sensitivity by a factor of 100 starting in the next few years. After 150 days of operation the projected COMET Phase-I sensitivity will be $\mathcal{R}_{\mu e} < 7 \times 10^{-15}$ at 90% C.L. [28]. The Mu2e experiment is under construction too and aims to improve the current sensitivity by four orders of magnitude by the mid 2020s. Since, this thesis is focused on the Mu2e experiment, more details on it will be provided in the following chapters. COMET Phase-II is a proposed upgrade to COMET Phase-I that would achieve a sensitivitu similar to that of the Mu2e experiment in [29] in the following years. In Figure 1.10 the planned schedules for current CLFV experiments [30] is reported.
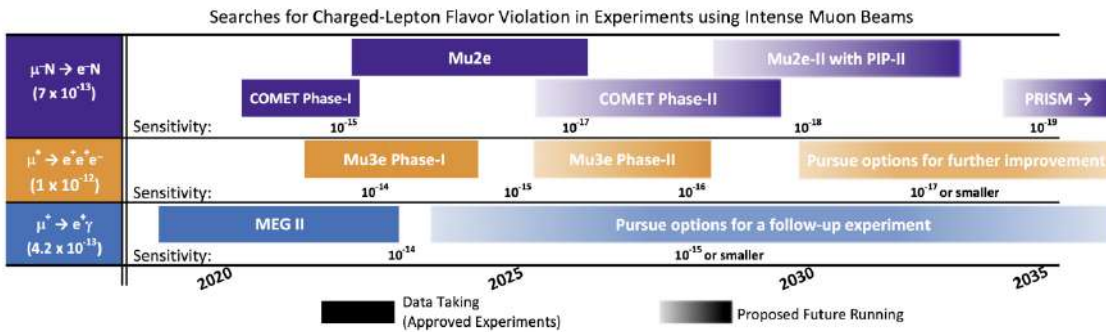


**Figure 1.10:** Planned data taking schedules for current experiments that search for CLFV. Also shown the possible schedules for future proposed upgrades to these experiments.

### 1.3.0.1 $\mu - e$ experimental signature

As already mentioned, the $\mu$-e conversion has a distinctive signature of the monochromatic electron with energy evaluated as:

$$E_e = m_\mu - B_\mu - E_{recoil} \approx m_\mu - B_\mu = 104.96 \text{MeV} \tag{1.4}$$

where $m_\mu = 105.6$ MeV is the muon mass, $B_\mu \simeq Z^2 \alpha^2 m_\mu / 2$ is the muonic binding energy for a nucleus with atomic number $Z$, and $E_{recoil} = (m_\mu - B_\mu)^2 / 2m_N$ is the nuclear-recoil energy. Since $B_\mu$ has a different values depending on the selected nucleus, the conversion electron energy changes too.

In the Mu2e experiment, muons are stopped in an $^{27}$Al target and form the muonic atom. Then after $\sim 10^{-10}$ s, the muons fall in the 1S ground state emitting photons. Finally, as depicted in Figure 1.11, the muons can:

- Decay In Orbit (DIO) $\mu^- \to e^- \nu_\mu \overline{\nu_e}$, (39% of the cases);

- undergo a nuclear capture $\mu^- p \to \nu_\mu n$ ,(61% of the cases);

- coherently interact with the whole nucleus and eventually convert into electron with $E_e = 104.96$ MeV.
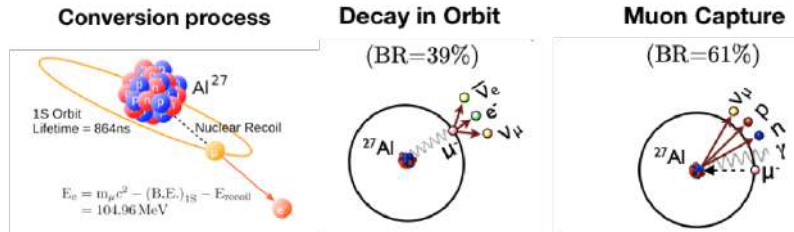


**Figure 1.11:** Processes arising after the creation of the muonic atom. Left: the conversion of a muon into an electron without the neutrino emission. Center: Muon decay in orbit ($\mathcal{BR} = 39\%$). Right: Muon capture ( $\mathcal{BR} = 61\%$).

### 1.3.0.2 Definition of Conversion Rate

The aim of the Mu2e experiment is to measure the ratio $\mathcal{R}_{\mu e}$ between the rates of $\mu - e$ coherent conversion process in the field of a nucleus and of muon captures:

$$R_{\mu e} = \frac{\Gamma(\mu^- + N(Z,A) \to e^- + N(Z,A))}{\Gamma(\mu^- + N(Z,A) \to \nu_\mu + N(Z-1,A))} \tag{1.5}$$

The Single Event Sensitivity (SES) is defined as the conversion rate for which the expected number of events will be one. The Mu2e experiment aims to reach a SES of $\sim 3 \times 10^{-17}$. If conversion signals will not be observed, the Mu2e experiment will set an upper limit on $R_{\mu e} < 8 \times 10^{-17}$. In order to keep stable this level of sensitivity the number of background events needs to be smaller than 0.5.

### 1.3.0.3 Backgrounds to the conversion process

There are many processes that can mimic the $\mu - e$ conversion experimental signature, in particular:

- **Intrinsic processes scaling with beam intensity like muon decay in orbit (DIO) and radiative muon capture (RMC):** the DIO represents one of the most important background source for the $\mu^- N \to e^- N$ process. Differently from the free muon decay, where the kinematic endpoint would not exceed 52.8 MeV (when the electron and two neutrinos are emitted in opposite directions), in a DIO the outgoing electron can exchange momentum with the aluminum nucleus and reach, with very small probability ($\mathcal{O}(10^{-17})$), the kinematic endpoint of the conversion electron. The DIO energy spectrum has been calculated in [31] and is reported in Figure 1.12. The nuclear recoil slightly distorts the Michel peak and originates a small tail that extends out to the conversion energy. Looking at the DIO spectrum on a log scale, it can be seen that the occurrence of DIO electrons above 100 MeV is still relevant when compared to a signal with a branching ratio of $\mathcal{O}(10^{-17})$. To date, because of the high muon rate needed, there are no precise measurements of DIO spectrum near the conversion electron energy, causing the theoretical estimate to be relevant in the uncertainty evaluation. Howe ver, the latest theoretical calculation [32], which takes into account nuclear effects, gives an uncertainty near the endpoint smaller than 20%.

  Another relevant process is the RMC where the muon can be absorbed by the nucleus of the target, emitting a photon through the process $\mu + N(Z, A) \to \gamma + \nu_\mu + N(Z - 1, A)$. These photons can convert to an $e^- e^+$ pair in the stopping target or other surrounding materials, producing an electron near the conversion electron energy. It is possible to reduce the impact of this process
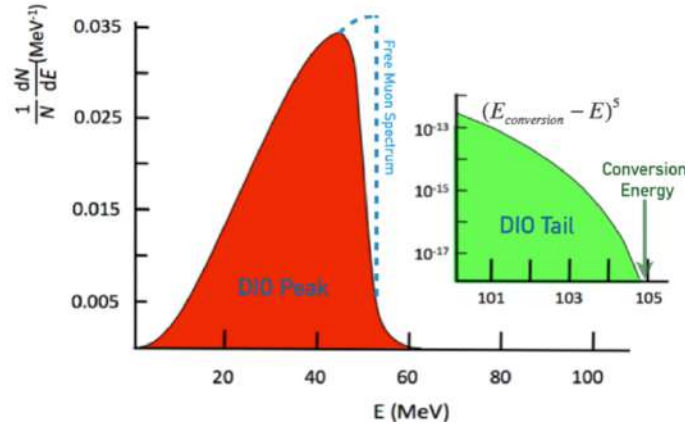
**Figure 1.12:** Electron energy spectrum from muon DIO in aluminum. The dotted line represents the spectrum of the free muon decay.

choosing the target material, to ensure that the photon energy is below the conversion electron energy. This process represents the main background for the $\mu^- \to e^+$ process. Further details can be found in Chapter 7.

A high resolution detector reduces the effect of these backgrounds since, neglecting resolution effects, there are no intrinsic physics backgrounds that have the same energy as the electron from the conversion signal;

- **Processes that are delayed because of particles that spiral slowly down the muon beam line:** examples of this kind of background are antiprotons and neutrons. If produced on the primary target, antiprotons can be a background source due to their low speed, thus arriving delayed on the detector surface. These backgrounds can be reduced by having a sufficiently long muon beam line and using a time delayed acquisition window. Antiprotons are reduced to a negligible contribution by means of a specific absorbers in the middle section of the experiment (see Chapter 2);

- **Prompt processes in which the detected electron is nearly coincident in time with the arrival of a beam particle at the muon stopping target:** the Radiative Pion Capture (RPC) is one of these prompt processes. The impact of these events is greatly reduced by using a bunched beam and recording only data in a delayed time window. However, these prompt backgrounds could still cause problems if there are protons leaking out of the main proton

pulses and into the gaps between them. Therefore, a high level of "extinction", defined as the ratio of beam between pulses and the beam contained in a pulse, is required to achieve the design SES.

Other three additional sources contribute to the background: (i) pions that have not decayed by the time they reach the stopping target can be captured immediately by the nucleus, (ii) a small fraction of pions can decay directly in high energy electrons (despite having a small BR of $1.23 \times 10^{-4}$), (iii) muons can decay in flight and, if they have a momentum greater than 77 MeV, could produce an electron with an energy in the conversion signal region;

- **Electrons or muons initiated by cosmic rays** which can induce a background event in the detector but can be reduced and detected by using a cosmic ray veto.

In Table 1.2 all process contributing to the total background of 0.32 event for the total Mu2e lifetimeare listed.

| Category | Background process | Estimated Yield (events) |
|---|---|---|
| Intrinsic | Decay in orbit (DIO) | $0.144 \pm 0.028$ (stat) $\pm 0.11$ (syst) |
| | Muon Capture (RMC) | $0.000 \pm 0.004$ |
| Late Arriving | Pion Capture (RPC) | $0.021 \pm 0.001$ (stat) $\pm 0.002$ (syst) |
| | Muon decay in flight | $< 0.003$ |
| | Pion decay in flight | $0.001 \pm < 0.001$ |
| | Beam electrons | $(2.1 \pm 1.0) \times 10^{-4}$ |
| Miscellaneous | Antiproton induced | $0.040 \pm 0.001$ (stat) $\pm 0.020$ (syst) |
| | Cosmic rays | $0.209 \pm 0.0022$ (stat) $\pm 0.055$ (syst) |
| | Total | $0.41 \pm 0.13$ (stat+syst) |

**Table 1.2:** Expected background list as evaluated by full simulation.

## 1.4 Lepton Number Violation (LNV)

As well as for CLFV, an observation of LNV will represent a clear sign of NP; indeed in the SM, the Lepton Number can be violated only by non perturbative processes

not appearing at low energies [33].

Processes with the change of Lepton Number by 2 ($\Delta L = 2$) have been mostly explored through the neutrinoless double-beta ($0\nu\beta\beta$) decay, which correspond to an investigation on the *ee* sector. In the SM, it is not possible to build a Feynman diagram describing the neutrinoless double beta decay $(Z, A) \rightarrow (Z + 2, A) + 2e^-$, in which a nucleus with atomic number Z and mass number A decays such that, although no lepton has been present in the initial state, two electrons appear in the final state. At the moment $0\nu\beta\beta$ has set the most stringent limit on this process: $T_{1/2}^{0\nu\beta\beta} > 1.1 \times 10^{26}$ year 90% CL obtained with the GERDA experiment [34].

The $0\nu\beta\beta$ decay has crucial role also in Neutrino Physics since it would allow the determination of the neutrino nature, in fact it can occur only if neutrinos are Majorana particle, i.e. they coincide with their own anti-particles, or through a new particle appearing at high energy scale ($>$ TeV).

Another process which is complementary to the $0\nu\beta\beta$ decay in the $\Delta L = 2$ processes is the $\mu^- - e^+$ conversion. In Figure 1.13 the diagrams for $0\nu\beta\beta$ and $\mu^- - e^+$ conversion ($\mu^- + N(A, Z) \rightarrow e^+ + N(A, Z - 2)$) are reported: while $0\nu\beta\beta$ decay can only detect LNV, $\mu^- - e^+$ conversion is an example of both CLFV and LNV. There are however other searches that can be undertaken like the $\mu^- - e^+$ conver-
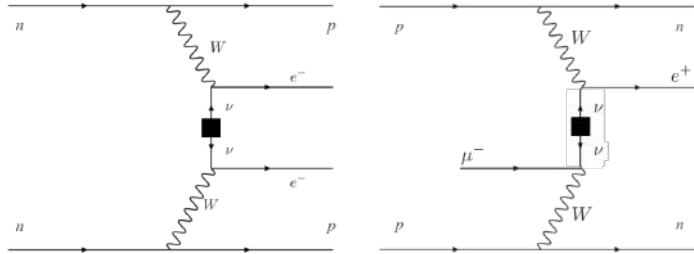


**Figure 1.13:** Left: diagram of the $0\nu\beta\beta$ decay. Right: diagram of the $\mu^- \rightarrow e^+$ conversion

sion ([35]-[27]) and the kaon decays ([41]-[44]). In recent publications ([45]- [46]), new computations of the rate of LNV and CLFV muon conversion processes have been presented. A crucial point is the existence of two operator (dimension 7 and dimension 9) contributing only to the $\mu^- - e^+$ conversion and not to $0\nu\beta\beta$. This means that there is no guarantee that the LNV will manifest primarily in the $0\nu\beta\beta$.

Due to the interesting opportunity, the Mu2e experiment is investigating the feasibility of searching for $\mu^- - e^+$ conversion. This search is the main physics

subject of the thesis.

The previous experiments assumed that the $\mu^- \to e^+$ conversion was mediated either through a Giant Dipole Resonance (GDR) or a Ground State (GS) transition. For example, in [27] the GDR was modeled with a Breit-Wigner distribution with 20 MeV excitation energy and 20 MeV width. As shown in Figure 1.14, thanks to better data existing today (the EXFOR database [47]), the GDR in $^{27}$Al can be fitted with a Breit-Wigner with 21.1 MeV mean and a width of 6.7 MeV.

 For a conversion mediated by GDR and a stopping target made of aluminum, as in
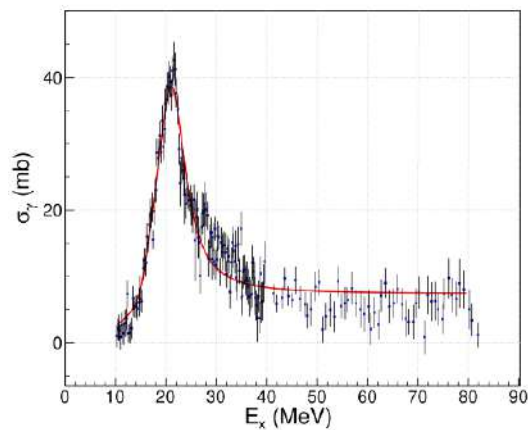


**Figure 1.14:** Shape of the GDR on $^{27}$Al using the EXFOR database. A Breit-Wigner is used to fit the data

Mu2e, the positron energy will be $E_{e+} = 83.9$ MeV; in this case the search will be overwhelmed by the much higher rate of RMC background. In case of a conversion mediated by ground state transition, the expected value of the positron energy, considering an aluminum target, is $E_{e+} = 92.3$ MeV. Calculations [48] show that, in the aluminum case, a significant fraction ($\sim 40\%$) is realized via the ground state transition, giving the Mu2e experiment the opportunity to search for this process.

## 1.4.1 Description of the previous results

In the long history of CLFV and LNV, several experiments looked for the the muon into positron conversion process. The "latest" results came from the SINDRUM II experiment [27] in 1998. In the following a brief overview of the results previously

obtained with the TRIUMF[39] and SINDRUM II experiment is reported. Both experiments obtained their results using a Titanium stopping target.

### 1.4.2 TRIUMF results

The TRIUMF TPC experiment was designed to search for the muon into electron or positron conversion at the level of $10^{-12}$. Scintillation counters were used to detect the beam particles and to define the muon stopped in the target. Charged particles emitted from the target were detected using a Time Projection Chamber located in a uniform magnetic field, in Figure 1.15 the experimental setup of the TPC is reported. The data taking for $\mu^- - e^-$ and $\mu^- - e^+$ conversion was simultaneous.
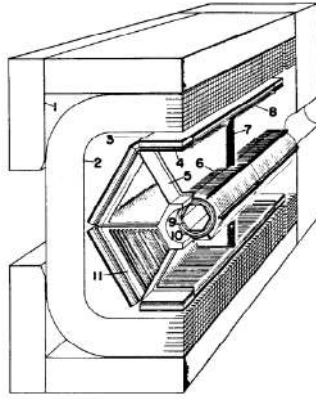


**Figure 1.15:** A prospective view of the TRIUMF experiment. 1) Magnet iron, 2) coil, 3) outer trigger scintillator, 4) outer trigger proportional counters, 5) endcap support frame, 6) central electric field cage wires, 7) central high voltage plane, 8) outer electric field cage wires, 9) inner trigger scintillators, 10) inner trigger cylindrical proportional wire chamber, 11) endcap proportional wire modules

The target used for the search was made of titanium; the expected positron energy is $E_{e^+}^{Ti} = 96.4$ MeV. As shown in Figure 1.16, selecting a momentum range from 75-130 MeV/c, no positrons were observed for momentum $> 92$ MeV. In the case of the GDR, they considered an avarage nuclear excitation energy of 20 MeV and a width of 20 MeV obtaing a branching ratio at 90% C.L. of:

$$R_+(Ti) = \frac{\Gamma(\mu^- + Ti \rightarrow e^+ + Ca)}{\Gamma(\mu^- Ti \text{ capture}} < 1.7 \times 10^{-10} \tag{1.6}$$
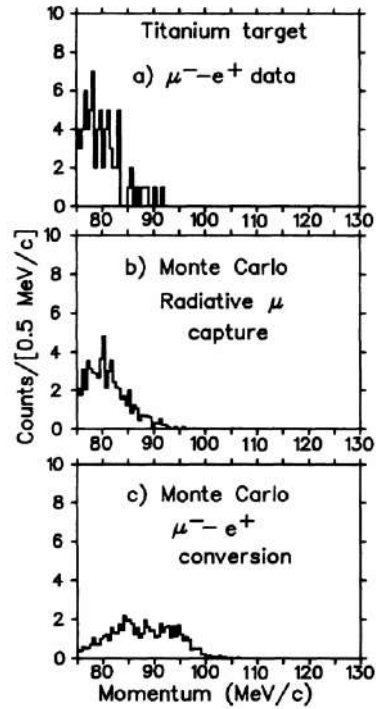
**Figure 1.16:** Positron momentum spectrum from the Ti target in the momentum region 75-130 MeV/e for data (top), Monte Carlo simulation of the radiative muon capture with asymmetric photon conversion background (middle), and Monte Carlo simulation of the muon-positron conversion process assuming average nuclear excitation <E>=20 MeV and width $\Gamma = 20$ MeV (bottom).

### 1.4.3  SINDRUM II results

SINDRUM II is the latest esperiment that studied the CLFV muon conversions processes. The muon beam was produced by a 590 MeV proton beam hitting a carbon production target. The backward produced particles $(\pi, \mu$ and $e)$ were then transported by a secondary beam line to a degrader connected to the transport solenoid with a 1.2 T magnetic field.

Here, the muon beam was stopped on a titanium target and the helical trajectories of the emitted electrons were reconstructed by two drift chambers. Trigger and timing were provided by scintillation and Cherenkov hodoscopes. A schematic view of the experiment is reported in Figure 1.17.

After all the selection cuts, the positron sample, see Figure 1.18, showed a fast falling momentum distribution with an endpoint around 92.3 MeV/c, and a single
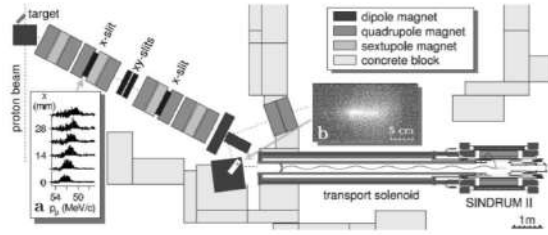
**Figure 1.17:** Schematic plain view of the SINDRUM II experiment.

signal candidate at 95.7 MeV/c. In Figure 1.18 the predicted MC results for ground
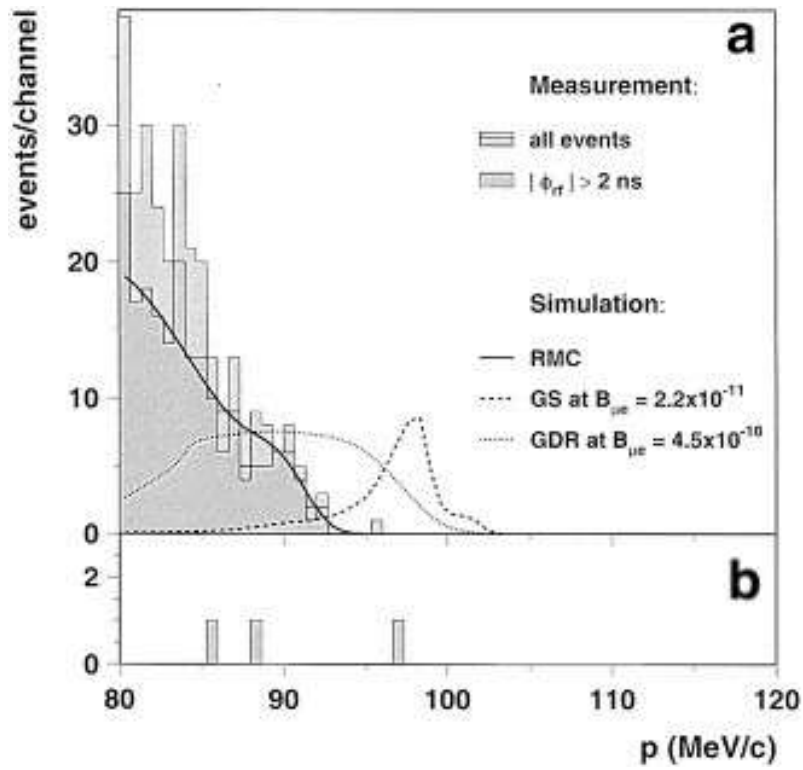


**Figure 1.18:** Positron momentum distributions for measuring periods with (a) and without (b) muon beam.

state and GDR transitions are reported. Considering the events acquired off beam, an event in the signal region was present, so that the isolated event observed at 95.7 MeV/c could be explained by a cosmic ray background. The branching ratios obtained were:

$$B_{\mu^-e^+}^{GS} < 1.7 \times 10^{-12}(90\%C.L)$$
$$B_{\mu^-e^+}^{GDR} < 3.6 \times 10^{-11}(90\%C.L)$$

(1.7)

# Chapter 2

# The Mu2e experiment

The goal of the Mu2e experiment is to search for the neutrinoless, coherent conversion of muons into electrons in the field of a nucleus and improve by four orders of magnitude the previous sensitivity set by SINDRUM II experiment. This corresponds to achieve a limit on the ratio between the conversion and nuclear muon capture rates $R_{\mu e}$ of :

$$R_{\mu e} < 8 \times 10^{-17} \text{ @ } 90\% \text{ C.L} \tag{2.1}$$

## 2.1 Drawings guidelines

The design of the Mu2e experiment is based on that of two previous proposed experiments: the MELC experiment [49], planned for the Moscow Meson Factory at the Russia's Institute for Nuclear Research , and the MECO [50] experiment, proposed in 2001 at the Brookhaven Laboratory (USA)[51]; both of them did not succeed in starting the construction phase.

The research and development for the Mu2e experiment started in 2009. In 2016 Mu2e received the approval of full Critical Decision (CD)-3, obtaining the permission to start the construction for the accelerator, the magnetic system, the muon beam line and all the detector components. At the moment of writing the detectors are expected to be installed by the end of the 2021 and they will start their commissioning in 2022.

In the next chapters, a more detailed description of the solenoids and detectors is reported. A short description of the accelerator system is also provided.

In order to achieve the designed single event sensitivity, the produced muon beam and the detector must meet strict requirements:

- an efficient production and transport of the muon beam to the stopping target;

- a very high rate: a large number of stopped muons is essential to improve previous experiments results. The present proposed rate is of $4.21 \times 10^{10} \mu^-/$s. A high intensity increase is also aimed at the PSI, where the High Intensity Muon Beam (HIMB) [52] project is developing a polarized muon beam lines with intensity of $(O)(10^{10})\mu^-/$s for the proposed upgrade of the Mu3e experiment;

- a pulsed beam structure and a delayed TDAQ window: in order to suppress the prompt background, the muons hitting the stopping target should be distributed in a narrow time burst ($< 200$ ns) as shown in Figure 2.1, each one separated from the other by intervals of $\sim 1.7~\mu$s (i.e. larger than 826 ns, the muonic aluminum lifetime). This is guided by the observation that the result of the SINDRUM II experiment was ultimately limited by the need of suppressing the prompt background. Mu2e will take data $\sim 700$ ns after the
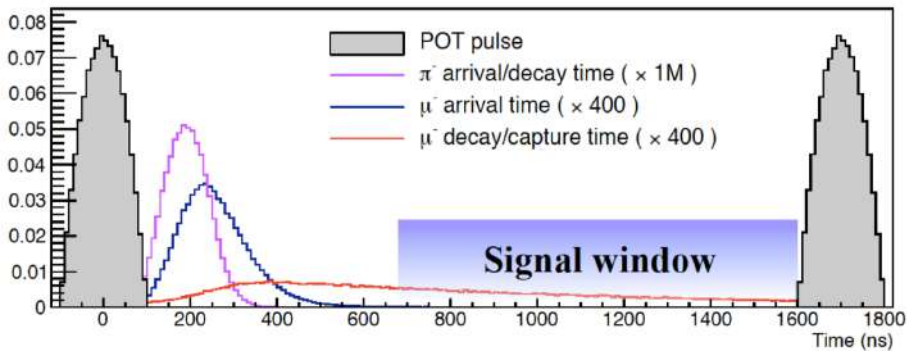


**Figure 2.1:** Timing structure of the Mu2e beam.

injection bursts, to let the prompt background (especially pion capture) to subside. The data taking time window will then close 925 ns after, just before the arrival of the next bunch;

- Extinction: between-bursts extinction is fundamental to suppress background generated by unwanted beam between pulses.

- A high precision detector ($\mathcal{O}(100)$keV/c) for momentum selection to separate DIO background from Conversion Electron signals.

## 2.2 The experimental setup

The Mu2e apparatus is extensively documented in its Technical Design Report [53]. As shown in Figure 2.2, the layout of the system shows a peculiar S-shape for the Superconducting Solenoid Magnet System. To limit backgrounds from muons, that might stop on gas atoms, and to reduce the contribution of multiple scattering for low momentum particles, the inner bores of the solenoids are evacuated to $10^{-4}$ Torr. The solenoids are organized into 3 sub-systems:
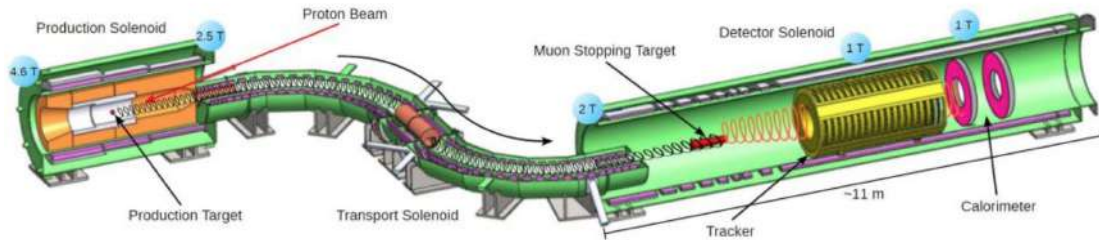


**Figure 2.2:** Schematic view of the experimental apparatus.

- **Production Solenoid (PS):** where a pulsed 8 GeV proton beam, coming from the Fermilab Accelerator System, [54] hits a tungsten target, producing mostly pions;

- **Transport Solenoid (TS):** pions are focused and collected by the lens provided by the PS graded magnetic field into the TS, that selects and transports negatively charged secondary muons to a stopping target located in the next solenoid. It is characterised by an S-shape, long enough to allow the decay of all hadrons while suppressing the neutral particles. The momentum spectrum

of the transported muon beam must be $< 100$ MeV/c to ensure that a significant fraction ($\sim 40\%$) of the muons can be stopped in a thin Al target (see Figure 2.9);

- **Detector Solenoid (DS):** contains the Muon Stopping Target, where negative, low momentum muons will impinge at high rate ($\sim 10$ GHz), and the detectors to identify the $\sim 105$ MeV conversion electrons. The Detector Solenoid is surrounded by a cosmic ray veto system. Outside the DS, a stopping target monitor is used to measure the total number of muon captures.

### 2.2.1 Accelerator system and proton beam

During the running time, Mu2e is expected to receive about $3.6 \times 10^{20}$ protons on the production target. The proton beam consists of a train of pulses separated by 1.7 $\mu$s. To keep late arrival backgrounds at an affordable level, the beam must be extinguished between successive pulses; the Extinction Factor should be EF$\leq 10^{10}$, EF is an important parameter used to estimate the proton beam quality. EF is defined as the the ratio between the number of protons in time and out-of-time with respect to the 250 ns full-width of the bunch itself.

A picture of the accelerator complex is shown in Figure 2.3
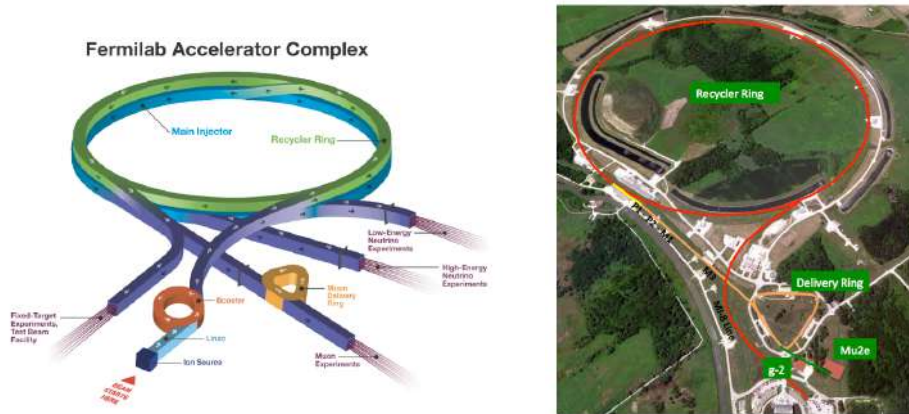


**Figure 2.3:** Layout of the accelerator complex providing the proton beam to Mu2e.

Starting from hydrogen gas, a Cockcroft-Walton generator accelerates negative hydrogen ions up to 750 keV. In a LINAC these ions are accelerated up to 400

MeV and the electrons are removed. Then protons are injected into the Booster
Ring, where they are accelerated and organised into 8 GeV batches before being
delivered to the Recycler Ring. As shown in Figure 2.4 bunching in 14 protons
batches is performed in the Recycler Ring at a rate of 15 Hz each cycle using a RF
manipulation sequence. In a cycle two batches are reserved for Mu2e, the other 12
are delivered to the NO$\nu$A experiment. Every 1.7 $\mu$s a proton bunch of $\sim 3 \times 10^7$
(referred as $\mu$bunch in the following) is injected into the Mu2e beam line using a
resonant extraction with an extinction factor of $10^5$[55]. A further extinction factor
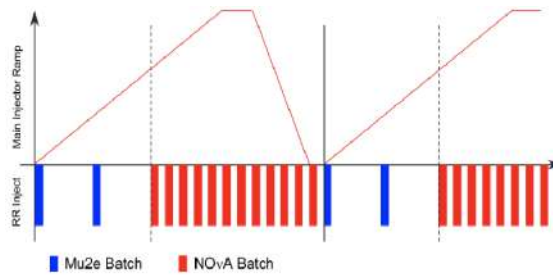


**Figure 2.4:** Time structure of the proton batches from the Recycler Ring

of $10^7$ is provided by a system of resonant magnets and collimators in the beam
line, so to ensure a safety margin of two orders of magnitude on the extinction
requirement. An extinction monitor system, located above the Production Target,
is used to check that this extinction level is achieved (see Figure 2.5). It is designed
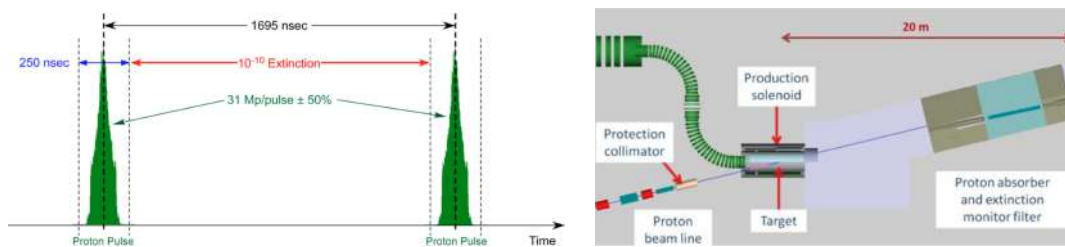


**Figure 2.5:** Left: the proton bunch structure required by the Mu2e experiment. Right: location
of the extinction monitor system.

to monitor the beam extinction and provides a measure of this EF in three-hour
running period. The monitor system consists of a collimator aimed at the target, a
set of trigger scintillators, a pixel telescope, and a muon range stack. The tracker is
intended to measure $\sim 4$ GeV/c tracks coming from the target.

## 2.3   The production Solenoid

The production solenoid is a high field superconducting magnet with a graded field varying from 4.6 T to 2.5 T. The solenoid is approximately 4 m long and has an inner bore diameter of about 1.5 m.

A shield structure made of bronze is placed in between the inner bore and the PS coil to limit its radiation damage. A sketch of the PS is reported in Figure 2.6 left. The 8 GeV proton beam enters in the middle of the PS and strikes a radiatively cooled tungsten target, producing mostly pions. After a long study the final design
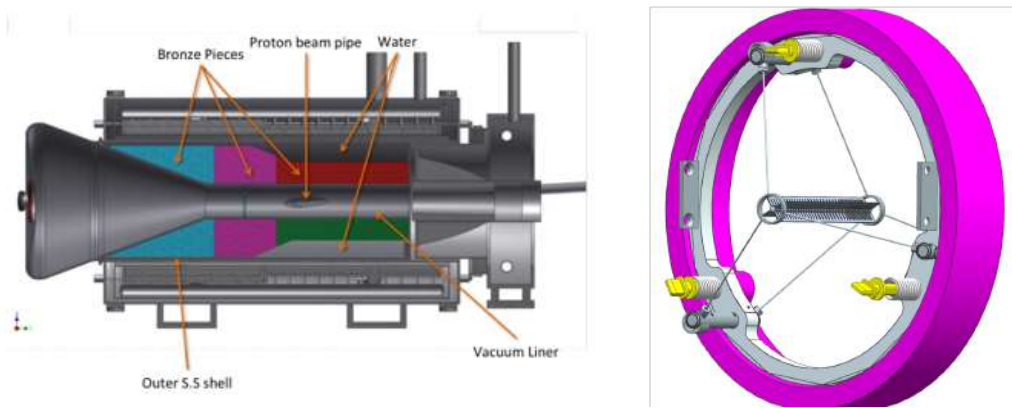


**Figure 2.6:** Left: layout of the Production Solenoid. Right: tungsten stopping target for the primary proton beam.

of the production target is shown in Figure 2.6 right. It is composed of 160 mm of segmented tungsten with four 1 mm thick $\times$ 13 mm tall fins ensuring the structure support. The tungsten has been chosen as target material because of its thermal properties: the high melting point and the low thermal expansion coefficient.

The axially graded magnetic field, creating a "magnetic bottle", reflects the charged particles emitted in the opposite side with respect to the TS entrance toward the low B-field regions, where the PS is linked to the TS. The $p_t/p$ ratio, in fact, decreases as the magnetic field decreases, enhancing the particle movement in the direction of decreasing gradient. This approach was validated by the MuSIC experiment R&D (at J- Park) [56]. The new design of the target better handles the problems due to temperature but it reduces of $\sim 17\%$ the muon yields( 0.0018 % to 0.0015 %).

## 2.4 The Transport Solenoid

The TS consists of 27 superconducting sections, both straight and toroidal. It is needed to select and transmit low energy negatively charged muons ($p < 80$ MeV/c) from the PS to the DS, using a series of collimators and absorbers installed inside. The Transport Solenoid consists of five distinct regions (Figure 2.7) :
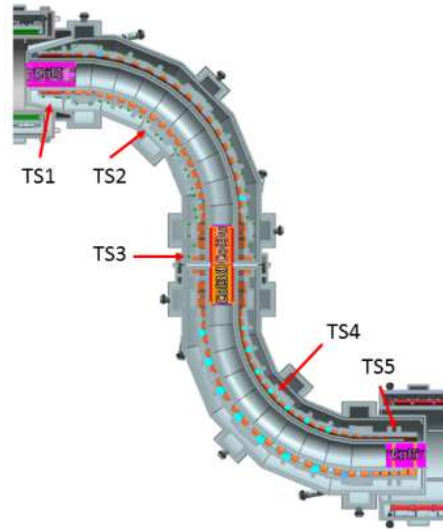


**Figure 2.7:** Transport Solenoid view.

- a 1 m long straight section (TS1) that links the PS to the TS and houses a collimator that selects particles with momentum lower than 100 MeV/c

- a 90° curved section (TS2) that avoid neutral particle from the PS to propagate into the DS;

- a second straight section about 2 m long (TS3) containing two collimators, for filtering particles based on charge and momentum, separated by a beryllium window, needed for stopping antiprotons;

- a second 90° curved section (TS4) that brings the beam back to its original direction and does not allow neutral particles from the beam interactions in the TS3 to reach the DS;

- a third straight section of 1 m length (TS5) that is equipped with a collimator for momentum selection.

## 2.5 Detector Solenoid

The Detector Solenoid is a large, low field magnet that houses the muon stopping target and the detectors to identify and analyze conversion electrons from the stopping target (Figure 2.8) .

It is nearly 11 m long with a bore diameter of about 2 m. The muon stopping
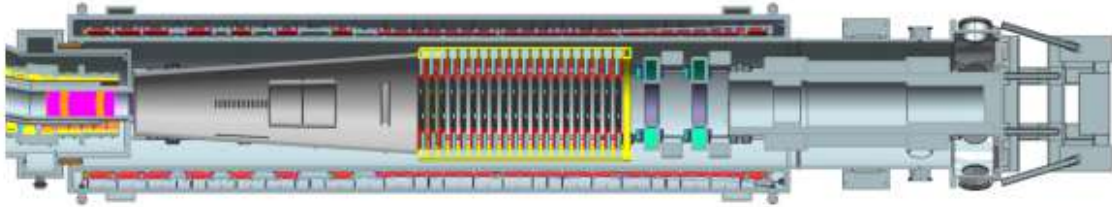


**Figure 2.8:** Detector Solenoid view.

target is placed in a graded field that varies from 2 to 1 Tesla so that it captures conversion electrons emitted in the direction opposite to the detectors and reflects them towards the detectors. The graded field is important also for reducing the background from high energy electrons: since they are accelerated towards the detector, their resulting angle is inconsistent with the angle of a conversion electron from the stopping target. The detectors reside in a field region that is relatively uniform.

### 2.5.1 The muon stopping target

The muon-stopping target is designed to optimise the production of stopped muons while minimising energy straggling of putative conversion electrons and backgrounds from materials supporting the target. There are a number of competing factors that must be evaluated to determine the appropriate element for the target material:

- the material should be chemically stable and sufficiently chemically pure so

that muons stopping in the impurity elements do not contribute significantly to the background;

- muon lifetime in a bound system has to be long compared to the transit time of prompt backgrounds (greater than a few hundred ns). The muon lifetime in the target should also be well matched to the time between beam pulses;

- the expected conversion rate increases with atomic number, reaching maximum with tungsten and antimony, then drops. However, the lifetime of muonic atoms decreases with increasing atomic number. The target element must be chosen to maximise the sensitivity of the experiment to $\mu - e$ conversion.

The target baseline design, shown in Figure 2.9 (left) is composed of 37 concentric aluminum disks, of 100 $\mu$m thickness, with 22.2 mm disk-to-disk spacing. The target disks are supported by thin tungsten wires and attached to the target support structure. Also the geometry of the target plays an important role in reaching the
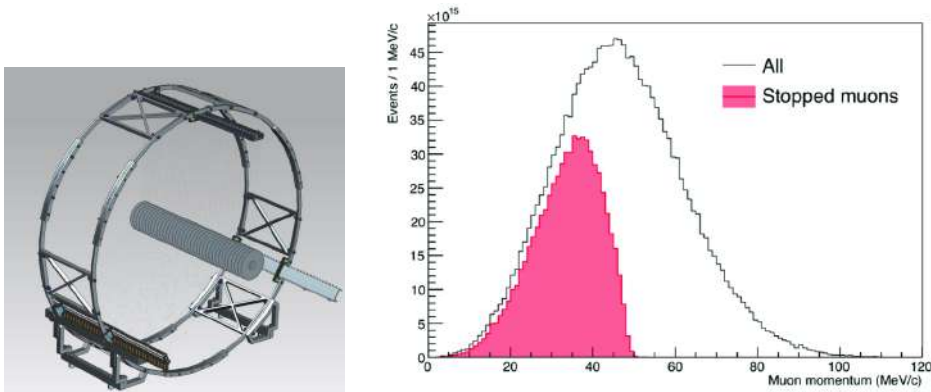


**Figure 2.9:** Left: View of the Stopping Target. Right: Momentum distribution of all muons reaching the Stopping Target together with those that do stop, normalized to the standard exposure of $3.6 \times 10^{20}$ POT

expected sensitivity:

- The target must be sufficiently thick in the direction of the muon beam trajectories to stop a large fraction of the incoming muons. The target should stop at least 40% of the transported muons to reach the desired sensitivity given the expected proton flux and the design of the solenoid system (see Figure 2.9 (right));

- the target geometry must not significantly degrade resolution due to the path length of hypothetical conversion electrons ;

- thickness and geometry should be tuned to control background from Bremsstrahlung caused by beam electrons traversing the target, delta rays produced in the target by energetic cosmic ray muons, other cosmic ray interactions, scattering of the incoming beam into detectors, etc.;

### 2.5.2   The straw tubes tracker

The Mu2e tracker measures the trajectories curvature of the particles to reconstruct their momentum [57]. The material of the tracker must be as low as possible to reduce the multiple scattering, which is the main source of errors in the reconstruction procedure. Moreover, the high rates of the Mu2e environment can generate background from spurious hits of low energy particles, which can combine mimicking a CE trajectory. In Figure 2.10 (left) the final tracker design is reported; it consists of 23040 drift straw tubes placed transverse to the axis of the DS. The choice for
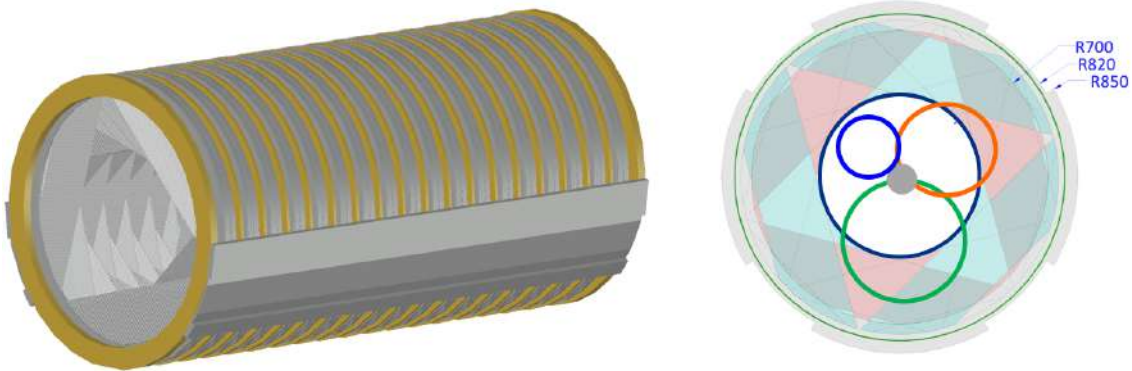


**Figure 2.10:** Left: The Mu2e straw tubes tracker. Right: cross sectional view of the Mu2e tracker stations with the trajectories of a 105 MeV CE (green circle) and a 53 MeV Michel electron (orange circle) superimposed. The disk in the center is the Stopping Target. Electrons with energies smaller than 53 MeV (blue circle) miss the tracker passing through the central hole.

drift gas is Argon: $CO_2$(80:20) with a maximum operating voltage of 1500 V. The basic tracker element is a 25 $\mu$m gold plated tungsten sense wire centered in a 5 mm diameter tube, referred to as a straw. Each straw is made of two layers of 6 $\mu$m Mylar, spiral wound, with a 3 $\mu$m layer of adhesive between layers. The

total thickness of the straw wall is 15 $\mu$m. The inner surface has 500 Å of aluminum overlaid with 200 Å of gold as the cathode layer. The outer surface has 500 Å of aluminum to act as additional electrostatic shielding and to reduce the leak rate. The straws vary in active length from 334 mm to 1174 mm and are supported only at their ends.

Groups of 96 straws are assembled into panels. In order to reduce the "right-left ambiguity", each panels is composed of two layers of staggered straws. Six panels (three per side rotated by 120°) are assembled into planes. Each face of the planes is made of three panels, rotated by 30° .

A pair of planes makes a station, each station is separated by 46 mm and is rotated of 180° around the vertical axis with respect to the first plane. The Mu2e tracker is composed of 18 stations.

Using this design all the electrons with low momentum, p < 53 MeV, will pass through the central hole, increasing the tracker purity (see Figure 2.10 right) As shown in Figure 2.11 the tracker is required to have a high-side resolution of $\sigma \sim$120 - 180 keV with small positive tails, since these tails could increase the contribution of the background events, promoted into the signal region, from the fast falling DIO spectrum.
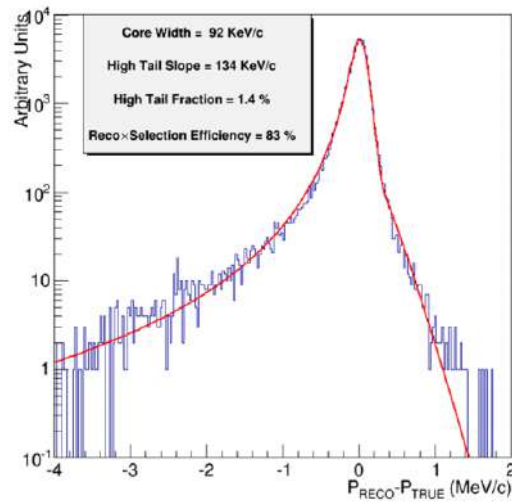


**Figure 2.11:** Tracker momentum resolution with conversion electrons. Full background overlay and pattern recognition included. Fit to a split double Gaussian with standard track fit quality cuts. The core width satisfies the 180 keV momentum resolution requirement.

### 2.5.3    The crystal calorimeter

The Mu2e calorimeter has to reject backgrounds to a level consistent with single
event sensitivity for $\mu$-e conversion of the order of $3 \times 10^{-17}$. Such background
could be produced by cosmic ray muons not vetoed by the Cosmic Ray Veto system
producing a track that seems to come from the target with a momentum in the 105
MeV acceptance window. The primary purpose of the Mu2e calorimeter is to provide
a second set of measurements that complements the information of the tracker (e.g.
particle identification) and enables us to reject these backgrounds. A calorimeter
with good energy ($\sigma_E/E = \mathcal{O}(10\%)$) and time resolution ($\sigma_t < 500$ps) at 100 MeV
can achieve such task. Besides particle identification the calorimeter:

- provides the means to implement an independent trigger based on the sum
  and pattern of energy deposition;

- provides a "seed" to improve tracker pattern recognition and reconstruction
  efficiency;

- has large acceptance for signal electrons within the acceptance of the tracker.

A more detailed description of the Mu2e crystal calorimeter is given in Chapter 3.

### 2.5.4    Muon beam stop

The Muon Beam Stop (MBS) is located at the downstream end of the DS bore, and
is designed to absorb beam particles that reach the downstream end of the solenoid
while minimizing the background within the bore of the DS and the CRV .
The MBS consists of several concentric cylindrical structures of stainless steel and
high density polyethylene; it is coaxial with the DS warm bore, and its end plug is
on the downstream end of the DS.

### 2.5.5    Cosmic Ray Veto (CRV)

Cosmic-ray(CR) muons rain down upon the detector at a rate of about 15000 per
second. Roughly once per day one CR will produce a conversion-like event, either

by the muon itself being misidentified as an electron, or decaying into an electron, or knocking off a 105 MeV electron in the Detector Solenoid material. The CRV system provides both a passive shielding (thick layer of concrete surrounding the DS) and an active veto, with a system of four layers of long scintillator strips, with aluminum layer between them. It covers the DS and the last part of the TS, corresponding to an area of 336 m$^2$, using 86 module of 15 different types (Figure 2.12).

Each module is composed of 4 layers of extruded polystyrene scintillator counters,
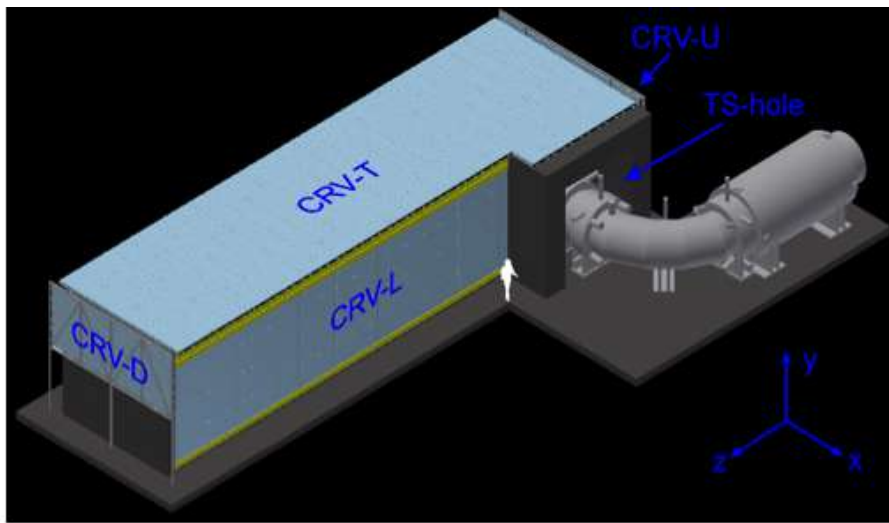


**Figure 2.12:** 3D view of the Cosmic Ray Veto.

with TiO$_2$ coating, and embedded wavelength shifting fibers, read out by SiPMs. The CRV design is driven by the need for excellent muon veto efficiency (99.99%). To obtain it the CRV has to ensure a large area coverage, the possibility to operate in a high-background environment and grant the access to the electronics. Design of the Cosmic Ray Veto is almost complete, prototypes of all components have been built, and fabrication started in 2018.

## 2.6 Status of the construction

In this section the status of the construction of the different components of the Mu2e experiment is reported. The calorimeter status will be described in Chapter 3

## 2.6.1    Accelerator

During the last period the design of Heat and Radiation Shield (HRS), shown in
Figure  2.13 has been completed.  It will be made of a bronze cylinder and water.  The
updated delivery schedule expects the system to be ready for the beginning of 2020.
As far as the beam line is concerned, the Vacuum system is completely installed and
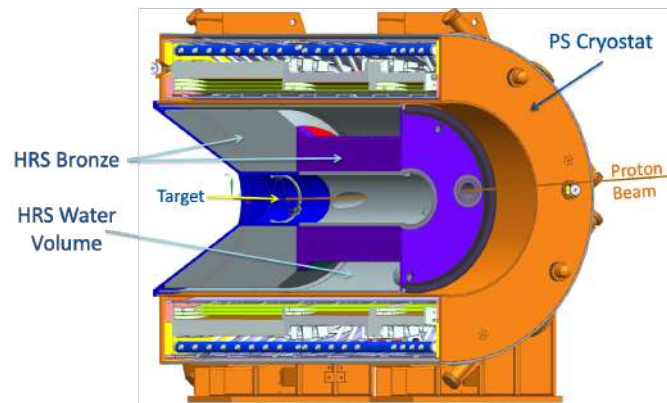


**Figure 2.13:**  Design of the HRS surrounding the PS.

near ready for operation up to the diagnostic absorber (see Figure 2.14).  Completion
of these areas will allow for 8 Gev proton to be transported for the first time in April
2020.
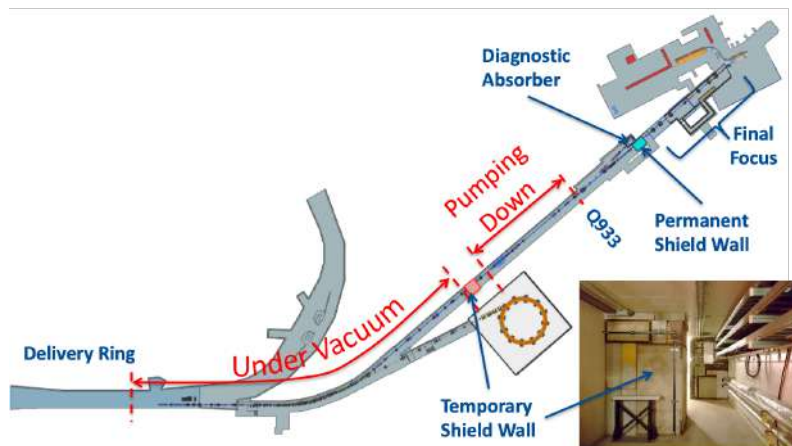


**Figure 2.14:** Sketch of the muon beam line up to the experimental hall with reported the status
of the under vacuum procedure.

## 2.6.2 Solenoids

At the moment of writing, the construction of the different components of the solenoid system is not yet concluded: concerning the cryogenic system, all the components have arrived in Fermilab and are now in assembly and test phase.

The PS and the DS are produced by the General Atomics, GA, (San Diego, Ca USA) [58] while the TS is produced by the ASG Superconductors (Genova, Italy) [59]. The conductor construction is already completed and the winding procedure is started for the PS (Figure 2.15 (left)) an the DS. Units of the TS are undergoing warm, cold (Figure 2.15(right)), and magnetic acceptance tests prior to assembly.



**Figure 2.15:** Left: picture of the winding procedure of the PS. Right: TS unit, attached to the top of the cryostat, being craned to the cryostat for cold testing.

## 2.6.3 Tracker

The panels pre-production started in February 2019 in the laboratories of the University of Minnesota (Minneapolis). The expected conclusion of the straw production is May 2020. The starting point of the panel production is the straw preparation: after having been laser cut, each straw undergoes a resistance, leak and length test. Then, in 6 days, 96 straws are assembled together to make a panel. Some pictures of the different operations performed to obtain the panel are reported in Figure 2.16.

All these procedures can be performed simultaneously on a different panel so that
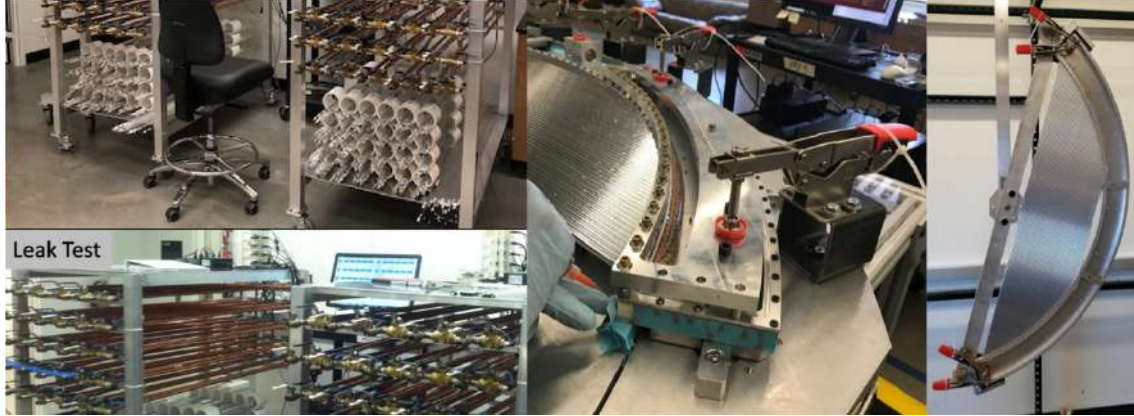


**Figure 2.16:** Top left: straw storage system. Bottom left: leak test. Middle: panel assembly. Right: an assembled panel waiting to be leak test with alcohol.

it is possible to have one panel assembled per day, assuming six assembly stations working synchronously. Moreover, a test beam on a fully instrumented panel has been organized for the end 2019.

At the moment of writing a 8 channels prototype have acquired cosmic rays event to study the longitudinal and transverse resolution. The results, shown in Figure 2.17, are well within the physics requirements and present a good agreement with the simulation.
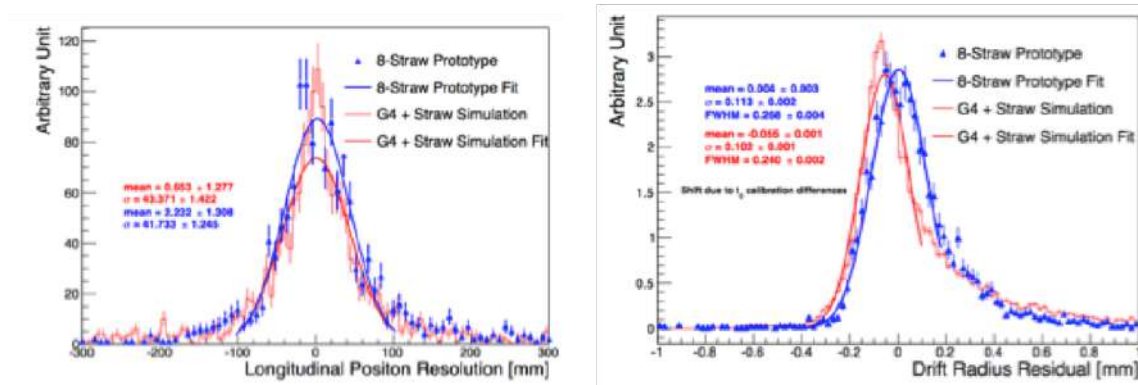


**Figure 2.17:** Left: longitudinal resolution with a 8 channels tracker prototype. The obtained resolution values are $\sigma_{data} = 42 \pm 0.1$ mm and $\sigma_{MC} = 43 \pm 0.1$ mm. Right: transverse resolution with a 8 channels tracker prototype. The obtained resolution values are $\sigma_{data} = 0.133 \pm 0.022$ mm and $\sigma_{MC} = 0.102 \pm 0.001$ mm

### 2.6.4 Cosmic Ray Veto

The di-counters production started in June 2018 and at the moment of writing $\sim$ half of them has been produced. A Cosmic Ray Test Stand has been built to test the modules with the cosmic rays; it is composed of Large-area scintillators paddles used as trigger and the test modules. In Figure 2.18 an example of a recorded CR event is reported.
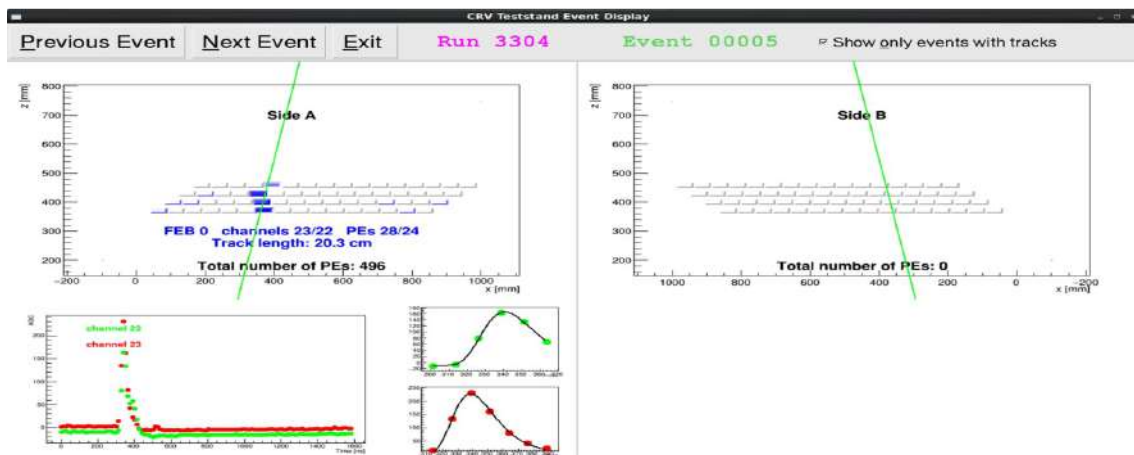


**Figure 2.18:** Track pair acquired with the CRTS and plotted in its User Interface

# Chapter 3

# The Mu2e crystal electromagnetic calorimeter

To validate the charged particle reconstructed by the tracker the Mu2e calorimeter provides information about its energy, timing and position, adding particle ID capabilities to reject muons and antiprotons interactions mimicking the signal. In addition, the calorimeter should be also fast enough to provide a tracker independent software trigger and also help the tracks seeding [60]. To accomplish these requirements it has to maximise the acceptance for $\sim 105$ MeV/c Conversion Electron (CE) tracks, operate in vacuum and survive in the "harsh" Mu2e environment. Summarizing, the design of the calorimeter is driven by the need to complement the tracker and the CRV in rejecting backgrounds to reach the required SES for the muon conversion processes.

## 3.1 Requirements

The previously stated tasks were translated in the following calorimeter performances requirements [53]:

- an energy resolution better than $\sigma_E/E = \mathcal{O}(10\%)$ (at 105 MeV), to distinguish it from the $\sim$40 MeV energy deposit from 105 MeV/c muons mimicking the signal;

- a timing resolution better than $\sim$ 0.5 ns (at 105 MeV), to ensure that the energy depositions in the calorimeter are in time with the conversion electrons reconstructed by the tracker and also improve the PID;

- a position resolution ($\sigma_{r,z}$) better than 1 cm, to match the position of the energy deposit with the extrapolated trajectory of a reconstructed track;

- keep an efficient operation in the high-radiation Mu2e environment, maintaining its functionality for radiation exposures up to $\sim$15 krad/year in the hottest region and for a neutron flux equivalent to $10^{12}$ MeV/cm$^2$ / year, inside an evacuated region ($10^{-4}$ Torr) of the Detector Solenoid that provides 1 T axial magnetic field. The radiation limits include specific safety factors related to MC evaluation $\times 3$, lot production ($\times 2$) or rate value ($\times 2$) in case pf electronics ;

- a fast enough response in order to handle the experimental high rate ($\tau < 40$ ns);

- a temperature and gain stability within $\pm$ 0.5%, to not deteriorate the energy resolution.

- Reliability and redundancy to operate in vacuum for one year without any interruptions.

## 3.2 Design

In the 105 MeV energy regime, a total absorption calorimeter employing a homogeneous continuous medium is required to meet the Mu2e requirements. A long R&D phase has been carried out to define the detector design, that was concluded in 2015 with the final technical choice [61][62]. The Mu2e calorimeter final design consists of two disks whose dimensions were optimised to maximise the acceptance for CEs. In Figure 3.1 the design of the calorimeter is shown: two annular disks with an inner (outer) radius of 35 cm (66 cm) and a relative distance of 70 cm, corresponding to $\sim$ half pitch of the helical CE trajectory. Each disk is composed of 674 square based scintillating crystals of $3.4 \times 3.4 \times 20$ cm$^3$ . To improve the reliability, each crystal is readout by two SiPMs and wrapped with a 150 $\mu$m foil of

Tyvek. The Front-End Electronics (FEE) is mounted on the rear side of each disk on the SiPMS pins, while voltage distribution, slow control and digitizer electronics are housed behind each disk in custom crates. Each Fee/SiPMs/Crystal system has its own independent powering and readout channel. Digital electronics provide a sampling at 5 ns to allow timing reconstruction and pileup separation. A laser flasher system provides light to each crystal for relative calibration and monitoring purposes. A pipes system, mounted on the front side (facing the tracker) of each disk, with a radioactive liquid source circulating inside, provides absolute calibration and a channel by channel energy scale.
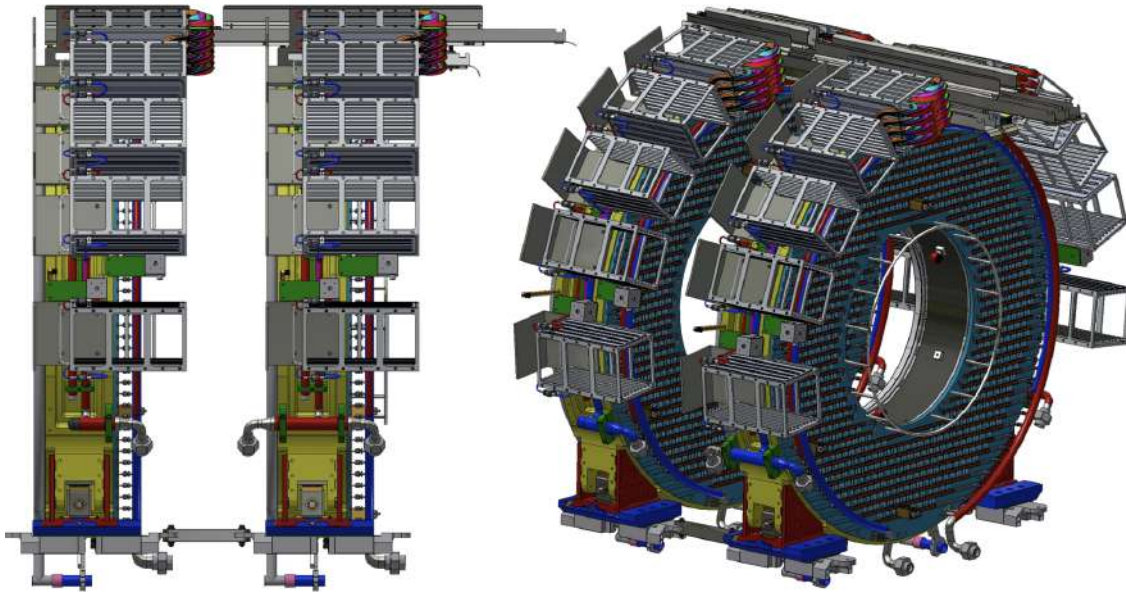


**Figure 3.1:** Top (left) and front (right) view of the two disks of the calorimeter

### 3.2.1 Crystals

Different types of crystals have been considered for the Mu2e calorimeter: Lutetium-Yttrium OxyorthoSilicate (LYSO) [63], Lead Tungstate ($PbWO_4$), Barium Fluoride ($BaF_2$) [64] and pure undoped Cesium Iodide (CsI). Table 3.1 compares properties of the crystals considered. In the Mu2e Conceptual Design Report [65] of 2012, the calorimeter baseline was based on LYSO crystals. Since then, an extensive R&D program has been carried out to study this option [66][67]. The cost of a LYSO

| Property | BaF$_2$ | LYSO | CsI | PbWO$_4$ |
|---|---|---|---|---|
| Density [g/cm$^3$] | 4.89 | 7.28 | 4.51 | 8.28 |
| Radiation length X$_0$ [cm] | 2.03 | 1.14 | 1.86 | 0.9 |
| Molière radius [cm] | 3.10 | 2.07 | 3.57 | 2.0 |
| Interaction length [cm] | 30.7 | 20.9 | 39.3 | 20.7 |
| $dE/dx$ [MeV/cm] | 6.5 | 10.0 | 5.56 | 13.0 |
| Refractive Index at $\lambda_{max}$ | 1.50 | 1.82 | 1.95 | 2.20 |
| Peak luminescence [nm] | 220, 300 | 402 | 310 | 420 |
| Decay time $\tau$ [ns] | 0.9, 650 | 40 | 26 | 30,10 |
| Light yield (compared to NaI(Tl)) [%] | 4.1, 36 | 85 | 3.6 | 0.3,0.1 |
| Hygroscopicity | None | None | Slight | None |

**Table 3.1:** Comparison of crystal properties for LYSO, BaF$_2$, pure CsI and PbWO$_4$.

calorimeter became unaffordable, due to the increase in the lutetium price. PbWO$_4$ option was excluded for its low light yield. As an alternative, BaF$_2$ and CsI crystals were considered having very similar properties in terms of light output and radiation length. BaF$_2$ has a fast component (0.9 ns) at 218 nm, but presents an important slow component above 280 nm (decay time ∼650 ns). Therefore, it needs to be coupled with photosensors able to suppress this slow component.

The absence of a "solar-blind" photosensor in this wavelength region made this option too risky to be chosen. On the other side, CsI crystals represented a good compromise for their properties and for a good matching with new generation photo-sensors. For these reasons, it has been selected as the final scintillator choice [68][69] after the construction and test of a small size prototype. The chosen length of the crystals (200 mm) corresponds to just 10 radiation lengths ($X_0$), however when considering the average CE incidence angle (50°), the effective length becomes ∼ 300 mm that corresponding to an acceptable shower containment of 15 $X_0$. Pure CsI has an emission spectrum [70] characterised by: a fast emission peak at 315 nm, with a decay time of about 30 ns, and a very small fraction of a slow emission with a decay time of ∼ 1 $\mu$s due to residual impurities in the crystal growth. Figure 3.2 shows the signal of a CsI sample crystal tested with a $^{22}$Na source and readout
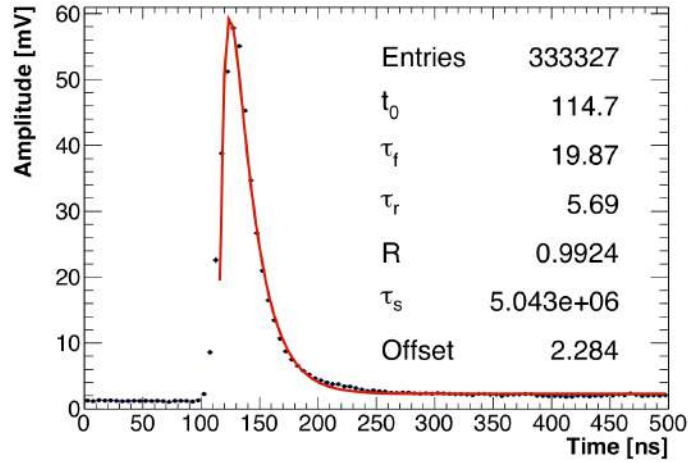
**Figure 3.2:** CsI signal with a super imposed triple exponential fit function (red), showing the fast ($\tau_f$) and slow ($\tau_s$) decay times; $\tau_r$ represents the rise time.

with a UV-extended Photomultiplier. The red line represents a triple exponential fit function, used to evaluate the rise and the decay times. The fast component resulted to be around 20 ns, while the slow one is the order of 1 $\mu$s.

Dedicated studies demonstrated that Tyvek is approximately 90% reflective for the CsI emission wavelength. Moreover, an air gap of 2 mm will be present between the crystal and the sensor readout unit, to reduce thermal coupling and to avoid using of any kind of glue or other material that can produce outgassing in vacuum or deteriorate with radiation.

A detailed description on the crystals requirements and the Quality Control tests is reported in Chapter 4

## 3.2.2 Readout sensor

The Mu2e calorimeter photosensors have to operate in a 1 T magnetic field, which drove the choice of the solid state photodetector such as Silicon PhotoMultipliers (SiPMs). In order to ensure an optimal coupling with the CsI scintillation emission, the photosensor should provide a good quantum efficiency at 310 nm. The calorimeter will be accessible for maintenance only once a year, so the photosensors must have a good reliability to avoid any deterioration of the expected calorimeter performance. Redundancy is a good mean to increase reliability, so each crystal is equipped with two photosensors, each one readout independently, for a total of

2696 SiPM and electronics channels. SiPMs are photon-counting devices made by one planar matrix of several avalanche photodiode (APD) pixels of the same shape, dimensions and construction features that are operating in Geiger mode. The SiPM operates at inverse polarization above the breakdown voltage and its pixel is coupled to a quenching resistor [71]. For the baseline calorimeter a custom SiPM has been designed: it consists of a large area $2 \times 3$ array of individual UV-extended $6 \times 6$ mm$^2$ SiPM cells. Each cell is composed by 14400 pixels of $50 \times 50$ $\mu$m$^2$ dimensions. The device Photon Detection Efficiency (PDE) depends on its energy (or wavelength), as shown in Figure 3.3 (left). The PDE is the product of three main factors

$$PDE(\lambda, V_{br}) = QE(\lambda) \times \epsilon_{av}(V_{br}) \times F \qquad (3.1)$$

where QE($\lambda$) is the quantum efficiency at a given wavelength $\lambda$, $\epsilon_{av}(V_{br})$ is the efficiency to trigger an avalanche process in the depletion region produced at the breakdown voltage V$_{br}$ and F (Filling factor) is the ratio between the sensor sensitive area and its overall transverse dimension. The chosen photosensor for the Mu2e calorimeter is a TSV-SPL SiPM from Hamamatsu [72]. SPL stands for Silicon Protection Layer, meaning an optical layer different from the standard epoxy used for the detection of blue wavelengths. The blue markers in Figure 3.3 show its PDE compared to similar devices [73]. In the UV range, 250-350 nm, the PDE of this UV-enhanced SiPM is of $\mathcal{O}(30)\%$, which is a factor $\sim 6$ better than a standard Hamamatsu SiPM.

These devices operate at low voltage while featuring a very high gain, a high PDE, a high-speed of response, an excellent time resolution and a wide spectral response range. Over the breakdown voltage, the SiPM gain is linearly related to its inverse polarization voltage as follows:

$$G = \frac{Q}{e} = \frac{(V_{bias} - V_{br}) \cdot C_{pixel}}{e}, \qquad (3.2)$$

where $V_{bias}$ is the voltage applied to the SiPM and $C_{Pixel}$ is the capacitance of a single pixel. The analog sum of the output of each pixel forms the SiPM output. Assuming all pixels to be identical and producing the same charge, the number of impinging photons is directly proportional to the charge output. When a SiPM is hit by one photon, there is a dead time (also called recovery or quenching time), due to the presence of the quenching circuit. The digital nature of the device appears
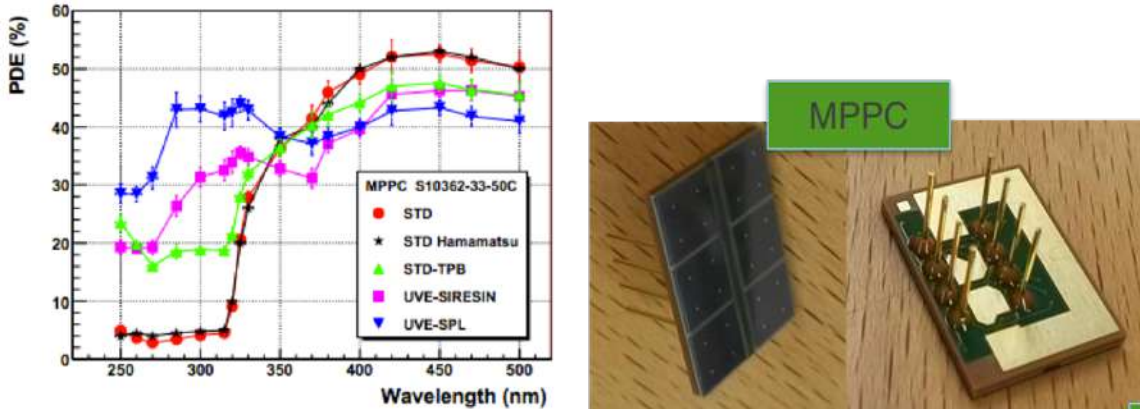
**Figure 3.3:** Left: PDE as a function of the wavelength for four SiPM prototypes. The typical PDE values of the standard SiPM S10362-33-50C from Hamamatsu are shown for comparison. These measurements were performed at 25° and include effects of cross-talk and after-pulses. Right: picture of Mu2e SiPM.

when a large flux of incident photons arrives on the SiPM area, since the number of fired pixels will saturate following the relation:

$$N = N_{max}(1 - e^{-\frac{\mu}{N_{max}}}), \tag{3.3}$$

where $N$ is the number of active pixels, $N_{max}$ is the total number of SiPM pixels and $\mu = N_\gamma \cdot PDE$ is the number of incident photons rescaled with the PDE. In order to get a linear response on the calorimeter is mandatory to select the $N_{max}$ in a way that the sensors operate in a region of photon flux $<< N_{max}$ . A basic rule is to keep it $< 5\%$. A detailed discussion about the photosensors requirements and selection tests are discussed in details in Chapter 5.

### 3.2.3 Front End Electronics

The Front-End Electronics (FEE) consists of two discrete and independent boards (Amp-HV) for each crystal that are directly connected to the back of the photosensor pins. These provide both the amplification and shaping stage, and a local linear regulation of the photosensor bias voltage (Fig. 3.4). The FEE board implements also the readout of current and temperature sensors, whose values are then transferred to the Detector Control System. The Amp-HV board requirements are the following:
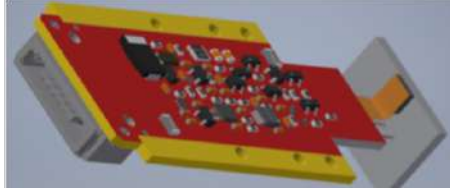
**Figure 3.4:** CAD drawing of the the AMP-HV integrated circuit with also a SiPM installed.

- two settable amplification values: 2 or 4, with a transipedance low noise amplifier;

- a signal rise time larger than 25 ns (5 times the digitizer sampling time) in order to allow at least five points to determine with precision the signal leading edge and therefore grant a good time resolution;

- a short falling time to improve pileup rejection;

- a high precision and stability in regulating and keeping the operation voltage of the photosensors ($\Delta V_{op}$< 20 mV);

- sustain a rate of 1 MHz/channel, while maintaining a stable gain, signal shape and the pileup rejection capability;

- a stable output regardless the increase of the average current due to irradiation of the photosensors or the radiation induced noise in the crystals, assuming those contributions to be contained below 2 mA;

- a low power consumption.

The FEE equivalent circuit, satisfying these requirements, is reported in Figure 3.5. A pair of Amp-HV chips and one of photosensors are arranged in a modular unit called SiPM-holder, as shown in Figure 3.6. The holder is composed of a copper support where the two SiPMs of each crystal are plugged. The support holds also the two FEE electronic boards in thermal contact by means of bridge resistors. The FEE boards are shielded by a surrounding copper Faraday cage. The last component of the holders is the optical fiber needle that will bring the light from the laser calibration system to the crystal surface, illuminating by diffusion in the Tyvek the photosensors. Each group of 20 Amp-HV boards are controlled by a dedicated
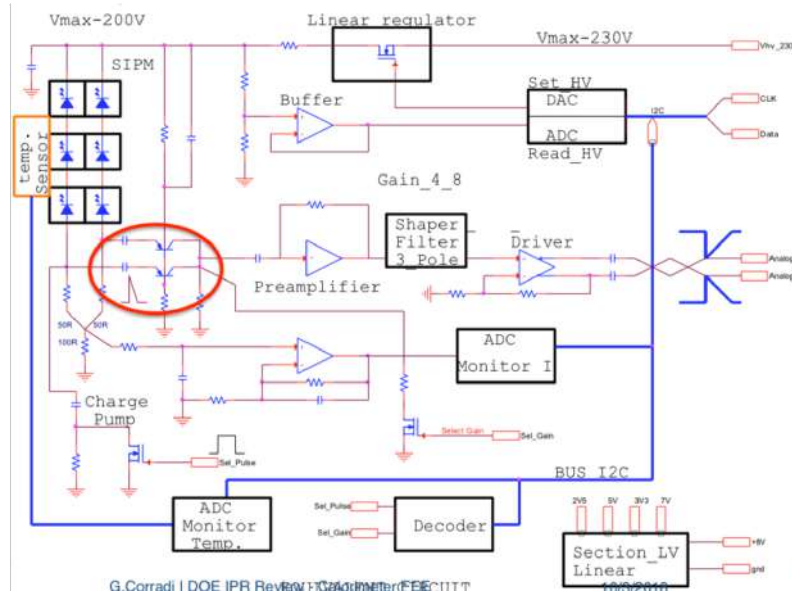
**Figure 3.5:** Layout of the equivalent circuit for the AMP-HV chip.
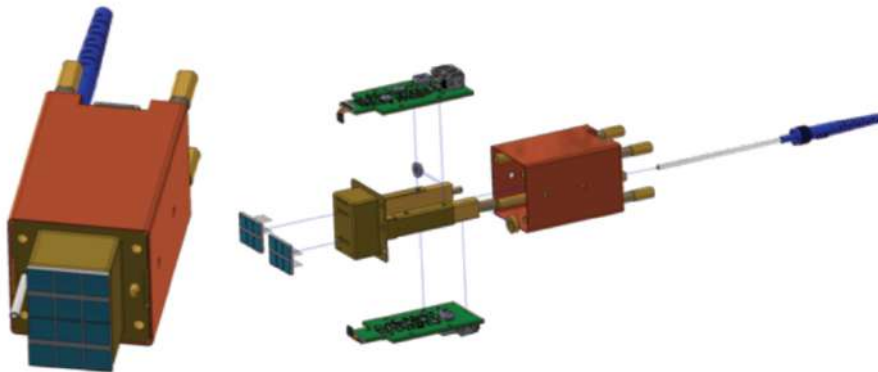


**Figure 3.6:** Left: assembly of the FEE holder. Right: exploded view of the FEE holder with all the components. Two SiPMs glued on the inner cupper support, FEE AMP-HV boards, Faraday cage and needle for insertion of the optical fiber.

Mezzanine Board (MB), where an ARM controller supervises the distribution of the low and high voltages reference values, while setting and reading back the locally regulated voltages. From each MB, sets of 20 signals are sent in differential way to the waveform digitizer (DIRAC) board (see next section). The parameters read out/set by the MB pass to the DIRAC boards, which then communicate with the TDAQ and the Detector Control System through an optical link. Both disks are

subdivided into 34 similar pseudo-azimuthal sectors, each one grouping 20 crystals.

### 3.2.4   Trigger Data Acquisition System (TDAQ)

The calorimeter has a total of 2696 fast analog signals to be digitized after being amplified and shaped by the FEE. On average, pulses of 150 ns maximum width with a rise time of $> 25$ ns are expected as input to the digitization state with a dynamic range of 2 V. The simulated shape of signals is shown in Figure 3.7 (left); this width and shape are the results of convolution between the CsI emission time, the SiPM quenching time and the FEE amplification and shaping parameters. A comparison of the experimental signal obtained with a cosmic event acquired with the DIRAC board and a digitizer from CAEN is reported in Figure 3.7 (right). The two waveforms present a similar amplitude.
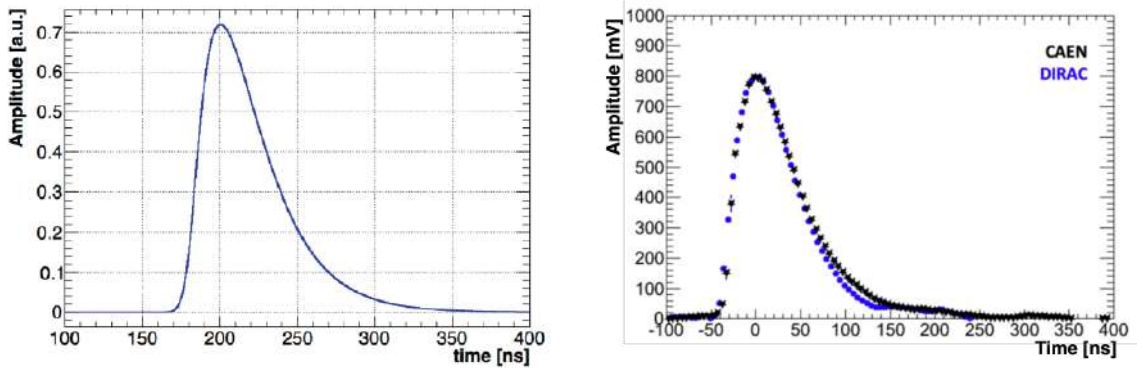


**Figure 3.7:** Left: Monte Carlo simulation of the CsI + SiPM + FEE waveform. Right: Cosmic event digitized with the DIRAC board (blue dot) and with a commercial digitizer (black star).

The digitizing system contains 140 DIRAC boards arranged in 10 crates per disk. Each DIRAC board is cooled through an copper cold plate that is kept in thermal contact with the highest dissipation components. The cold plate will be thermally connected to the crate custom aluminum structure through dedicated cardlocs. Simulations and study of the beam test data were used to optimize the digitization frequency and the bit resolution required to satisfy the Mu2e requirements: 200 Msps and 12 bits of resolution are a good compromise between performance, power dissipation, costs and overall data through-put

## 3.2.5 DIRAC

The DIRAC has to digitize and serialize analog data and send them upstream to the TDAQ system through a transceiver optical fiber. This board must also perform the zero suppression (i.e. remove signals below threshold) and provide the calculation of the baseline, mean charge and timing for each channel by means of running averages. Each board will handle 20 channels. The DIRAC block diagram is shown in Figure 3.8. After a long irradiation campaign, the basic components of the board have been
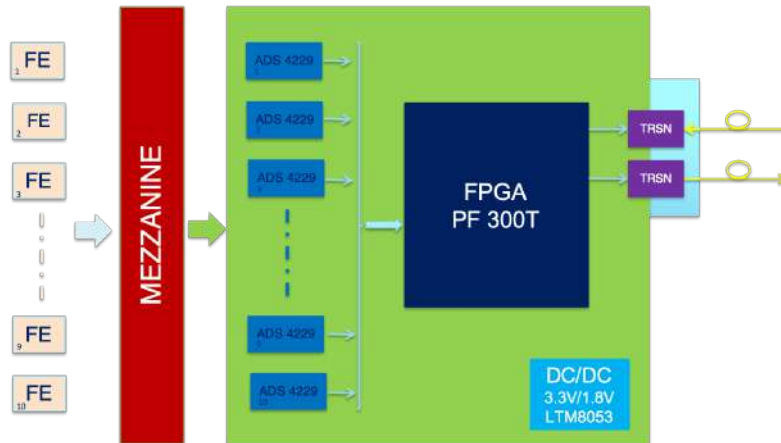


**Figure 3.8:** Block diagram for the Calorimeter Waveform Digitizer board, including also the MB and the Amp-HV chips: the principal components used are shown.

selected to stand a Total Ionizing Dose (TID) 3 krad (DC-DC converters, ADCs jitter cleaner, Double Rata Rate memories). For the FPGA, a new radiation hard version has been chosen to be consistent with the tracker choice and use the same firmware. The design is based on a FPGA belonging to to the Microsemi Smartfusion 2 family, model POLARFIRE. A very accurate jitter cleaner (LMK04828) will reduce the incoming clock jitter to less then 100 ps and distribute it to the ADCs and to the FPGA. Signals will be sampled by 10 double-channels high-speed ADCs (ADS4229) and the FPGA will perform the online operation on data and the transmission to the servers [74].

## 3.3    Mechanical Structure

The calorimeter mechanical structure is designed to support the layout of the crystals
by piling then up in a self-standing array organized in consecutive staggered rows.
The active area of the Mu2e calorimeter consists of two annular disks of 674 staggered
crystals with a square parallelepid shape, each one wrapped with a 150 $\mu$m thickness
reflective Tyvek sheet for a total weight of 700 Kg.

Figure 3.9 shows an exploded view of all the elements composing each disk. Each
crystals array is supported by two coaxial cylinders. The inner cylinder must be as
thin and light as possible in order to minimize the passive material in the region
where spiraling background electrons are concentrated. The outer cylinder is as
robust as required to support the load of the crystals. Each disk has two cover plates.
The plate facing the beam is made of carbon fiber to minimize the degradation of the
electron energy, while the back plate can be also very robust since it is needed also to
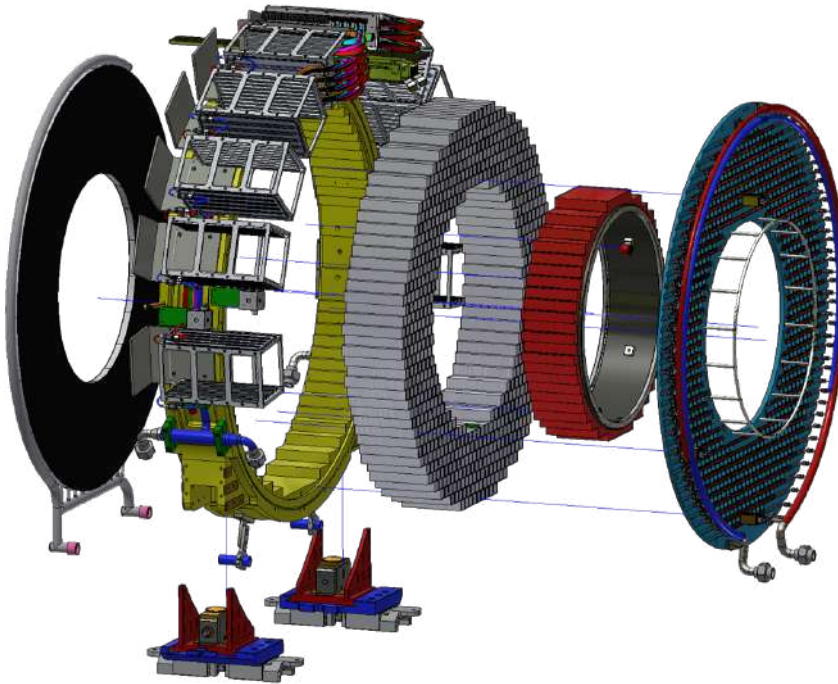support the SiPMs, the FEE and the SiPM cooling lines. The crystal arrangement



**Figure 3.9:** Exploded view of the components of the Mu2e calorimeter annular disks.

is self-supporting, with the load carried primarily by the outer ring. A catenary

structure resembling a Roman arch is constructed to reduce the overall load on the inner cylinder. The back plane will be built of plastic material with good outgassing properties, like PEEK. It provides support for the FEE electronics and SiPM holders and hosts the cooling pipes to dissipate the power of the electronics and cool down the sensors. The back plate will provide visual access to each crystal. The Front Plate will embed the piping for running the source calibration fluid.

### 3.3.1  Vacuum system/test

To reduce multiple scattering of CEs and muon stop on air molecules and prevent discharge from detector high voltage, the entire muon beam-line, DS included, must have an internal pressure of $10^{-4}$ Torr ($\sim 10^{-7}$ atm). To reach this value, the required limit for the outgassing rate of the whole calorimeter has been set at $8 \times 10^{-3}$ Torr liter/s. This value is 1/10 of the allowed tracker outgassing (that has to deal also with gas leaks from the straws) in order to make the calorimeter contribution negligible. The outgassing contribution of the calorimeter not-standard materials has been measured at the LNF-vacuum facility using the "known conductance" method [75], to determine the overall calorimeter outgassing level.The outgassing measured values are summarized in Table 3.2.

### 3.3.2  Cooling System

Since electronics will operate inside a vacuum cryostat at $10^{-4}$ Torr, the cooling is a crucial element of the calorimeter. The power generated by SiPMs, FEE and read out electronics must be removed within temperature values acceptable for the correct operation of each device. Furthermore, the difficult access to components requires a cooling system free of fault and maintenance for at least one year. The cooling system has to maintain SiPM temperature at $\sim 0°$C to minimize their dark current: this is obtained by choosing as refrigerating fluid a mixture of 35% MPG (Monopropylene glycol) aqueous solution. This fluid has good thermal properties, a low pumping power at -10 °C and the freezing temperature at -17°C. To ensure a good thermal contact, the cooling pipes are vacuum brazed to a C profile posed on the PEEK backplane and the SiPM holders are directly bolted to it, the distri-

| Component | Q *[Torr·liters/s]* |
|---|---|
| Crystal+Tyvek | $2.4 \times 10^{-3}$ |
| SiPM+FEE + holders | $2.1 \times 10^{-3}$ |
| Diffusive Spheres | $0.12 \times 10^{-3}$ |
| Laser Optical Fibers | $0.36 \times 10^{-3}$ |
| Patch-Panel- IFB Service Cables | $0.10 \times 10^{-3}$ |
| New Cables, no connectors | $0.01 \times 10^{-4}$ |
| UL on connectors | $< 0.6 \times 10^{-3}$ |
| V1 Dirac Boards + Copper +paste | $1.1 \times 10^{-3}$ |
| Mezzanine Boards | $< 0.6 \times 10^{-3}$ |
| Shells+Connectors MB | $< 0.3 \times 10^{-3}$ |
| Total | $< 7.8 \times 10^{-3}$ |

**Table 3.2:** Outgassing measurements of calorimeter components.

bution of the cooling line is reported in Figure 3.10. The maximum temperature
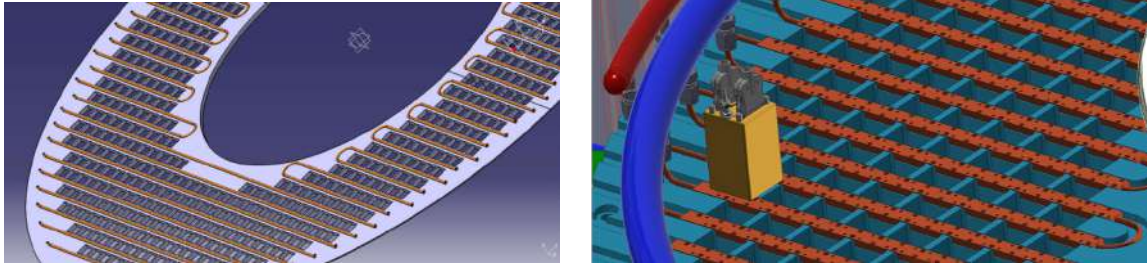


**Figure 3.10:** Left: view of the cooling back plate. Right: detail of the SiPM/FEE holders connected to the cooling lines. The thermal contact is obtained thanks to 2.5 mm screws.

of the electronic components (60 °C) is set to the half specified values (120 °C). In the Mu2e calorimeter, the crates not only house the readout electronics cards but also provide their refrigeration. The crates are integrally made of aluminum alloys. Joints are made using Tungsten Inert Gas (TIG) welding (Figure 3.11 (left)). As shown in Figure 3.11 (right), a custom copper plate over each board, fixed to the crate with two cardlocs, ensures the thermal contact between the integrated components and the crate. To guarantee the mechanical detector precision, the uniformity
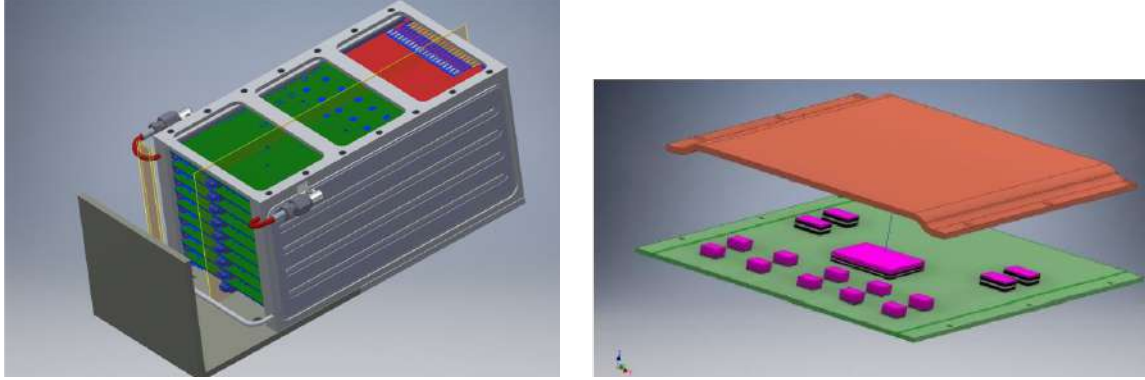
**Figure 3.11:** Left: views of the overall assembly of a calorimeter crate. Right: view of the cooling of the DIRAC board: the pink blocks represent the Thermal Interface Material that allows the thermal contact between the top cover and and the thermal plate.

of the temperature of the cooling fluid inside the pipes has been set at the level of 2°C. A long set of thermal measurements have been carried out on prototypes (board, SiPM sensors and crates) at INFN Pisa and on the full size calorimeter prototype at the National Laboratory of Frascati. These studies have shown that the temperature gradient on the crystals is under control an equilibrium temperature of the mechanical structure is achievable and the SiPMs can be cooled down at the required level with circuit losses in good agreement with the thermal simulation.

## 3.4 The calibration systems

The high sensitivity required to the Mu2e experiment implies a special care in detector calibration to avoid any related systematic effects. In the calorimeter both time and energy need calibration. To monitor the calorimeter performance, different independent calibration methods will be followed using:

- a laser pulsing system;

- a radioactive source;

- cosmic-ray muons.

- the decays of stopped muons, pions;

### 3.4.1   Laser system

A laser monitor system is used to control the photosensors gains, charge and timing resolutions, as well as to perform a fast equalisation of time offsets. A green light laser has been chosen since its wavelengths is in a region far away from the CsI emission peak (310 nm) and the transmittance changes due to irradiation are expected to be small. The overall system is depicted in Figure 3.12. A pulsed laser sends light through standard collimation optics to an optical splitting system to divide the beam into 8 equal sub-beams. By means of eight 1 mm diameter, 60 m long quartz
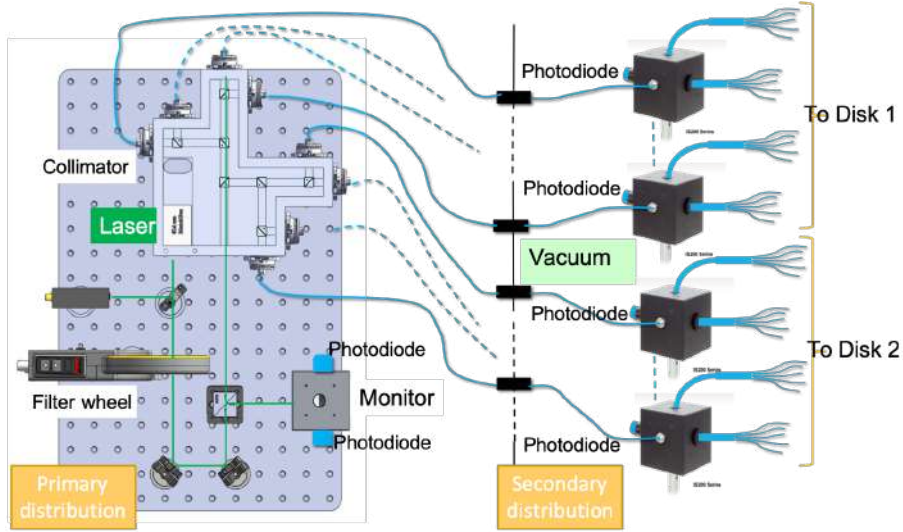


**Figure 3.12:** Picture of the primary and secondary distribution system built in Fermilab.

fibers, the light is brought inside the DS. On each disk, there are four integrating spheres with one input for the incoming fiber, two outputs for the secondary fibers bundles and one output for a monitoring photodiode .

Each bundle is composed of 110 silica fibers with 200 $\mu$m diameter and Fluorine-Doped Silica cladding, for a total of 880 fibers/disk. The end of each optical fiber is inserted in a dedicated custom needle so to arrive up to the readout side of the detector, where is inserted in the FEE/SiPM holders. In this way, the light arriving from the fibers illuminates the crystal and is readout by the photosensors. A laser pulse corresponding to an energy deposition of 50 MeV is sent at each spill-off period, i.e. once $\sim$1.4 s. The laser system is expected to provide a 0.5% equalisation of all channels in 25 minutes.

## 3.4.2 Radioactive source

A liquid radioactive source (Fluorinert$^{TM}$) will provide an absolute energy scale and a fast response equalization between crystals. This liquid source circulates through aluminum pipes on both disks surface, and is activated by a neutron source, producing the following decay chain:

$$^{19}F + n \rightarrow \; ^{16}N + \alpha$$
$$^{16}N \rightarrow \; ^{16}O^* + \beta^- + \bar{\nu}_e \; (\tau_{1/2} = 7\text{s})$$
$$^{16}O^* \rightarrow \; ^{16}O + \gamma(6.13 \text{ MeV})$$
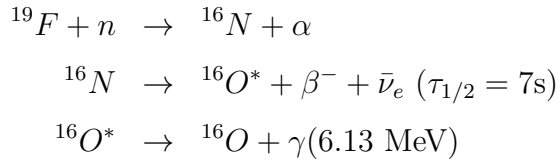
The source of neutrons is a deuterium-tritium (DT) neutron generator, providing a neutron spectrum peaked around 14 MeV. The $^{16}$N half-life is 7.13 s, with dominant $\beta$ transitions of average energy 1.942 MeV (fraction 0.662) and 4.980 MeV to the $^{16}$O ground state (fraction 0.280). The dominant photon line in the oxygen daughter is at 6.129 MeV, occurring in a fraction 0.670 of $^{16}$N decays. The next most frequent gamma transition is at 7.115 MeV with a fraction of 0.049 [76] The liquid source circuit consists of 12 Al pipes, 0.5 mm thick, with a diameter of 3/8 inches and a length which ranges from 1.5 to 1.7 m. The selected geometry allows to have an uniform illumination of the disk with a variation in the intensity smaller than 5% [77]. The 6.13 MeV photons interact with the crystals: the overall energy distribution as reconstructed by the calorimeter is shown in Figure 3.13. In this distribution the different contributions are shown: the full absorption peak at 6.13 MeV, the two escape peaks [53] respectively at 5.62 MeV and at 5.11 MeV; these peaks are then superimposed to the Compton spectrum.

The source rate is expected to be $\sim 10^4$ photons/crystal/10 minutes. The level of the equalisation that could be reach is of about 1.5%. This 10 minutes long calibration will be performed once a week, to check the absolute energy scale of the calorimeter, at low energy.

## 3.4.3 DIO Muons and Pion Decays

For energy calibration at a scale closer to 100 MeV, muons and pions decays will be used. The most promising decay channels are:
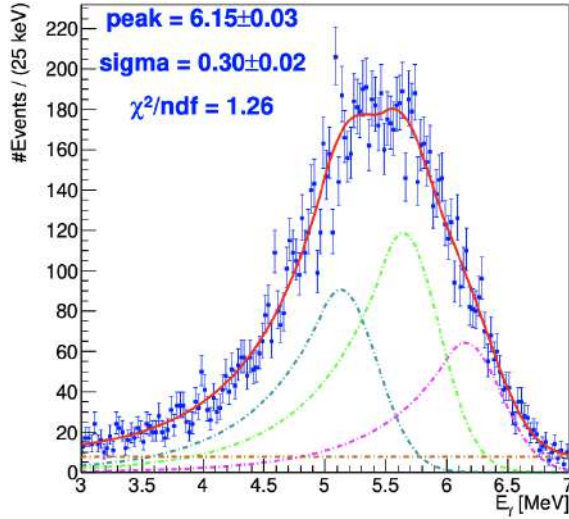
**Figure 3.13:** Energy spectrum for a crystal irradiated with 6.13 MeV photons from an $^{16}O^*$ source supposing $Npe = 20$.

- $\pi^+ \to e^+ \nu_e$ decays of pions, that produces a monochromatic positron of about 69.8 MeV;

- electrons from decay in orbit muons (DIOs), $\mu^- \to e^- \nu_\mu \bar{\nu}_e$ that have a characteristic spectrum edge at 52.8 MeV.

After matching the calorimeter cluster with the electron/positron track, the particle momentum is derived by the tracker with an accuracy much better than 0.5%, so allowing an energy calibration of the calorimeter with similar accuracy.

Unfortunately, at nominal field, both particles decay illuminate only a reduced part of the detector, due to the relation between the particle momentum and the radial coordinate. Dedicated runs at reduced magnetic fields will be required to provide a uniform coverage of all calorimeter crystals. Furthermore, when the magnetic field is reduced, the rate of particles on the detectors dramatically increases and the tracker resolution deteriorates: a reduction of the beam intensity is therefore required. DIO electron calibration does not require any modification of the beam line and can be performed in shorter times due to the larger available statistics. For this calibration, the magnetic field must be reduced to 0.5 T and the intensity at 50% of the nominal value.

### 3.4.4 Cosmic Rays

Cosmic rays calibration of the Mu2e calorimeter is complementary to all other calibration techniques described before. Cosmic ray events can be acquired during normal run operations with a dedicated trigger. The energy calibration is performed by reconstructing the cosmic muon path length and measuring the energy deposit released on the calorimeter crystals. The distribution of deposited energy in a single crystal is shown in Figure 3.14: the minimum ionizing particle peak for the Mu2e CsI crystals corresponds to a 20 MeV energy deposition.
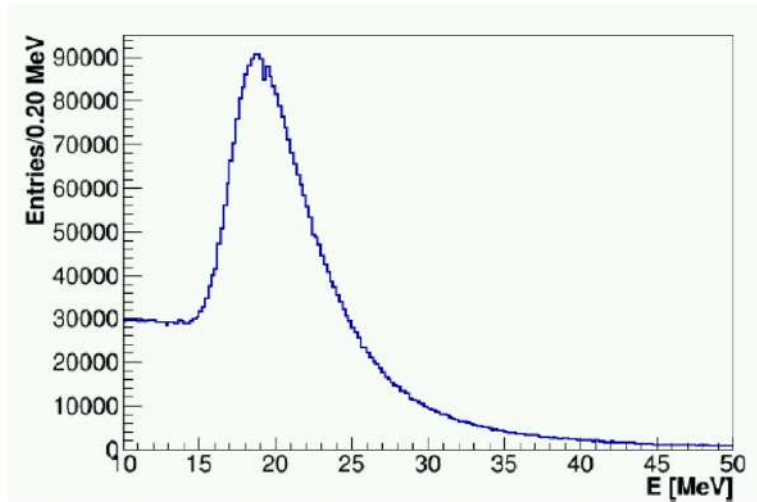


**Figure 3.14:** Distribution of the energy released by a cosmic muons in a single crystal.

The expected energy equalization is at the level of ∼1%, providing a small contribution to the calorimeter energy resolution. Since cosmic muons are relativistic particles, the time they take to cross the calorimeter can be used to align the time offsets among channels without relying to any external time reference. Following this procedure, the alignment of the time offsets alignment is expected to be within ∼50 ps. Simulation shows a rate of 15 Hz for cosmic events useful for calibration purposes, corresponding to 1000 events/crystal after ∼5 hours.

## 3.5   Simulation of the calorimeter performance

Calorimeter performance has been studied using Monte Carlo. The Event simulation proceeds in several steps. The interaction of the incident particle with the crystals is first simulated by GEANT4 [78] and the deposited energy is then converted into optical photons, taking into account an average photoelectron yield of 30 p.e./MeV and a Longitudinal Response Uniformity of few % along the crystal axis. The response of each SiPM is then simulated, including a Poissonian photostatistic fluctuation and a gaussian distributed electronic noise (150 keV equivalent). A fully digitized waveform shape is introduced as a function of number of photoelectrons. The individual hits are extracted by the single waveforms, including the possibility of multiple pile-up contributions, to form the final crystal hits. The generated pulses are then processed for reconstructing timing and energy. Time is reconstructed by performing a fit to the leading edge with an analytic function, while energy is reconstructed by integrating the pulse (detailed description of both algorithms is reported in the next chapter). Calorimeter clusters are finally formed by means of a dedicated algorithm described in the following.

### 3.5.1   Geometry

The dimension and shape of the calorimeter disks were the first issue addressed by the simulation. A simplified algorithm to estimate the signal efficiency as a function of the disk dimension was used to select the acceptable configurations. The separation between disks was set to 70 cm, corresponding approximately to a half CE wavelength. A full simulation was performed to confirm the preliminary results and select the final geometry: a crystal size of 34 mm with inner and outer disk radii of 374 mm and 660 mm, respectively. This solution is robust against small variations of the crystal size. The distance between the disks was then re-evaluated, confirming the value of 70 cm as optimal. The position of the disk with respect to the tracker has a negligible impact on the efficiency, as expected from translational invariance. Finally, the crystal length was studied, and a value of 20 cm, corresponding to approximately 10 $X_0$ chosen. Since the expected incident angle of a CE is $\sim 55°$, the crystal length ensure enough shower containment. Moreover, this geometry ensures

sufficient space to mount the readout at the back of the crystals while maintaining high reconstruction efficiency and limiting the number of readout channels.

### 3.5.2 Cluster reconstruction

The clustering algorithm starts by taking the crystal with the largest reconstructed energy as a seed, and adding one by one crystals that satisfies the following requirements:

- have a common side with the crystals already included;

- have reconstructed time within $\pm 10$ ns from the seed crystal time;

- have reconstructed energy 3 times larger than the expected electronic noise.

### 3.5.3 Energy resolution

The energy resolution has been estimated by simulating $\mu N \rightarrow e N$ conversion electrons (E=104.97 MeV) together with the expected background.

The distribution of the difference between the true signal electron energy obtained by simulation (EMC) and the reconstructed cluster energy (E) is plotted in Figure 3.15 (left). The distribution shows an higher left tail due to leakage. The energy resolution has been estimated as FWHM/2.35 = (3.8$\pm$0.1) MeV of the distribution, which is about 5 MeV RMS.

The resolution depends on crystals characteristics, such as light yield and longitudinal response uniformity. A dedicated simulation study (Fig. 3.16) showed that a longitudinal response uniformity below 5% and a light yield above 20-30 p.e/MeV are sufficient to achieve good resolution.

### 3.5.4 Coordinate resolution

The cluster position is necessary to match the reconstructed tracks with the calorimeter cluster. These coordinates are obtained using the linear energy weighted mean.
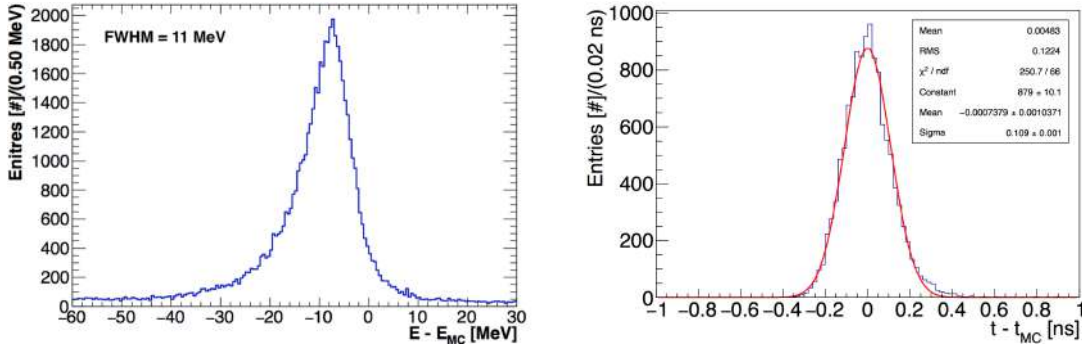
**Figure 3.15:** Left: distribution in energy residuals between the reconstructed cluster energy and the Monte Carlo value. Right: distribution of the time residuals between the reconstructed cluster time (t) and the Monte Carlo truth ($t_{MC}$).
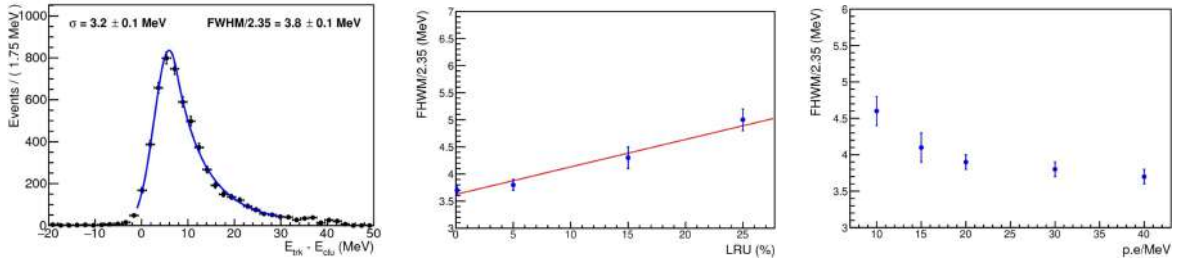


**Figure 3.16:** Left: energy resolution fit with a double-sided Crystal Ball function, quoting both core resolution ($\sigma$) and FHWM/2.35. The core resolution is more sensitive to the pile-up, while the FHWM is more representative of the "total" resolution. Middle: FHWM/2.35 as a function of crystal longitudinal response uniformity. Right: FHWM/2.35 as a function of crystal light yield.

The coordinate resolution has been estimated by simulating $\mu N \to e N$ conversion electrons together with the expected background. The distribution of the difference between the predicted and actual position of the track at the calorimeter surface demonstrates that a coordinate resolution of about 6 mm can be achieved [53].

### 3.5.5 Time resolution

As already mentioned, the simulation of the signal digitization process has been modeled using as input the waveform acquired with an experimental test. Assuming a constant pulse shape, the best accuracy is achieved by setting the signal time at a threshold corresponding to a constant fraction (CF) of the pulse height.

The cluster time is then defined as the linear energy weighted time of all the

crystals belonging to the cluster. The time resolution has been estimated by simulating conversion electrons. Figure 3.15 (right) shows the time residuals between the reconstructed cluster time and the Monte Carlo truth. A Gaussian fit to this distribution shows that the expected time resolution is of about 110 ps.

## 3.5.6 Radiation environment

Since the Mu2e experiment has an harsh environment, the calorimeter active components has to withstand to a non-negligible amount of ionising and non-ionising dose. In general, all known crystals suffer from some radiation damage. There are three possible damage effects [79] in scintillator crystals:

- damage to the scintillation-mechanism;

- radiation-induced absorption;

- radiation-induced phosphorescence.

A damaged scintillation mechanism would reduce Light Yield (LY) and may also change the Longitudinal Response Uniformity (LRU) along the crystal if the radiation profile is not uniform along the crystal axis. Photons' absorption induced by radiation reduces the light attenuation length. Contrary to other crystals, in CsI thermal annealing and optical bleaching were found to be not effective to recover this effect [80]. Moreover, radiation-induced afterglow causes a Radiation Induced Noise (RIN) that can increase the dark current in photo-detectors.

In order to understand the radiation environment of the Mu2e calorimeter crystals, a detailed simulation was performed to include all expected radiation sources as summarized in the following list:

- beam flash: all particles within the beam that do not represent a muon stopped either in the Al Stopping Target or the muon-beam dump;

- DIO electrons;

- neutrons, protons and photons produced in the stopping target via nuclear capture;

- particles produced by muons stopped outside the Al stopping target (OOT).

### 3.5.6.1   Ionising dose

The Mu2e radiation environment is calculated with a GEANT-4 based full simulation. The dose is dominated by the contribution of the beam flash, with a smaller component due to electrons from muons decaying in orbit, neutrons, protons, and photons. The distribution of the dose averaged [81] over the full disk as a function of the radius is reported in Figure 3.17, The averaged dose ranges 3.5-0.5  krad/years on the first disk and 1.1 - 0.09 krad/year on the second disk.  The SiPMs are modeled
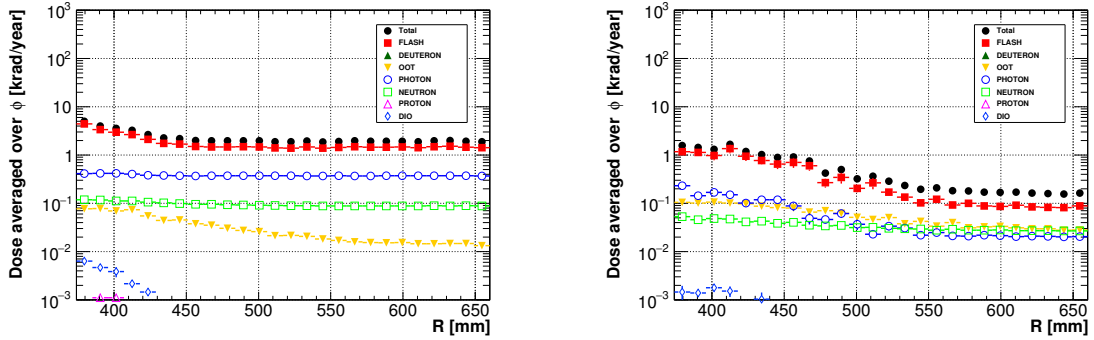


**Figure 3.17:** Expected dose in the front (left) and back (right) CsI disks as a function the radii where the crystals are located. The different contributions are also shown.

as $^9$Si boxes of $18 \times 12 \times 2$ mm$^3$.  The distribution of the dose averaged over the full disk as a function of the radius is shown in Figure  3.18; in the front disk the dose/year ranges from $\sim$2 krad down to $\sim$0.4 krad, while for the back disk, it scales from $\sim$ 1.5 krad down to $\sim$ 0.2 krad.

For the back disk, the contribution coming from the $\mu$ out-of-target (OOT) becomes comparable to the one from the"beam-flash" at radii larger $\sim$ 540 mm.

The FEE boards are modeled as a $30 \times 58 \times 3$ mm$^3$ box made of a compound of Si, Au, Al, Cu and Polyethylene. In the front disk the dose/year ranges from $\sim$ 4 krad down to $\sim$ 0.4 krad, while for the back disk, it scales from $\sim$ 2 krad down to $\sim$ 0.3 krad. The distribution of the dose averaged over the full disk as a function of the radius is shown in Figure 3.19.

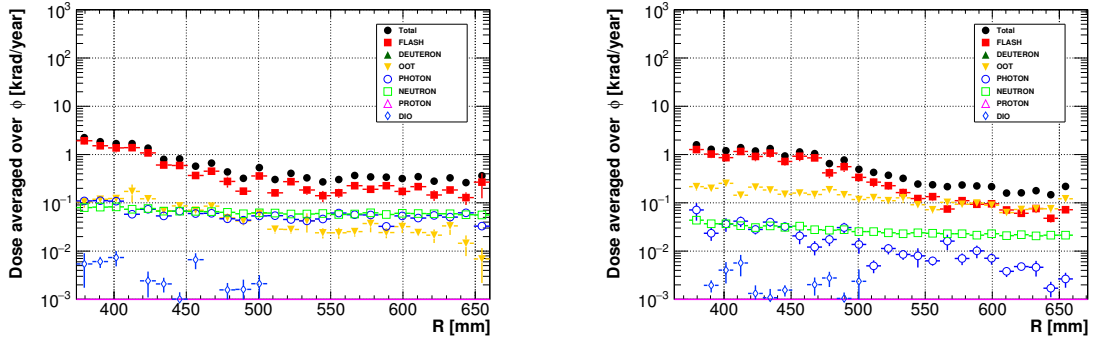In Figure 3.20 the expected average dose for the MB+DIRAC boards is shown.

**Figure 3.18:** Averaged dose deposited in the SiPM of the front (left) and back (right) disks as a function of the radii where the crystals are located. The different contributions are also shown.
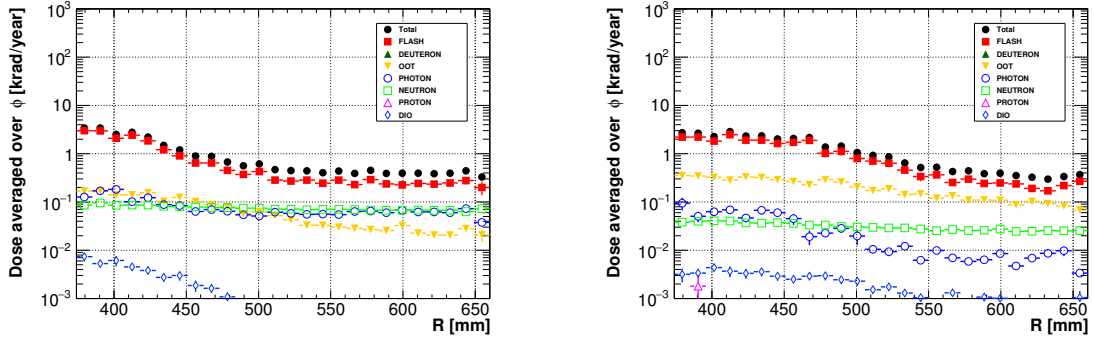


**Figure 3.19:** Averaged dose deposited in the FEE board of the front (left) and back (right) disks as a function of the radii where the crystals are located. The different contributions are also shown.

The board-Id convention sets to 0 the one closer to the crystals and to 8 the board closer to the cryostat. On both disks, the maximum average dose smaller than $\sim$ 0.3 krad/year.

### 3.5.6.2 Neutron fluence

In neutron interactions, the energy is primarily deposited by non-ionizing processes, resulting in damages due to atoms displaced from their position in the lattice structure. For neutron energies between 50 keV and 14 MeV, the neutron-matter interaction mainly proceeds through neutron-neutron elastic scattering (n,n), or inelastic neutron-neutron scattering (n,n'), neutron-proton (n, p) and neutron-alpha (n,$\alpha$) interactions. About half of the neutron energy is transferred to the nucleus (detailed

**Figure 3.20:** Averaged dose deposited in the Mezzanine+Dirac board system of the front (left) and back (right) disks as a function of the radii where the crystals are located. The different contributions are also shown.
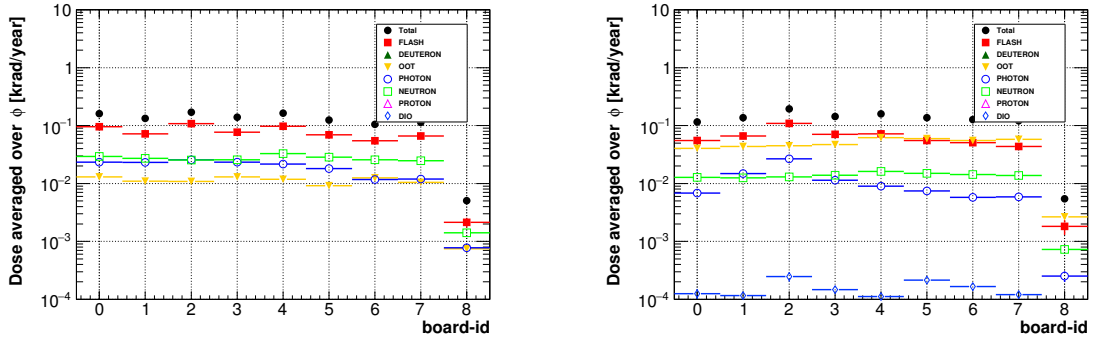
calculations are given in [82]). The displacement damage induced by neutrons in Si based devices is usually normalized to the damage induced by 1 MeV neutrons, referred to as "1 MeV equivalent damage" [83]. The expected neutron fluence on SiPMs as a function of their position in radius is shown in Figure 3.21. On both disks, the expected neutron flux is below $6 \times 10^{10}$ $n_{1MeV-eq}/cm^2/year$.



**Figure 3.21:** 1 MeV-equivalent neutron flux as a function of the radial position at the back face of the front (left) and back (right) disk. The backgrounds representing less than 1% of the total flux are not drawn.

The neutron flux was also studied for the crates. Figure 3.22 shows the expected flux on the front side of the crates (where the W/Cu shields are located). On both disk the flux on the front side are below $2 \times 10^{10}$ $n_{1MeV-eq}/cm^2/year$.
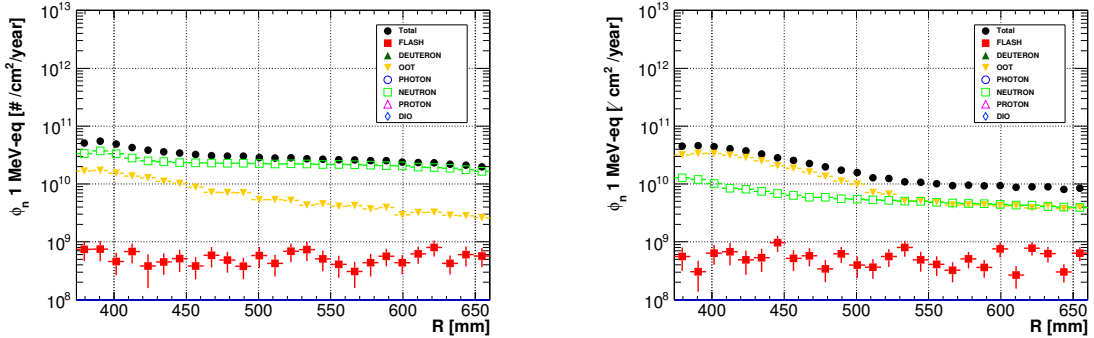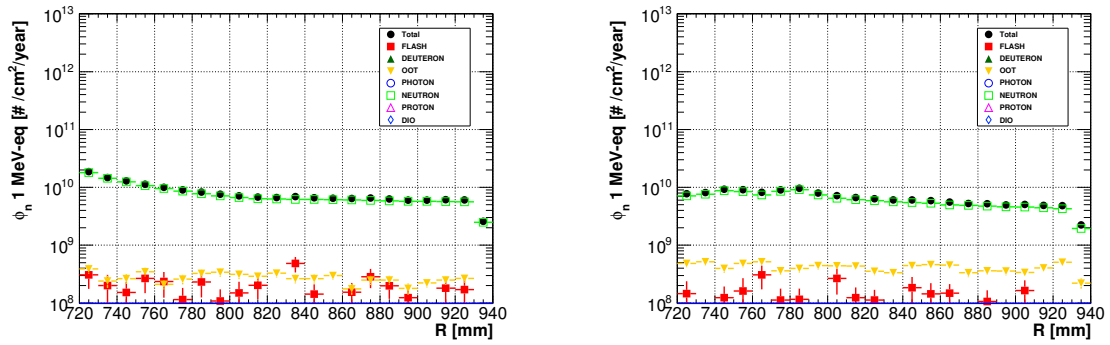
**Figure 3.22:** 1 MeV-equivalent neutron flux as a function of the radial position at the crate front shield side of the front (left) and back (right) disk. The backgrounds representing less than 1% of the total flux are not drawn.

## 3.5.7   Particle identification and muon rejection

Although the tracker momentum resolution is sufficient to distinguish a CE signal from background and it is much better than what a calorimeter can achieve (200 keV instead of few MeV at conversion energy), its single information is not enough to distinguish among particles types. This is doable combining together tracker and calorimeter information. The signals from the tracker and from the calorimeter are correlated in time. The time of the calorimeter signal, indeed, should be comparable to the time of impact of the extrapolated tracks from the tracker. The difference between these two times should be less than 0.5 ns and this value drives the timing resolution requirement of the calorimeter [53].

The calorimeter timing information can be used by the cluster reconstruction algorithm for the cluster reconstruction itself, a good time resolution helps in the connection and rejection of cells to the cluster and in the cluster merging. Moreover, timing information can also be used to improve the pattern recognition in the tracker. Finally the timing can add discriminating power to the particle identification of $\mu$ with respect to the electrons (PID). Figure 3.23 shows how the calorimeter allows a simplification of the pattern recognition: the speed and efficiency of tracker reconstruction is improved by selecting tracker hits compatible with the time ($|\Delta t| < 50$ ns) and azimuthal angle of calorimeter clusters.

The main goal of the PID in Mu2e is to separate potential electron candidates
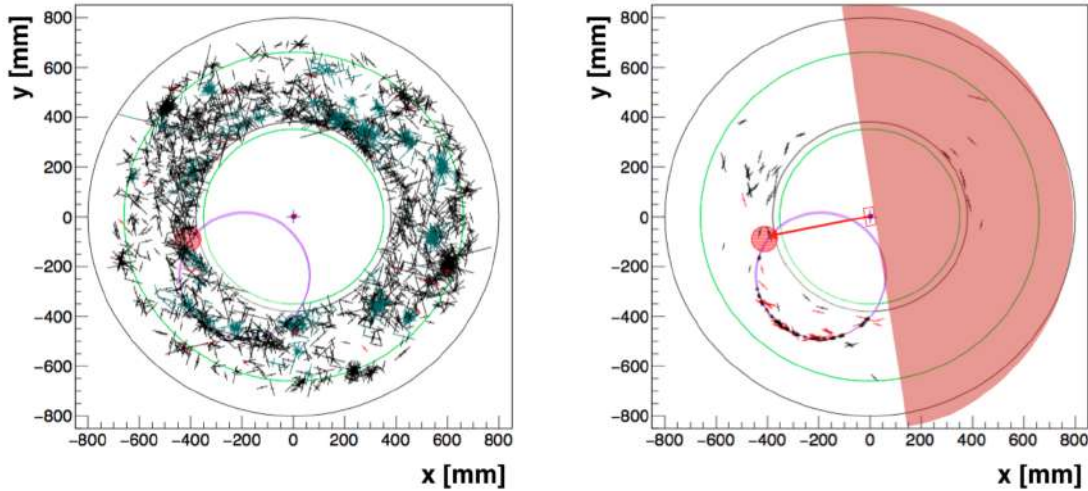
**Figure 3.23:** Distribution of the hits in the tracker before (left) and after (right) the application of a timing window based on timing information in the calorimeter. The situation for the pattern recognition is dramatically improved: fitting a helix to the selected tracker hits and calorimeter cluster increases the tracking efficiency by 9%

from muons which could be associated with the beam or produced in the showers generated by cosmic rays. Cosmic rays generate two distinct categories of background events: muons trapped in the magnetic field of the DS and electrons produced in a cosmic muon interaction with detector material. Studies on cosmic ray induced background, assuming a CRV inefficiency of about $10^{-4}$, showed that after three years of data taking one could expect about three events in which negative cosmic muons in the momentum range $103.5 < p < 105$ MeV/c enter the detector, while not being detected by the CRV counters and surviving all analysis cuts [84]. The event display of a such kind of event is shown in Figure 3.24.

Thus, to keep the total background from cosmic rays at a level below 0.01 events, a muon rejection factor $> 200$ is required. The $dE/dx$ information from the Mu2e tracker provides minor PID capabilities [85]. To reach a muon rejection factor of 200, the efficiency of the electron identification based on tracker-only information would be below 50%. The energy measurement from the calorimeter and the time-of-flight measurement that results from both detector measurements provide information for an efficient separation of electrons from muons. In Figure 3.25 the distributions of the time difference between the track and cluster times and the $E/p$ are reported both for muons and electrons at 105 MeV/c, showing a clear separation between the
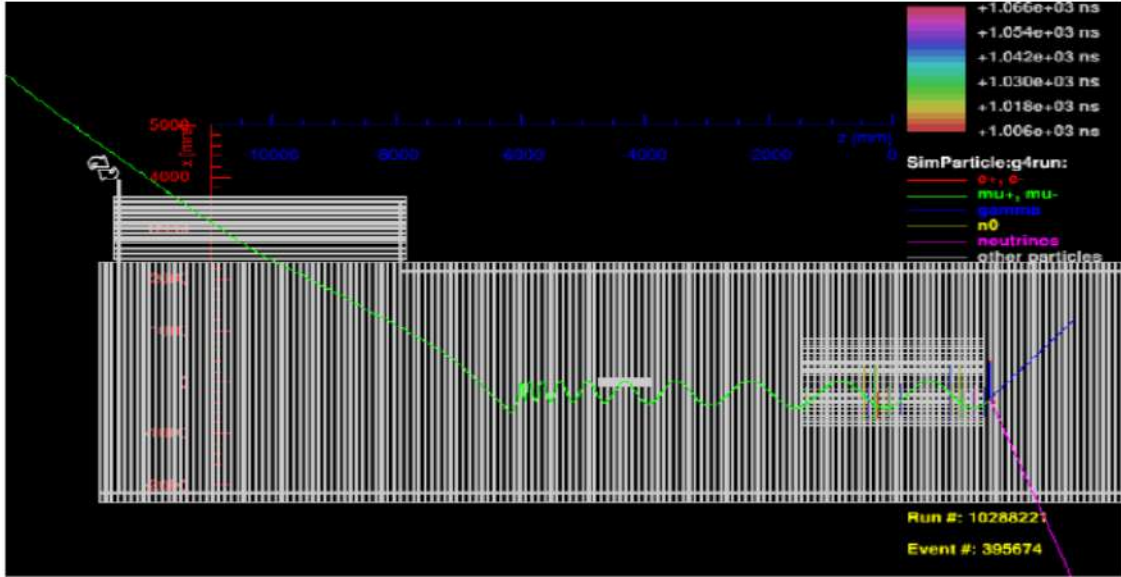
**Figure 3.24:** Event display of a negative muon from cosmic rays mimicking a CE signal.

two particles. A PID likelihood is built combining these two variables.
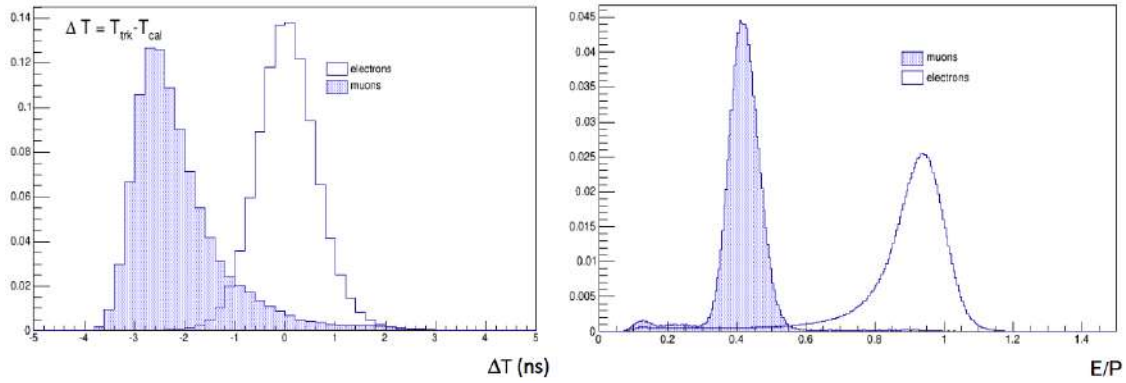


**Figure 3.25:** Distributions of time difference, $\Delta t$, between the track and the cluster (left) and $E/P$ (right) for 105 MeV/c electrons and muons [53].

The calorimeter acceptance has been optimized to reveal 99.4±0.1 % of the CEs produced from the stopping target, with tracks passing quality cuts defined in[86] and producing a calorimeter cluster with $E > 10$ MeV from the conversion electron. Therefore a reconstructed CE candidate event is required to have a calorimeter cluster, pointed to by a track.

### 3.5.8   The calorimeter trigger

In the current design, the Mu2e trigger consists of a set of software algorithms, aiming to filter with the highest possible efficiency the events of physics interest, while keeping the total rate under 2 kHz and the data rate to tape below 0.7 GB/s. Among the events of physics interest one has to include the control samples needed to calibrate the tracker and the calorimeter (i.e. DIO events and cosmic rays) or to evaluate the backgrounds for the conversion electron analysis (like the radiative pion capture events). The global requirements for the Mu2e trigger are: i) an efficiency better than 90% on the Mu2e physics data set; ii) a background rejection factor larger than 100; iii) a processing time shorter than 3.6 ms/event.

A dedicated study, based on a boost decision tree (BDT) multivariate classifier, demonstrated that a calorimeter standalone trigger can fulfill all these requirements [87] [88], by combining timing, radial position, energy and cluster topology information. The BDT classification training for the trigger has been performed using the 4.1.2 TMVA (Toolkit for Multivariate Data Analysis) libraries, provided by ROOT analysis tools [89]. The trigger classifier has been trained using ∼12000 events with CEs mixed with the expected spurious hits coming from the majority of the background sources and the same amount of pure background events. In order to optimize the efficiency on the Mu2e physics dataset, the standard Mu2e quality cuts [86] have been applied to define the CE training sample. No preselection cuts were applied to the background training sample. Different training categories have been used for the two calorimeter disks, to take into account their different occupancy and signal to background ratio. Figure 3.26 (left) reports the classifier efficiency on CEs versus the radial position of the electron impact point on the calorimeter. The efficiency drops below 80% when the radial position goes below 425 mm: this corresponds to the radius of the inner ring of crystals in the calorimeter disks. A small efficiency drop is also seen when the shower peak approaches the external edge of the disk and can be explained by the lateral energy leakage effect. On Figure 3.26 (right), the classifier efficiency on CEs versus the electron impact time on the calorimeter is shown: the efficiency is above 80% at times earlier that 700 ns that is the value used for the analysis and is steadily above 90% above 900 ns. The overall trigger efficiency is 90.5%.
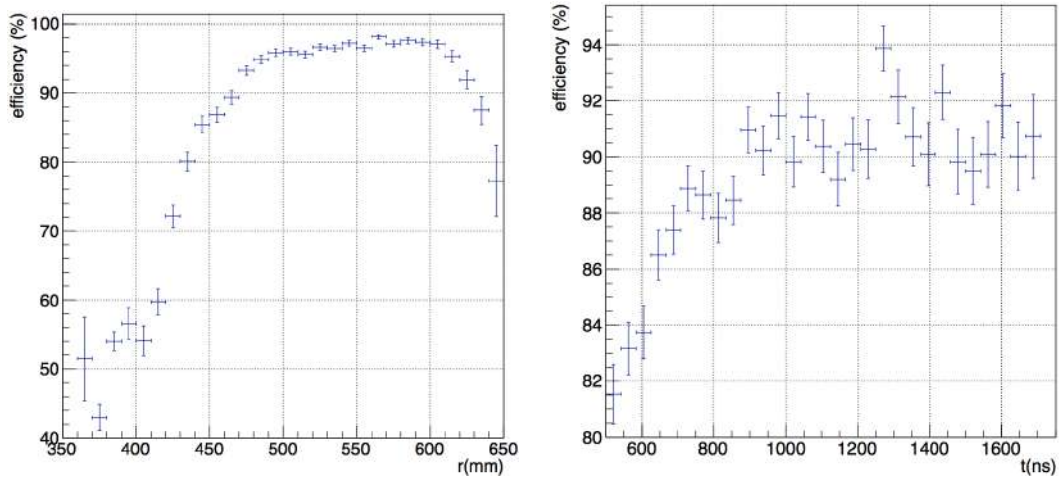
**Figure 3.26:** Left: CE BDT efficiency versus the conversion electron impact radial position after preselection. Right: CE BDT efficiency versus the conversion electron time position after pre-selection.

This trigger will take the form of a High Level Trigger filter that will be used after streaming the events to the online computing farm, but before storing data on disk. The most important aspect of this filter is that it is fully independent from the tracker. It is important for smooth start-up of the experiment when running conditions are not perfectly known and for determining the tracker trigger efficiency. The average processing time is 0.9 ms/event and may be improved by performing the digitizer waveform peak search at the FPGA level in the DIRAC board.

# Chapter 4

# Quality Control of the Mu2e Crystals

The physics requirements discussed in the Final Calorimeter Technical Design Report [90] were used to define a set of specifications on the mechanical, scintillation and radiation hardness properties of the undoped CsI crystals. The tolerances on their mechanical dimensions and shape are critical to allow a correct stacking and alignment inside the calorimeter disks. The optical properties are crucial to reach the required time and energy resolution of the detector. The radiation hardness ensures correct operation in the "harsh" Mu2e environment. At the end of 2016, a crystal pre-production selected three international vendors to control the crystals properties and allowed to chose the final providers for the calorimeter construction. The vendors for the Mu2e pre-production crystals were: Amcrys (Ukraine) [91], Saint Gobain (France) [92] and Siccas (China)[93]. Each vendor was required to produce 24 crystals to be fully characterised. At the end of this process, the selected vendors were Siccas and Saint Gobain. Information on the test performed on the pre-production crystals are reported in [94]. A detailed description of the tests performed to qualify the final production is reported in this chapter.

The Quality Control (QC) procedure works as follows: a batch of 60 crystals is shipped from each producer and received at the FNAL Shipping and Receiving office and then sent to the Mu2e Calorimeter laboratory in SiDET, Lab A [95]. Here a visual survey is carried out to control the absence of big defects such as large

notches, dents, scratches or bubbles. Soon after, the mechanical specifications are measured with the Coordinate Measuring Machine (CMM) always in SiDET.

Each crystal that does not pass the mechanical requirements is rejected and send back to the producer. Then the crystals are wrapped and the measurements of the optical properties and Radiation Induced Noise (RIN) are performed. Finally the crystals are placed in drawers where $N_2$ is flown to keep the crystals in a humidity free environment. The radiation hardness tests are carried out on a small randomly selected sample in Caltech, Pasadena (USA).

## 4.1   Mechanical Properties

Each calorimeter disk is composed by an external annular aluminum shell that provides a self-supporting structure. The crystals will be piled up inside this shell without any dedicated alveolar structure. An inner ring in Carbon Fiber allows to stack crystals around the center hole. Due to this procedure, the tolerances on the dimension and shape of the crystals are critical to allow a correct stacking and alignment of the 674 crystals per disk. Since the calorimeter will operate in vacuum,
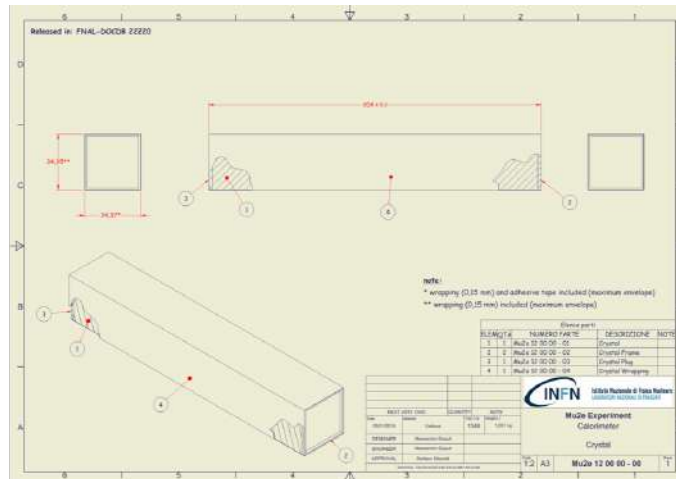


**Figure 4.1:** Technical draw of a Mu2e crystals. Dimensional tolerances are within 0.1 mm.

and in order to grant feasibility for access and replacement of the photosensors, the SiPMs will not be glued to the crystal read out face but they will be housed in an independent rigid structure (back or FEE-disk). A precise parallelepiped shape of

the crystal is also useful to ensure coplanarity among the crystals in the same layer, so to reduce any mechanical stress among crystals. A detailed engineering study defined a set of mechanical requirements as reported below:

- a well preserved mechanical integrity of the crystal (no cracks, chips, fingerprints or bubbles);

- the deviation from a perfect 3-dimensional parallelepiped has to be less than 100 $\mu$m;

- the mechanical tolerance for the transversal (longitudinal) dimensions has to be of $\pm$ 100 (200) $\mu$m.

These requirements are also summarised in the engineering drawings of Figure 4.1. After a visual inspection, the mechanical properties of these crystals are checked with of a Coordinate Measuring Machine (CMM) that acquires 112 point on each crystal: 20 points on each long face and 16 points on each small one. Starting from these measurements, the flatness of each face, the perpendicularity and the parallelism between faces are also determined. The results of the dimensional test are reported in Figure 4.2. The black line represents the requirement limits previously described. The red (green) distributions are the show the results of the CMM measurement of the Saint Gobain (Siccas) crystals. Several Saint Gobain crystals have been rejected because of they were out of the dimensional requirements.

In Figure 4.3, the number of crystals received from both vendors as a function of the elapsed time is reported. At the moment of writing, Siccas, as planned, has finished the delivery of the crystals.

## 4.1.1 Wrapping techniques

The crystals surviving the dimensional test are wrapped with Tyvek foils of 150 $\mu$m thickness and their lateral edges protected by a small plastic frame to avoid folding the Tyvek. Reflection on the side opposite to the readout is granted by a cap. The procedure used to wrap each crystal is summarised in Figure 4.4. During the data analysis of the large size prototype of the Mu2e Calorimeter (see Chapter6) an optical cross-talk between adjacent crystals of $\mathcal{O}(2\%)$ has been observed and
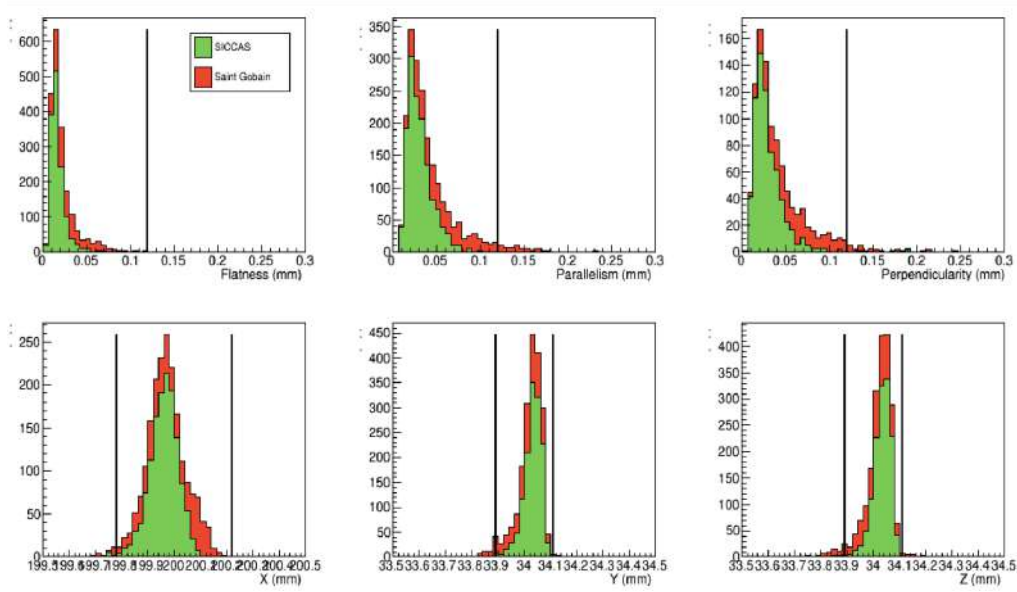
**Figure 4.2:** Results of the CMM measurements on the production crystals. Flatness (top left), parallelism (top center) and perpendicularity (top right) and the X (bottom left), Y (bottom center) and Z (bottom right) dimensions. The black lines represent the requirements.

lately confirmed with laser measurements. A single Tedlar [96] foil will be wrapped between crystal planes and another one glued on Tyvek wrapping, on the aluminum tape side. The procedure sequence is reported in Figure 4.5.

## 4.2   Scintillation properties

One of the most relevant property of a scintillator is the Light Yield (LY), which is defined as the number of photons produced per unit of energy deposited by a crossing charged particle in the scintillator. The absolute value ($LY_{abs}$) is a material specific constant and depends mainly on the energy band gap of the scintillation mechanism. The experimental number assigned to each crystal is the number of detected photo-electrons per MeV (LY). This number is related to $LY_{abs}$ according to the following relation:

$$LY = LY_{abs} \times \epsilon_L \times \epsilon_A \times \epsilon_{QE},$$
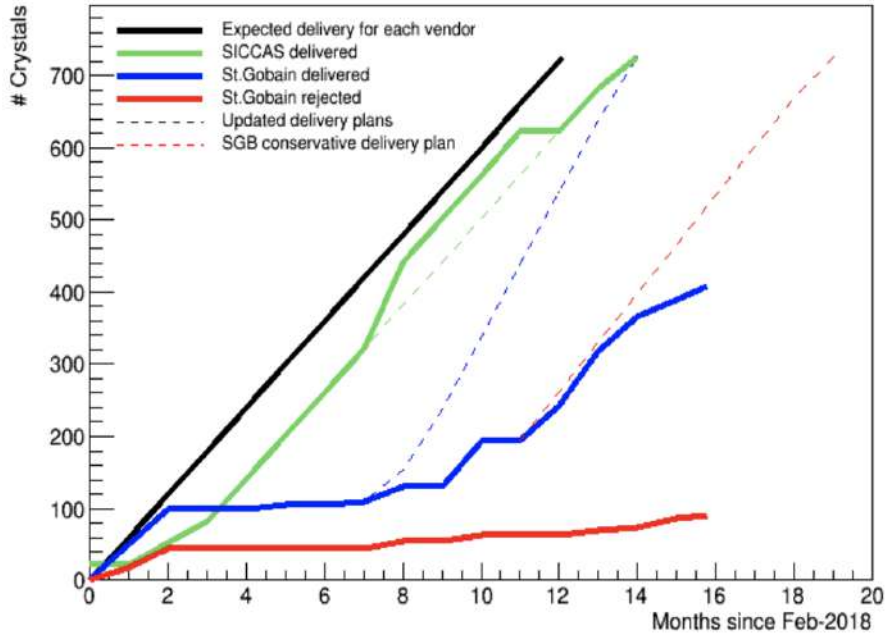
where:

**Figure 4.3:** Status of the crystal arriving in the QA room in SiDET, the black line represents the expected crystals delivery for both vendors, the dashed and the solid green lines represent respectively the expected and the effective delivery plan of crystals from Siccas. The dashed and the solid blue lines and the dashed red line represent respectively the original, the effective and the updated plan of the delivery of crystals from Saint Gobain. The solid red line is the number of rejected crystal from Saint Gobain.

- $\epsilon_L$ is the optical transmission efficiency of the scintillating photons from the interaction point through the end of the crystal where the photosensor is located;

- $\epsilon_A$ is a geometrical coupling factor between the crystal and the photodetector active area;

- $\epsilon_{QE}$ represents the quantum efficiency of the photodetector coupled to the crystal.

The light transmission within the crystal depends also on the presence of impurities that might produce internal absorption: therefore another important optical property to control is the Longitudinal Response Uniformity (LRU), that describes the dependence of the $LY_{pe}$ on the impact position of the incident particle along
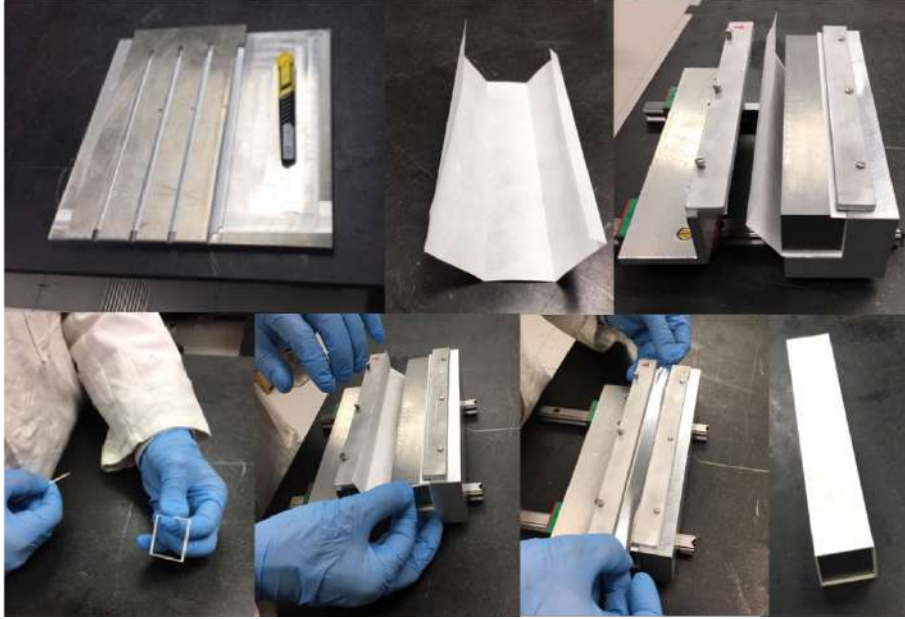
**Figure 4.4:** Picture of the several steps of the wrapping procedure.
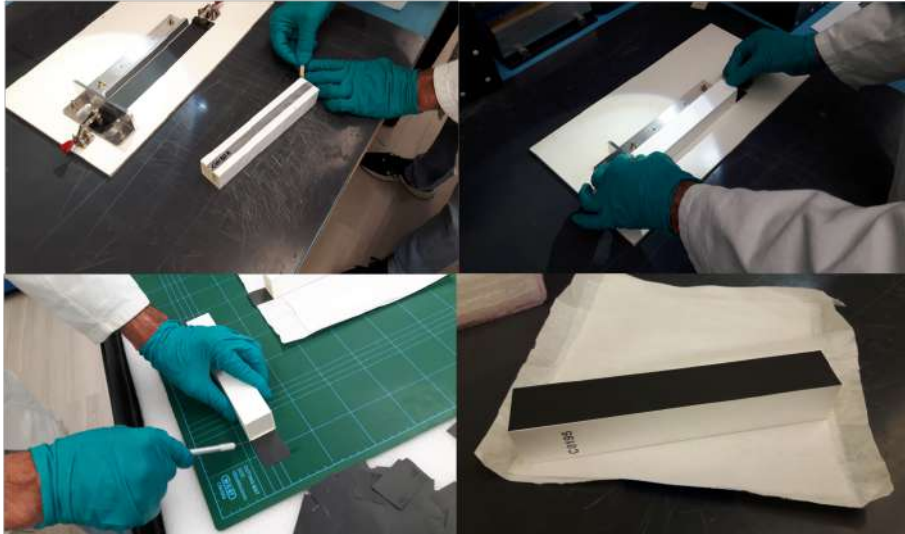


**Figure 4.5:** Steps necessary to add the Tedlar foil to the crystals wrapped.

the crystal longitudinal axis. The LRU final value is, indeed, a convolution of several effects: internal absorption, reflection, wrapping material and sensor coupling medium. The LRU is studied by measuring the LY along the axis. As previously described, the undoped CsI has an emission spectrum characterised by a fast emission peak at 315 nm with a time width of 20÷30 ns. In addition to this fast scintillation component, commercially available undoped CsI crystals may present a slow scin-

tillation component due to the presence of residual impurities or defects. This slow component has a decay time of a few $\mu$s in the wavelength region above 400 nm [97]. Moreover, it could be source of harmful pileup effects if not kept under control. In Figure 4.6(left), the emission spectra of the undoped CsI is reported. Figure 4.6



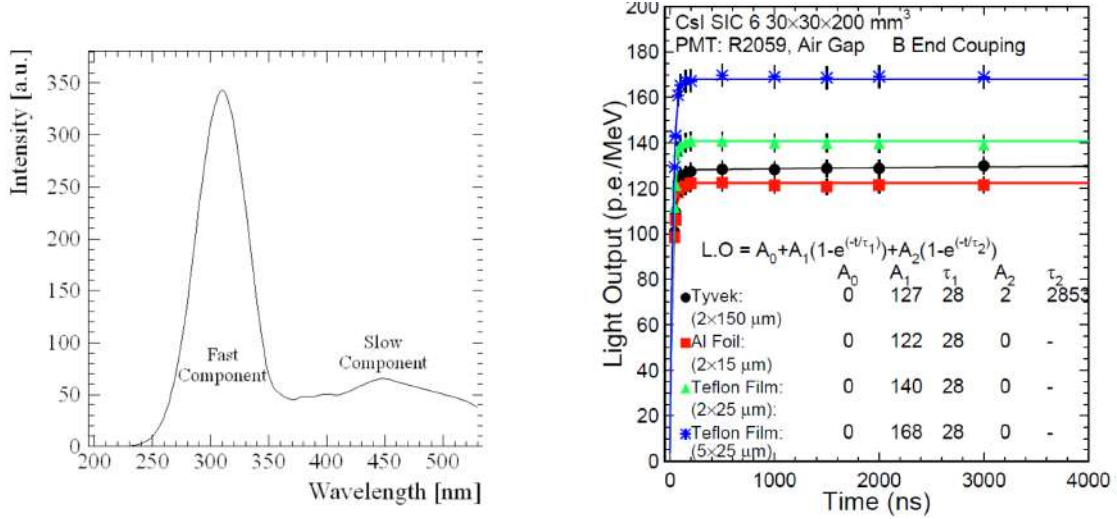**Figure 4.6:** Left: CsI emission spectrum. Right: Light output as a function of the time obtained wrapping the crystal with different material: Tyvek (black), Al foil (red), and two different thickness of Teflon films (green and blue).

(right) shows the LY (or light output, LO) as a function of the integration time for a 20 cm long CsI sample with different wrapping materials when irradiated with $^{22}$Na source. The dependence of the response on the integration time is well described by the function:

$$LY(t) = A_0 + A_1(1 - e^{-t/\tau}) \quad , \tag{4.1}$$

where $A_0$ and $A_1$ are the LY of the slow and fast component respectively, and $\tau$ is the decay time of the fast component. Fit results show that the slow component is negligible while the overall decay time of this CsI sample can be well fit with a single a fast decay component of 28 ns.

The relative contribution of the fast component can be monitored on different CsI crystals by calculating the F/T ratio, F/T= $Q_{int}/Q_{tot}$, where $Q_{int}$ ($Q_{tot}$) is the charge integrated in 200 ns (3 $\mu$s). The F/T ratio is an observable commonly used in crystal calorimetry to quote the quality of the crystals and to evaluate the relevance of the slow component. A tight requirement on the F/T variable has been set

for the Mu2e crystals.

## 4.3   Optical parameters

### 4.3.1   Requirements for the crystals

From a Monte Carlo study and from a preliminary test on few commercially available CsI crystals, a set of selection criteria on the crystal optical parameters were derived. These requirements have been applied in the following measurement conditions:

- each crystal is wrapped, on all faces excluding the read out one, with a 150 $\mu$m thick Tyvek foil;

- each crystal is read out with an UV-extended PMT, such as an Hamamatsu-R2059 or a ET-9202QB, through an air-gap. No optical glue or grease are applied to the read out sensors;

- plastic frames and cups are used to simplify the wrapping procedure (see 4.1.1

In these conditions, our technical specifications for acceptance are:

- a LY above 100 p.e./MeV;

- an energy resolution better than 20% at 511 keV;

- an LRU, defined as the RMS of the LY measured in 8 or more points along the longitudinal axis, less than 5%;

- a ratio between fast and total light yield components, F/T, above 75 %.

Crystals not meeting these selection requirements are discarded.

## 4.3.2  Optical properties measurement

A picture of the automatic QC station can be found in Figure 4.7. Before moving the crystal in measuring position, a LED emitting at 350 nm, driven with a CAEN LED driver, is fired with a pulsing frequency of 100 Hz to perform a fast calculation of the PMT gain thus allowing to follow gain variation along time.
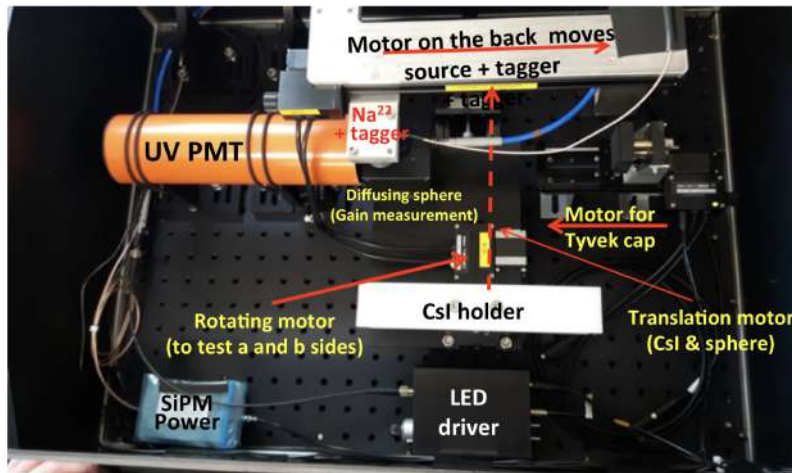


**Figure 4.7:** Layout of the station devoted to measure the optical properties of the crystals.

The crystal under test is inserted in a well precise CsI holder that, by means of a translational stepper motor, can be positioned in the center of the PMT photocatode at a distance that is typically below 500 $\mu$m. In the QA-station we use an additional translational stepper motor to move a very precise Tyvek cap in the free side. This, together with a rotating motor, allows to check both sides without dismounting the crystal during measurement. When the crystal is positioned in the right place in front of the PMT, an additional motor moves the $^{22}$Na source along the crystal axis and data are acquired with a CAEN Desktop Digitizer.

The small activity $^{22}$Na source is inserted inside an aluminum collimator. Above the source a small LYSO $(3 \times 3 \times 10)$ mm$^3$ crystal connected to a 3$\times$3 mm$^2$ Hamamatsu SiPM is positioned, in order to tag one of the two 511 keV photons coming from the annihilation process in $^{22}$Na. The SiPM signal is used also for triggering purposes. The collimation system on the aluminum holder is of around 8 mm diameter to make a small spot on the crystal face illuminated by the source. For each position the signals of the SiPM and of the PMT connected to the crystals are registered. A Labview program is used to start the readout with the Data Acquisition system

both for the source scan and the LED gain measurements. The same program also drives the data analysis in real time, thus allowing to get a complete result on the crystal in few tens of seconds after the completion of the scan. Collecting 20.000 events/position requires $\sim$ 1 minute, so that considering 8 position/side the total time necessary to measure a crystal is $\sim$ 20 minutes. At the moment of writing 1215 crystals have been already tested.

### 4.3.3   LY, LRU, Energy Resolution and F/T measurements

Figure 4.8, shows an example of recorded waveforms for the LYSO tagging system (left) and a crystal under test (right). LYSO signals are typically within 400 ns from the trigger, with a 50 ns delay, so that the charge is obtained integrating in the range between 50 and 450 ns. The baseline is evaluated using the interval region below 50 ns.

An example of the resulting charge distribution is shown in Figure 4.9. The peak
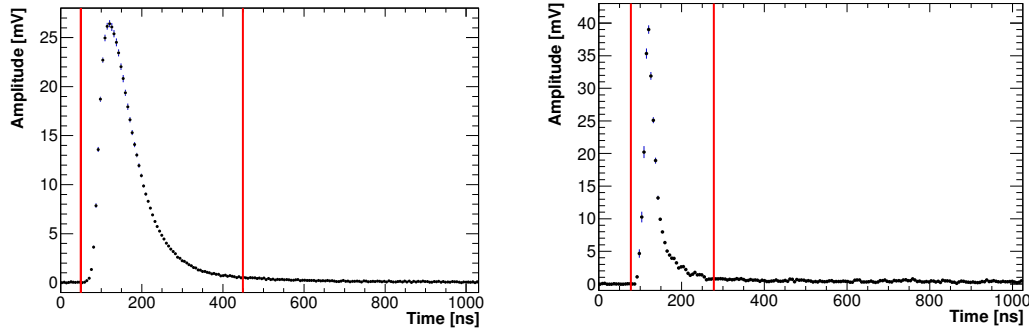


**Figure 4.8:** Left: Digitized waveform of the LYSO tag system. Right: Digitized waveform produced by the 511 keV photon in the pure CsI crystal. The red lines represent the integration range.

of the 511 keV photons for the tag is extracted performing an asymmetric Gaussian fit around the maximum of the charge distribution. Events for further processing are selected by applying a 2 $\sigma$ cut around the tag distribution peak. The charge deposited in the crystal is obtained integrating the signal in the range between 40 ns before and 160 ns after the amplitude peak, $T_{mean}$. The baseline is evaluated using the interval region below 40 ns. To reduce random coincidences, a cut on $T_{mean}$

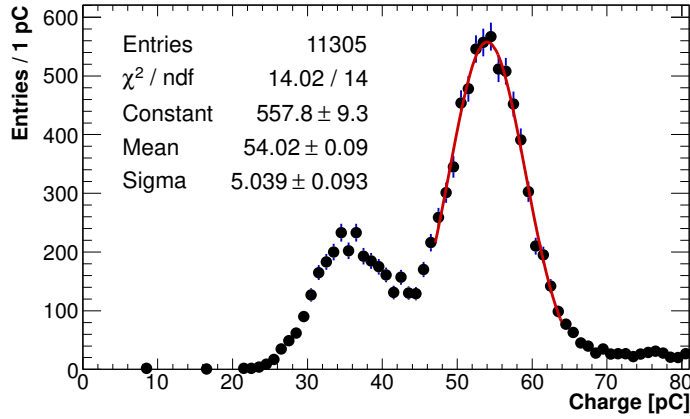**Figure 4.9:** Charge distribution of the LYSO-tag system. The distribution red fit is a gaussian function used to evaluate the mean value and the $\sigma$ of the distribution. Events are selected only if their peak time is around $\pm 2\,\sigma$ of the mean value.

is used: signals are selected only if their peak time is around $\pm 3\,\sigma$ of the time distribution mean value evaluated with a Gaussian fit (see Figure 4.10, left). In Figure 4.10 (right), a charge distribution example for one of the crystal under test, after this selection criteria, is reported. The spectra is very clean and the peak due to the 511 keV photon is clearly visible. An asymmetric Gaussian fit is performed
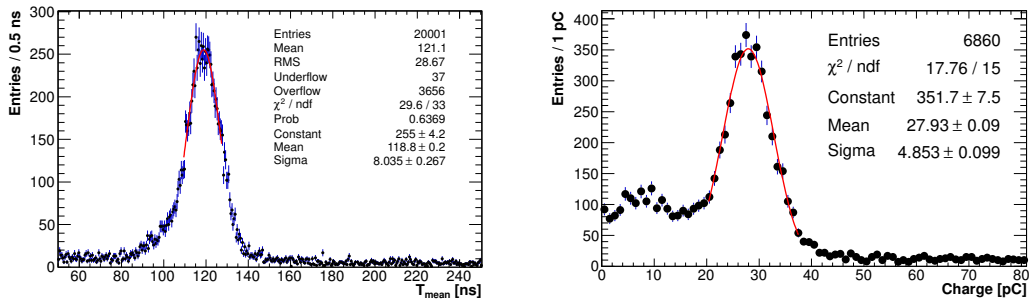


**Figure 4.10:** Left: Time distribution mean value, fitted with a gaussian function to evaluate the mean value and the $\sigma$ of the distribution. Events are selected only if their peak time is around $\pm 3\,\sigma$ of the mean value. Right: Charge distribution of the crystal under test after the timing selection and the TAG charge cuts.

around the 511 keV photon peak to extract the peak position, $\mu_Q$, with a few per mil precision. Since the number of photoelectrons follows the Poisson statistics, the

**Figure 4.11:** Left: Definition of the F/T ratio. Right: Ratio between $Q_{INT}$ and the total charge $Q_{TOT}$ as a function of the integration gate for some SICCAS crystals.

LY is obtained from the formula:

$$LY = \frac{N_{p.e.}}{MeV} = \frac{\mu_Q}{G_{PMT} \times E_\gamma \times q_e}, \tag{4.2}$$

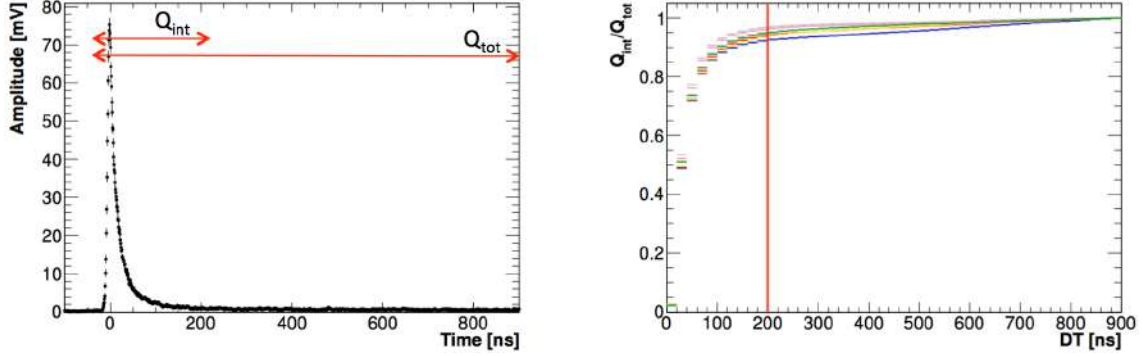where $G_{PMT}$ is the PMT gain at the operational voltage, $E_\gamma$ is the energy of the $^{22}$Na photon and $q_e$ is the elementary charge of the electron. The LRU is defined as the RMS of the eight LY values. The intrinsic energy resolution of the crystal at 511 keV is obtained by fitting the $^{22}$Na photon peak in each charge spectra of the longitudinal scan and by averaging the obtained resolutions. The fast and slow components have been studied looking at the distribution of the ratio $Q_{INT}/Q_{TOT}$ as a function of the integration gate in steps of 20 ns. $Q_{INT}$ is the charge integrated from the beginning of the signal up to the step under consideration, while $Q_{TOT}$ is the charge integrated over 3 $\mu$s range (Fig. 4.11, left). For each $Q_{INT}$, a profile histogram is constructed. The profile is then fit according to the following parametrisation:

$$\frac{Q_{INT}}{Q_{TOT}} = P_0 \cdot (1 - e^{-\Delta_t/\tau_1}) + P_2 \cdot (1 - e^{-\Delta_t/\tau_2}), \tag{4.3}$$

where $\tau_1$ and $\tau_2$ are respectively the decay time of fast and slow components. The reference ratio, used in the QC procedure is the signal integrated in 200 ns. A summary of all these properties measured on each crystal tested is reported in Figure 4.12.

The optical parameters measured are well in agreement with required specification. For the LY (top left of Figure 4.12) , there are variation along the produced sample up to a factor of two with respect to the acceptance value and a difference
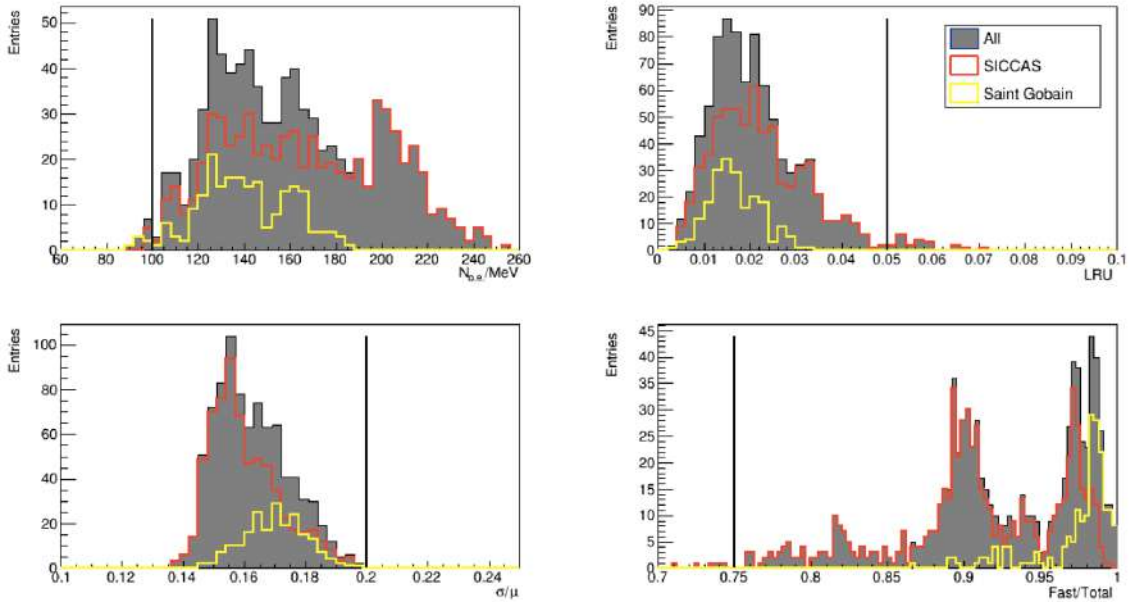
**Figure 4.12:** Number of photoelectrons (top left), LRU (top right), energy resolution (bottom left) and fast over total ration (bottom left) distributions for Saint Gobain (yellow) and Siccas (red). The comulative distributions are reported in grey. The black lines represent the experiment requirements.

of +3% in the average LY between Siccas and Saint Gobain.

The LRU (top right of Figure 4.12) is impressively good with respect to the pre-production sample tested. Indeed the average of the distribution shows LRU $\sim 2\%$ with tails > 5%.

The energy resolution (bottom left of Figure 4.12) at 511 keV is consistently better that 20% with averages of 15% for Siccas and 17.5% for Saint Gobain as related to the different LY.

Finally the F/T (bottom right of Figure 4.12) ratio is also very good; for this variable the Saint Gobain crystals are excellent showing a realy pure CsI salt, since they have a F/T$\geq$ 95%, i.e. a completely negligible slow component.

## 4.4 Radiation Hardness of undoped CsI crystals

Another important feature to be checked for the crystals is their radiation hardness, since the light output and the other optical properties can change in a high

radiation environment, thus degrading time and energy resolution. As discussed in Section 3.5.6,the expected ionising dose in the hottest region of the front disk is $\sim$ 90 krad in 5 years and the expected neutron fluence at 1 MeV equivalent energy is $3 \times 10^{12}$ neutrons/cm$^2$. In dedicated irradiation studies [98], neutrons showed to damage CsI properties much less than exposing it to a total ionisation dose (TID): a negligible variation in optical properties has been measured, testing crystals after an exposure up to $10^{12}$ neutrons/cm$^2$. On the other side, exposing 20 cm long un-doped CsI crystals to a ionisation dose resulted to reduce the light output at 70% - 80% after a TID exposure of 100 krad. Similarly from independent tests, the Radiation Induced Noise (RIN) due to ionization is observed to be much larger than that induced by neutrons. The final quality control on radiation hardness is carried out using only ionisation dose tests. After adding a safety factor to the dose rate evaluated by simulation, the calorimeter radiation hardness requirements become:

- a RIN smaller than 0.6 MeV for a dose rate of 1.8 rad/h.

- a LY higher than 85% (60%) of the initial value after receiving a TID of 10 krad (100 krad);

### 4.4.1   Radiation Induced Noise (RIN) measurement

After completing the optical properties measurement, a group of six crystals is inserted inside a light tight drawer (see Figure 4.13) and each of them is coupled to 2 Mu2e SiPMs. The number of radiation induced photoelectrons per unit of dose rate, F, is determined according to the formula:

$$F = \frac{I_{RIN}}{G_{SiPM} \times q_e} \cdot \frac{1}{\phi_{lab}}, \tag{4.4}$$

where $I_{RIN}$ is the current acquired while the source was on top of crystal, $G_{SiPM} = 8 \times 10^5$ is the gain of the SiPM, $q_e$ is the electron charge and $\phi_{lab} = 42$mrad/h is the source dose rate. In order to evaluate the number of background photoelectrons due to RIN in the final signal, N$_{RIN}$, F has to be re-scaled to the dose rate expected in Mu2e operation environment, $\phi_{Mu2e} \sim 1.8$ rad/h, and then integrated in the 200 ns gate of a typical calorimeter signal:

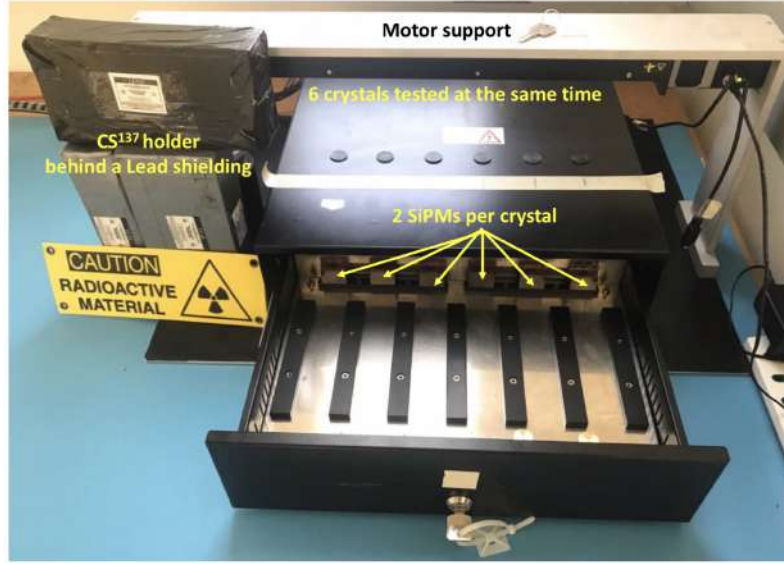$$N_{RIN} = F \times \phi_{Mu2e} \times 200 \text{ ns.} \tag{4.5}$$

**Figure 4.13:** Layout of the RIN station.

The RIN in MeV is then obtained as the statistical fluctuations of $N_{RIN}$ normalized to the crystal under study LY:

$$RIN = \frac{\sqrt{N_{RIN}}}{LY} \tag{4.6}$$

After few minutes of acquisition of the SiPM dark current, an intense $^{137}$Cs source, remotely controlled by a translational stepper motor, stops at the center of the top face of each crystal for one minute. The movement of the motor is controlled by Labview. The motor allows a very precise positioning of the source with respect to the crystal center. The distance between the crystal and the bottom face of the source holder is $\sim 10$ cm. A 20-channel Multiplexer is used to read the 6 voltages. The results of a RIN scan is reported in Figure 4.14. Since the activity of the $^{137}$Cs source is 10 mCi, it is shielded in a $\sim 3$ cm thick lead case. At the center of the holder, a 1.5 mm diameter collimator reduces the dose and restrict the photon emission to the crystal direction. Additional lead shielding is placed at the "source garage". The measured RIN values for all the accepted crystals are reported in Figure 4.15.
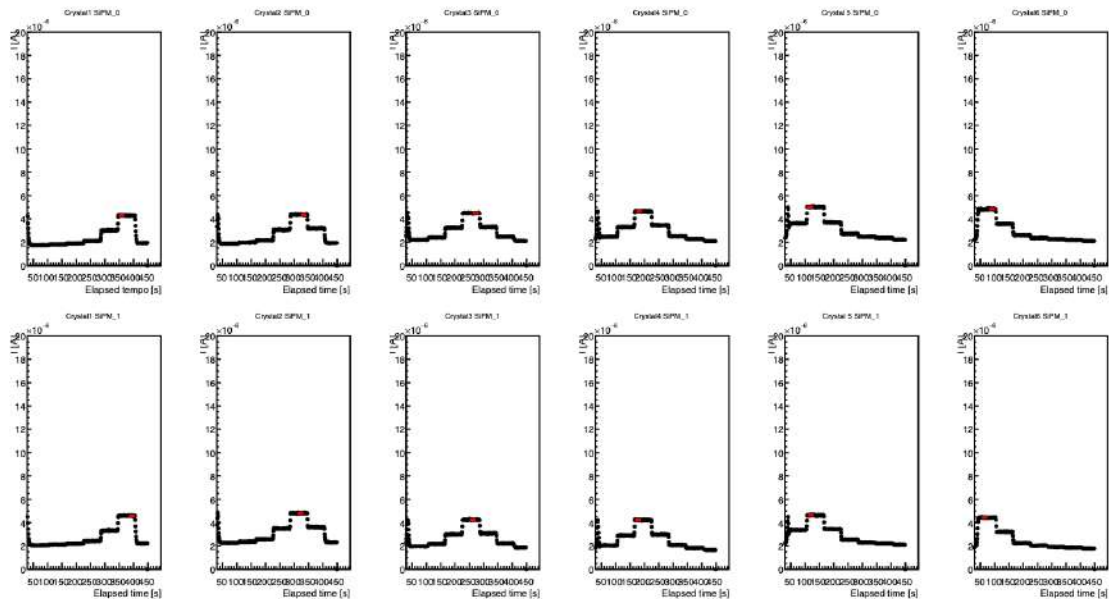
**Figure 4.14:** Current acquired with the RIN station with both SiPMs reading the six crystals.



**Figure 4.15:** RIN measurement results for Saint Gobain (Red) and Siccas (green) crystals.

## 4.4.2  Irradiation studies

At the moment of writing 16 crystals, 10 from Siccas and 6 from Saint Gobain have been irradiated at the $^{137}$Cs $\gamma$-ray Irradiation Facility at Caltech, in two step to 10 and 100 krad.

After each step of irradiation the crystals optical properties were tested as explained

in4.3.2. The optical properties of the irradiated crystals are reported in Figure 4.16. The average LY is 136 (109)p.e./MeV for ten Siccas crystals and 109 (96) p.e./MeV
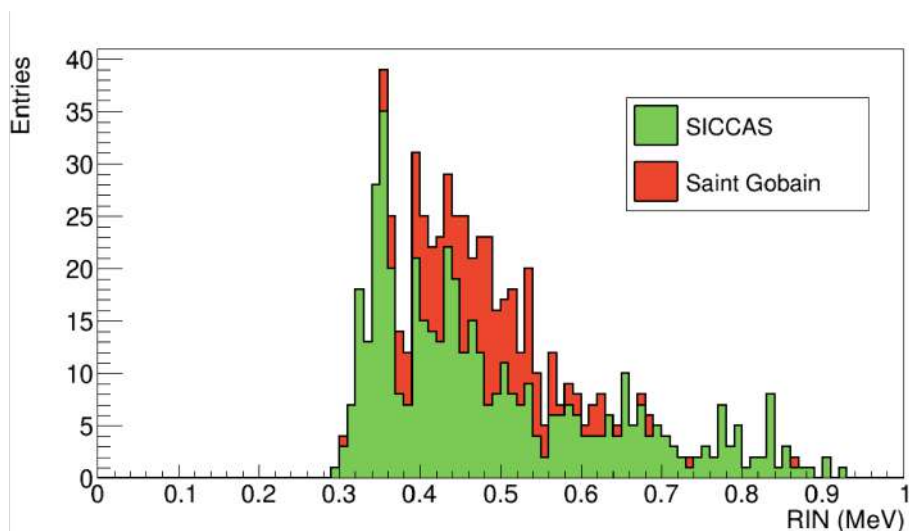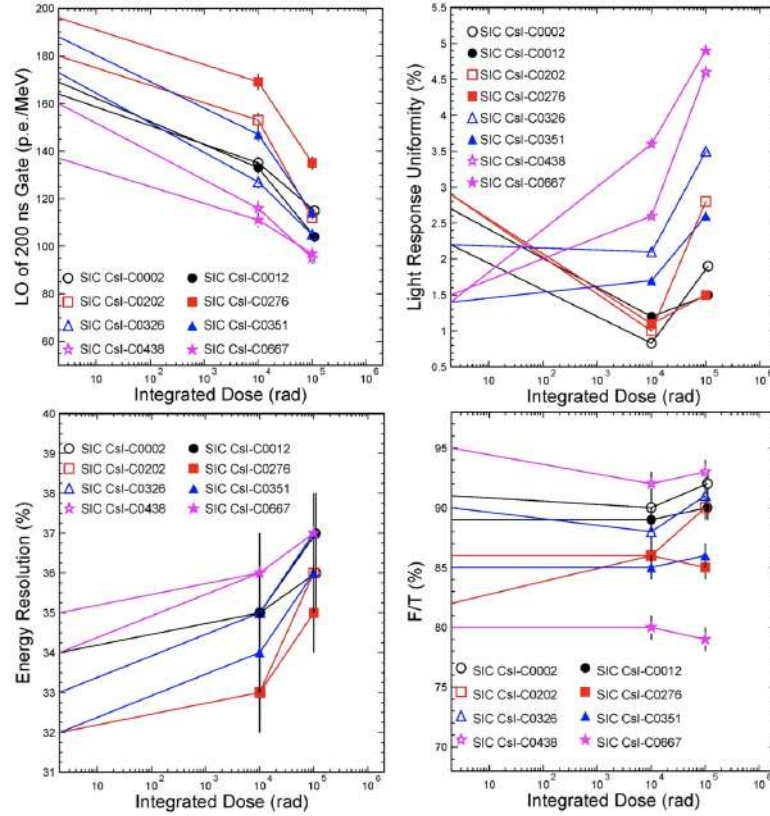


**Figure 4.16:** LY (top left), LRU (top right), energy resolution (bottom left) and fast/total ratio (bottom right) measurement before, after 10 krad and 100 krad radiation.

for six Saint Gobain after 10 (100) krad. This corresponds to losses of 19% and 35% and 27% and 36%. Only one crystal has failed the Mu2e radiation damage spec after 100 krad. These 16 crystals have been irradiated in different moment during the QC process, in this way it is possible to monitor the status of the irradiated crystal along the time. No recovery has been observed up to 884 and 501 days for two CsI crystals each from Saint Gobain and Siccas, respectively.

# Chapter 5

# Quality control of SiPMs and electronics

After having chosen a technical solution for the Mu2e calorimeter, the undoped CsI crystal coupled with UV extended SiPMs solution for the Mu2e calorimeter, a long R&D phase started to select the vendors that better fulfilled the Mu2e requirements. For the each 6×6 mm$^2$ cell of the Mu2e sensors the technical specifications are here summarized:

- a Photon Detection Efficiency (PDE) larger that 20 % at 315 nm, the emission peak of the CsI;

- a gain larger than $10^6$ at the operational voltage V$_{op} = V_{br} + 3$ V;

- a recovery time ($\tau$) smaller than 100 ns, when measured on a load larger than 15 $\Omega$;

- maximum acceptable operation voltage spread among the 6 SiPM cells of $\pm$ 0.5 %;

- maximum acceptable dark current (I$_d$) spread at V$_{op}$ among the 6 SiPM cells of $\pm$15 %;

- dark current smaller than 10 mA at operation voltage and a gain reduction smaller than a factor 4 while irradiating SiPMs up to $3\times10^{12}$ n$_{1MeV}$/cm$^2$ at

20 °C

- Mean Time To Failure (MTTF) better than a million hours while operating at  0 °C.

During the pre-production phase, 50 Mu2e SiPMs were procured from three different vendors: AdvanSid (Italy) [99], Hamamatsu (Japan) [72] and SensL (Ireland) [100]. A description of the pre-production procedure is reported in [101]. At the end of the characterisation of the pre-production samples, Hamamatsu resulted the best provider, especially in terms of radiation hardness.

Test stations have been designed by the Mu2e INFN-Pisa and LNF-INFN groups, as automatized tools to test the SiPMs performances of the $\sim$ 3000 Mu2e SiPMs necessary for the construction of the Mu2e electromagnetic calorimeter.

The Quality Control (QC) procedure of these SiPMs works similarly to that of the crystals one: 300 SiPMs/month are shipped from the producer to the Mu2e Calorimeter laboratory in SiDet (FNAL). Here a visual survey is carried out to control the absence of big defects. Soon after, their mechanical specifications are controlled. If the SiPMs are in agreement with the mechanical specifications they are fully characterized in a dedicated station. 20 SiPMs are then randomly selected, 15 are used for the Mean Time To Failure (MTTF) evaluation while 5 are irradiated at the Helmholtz-Zentrum Dresden Rossendorf (HZDR) irradiation facility.

## 5.1   Mechanical Properties

The SiPMs mechanical dimensions are verified by means of a custom laser station with a 100 $\mu$m tolerance, a picture of the station is reported in Figure 5.1. If the SiPMs do not pass these specifications "survey" they are rejected so that they can be used for radiation test or are sent back to the producer.

## 5.2   SiPM characterisation station

The station dedicated to the SiPMs characterization is able to host 25 SiPM at the same time without opening the box and allows to perform the measurement at tree
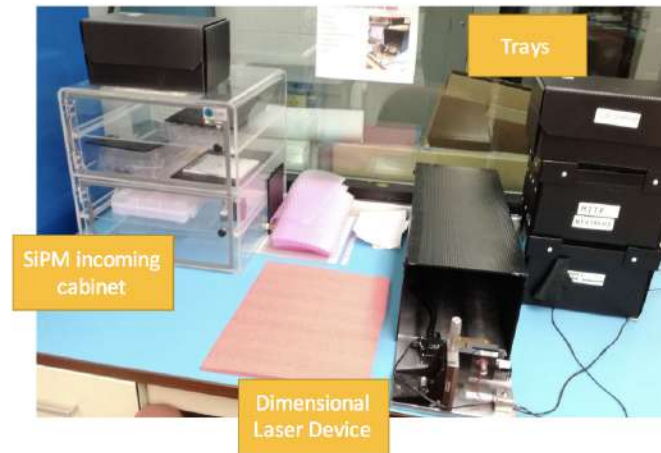
**Figure 5.1:** Picture of the station that check the SiPMs dimensions.

different temperatures (25° C, 0° C, -10° C ). A sketch of the station is shown in Figure 5.2.

The central sensor and the four ones at the corners of the board have been calibrated and used as reference for the stability and uniformity of the light.
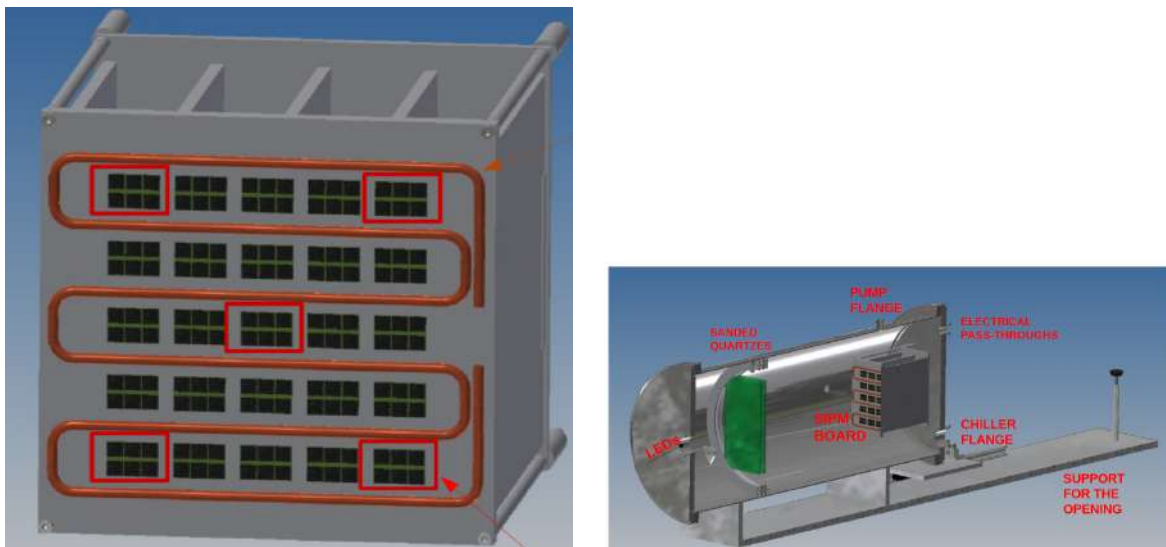


**Figure 5.2:** Left: drawing of the cooled copper plate with the sensors plugged. The highlighted sensors are used as reference. Right: drawings of the automatized test station for SiPMs.

The station is installed inside a 70 cm long aluminum barrel with diameter of 32 cm, designed for vacuum tests down to $10^{-1}$ Torr. The sensors tested are plugged into a copper plate in thermal contact with a cooling coil refrigerated by an external

chiller system. The light of an UV LED, positioned at one end of the barrel, is made uniform using by a couple of sanded quartz far ∼50 cm from the sensors plate. After the diffusion, a deviation from uniformity smaller than 5% is expected.

The readout electronics consists of 5 boards that host the relays used to select the cell to be tested among the 150 installed (six cells on each SiPM and 25 SiPMs plugged in the box) on the plate. Relays are driven by a microcontroller installed on another board that manages the communication with the control software of the station. At the moment of writing all sensors have been tested. Only 48 out of 3950 tested SiPMs have been rejected, that corresponds to 1.2 % of the total.

### 5.2.1   Measurement of breakdown voltage and dark current

To measure the breakdown voltage, an I-V scan is performed for each Mu2e SiPM cell. When the $V_{bias}$ starts increasing, the generated carriers have enough energy to impact atoms in the depletion region, but still insufficient to start an avalanche. The current continues to increase more rapidly at each subsequent voltage step. The breakdown voltage ($V_{br}$) is evaluated as the point where the curve behavior changes from a convex function to a concave one. Hence, it is evaluated by finding the maximum of the current Logarithmic Derivative, $LD = d(logI)/dV$ [102]. The peak position is fitted with a Log-Normal function. Figure 5.3 reports an example of I-V scan and its derivative used to evaluate the $V_{br}$. The operational voltage of the single cell is defined as $V_{op} = V_{br} + 3$ V.

In Figure 5.4 the measured breakdown voltages are reported as a function of the SiPM ID; the visible dependence is due to differences in the silicon wafers. In Figure 5.5 the RMS of the measured $V_{br}$ and of the dark current at operational voltage for the cells tested are reported at different temperatures. At the moment of writing, still few SiPMs, that were tested at 25° C, need to be measured again at 20° and this is why there are part of the plot at 25° C and other at 20°. The red lines represent the limits on the acceptable values. Only 2% of the SiPMs was rejected because the RMS of the dark current was greater than the 15% acceptance limit.
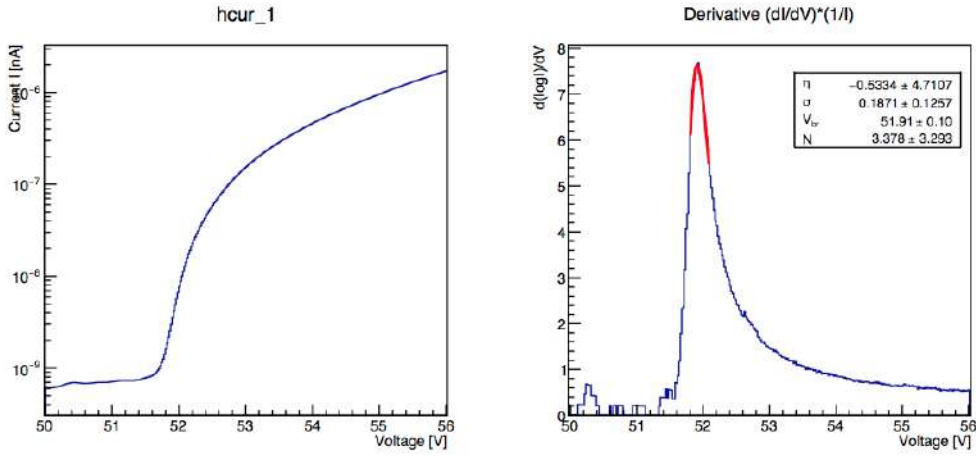
**Figure 5.3:** Left: example of an I-V scan. Right: Dark current logarithmic derivative as function of the bias voltage applied to the SiPM. The red line represents the Log-Normal fit used to determine the breakdown voltage value.
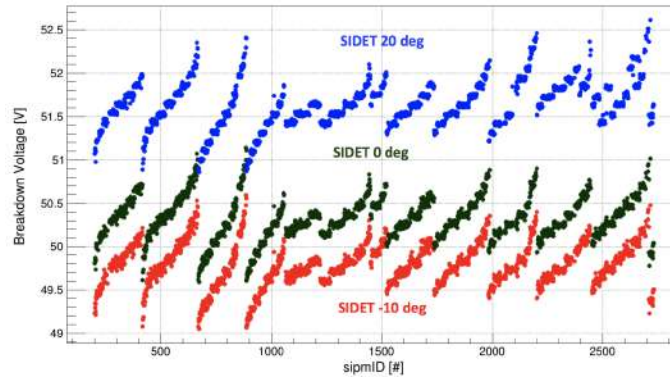


**Figure 5.4:** Breakdown voltage measured at three different temperature (-10 ° Cin red, 0 ° C in green, 20 ° C in blue) as a function of the SiPM identification number.

## 5.2.2 Measurement of the gain at operational voltage

The measurement of the Gain× PDE can be performed normalising the incident light on the sensors with the one arriving on a reference as follows:

$$G \times PDE = \frac{I_i}{I_{ref}} \times \frac{\text{Light Profile}(x_{ref}, y_{ref})}{\text{Light Profile}(x_i, y_i)} \times (G \times PDE)_{ref} \qquad (5.1)$$

where $I_i$ is the current of the i-th SiPM under test and $x_i$, $y_i$ its coordinates; $I_{ref}$, $x_{ref}$, $y_{ref}$ are the current and coordinates of the reference sensor, $(G \times PDE)_{ref}$ is its product of the gain and the PDE value, which is stable around $4 \times 10^5$ respectively
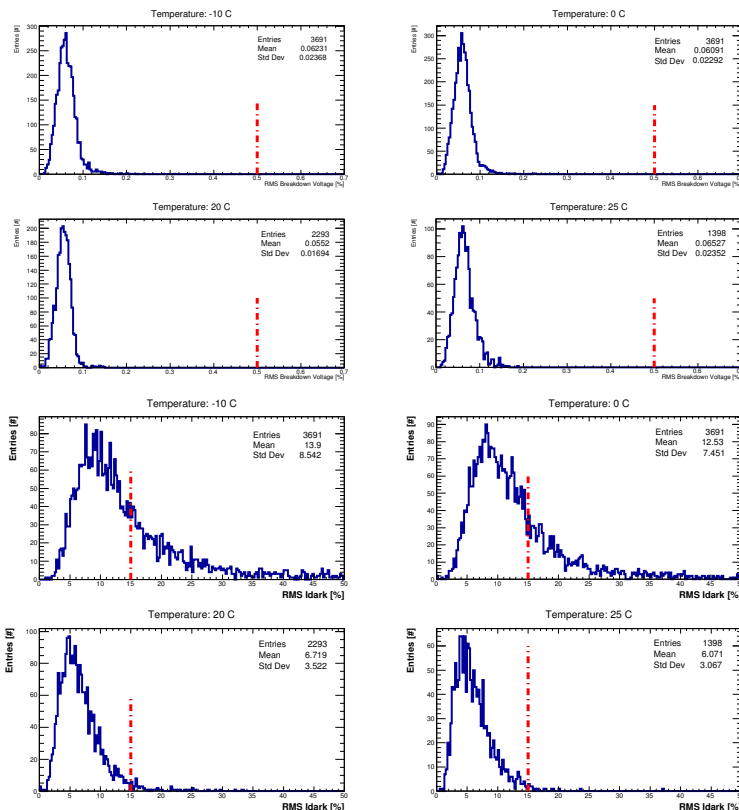
**Figure 5.5:** RMS of the Breakdown voltage test (top) and RMS of the dark current at operational voltage (bottom) of each cell of the SiPMs. The results are reported for the three different temperature tested. The red lines represent the limits on the acceptable values.

.

In Figure 5.6 the light intensity is reported as a function of the SiPMs position. The light is not uniform on the sensors plate but shows a gaussian profile. A good approximation of this profile has been obtained by fitting the sensors current biased at the operative voltage. The resulting residuals have an RMS $\sim 3\%$.

In Figure  5.7 the distribution obtained measuring the G  $\times$ PDE is reported at the three temperatures tested. The distribution shows a mean value of G$\times$PDE $\sim 4 \times 10^5$ with a production spread of about 4%.
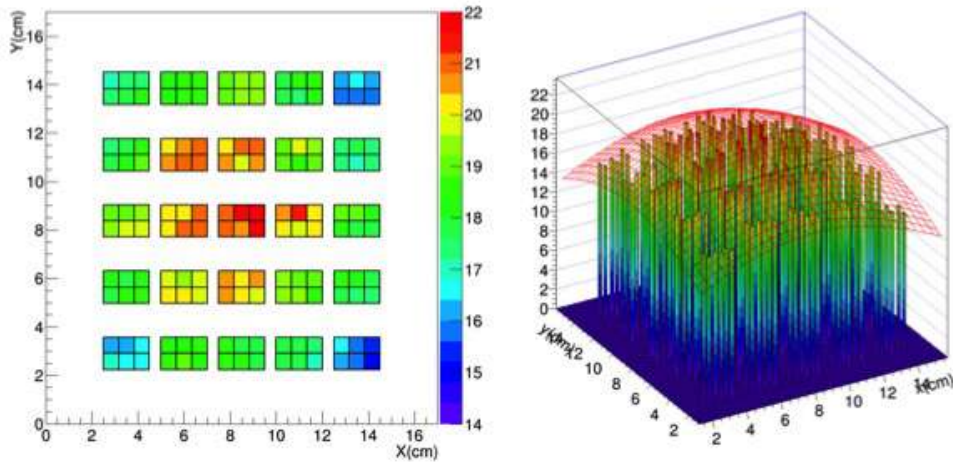
**Figure 5.6:** LED light intensity reaching the sensors under test.
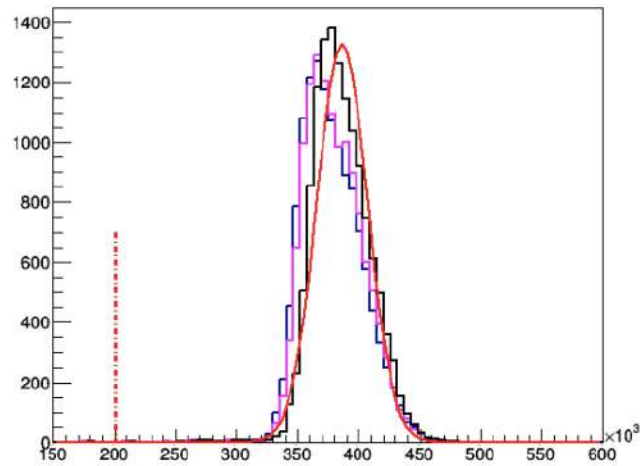


**Figure 5.7:** Gain $\times$ PDE at three temperature: -10 °C (Magenta), 0 °C (black) and blue (20°C). The red lines represent the limits on the acceptable values.

## 5.2.3 Irradiation test on production SiPMs

As derived from Section 3.5.6 the SiPMs have to withstand an ionising dose of 45 krad and a neutron fluence of $6.5 \times 10^{11}$ $n_{1MeV}/cm^2$. From each batch, 5 SiPMs were randomly selected and sent to the HZDR irradiation facility. There, the SiPMs were exposed unbiased to a neutron fluence of $\sim 10^{12}$ $n_{1MeV}/cm^2$.

The $I_{dark}$ increase was measured once the SiPMs were back at Fermilab. A scan around the operational voltage of the whole Mu2e SiPMs was performed measuring

the $I_{dark}$ at  0 ° and -10 °C. An example of the results of both measurements are reported in Figure 5.8. From these results it is clear that the SiPM will still operate



**Figure 5.8:** Dependence of the Mu2e SiPM dark current to the $\Delta V = V_{bias} - V_{br}$ at  0 ° (left) and -10 °C (right). Note that the operational voltage is defined as $V_{op} = V_{br} + 9$.

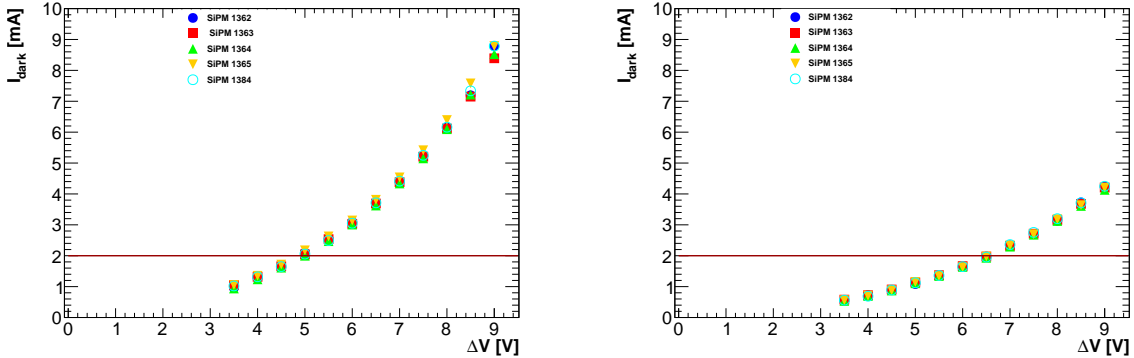when strongly irradiated reducing the temperature to -10 °C and the bias voltage of $\sim 3$ V. This correspond, as shown in Figure 5.9, to a reduction of 10 % in PDE and a factor 2 in gain.

### 5.2.4   MTTF test on production SiPMs

The need of running for one year inside the Detector Solenoid translates into a high requirement for the Mean Time To Failure (MTTF) of SiPMs. To increase redundancy, we read out each crystal with two independent photosensors, each one connected to a separated Front End Electronics and readout chain. In order not to spoil the detector resolution, we require to have no double dead SiPMs/crystal (at 95 % C.L.) after three years of running. A dedicated simulation translated this choice in achieving an MTTF operation value for the SiPMs larger than $10^6$ hours while operating at 0°C.

In order to evaluate the MTTF value during the SiPM production, we randomly selected 15 pieces on each production batch and measured them in the MTTF station. The achievable MTTF value (if all 15 pieces survive the test) is estimated as follows:

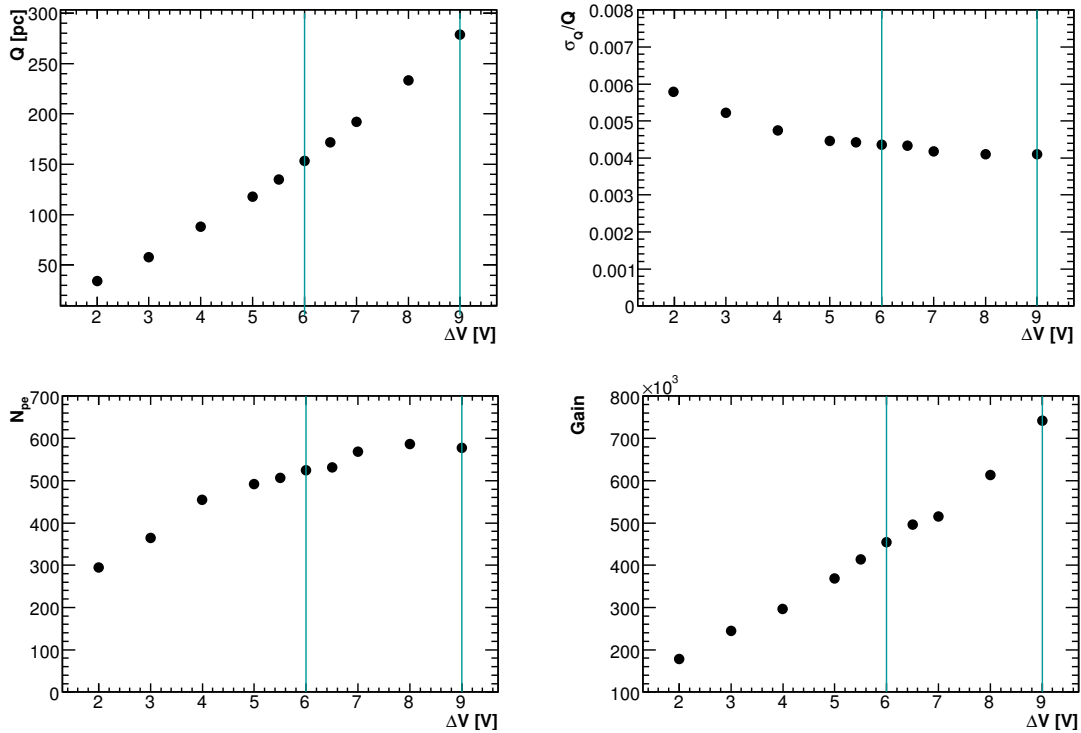$$MTTF = 0.5 \times N_{SiPM} \times N_{hours} \times AF, \tag{5.2}$$

**Figure 5.9:** Top Left: Charge of a Mu2e SiPM as function of the $\Delta V = V_{bias} - V_{br}$. Top Right: resolution of a Mu2e SiPM as function of the $\Delta V = V_{bias} - V_{br}$. Bottom Left: $N_{pe}$ of a Mu2e SiPM as function of the $\Delta V = V_{bias} - V_{br}$. Bottom Right: Gain of a Mu2e SiPM as function of the $\Delta V = V_{bias} - V_{br}$.

where $N_{SiPM}$ is the number of SiPMs under test, $N_{hours}$ is the number of hours under test and $AF$ is the Acceleration Factor extracted from the Arrhenius equation:

$$AF = e^{\frac{E_a}{k}\left[\frac{1}{T_{use}} - \frac{1}{T_{stress}}\right]}, \tag{5.3}$$

where $E_a = 0.7$ eV is the silicon activation energy, $k$ is the Boltzmann constant, $T_{use}$ is the running temperature in the experiment ($0°C$) while $T_{stress}$ is the stress temperature in the MTTF station. For a stress temperature of $65°C$, the acceleration factor is equal to 305. To test an MTTF at the level of $10^6$hours, the SiPMs under test were kept in the station for 342 hours, i.e. 18 days. A sketch of the MTTF box is reported in Figure 5.10

The 15 SiPMs are inserted into the insulated box made of an external PVC box and an internal aluminum box. A copper support for a series of four power resistors of 0.5 $\Omega$, responsible of heating the air, is placed inside the aluminum box. The resistors
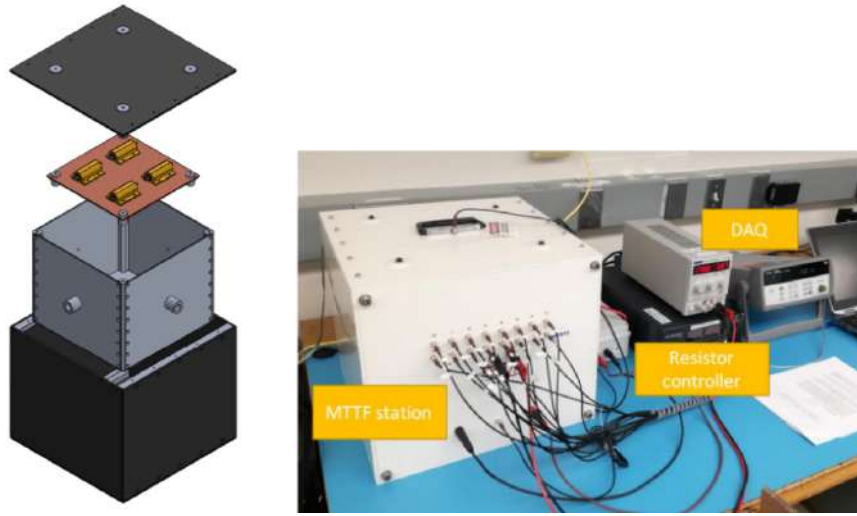
**Figure 5.10:** Left: Schematic view of the experimental setup. Right: Picture of the MTTF station.

are powered using an external control that ensures a stable internal temperature ($\pm 0.5$ °C) around the operating value. Both the air temperature and the copper radiator temperature are recorded through a PT 1000 sensor. The reached MTTF value at the after having tested all the Mu2e SiPM is $> 10^7$ hours. The mean current acquired as a function of the elapsed time is reported in Figure 5.11 for all the tested batches.

## 5.3   Irradiation studies of the FEE board

As stated in Section 3.5.6 the FEE chips are required to withstand a total dose of 100 krad and a neutron fluence of $\times 10^{12}$ $n_{1MeV}/cm^2$. The fourth version of FEE chips is under test and, in the following, a summary of the irradiation campaign performed on the previous versions of the electronics components are reported.

A first irradiation campaign took place in June 2018 at the Calliope facility of the ENEA Casaccia [103] . Here a $^{60}$Co source is used to produce photons with $E_\gamma = 1.25$ MeV. The irradiation plant is a large volume pool-type facility, where the source is arranged in a 25 $^{60}$Co rods with active area of 41 cm $\times$ 90 cm. The source activity during our test was $2.4 \times 10^{15}$ Bq. Several configurations have been irradiated up to
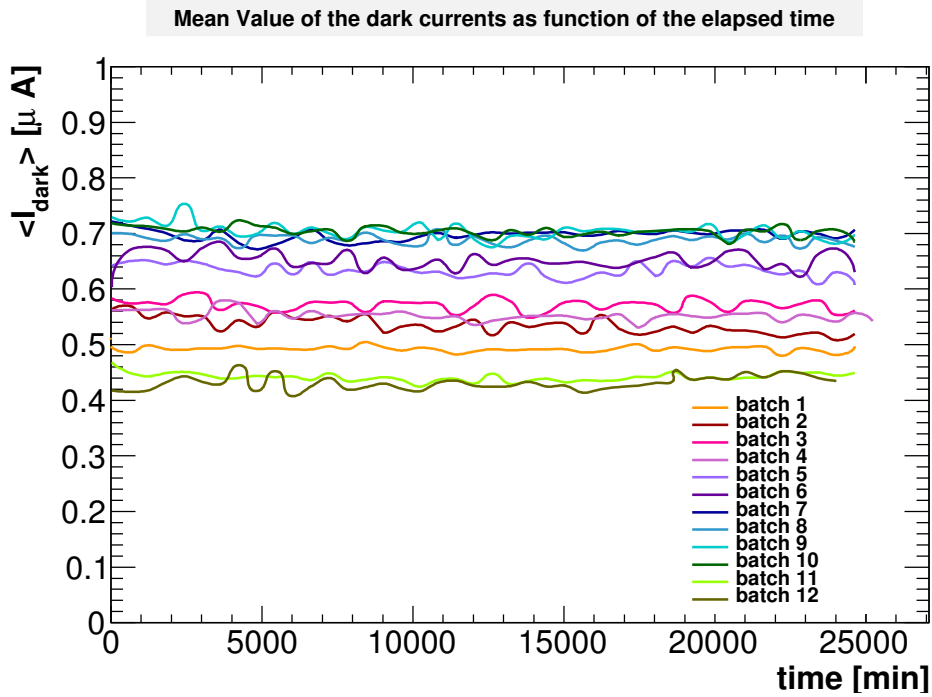
**Figure 5.11:** Mean value of the currents of 15 SiPMs as a function of the elapsed time during the MTTF test. The different line colors refers to different batches tested.

a total ionising dose of 70 krad to study the radiation hardness of the different FEE components.

The primary problems noticed concerned the HV regulator, the current and temperature readout. After failing this test, an intense phase of R&D and test started. In the following the setups used and the components tested, are described.

### 5.3.1    2018 irradiation campaign

A dedicated irradiation campaign started in November 2018 using both neutron and photons to certify radiation hardness the newly selected components. Since the on-board voltage regulator failed during the June test, the Mu2e FEE boards were biased using an external power supply. In order to distinguish the ADC failures to the DAC failure, a part of the FEE board had a fixed reference for the HV (obtained via resistive divider) instead of having mounted the HV DAC. Besides the standard Mu2e FEE board, two different backup solution were tested: a commercial differential BJT preamplifier (component A) and a certified radiation hard differential

BJT amplifier (component B). A commercial linear voltage regulator considered to be radiation hard -TL1963ADCQT [104]-(component C) was also irradiated.

In Figure 5.12, pictures of all these different tested components are reported. In
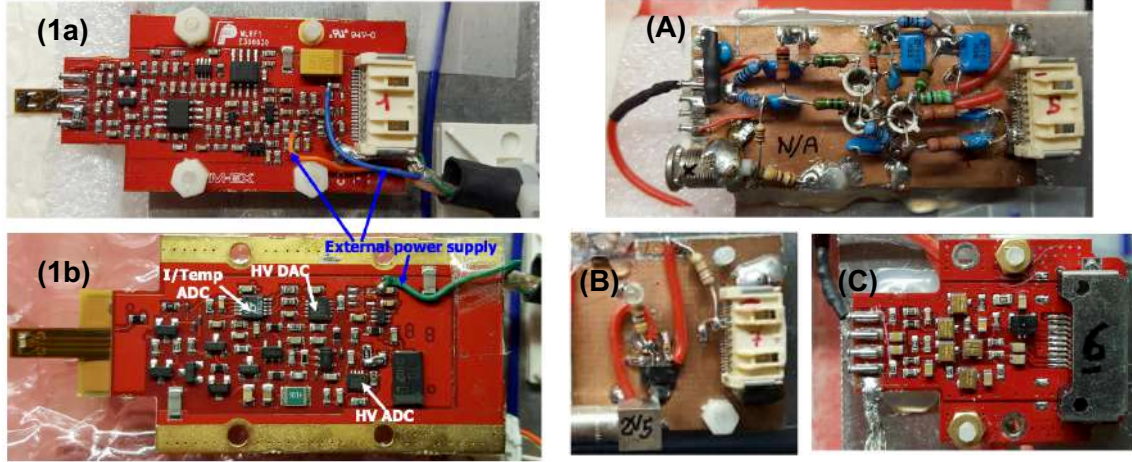


**Figure 5.12:** Picture of the several components tested: Official Mu2e board, preamplifier side (1a) and HV regulator side (1b); Commercial differential BJT preamplifier (A), Rad-hard differential BJT preamplifier (B) and Commercial linear voltage regulator (C).

order to get reliable results, data acquired with digital electronics (DAC and ADC via controller) were compared to the data collected by the analog electronics (signal preamplifier and HV regulator via 2 oscilloscopes).

### 5.3.1.1   Neutron test at FNG

The irradiation with neutrons was performed in the Frascati Neutron Generator (FNG) facility of the ENEA laboratory in Frascati [105]. Neutron generation at FNG is based on the $T(d,n)\alpha$ fusion reaction, to produce 14 MeV neutrons with a flux up to $1\times10^{11}$ neutrons/s in steady state or pulse mode.

As shown in Figure 5.13 four boards were mounted on a support $\sim 5$ cm away from the neutron gun. Backup component A and the linear voltage regulator as well as two Mu2e FEE board, with and without DAC, were tested. A NIM crate was place 5 m away from the source. The total fluence, collected in 4 hours, was $10^{12}$ $n_{1MeV}/cm^2$. As reported in Figure 5.14 no degradation has been observed from the digital acquisition of the Mu2e FEE board, the SiPM load was simulated through
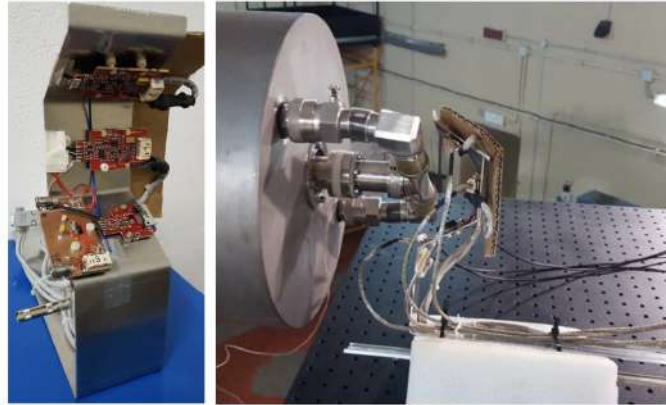
**Figure 5.13:** Experimental setup used during the neutron irradiation performed at the FNG facility of ENEA.

a 1 MΩ resistor. Also the components readout analogically, that is the Mu2e FEE
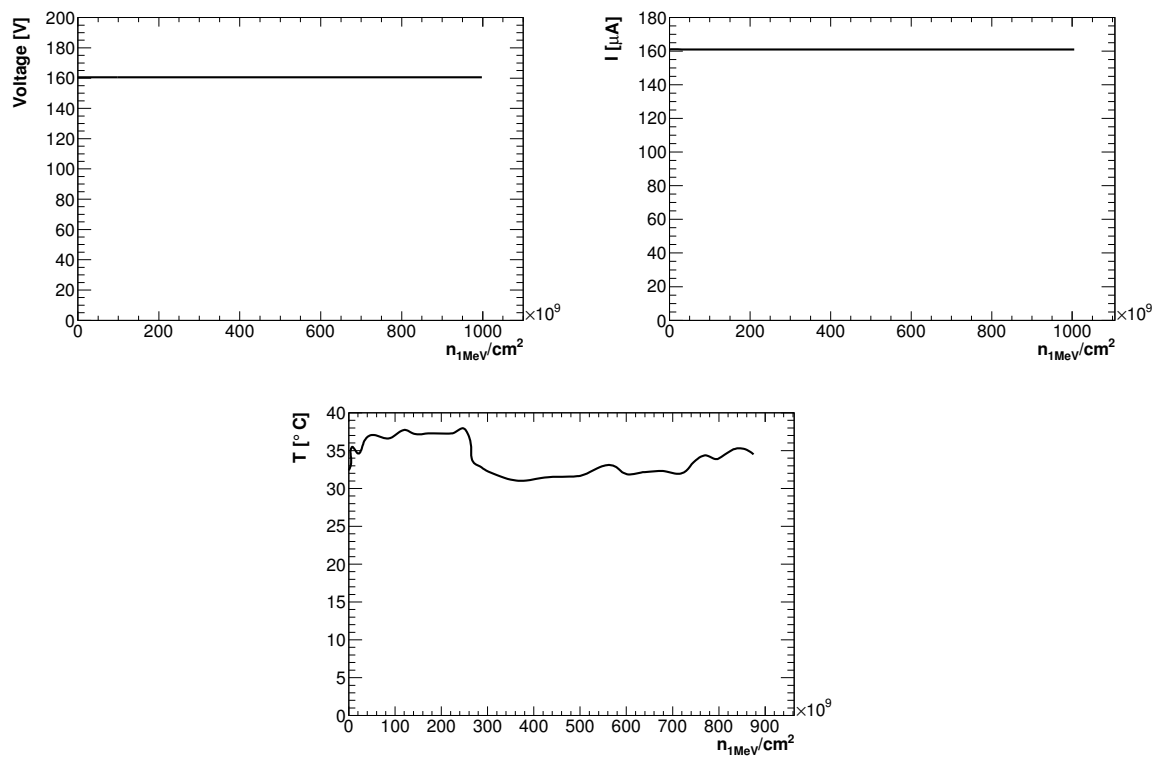


**Figure 5.14:** Mu2e FEE board with DAC. Top Left: Digital reading of the SiPM HV. Top Right: Digital reading of the current. Bottom: digital reading of the temperature.

board without DAC, the components A and C, did not presents variation as shown in Figure 5.15.
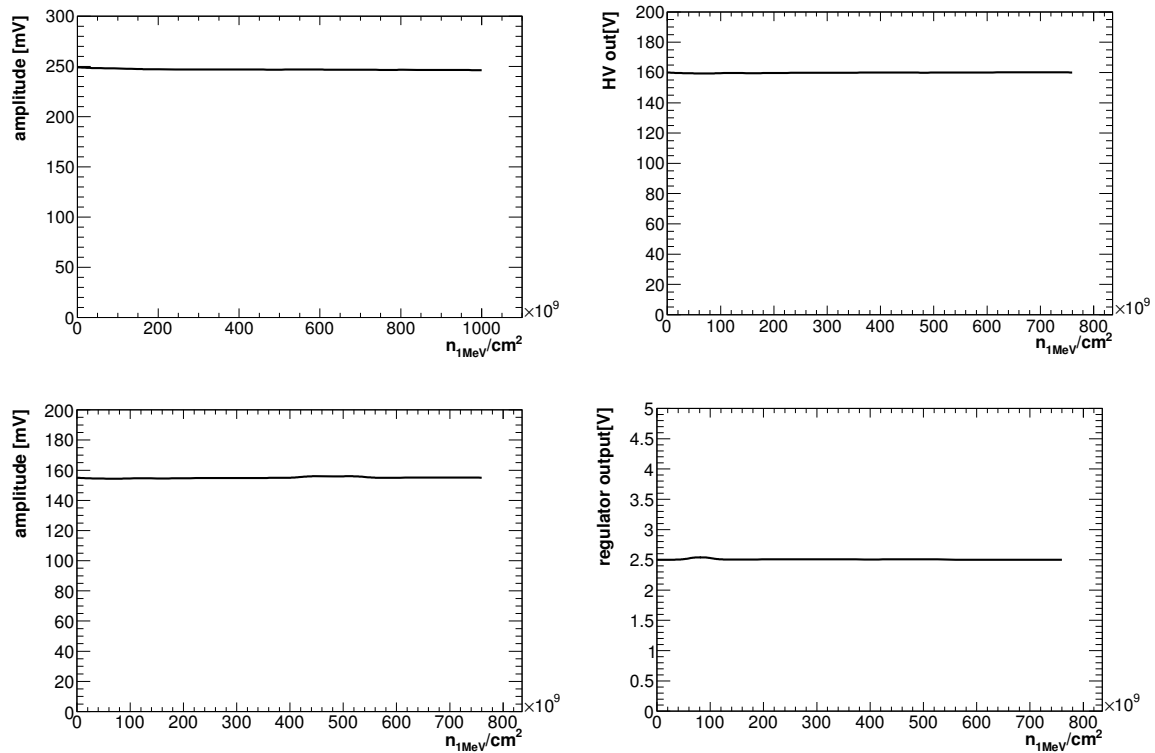
**Figure 5.15:** Top: HV output (Left) and pulse amplitude (Right) of Mu2e FEE board without DAC as a function of the neutron fluence. Bottom Left: Output pulse amplitude obtained with component A as function of the neutron fluence. Bottom Right: linear voltage regulator output as function of the neutron fluence delivered by the FNG facility.

### 5.3.1.2 Dose irradiation at Calliope

The dose irradiation was performed at the Calliope facility of the ENEA in Bracciano. As shown in Figure 5.16, seven boards (Component A,B,C and four Mu2e
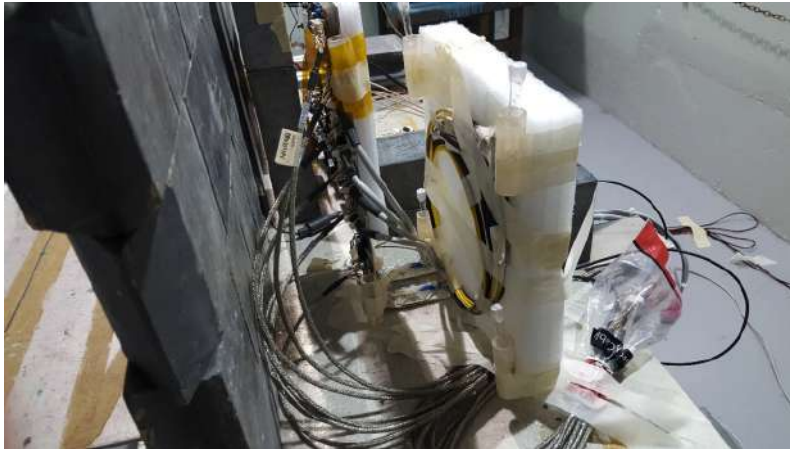


**Figure 5.16:** Experimental setup used during the $\gamma$ irradiation campaign.

FEE board, with and without DAC) were mounted on aluminum panel $30 \times 7 \times 0.3$ cm$^3$ and driven by a Mezzanine Board shielded by lead block in order not to be irradiated. The integrated dose collected was 120 krad. Figure 5.17 shows that the digital electronics was not able to withstand the dose expected, in particular after $\sim 10$ krad faults where detected in ADC. Figure 5.18 bottom left shows that also DAC was not able to withstand the dose after 23 krad. The analogical components instead did not present any faults during the irradiation as shown in Figure 5.18.

At the end of this combined irradiation it was clear that the high voltage preamplifier and linear regulator had perfect behavior, while the DAC, ADC as well as the local linear regulator low voltage need to be replaced.
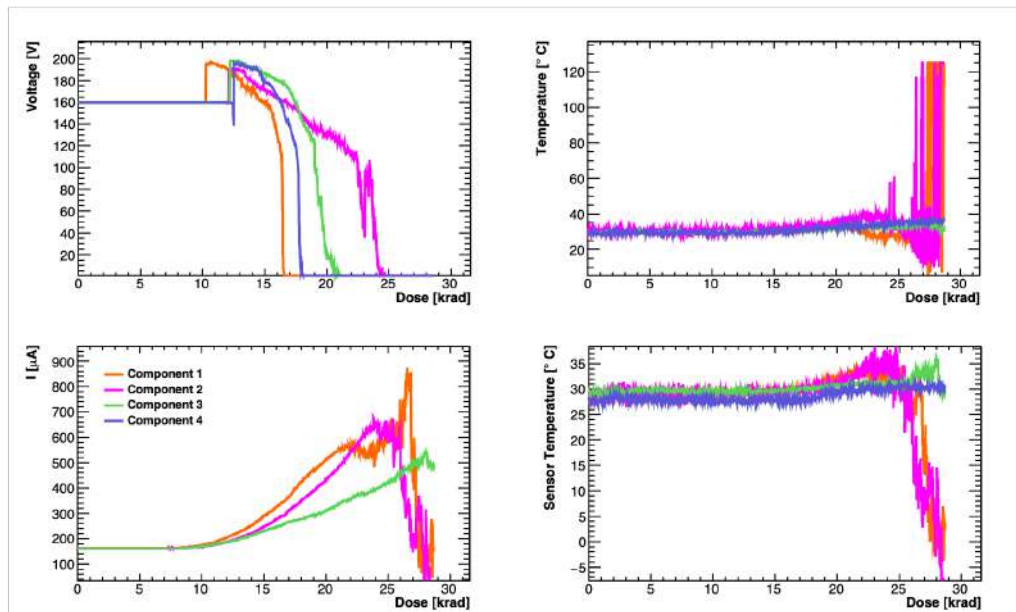
**Figure 5.17:** Voltage (Top Left), Board Temperature (Top Right), Simulated SiPM Current (Bottom Left) and Temperature (Bottom Right) readout from the four Mu2e FEE board.
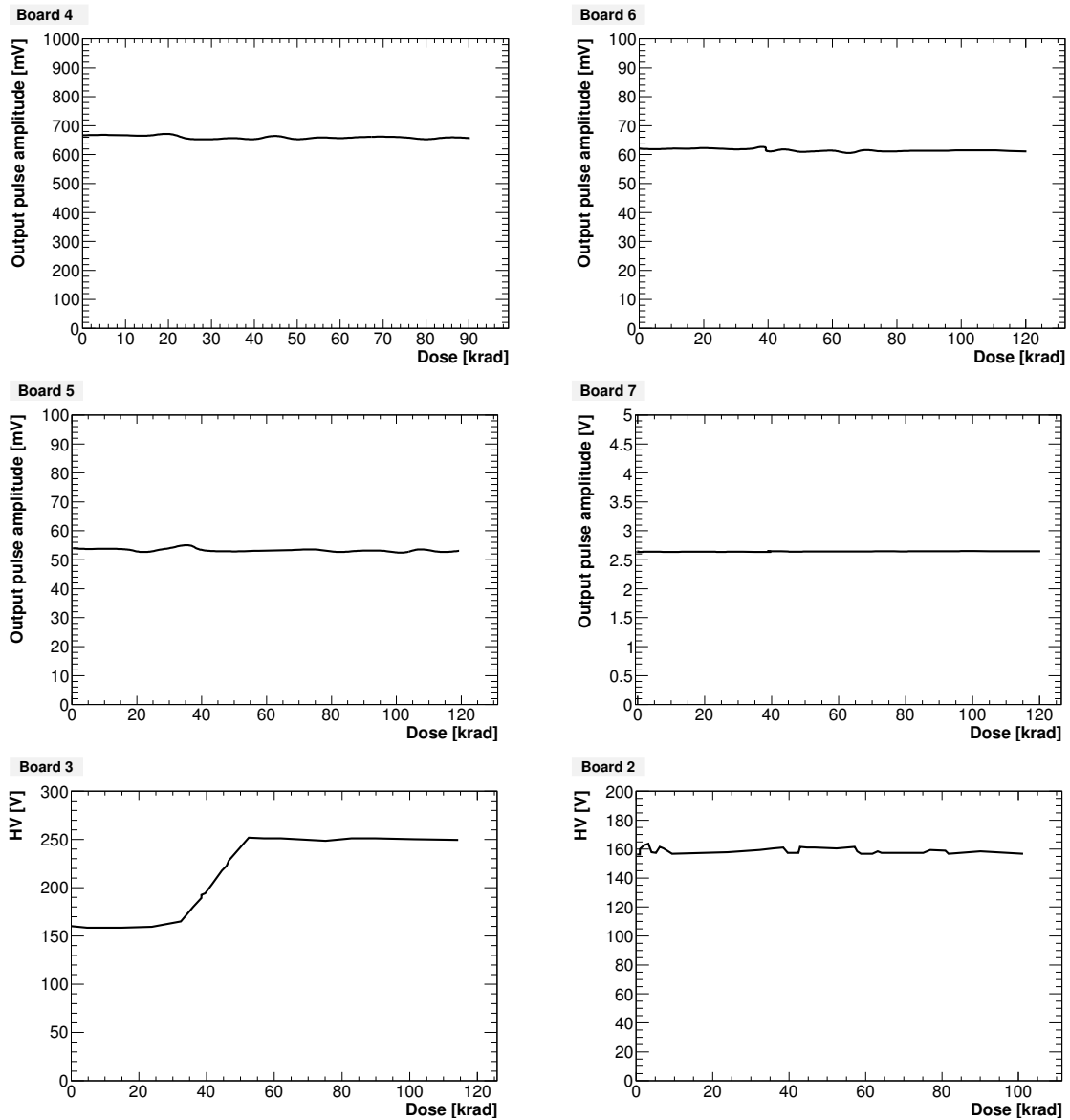
**Figure 5.18:** Top left: Analog output pulse amplitude reading on a standard preamplifier without DAC. Top right: Analog output pulse amplitude reading on a BJT rad-hard differential preamplifier. Middle left: Analog output pulse amplitude reading on a BJT commercial differential preamplifier. Middle right: Analog output reading on linear voltage regulator [TL1963ADCQT]. Bottom left: Analog HV reading on a standard regolator with DAC. Bottom right: Analog HV reading on a standard regulator without DAC.

### 5.3.2   Gamma irradiation campaign - January 2019

In January 2019 the boards mounting the new components were tested at the Calliope facility from ENEA up to a Total Ionizing dose of 100 krad. As shown in Figure 5.19 two chains of DAC and ADC were tested, one was irradiated up to 100 krad while the other one was shielded by lead blocks.



**Figure 5.19:** Experimental setup prepared for the irradiation of the ADC and DAC components.

DAC and ADC were controlled by the development board and the manufacturer's software. The DAC output (set to 1000 mV) drives an ADC input (full range 3300 mV) and is recorded by a scope every 10 minutes while the ADC output was recorded by software every 10 minutes. The results of the irradiation is shown in Figure 5.20

No problems were detected during this irradiation. The ADC and DAC components worked correctly, small differences depended both to ADC variation and noise. This did not represent a real problem since in the experiment the board will be equipped with auto-calibration in reference to the ADC calibrated DAC.

### 5.3.3   Single Event Upset (SEU) of the FEE at North Western Medicine Chicago Proton Center - April 2019

The calorimeter group needed to test the SEU for a proton fluence of $1.2 \times 10^{10}$/year, considering a safety factor of 12.
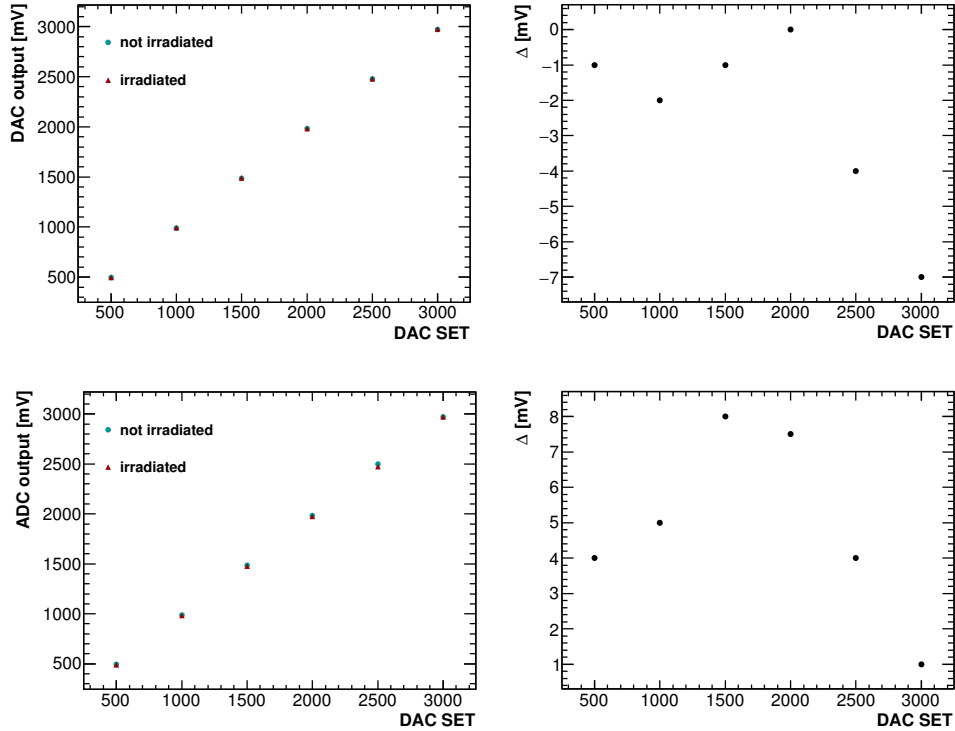
**Figure 5.20:** Top: Output of an irradiated and a not irradiated DAC (left) and their difference (right). Bottom: Output of an irradiated and a not irradiated ADC (left) and their difference (right).

A SEU test on the LPC1769FBD100 ARM Microcontroller installed on the MB was performed in April 2019 at the North Western Medicine Chicago Proton Center with a 200 MeV/c proton beam with a $\sim$ 10 cm beam spot. The experimental setup used is shown in Figure 5.21: the first version of MB (i.e. NIM format + 1 HV generator + Ethernet section), shielded with a lead bloc to protect the HV generator and the Ethernet controller, connected to 4 FEE chips:

- one chip posed in front of the the beam and read out with an AmProbe multimeter. The voltage was acquired at 1 Hz ;

- one chip shielded by a led block and readout by an Agilent data logger. The voltage was acquired at 2 Hz;

- two chips shielded by a led block and SiPMs plugged. Current and voltage were monitored with a Labview program at 0.016 Hz.

**Figure 5.21:** Experimental setup used for the SEU test of the calorimeter FEE chips.

Each 20 seconds a ramp up and a ramp down of the bias voltage from 145 V up to 165 V is performed.

Because of the $\sim$ 18 m connection LEMO cables (from the irradiation area to the control room), a voltage drop of about 5 V is observed. Several proton runs were taken. In Table 5.1 the flux, the fluence of the run and the total proton fluence are reported. In Figure 5.22 the results obtained with the FEE chips directly exposed

| Run [#] | Flux [p/(cm$^2$ s)] | Total Fluence per run [p/cm$^2$] | Total fluence[p/cm$^2$] |
|---------|---------------------|----------------------------------|-------------------------|
| 1 | $7.32 \times 10^6$ | $7.32 \times 10^8$ | $7.32 \times 10^8$ |
| 2 | $7.32 \times 10^6$ | $7.32 \times 10^8$ | $1.46 \times 10^9$ |
| 3 | $7.29 \times 10^6$ | $1.66 \times 10^9$ | $3.12 \times 10^9$ |
| 4 | $7.11 \times 10^6$ | $2.13 \times 10^9$ | $5.25 \times 10^9$ |
| 5 | $1.38 \times 10^7$ | $4.14 \times 10^9$ | $9.39 \times 10^9$ |
| 6 | $2.57 \times 10^7$ | $7.07 \times 10^9$ | $1.71 \times 10^{10}$ |
| 7 | $4.97 \times 10^7$ | $7.14 \times 10^9$ | $2.42 \times 10^{10}$ |
| 8 | $5.07 \times 10^7$ | $1.69 \times 10^{10}$ | $4.11 \times 10^{10}$ |
| 9 | $5.03 \times 10^7$ | $1.21 \times 10^{10}$ | $5.32 \times 10^{10}$ |

**Table 5.1:** Flux, fluence of the run and total proton fluence delivered in each proton run.

to the proton flux. The Labview program confirms the data taking stability with

beam. The dedicated data-loggers acquiring SiPM current and temperature showed stable SiPMs dark current and temperature during and after proton irradiation. Reading and setting the bias voltages still worked after all the "upsets" events. The Ethernet Board Single Event Upset looks to be the candidate for the few cases of interrupted communication.
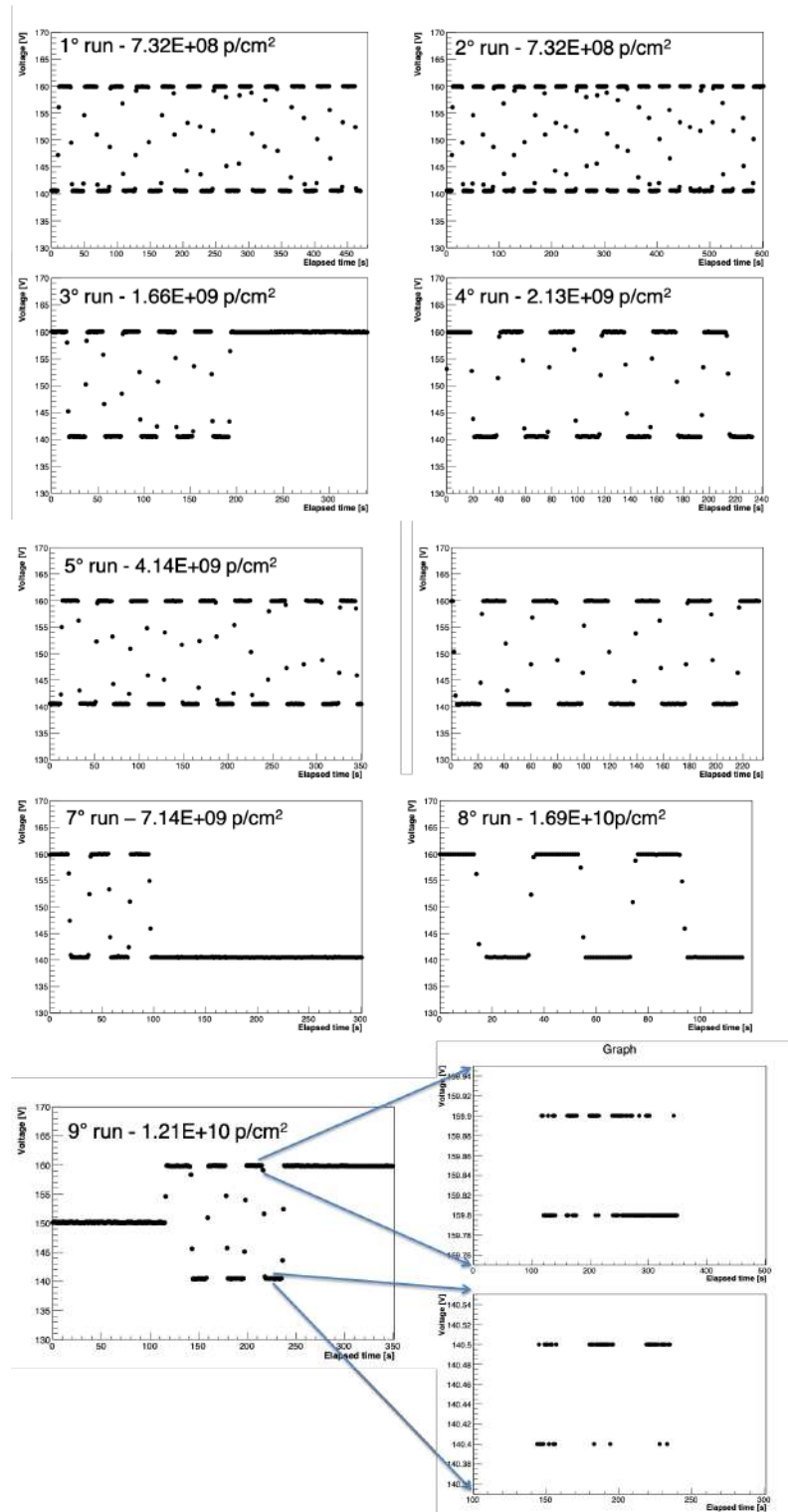
**Figure 5.22:** Ramp up and down performed during the nine run on the FEE board directly exposed to the proton flux in the bottom plot is also reported a zoomed view of the two value of breakdown voltage chosen; the steps shown are due to instrument sensitivity.

# Chapter 6

# Calorimeter prototype test beam

In this chapter, we describe the assembly and test of the large size calorimeter prototype named Module-0. The calorimeter has been exposed to an electron beam between 60 and 120 MeV at the Beam Test Facility (BTF) of LNF. Results on energy and time response and resolutions are presented both for particles impinging normally to the calorimeter surface or at grazing angles (50°) as in the experiment configuration. Simulation has also been tuned with data and a detailed data-MC comparison presented.

## 6.1 Experimental setup

### 6.1.1 Assembly and organization of Module-0 readout

A large size calorimeter prototype, dubbed Module-0, was built at the National Laboratories of Frascati (Frascati, Italy) in May 2017 using 51 crystals and 102 photosensors produced and qualified during the pre-production phase [108],[109]. Photosensors are attached with thermal glue on a galvanized copper holder and pins plugged in the FEE boards. The SiPM signals were amplified with the first prototype of the FEE electronics. On the same FEE boards, a local HV regulator allowed to set and read back the bias voltages. These boards are shielded by a copper Faraday cage. Similarly to the calorimeter disks, Module-0 is a structure of

staggered crystals with a size large enough to contain most of the electromagnetic shower of a 105 MeV electron beam. Module-0 was built trying to resemble as much as possible to the final disk. The back disk was done by Zedex insulator, instead of peek, but the cooling lines connecting the SiPM and FEE holders were produced with the final technique, thickness and shape. For the electron beam test, carried out in May 2017 at the Beam Test Facility (BTF) of the Laboratori Nazionali di Frascati, the detector was thermally stabilized at room temperature since the vacuum chamber was not ready yet. In Fig. 6.1, pictures of the Module-0 after assembly and after inserting the FEE chips are shown. At the moment of the test, the Mu2e



**Figure 6.1:** Pictures of the Module-0 during assembly: frontal view with crystals (Left) and back view with SiPM and FEE chips (Right).

custom calorimeter Waveform Digitizer (DIRAC) was still under development, so that two commercial CAEN V1742 high-speed digitizers boards were used to read-out the Module-0 signals. Each V1742 can acquire up to 32 channels simultaneously, sampling signals through four different DRS4 chips, which manage eight channels each. The DRS4 chip is a switched capacitor array, which can sample the input signal up to a frequency of 5 GHz. The sampling is done by loading charge on the capacitor array. The analog to digital conversion is done with an external 12 bit ADC and it requires about 180 $\mu$s. The digitizer was operating with a dynamic scale of 0 - 1 V and at 1 GHz sampling frequency, providing 1024 samples per trigger that resulted in a $\sim$ 1 $\mu$s acquisition window. As shown in Figure 6.2, we defined the readout in Rings surrounding the central crystal. Each increasing ring corresponds to a larger Moliere Radius, to improve the integration of the electromagnetic shower

in the case of electrons impinging normally to the calorimeter center.[1] Due to the
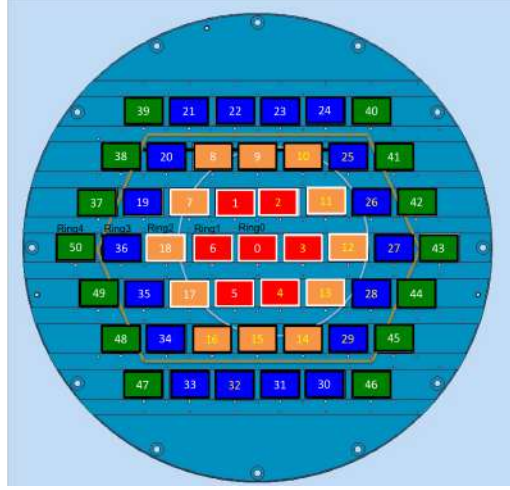


**Figure 6.2:** Channel arrangement in Rings in the Module-0. The two different colors refers to the different rings.

limited number of available channels in the DAQ system, only the central crystal and the first surrounding ring were equipped and readout with two sensors and two FEE boards per crystal. For the outer crystals, one of the sensors was left without FEE and unbiased. In total 58 SiPMs were readout. The remaining 6 digitizer channels were used to collect trigger and scintillating counters signals.

## 6.1.2 Description of Test Beam configuration

In Figure 6.3 the setup inside the experimental hall is shown. Energy and time measurements were obtained using an electron beam in the energy range between 60 and 120 MeV.

Figure 6.4 shows the transverse beam profile, as reconstructed by a Medpix detector placed in front on the beam; the beam profile is well represented by a Gaussian shape with a $\sigma_{xy}$ of $2 \div 3$ mm. The beam energy spread was evaluated by BTF experts to be of $\mathcal{O}(2\%)$ at 100 MeV.

---

[1] $X_0$=(CsI)1.86 cm and $R_m$(CsI) = 3.5 cm and therefore we expect the whole shower to be contained within the second ring.
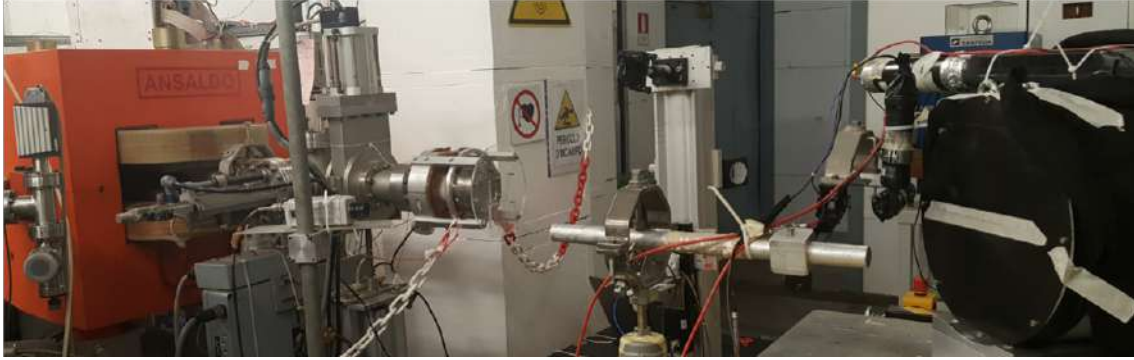
**Figure 6.3:** Experimental setup inside the BTF hall.  The Module-0 is covered with a black blanket.
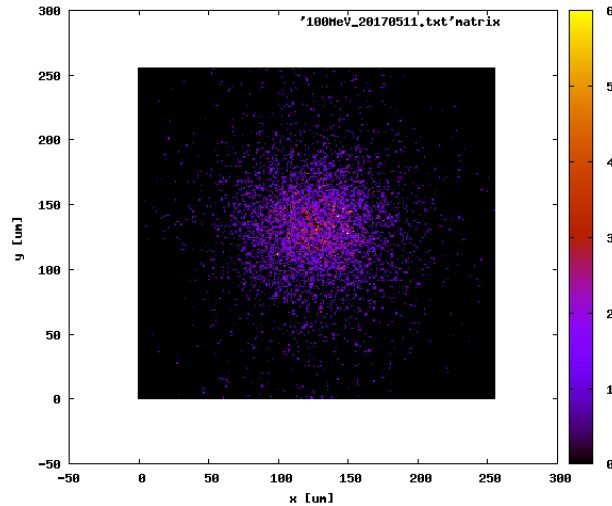


**Figure 6.4:** Transverse beam profile measured with a Medpix.

Two small plastic scintillating counters of $(50 \times 10 \times 20)$ mm$^3$, crossed at 90 degrees, were positioned on the beam axis, at few centimeters from the front face (that is the face opposite to the photosensors region) of Module-0.  These beam counters provided a trigger for electrons and allowed to measure particle multiplicity.  The beam was tuned in single-particle configuration reducing its intensity by means of dedicated slits, obtaining $\sim 0.7$ particles/bunch with a bunch rate of 50 Hz, as shown from the initial distribution observed in the beam counters (see Figure  6.5) and in the calorimeter.

 To select cosmic rays, a large plastic scintillator $(50 \times 50 \times 200$ mm$^3)$, was located above the calorimeter.  All scintillators were read out by photomultipliers.  The
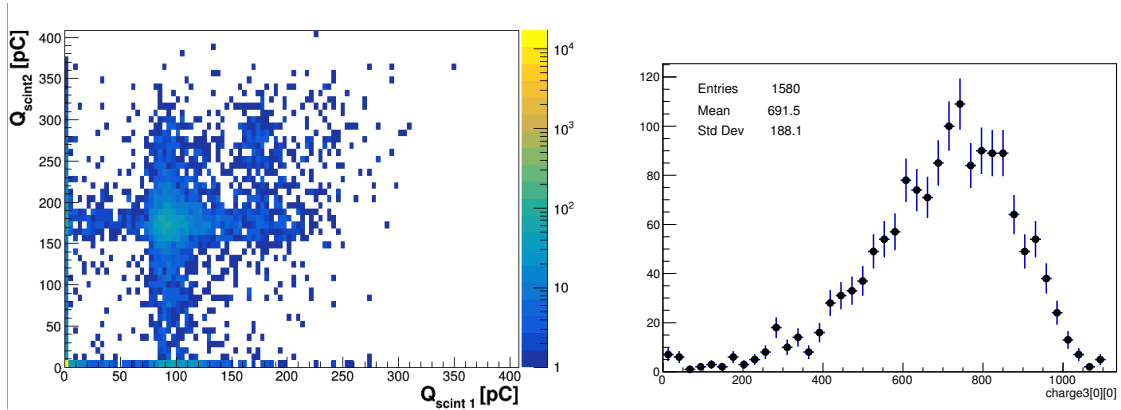
**Figure 6.5:** Left:Charge reconstructed on the two finger scintillators. Right: distribution of total charge in the central crystal.

temperature of the SiPMs was kept stable to 20 ℃ by using an external chiller, filled with water, connected to the Module-0 cooling pipes and monitored by the temperature sensors present on each FEE board. A calibration laser system was installed to monitor the response of the SiPMs coupled to the central crystal during running time. As shown in Figure 6.6 the maximum variation of the laser amplitude peak, due to changes in temperature, observed in few days of run was lower than 3% within each 1-2 hours running time. The laser stability $\Delta$ was evaluated per each run as: $\Delta = \frac{V_{\max} - V_{\min}}{V_{\mean}}$, where $V_{\max}$, $V_{\min}$, and $V_{\mean}$ are respectively the maximum, the minimum and the mean value of the laser waveform. Data were acquired for



**Figure 6.6:** Left: Variation of the response in the central crystal for Laser signals as a function of the trigger number for a run of 1.5 hours. Right: dependence of $\Delta$ along different runs.

one week by triggering with the OR logic of different trigger signals.
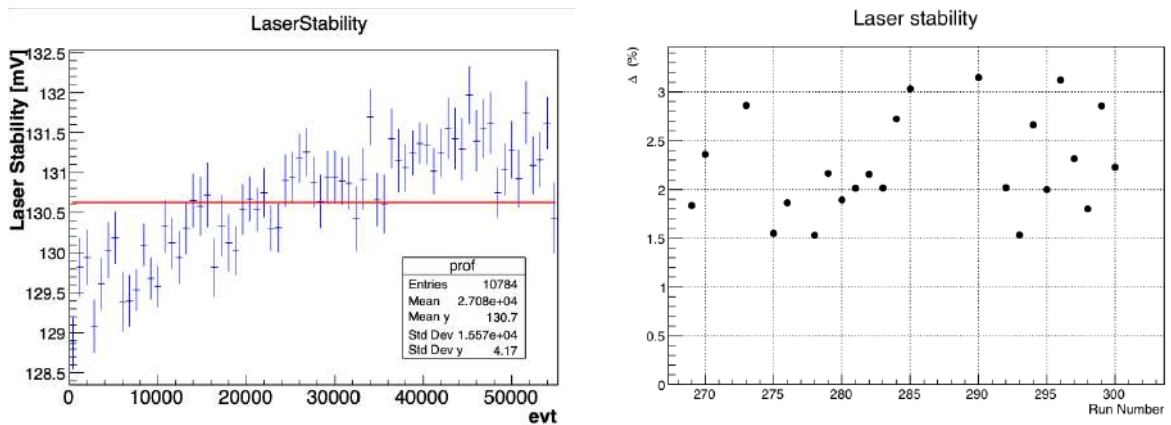
- the beam trigger (BT), produced by the coincidence of the discriminated signals of the two beam counters;

- a trigger (BTF) provided by the BTF system allowed to take beam events, without relying on our beam counters. This was mainly used to control the presence of a small background due to Bremsstrahlung photons coming with the beam that could go in accidental overlap with the beam electrons;

- a cosmic ray trigger (CRT) generated by the discriminated signals of the scintillation counter used to collect cosmic rays events for calibrations;

- a synchronisation signal from the Laser system (LT) allowed to acquire the laser pulses for monitoring purposes.

## 6.2 Charge Reconstruction and LY evaluation

The charge collected was estimated by numerical integration of the waveforms (see Fig.6.7 Left). Two different time windows were considered as integration gate:

- 450 ns integration gate (from 150 ns to 600 ns);

- 250 ns integration gate (from 150 ns to 400 ns).

Reduction of the integration gate reduces the noise as $\sqrt{\mathrm{DT}}$, where DT is the selected gate, allowing for improvement of the S/N for data analysis.
The signal width was mostly dominated by the SiPM and FEE shaping convolution, in fact during the pre-production phase, the CsI signal observed with PMT[2] was shorter than 200 ns. To confirm that a change in the integration gate did not degrade the performance of the matrix, the waveform obtained with a laser light pointed in the central crystal of the Module-0 was integrated in different time intervals. As shown in Figure 6.7 (Right), the charge resolution, defined as the ratio of the sigma and the mean value of the charge distribution fit with a Gaussian function, slightly

---

[2]2 inch UV extended photomultiplier (ET Enterprises, ET-9202QB)

improves from 350 ns down to 200 ns. This improves a little at ∼100 ns and then starts deteriorating. Since the real CsI light emission signal is larger than 100 ns we decided to be conservative and do not further reduce the gate below 250 ns.
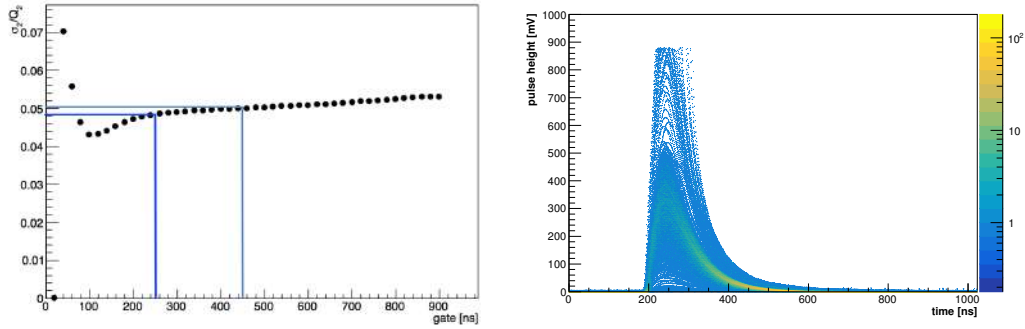


**Figure 6.7:** Left: charge resolution evaluated at different integration gates with a Laser Run. Right: waveform of 100 MeV electrons in the central crystal.

To avoid saturation, the amplification and the SiPMs HV values were adjusted for all channels. The initial gain-amplification value used for the preamplifier was 15 (30) for the G×1 (G×2) in the preamplifier switch respectively. As soon as the beam test started, a saturation at 100 MeV, both at the preamplifiers and at digitization level in the central channels (shown in Figure6.7 (Right)) was observed. A factor of 4 (8) gain reduction was needed at the preamplifier (MB) output to contain the maximum of the signal below the 2 (1) V saturation level. Therefore we decided to:

- reduce the operation voltage of the SiPMs: the bias voltage selected for all the SiPMs was $V_{bias} = (V_{op} - 6)$ V. The only exception is represented by the two SiPMs coupled to the central crystal that were biased at $V_{bias} = (V_{op} - 3)$ V. This reduction was tested offline in a dedicated setup to evaluate the effect on the response and on the PDE. We evaluated a response reduction of a factor of 1.3 and a photoelectron reduction of 0.04% for each Volt;

- reduce by a factor of ∼ 2 the preamplifier gain.

- reduce by a factor of 2 the output to not exceed the 1 V dynamic range in the CAEN digitizers (it will be 2 V in the final Mu2e setting);

After all these adjustments, we evaluated the number of photoelectrons observed at 100 MeV with the 250 ns integration gate. This was done by considering crystal with double readout and then evaluating the ratio between the charge distribution of the two SiPMs (see Figure 6.8) with the selected gate. For 100 MeV electrons in the central crystal the obtained value of NPE/MeV~22.
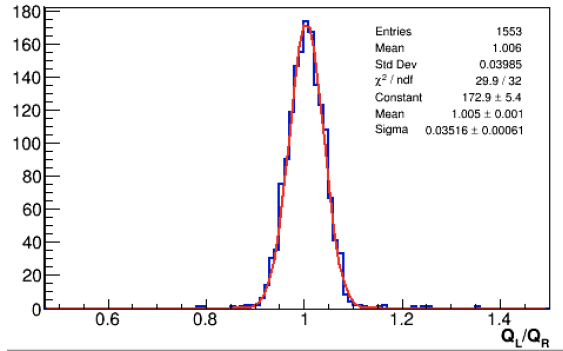


**Figure 6.8:** Distribution of the ratio of charge collected by two SiPMs coupled to the same crystal.

## 6.2.1 Pedestal evaluation and correction

During the test beam data taking in the BTF hall, the observed noise level resulted to be much higher ($\times 10$) with respect to that experienced in the assembly clean room. The only difference found was the digitizer system used. Moreover, the shape of the pedestal charge presented a double peak distribution, as observed in Figure 6.9.

To study in more detail this case, we defined a clean set of cuts to select noise events and better calculate the baseline:

- no charge deposit in the beam counters;

- no charge deposit in the scintillator used to veto cosmic ray events;

- no laser light in the central crystal.

**Figure 6.9:** Initial pedestal charge distribution

A first correction applied to the data consisted in fitting the pedestal waveform with a linear function and subtracting it to the signal waveform. Albeit a small improvement was observed, this correction function was not sufficient to eliminate the double peaks in the pedesta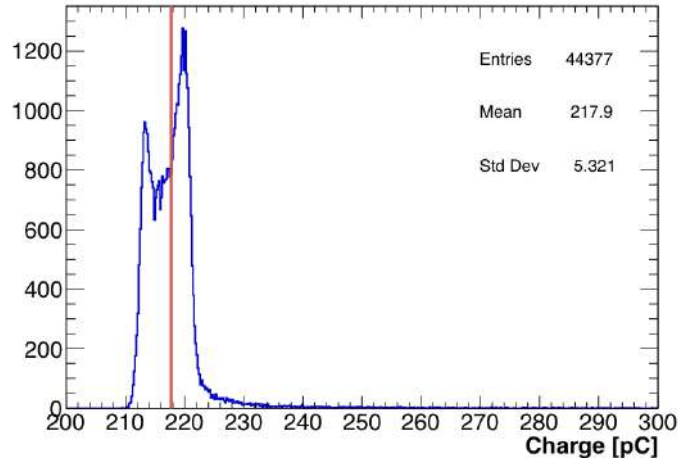l charge distribution. To improve the baseline correction, two correction functions (see Figure 6.10) were defined by splitting the pedestal charge distribution using the median (the red line reported in Figure 6.9) as separator. Doing this, two different baseline waveforms were derived for each channel:

- **Waveform right ($W_R$)**: average of baseline corresponding to the events that have a pedestal charge greater than its median value;

- **Waveform left ($W_L$)**: average of baseline corresponding to the events that have a pedestal charge smaller than its median value.

To choose the correct baseline to be subtracted to each waveform, a comparison between the mean values of the two correction functions and of the waveform under study is then performed in a time interval ([850,900] ns) away from the signal region. The correction selected is the one that minimises the difference between the two compared values. The results of the correction to the baseline is reported in Figure 6.11 where a scatter plot of the amplitude with respect to time is shown before (left) and after (right) the application of the correction. A much flatter behaviour is observed in the second case. In Figure 6.12, the original noise charge, the noise
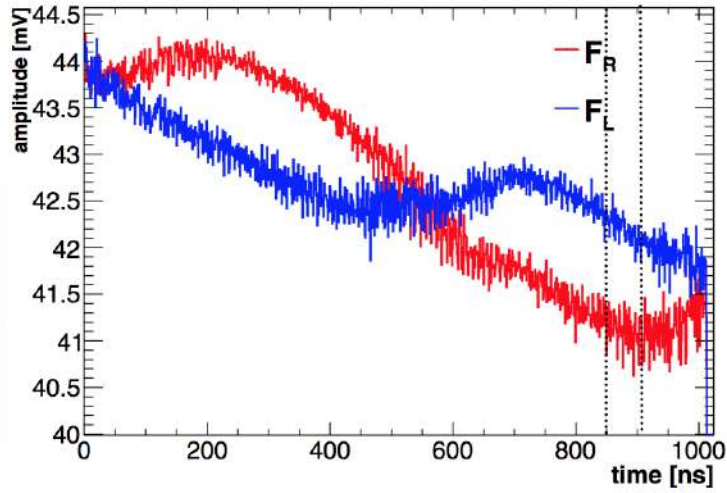
**Figure 6.10:** Correction functions for the "average" base line of noise runs obtained from $W_R$ and $W_S$.
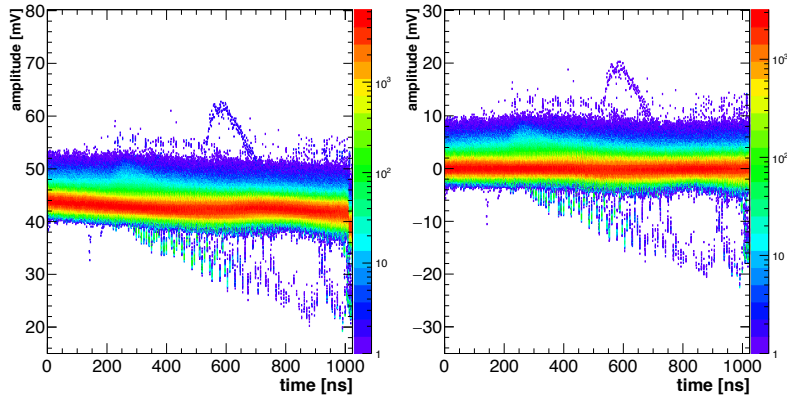


**Figure 6.11:** Baseline before(left) and after(right) the correction. In the example reported the channel under study corresponds to the central crystal.

charge evaluated in the narrowest time interval with the linear fit correction and the noise charge evaluated in the same interval with the baseline corrections applied are reported. The latter correction strongly reduces the two peaks behaviour and the pedestal charge distribution becomes much more similar to a Gaussian. The RMS values of the pedestal distribution obtained with the three different methods previously discussed are reported in Figure 6.13 left.
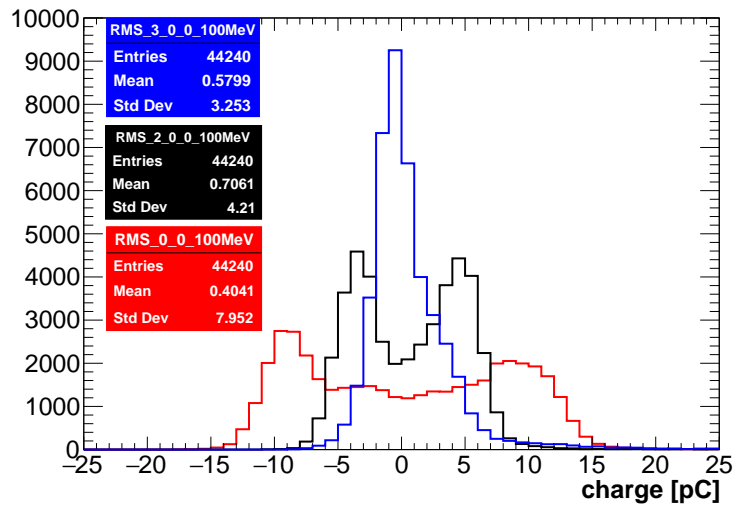
**Figure 6.12:** Comparison between different reconstruction of the pedestal charge in the central crystal of Module-0. Red: pedestal charge distribution evaluated in 450 ns without any baseline corrections, Black: pedestal charge distribution evaluated in 250 ns with the linear fit correction, Blue: pedestal charge distribution obtained with a 250 ns integration range and baseline correction with the two functions obtained from the waveform shape

## 6.2.2  Noise correlation

In order to check if any correlation between channels is observed in the calorimeter noise, we measured the RMS of the charge obtained summing up $N$ channels. This obtained RMS is then plotted as a function of the number of channels as shown in Figure 6.13.  The dependence is mostly linear, while the absence of correlation
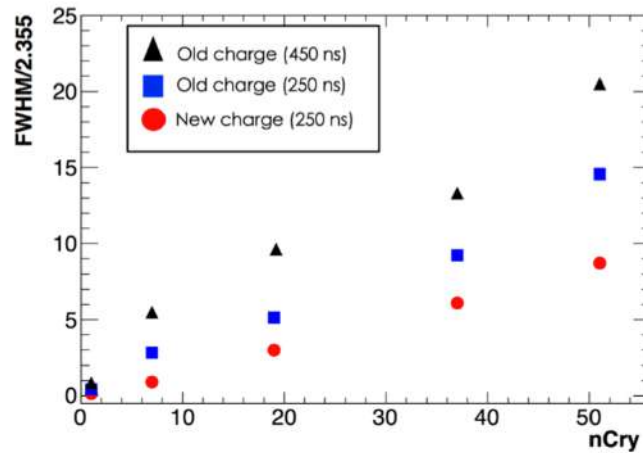


**Figure 6.13:** Dependence of the noise value obtained summing up several channels as a function of the number of channels for the three different evaluated charges

the dependence should have been proportional to the square root of the number of involved channels.

Indeed, due to the new CAEN digitizer boards, the noise between different Module-0 channels resulted to be highly correlated. A posteriori we realized that the presence of this noise was related to the DRS4 chip present in the CAEN board as shown also by other experiments that were using similar boards based on that chip. We also tested that noise disappeared when connecting a channel to the old WD. The correlation was evaluated choosing the first readout channel of the central crystal (Board 0-Channel 0) as reference. To reproduce the noise distribution of each channel in the Monte Carlo (MC) simulation, a sub sample (10000 events) of the noise events was saved on a simple text-file preserving all correlations among channels. This file was used to extract the noise for channels in a random order with respect to the MC simulation and then inserted in the MC files. This allowed to correctly evaluate the correlations observed in data and use the entire noise distribution of the different channels. The Data-MC comparison is shown in Figure 6.14.
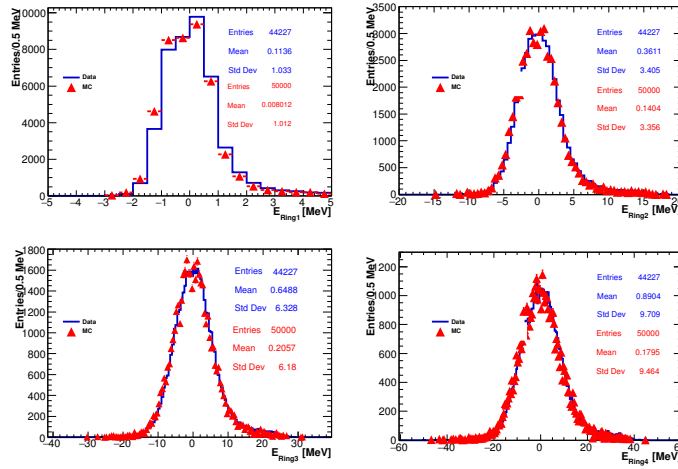
**Figure 6.14:** Data-MC comparison in different rings obtained adding an experimented noise sample to the Monte Carlo distribution

## 6.3 Single electron selection

The electrons from the BTF can have a multiplicity higher than one, so in addition of tuning the beam intensity and adjusting the collimator, a dedicated single-particle selection was necessary. We performed the following data rejection:

- Rejected events presenting a laser trigger;

- Rejected events with a cosmic trigger;

- Asked for a single particle in the beam counter charge distributions as shown in Fig. 6.15 (Left)

To provide a guide line of the reduction factors observed, we report here what obtained in a 100 MeV run for the central crystal in orthogonal configuration. We started with a total of 70000 DAQ collected events. The cosmic and laser rejection reduced the sample to 50000 (72%) events. The application of the single electron selection further reduce the sample to ∼1600 (∼ 2% of the original sample) events. To increase the statistics chains of different runs with the same energies have been used in the analysis.

**Figure 6.15:** Example of selection cuts. Left: cut on the charge distribution of one of the finger scintillator. Right: cut on the total energy reconstructed in the matrix, in this example the beam energy was 60 MeV

## 6.4   Correction of the amplifier non-linearity

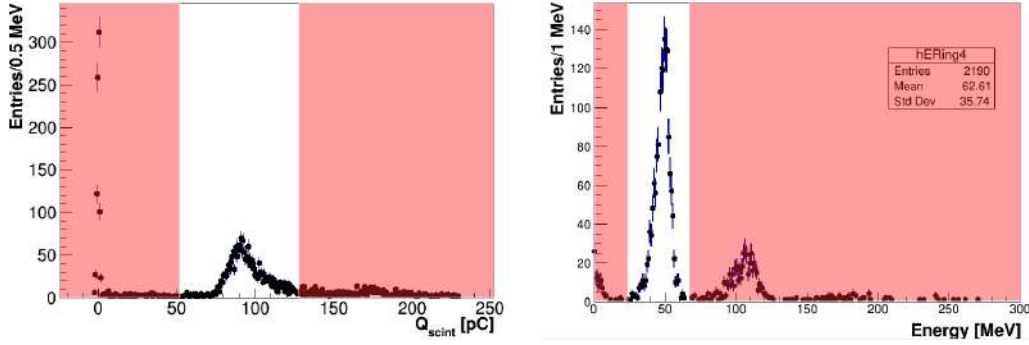After the test beam, the signal linearity, shape and output of the pre-amplifier and the behavior of the amplifier itself were accurately studied in the two different gain configurations as a bench-test. Measurements were then compared with a detailed simulations performed with SPICE [110]. The most relevant discovery was that the amplifier configuration G×2 presented a linear behavior while the configuration with G×1 shows a strong deviation by linearity at high pulse height values. To study the behaviour of the output pulse height as a function of the input current the result of a test performed enlightening a SiPM connected with a preamplifier with a LED is reported in Figure6.16 (left). When the signal amplitude becomes larger than 400 mV the amplifier looses its linearity. The blue line represents the expected linearity of the amplitude while the red line is the fit to the experimental data.

The charge of each signal was corrected per each event as follows:

$$\begin{cases} Q_i^{corr} = Q_i & \text{V}_i < 400 \\ Q_i^{corr} = Q_i \times \frac{V_i^{theo}}{V_i^{exp}} & \text{V}_i > 400 \text{ mV} \end{cases} \tag{6.1}$$

where $Q_i$ is the charge of the channel $i$, $V_i^{theo}$ is the theoretical signal amplitude and $V_i^{exp}$ is the maximum amplitude of the waveform of the channel $i$.

Figure 6.16 (right) shows the the correction function defined in Equation 6.1.
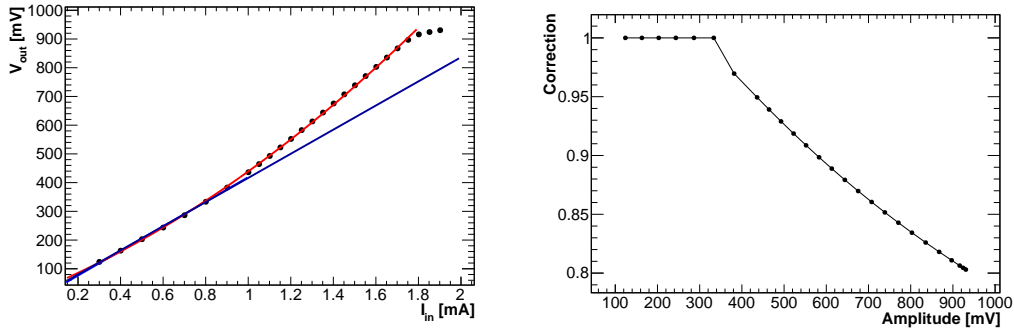
**Figure 6.16:** Left: Non-linearity of the amplifier: experimental data (black dots) vs the expected behaviour (blue line). Right: Correction function applied to the charge to the delete the amplifier non-linearity.

## 6.5 Channels equalization and energy scale

Due to the different composition in crystals, sensors and settings of Module-0, there was a large spread of response among the calorimeter channels. An offline equalisation of the response of each Module-0 channel was therefore necessary. Two strategies were followed:

- an equalization based on the beam energy deposition, performed for the two innermost rings of the Module-0;

- an equalization based on the cosmic rays energy deposition, carried out for all Module-0 channels.

Figure 6.17 shows a sketch of the crystals involved in these procedures.

In order to perform the beam equalisation, a 100 MeV electron beam was fired at the center of each crystal of the two innermost rings, for a total of 26 crystals. For each channel, the charge distribution of each biased SiPM was fit with a asymmetric Log-Normal [111] function and the mean charge obtained from the fit used as calibration factor, $B_i$. For the crystals with two sensors their average was used as calibration factor. The equalization parameter in the energy sum, $A_{i-0}$ is obtained as the ratio of the beam calibration factor with respect to the central crystal, $A_{i-0}^{beam} = B_i/B_0$. The statistical error associated to this procedure was of $\sim 1.5\%$ for each channel. An example of the fit performed is shown in Fig. 6.18 (left).
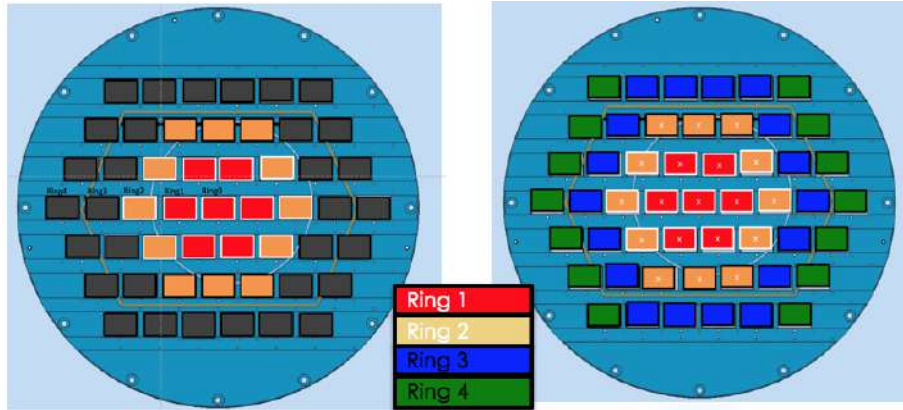
**Figure 6.17:** Crystals involved in the beam (right) and cosmic (left) equalization

The cosmic ray equalization was performed by selecting minimum ionizing particles
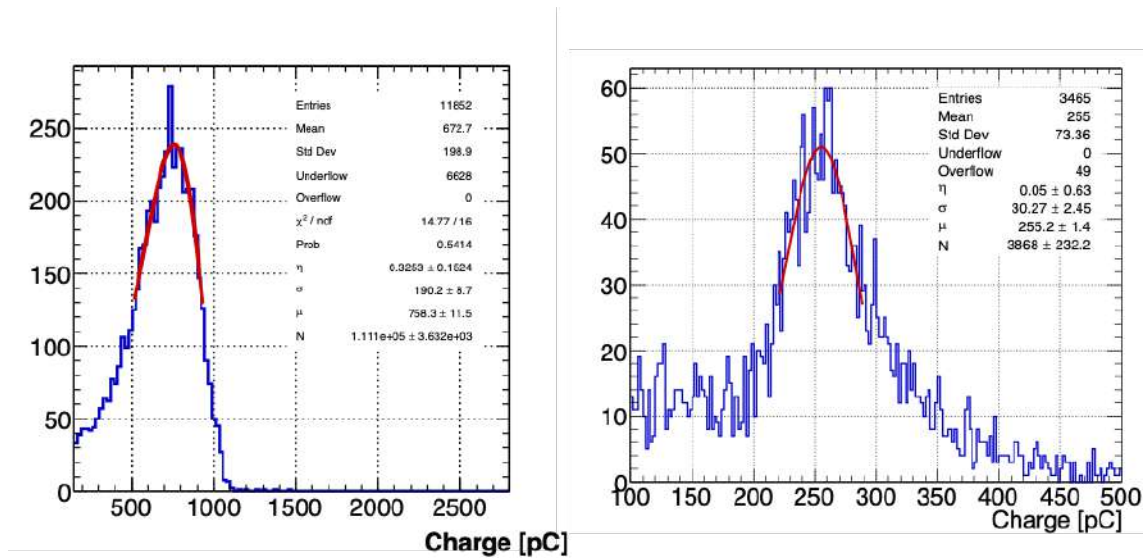


**Figure 6.18:** Charge deposited in a beam (left) and cosmic (right) event.

with the Cosmic trigger. Also in this case, the equalization parameter is obtained with respect to the central crystal $A_{i-0}^{cosmics} = C_i/C_0$ . The statistical error of each cosmic equalisation parameter, $C_i$, was of $\sim 0.5\%$. An example of the fit performed is shown in Fig. 6.18 right. To study the effect of possible systematic effect of the two methods, we have evaluated the ratio of the $A_i$ factors for beam and cosmic strategies of the 26 innermost channels. The distribution of the ratio between the two different $A_i$ is shown in Fig. 6.19. The average is well centered around 1 and the sigma of the distribution is of around 3%. For the offline equalization, the $A_i^{cosmics}$

factors obtained with the cosmics were used.
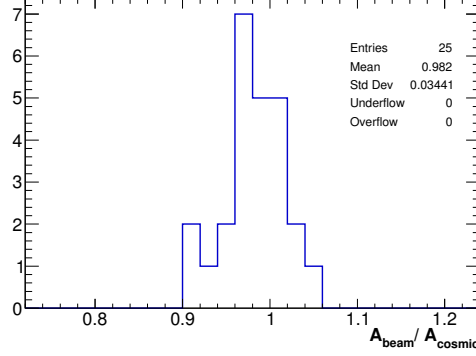


**Figure 6.19:** Ratio of $A_i$ factors for beam and cosmic calibration techniques.

The equalized total charge, $Q_{rec}$, was then defined as $Q_{rec} = \sum_{i=1,N}(Q_i * A_i^{cosmic})$, where $Q_i$ was the charge integration in 250 ns after correction for the baseline (see Section 6.2.1). Only the channels presenting a charge above a given threshold were included in the sum. The threshold selected corresponds to 3-times the noise measured on the i-th channel, $\sigma_i$. A good linearity in response is obtained (see Figure 6.20) in both matrix configuration. The energy scale factor resulted to be
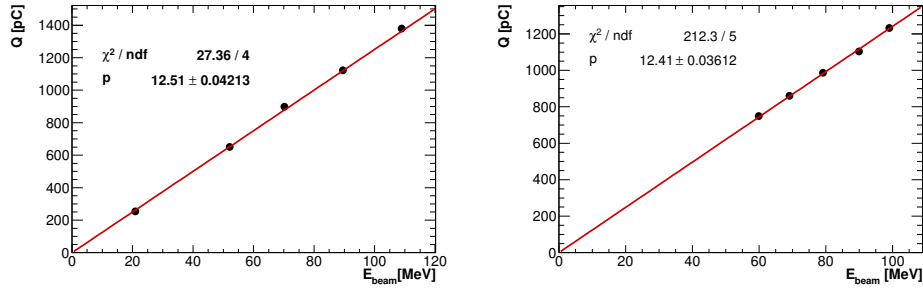


**Figure 6.20:** Reconstructed total charge as a function of the total energy deposition from simulation for the energy scan at 0 ° (Left) and 50 ° (Right) impinging angle.

$E_{sc} = (12.51 \pm 0.04$ pC/MeV for the orthogonal run. To all reconstructed charges to obtain the calibrated energy this factor was applied $E = Q_{rec} \times E_{sc}$. The same procedure was applied also to verify that the scale factor did not change in the tilted runs.

To check the effect of equalisation, the energy deposits on the crystals, fired with

the beam centered in two different position, after the equalisation have been compared. The results, reported in Figure 6.21, confirm the stability of the equalisation procedure.
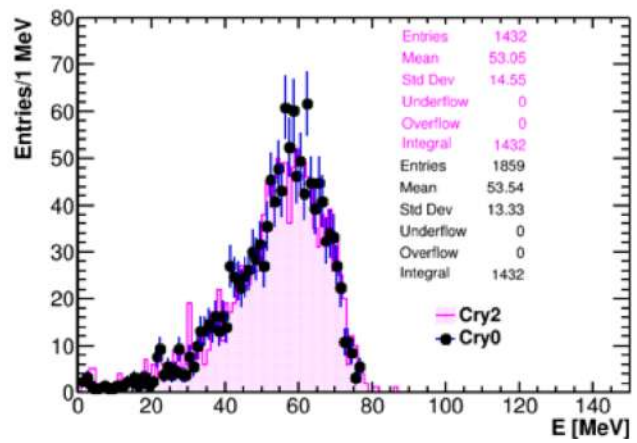


**Figure 6.21:** Energy deposit in two different crystal: $C_0$ (black dots) and $C_2$ (pink distribution).

## 6.6   Determination of the energy resolution

The energy resolution was evaluated as :

$$E_{\rm res} = \frac{\sigma_{E_{dep}}}{E_{dep}}, \tag{6.2}$$

where $\sigma_{E_{dep}}$ and $E_{dep}$ are respectively the sigma and the mean value of the fit performed on the energy distributions. The fit function used is a asymmetric LogNormal function:

$$f(E) = N\exp\left(-\frac{\ln^2\left[1 - \eta(E - \mu)/\sigma\right]}{2s_0^2}\right)\frac{\eta}{\sqrt{2\pi}\sigma s_0}, \tag{6.3}$$

where $N$ is the normalization parameter, $\mu$ is the position of the peak, $\sigma = {\rm FWHM}/2.35$, $\eta$ is the asymmetry parameter, and $s_0$ can be written as:

$$s_0 = \frac{2}{\xi}{\rm arcsinh}\left(\frac{\eta\xi}{2}\right), \xi = 2.35 \tag{6.4}$$

The energy resolution value obtained depends on the fit-range applied. A dedicated algorithm was developed to select the best fit range, that is the one that minimise the $\chi^2$.

## 6.6.1 Data-Monte Carlo comparison

Before reporting the final evaluation of the fits to the energy distribution performed on data and MC samples, a tuning of the simulation was carried out to improve the comparison of the shower distributions. The MC ingredients were the Geant-4 energy deposition, the addition of the photoelectron statistics and the correlated noise.

During comparison of the shower shape, we realised that an additional correction was needed: We found out that a small optical cross-talk was present in the detector.

### 6.6.1.1 Cross-Talk evaluation

By looking at data taken with the Laser trigger, we established the presence of a residual optical cross-talk among neighboring channels. The laser fiber was inserted only inside the SiPM holders of channel 0-0. In Fig. 6.22 the distribution of the pulse height for the channels surrounding the central crystals are shown. The central crystal had an average pulse height of $\sim 90$ mV.

The ratio between the cross-talk pulse heights and the central crystals is reported in Table 6.1 for the different channels as well as the cross-talk parameter corrected after the equalisation.

| Crystal Number | Cross-Talk parameter [%] | Cross-Talk parameter after equalisation [%] |
|:---:|:---:|:---:|
| 1 | $2.4 \pm 0.5$ | $3.0 \pm 0.6$ |
| 2 | $2.8 \pm 0.7$ | $2.5 \pm 0.6$ |
| 3 | $1.8 \pm 0.5$ | $1.7 \pm 0.4$ |
| 4 | $1.0 \pm 0.2$ | $1.1 \pm 0.2$ |
| 5 | $2.5 \pm 0.7$ | $2.6 \pm 0.7$ |
| 6 | $2.7 \pm 0.3$ | $3.5 \pm 0.4$ |

**Table 6.1:** Cross-Talk parameter evaluated from the data with a laser run.

The energy distributions obtained after adding different experimental effects to the Geant-4 deposited energy are shown in Figure 6.23. The original MC output is
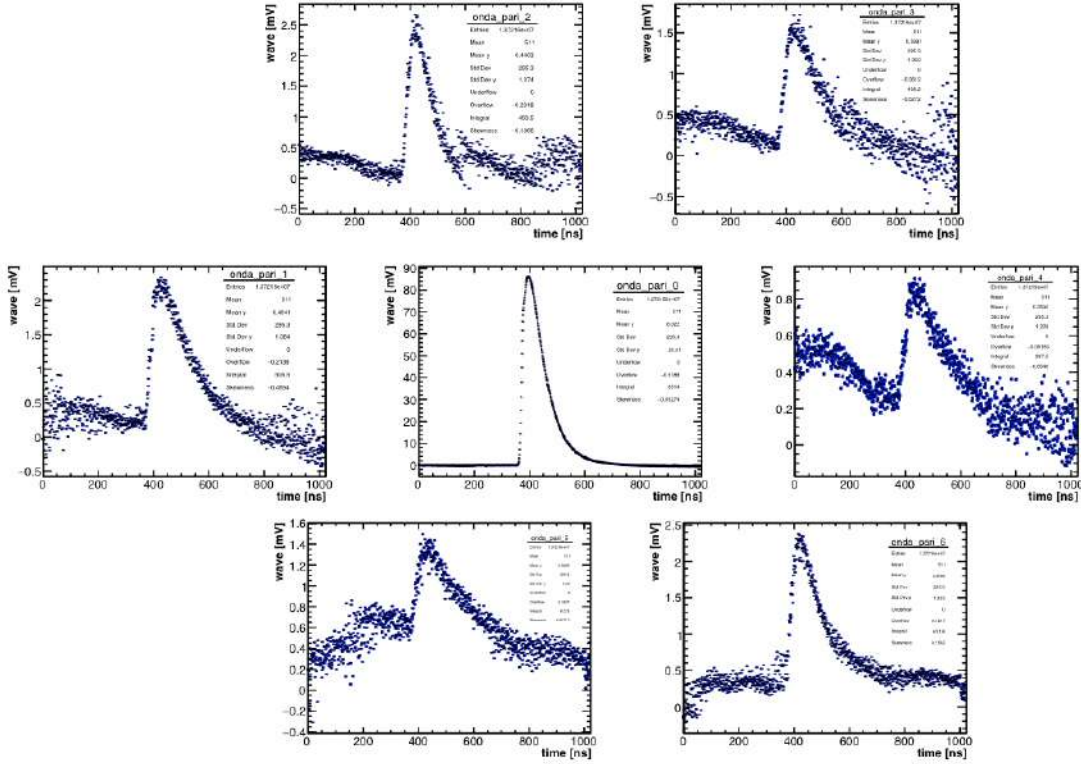
**Figure 6.22:** Waveform of the first ring obtained only with the laser light centered on the central crystal.

represented by the blue histogram. The first effect introduced was the Poissonian fluctuation of the number of collected photoelectrons (red histogram in Figure 6.23). In order to take into account this correction to the energy distribution, in each event the energy deposited in each crystal was randomly extracted from a Poisson distribution peaked at $\mu = 20$ p.e./MeV $\times$ E$_{\text{MC}}$. The value extracted was then divided by 20 again. The Gaussian noise, obtained for each event as explained in sect. 6.2.2, was added to this energy deposit (pink histogram in Figure 6.23). Finally, the cross-talk effect was included applying this simplified technique:

- Use the cross-talk contribution values of Table 6.1.

- Add to the energy of each channel of the first ring the cross-talk contribution, that is $E_i = E_i^{\text{MC}} + a_i^{\text{Xtalk}}$, where $a_i$ is the Cross-Talk parameter of the crystal $i$.
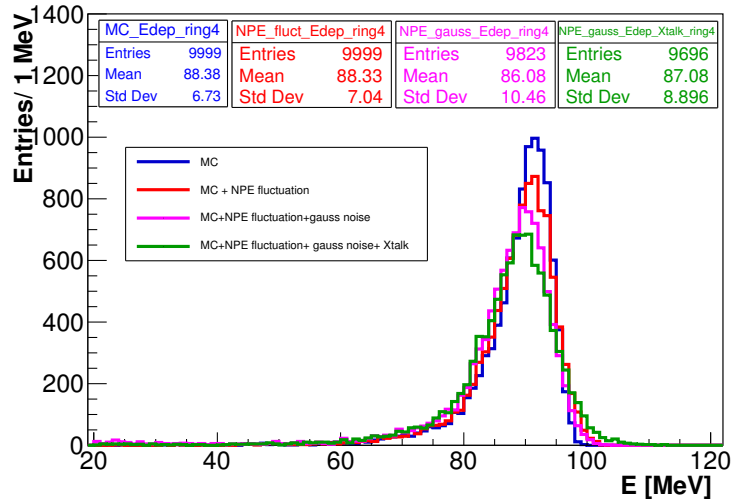
**Figure 6.23:** Monte Carlo energy deposit in the whole calorimeter prototype.

### 6.6.1.2   Data-MC comparison in the Ring around the central crystal

In Figure 6.24 and  6.25, the comparison between data and MC for the energy deposited in the central crystal and in the six neighboring crystals is shown. A sufficient data-Monte Carlo agreement is seen both in the orthogonal and tilted configuration.
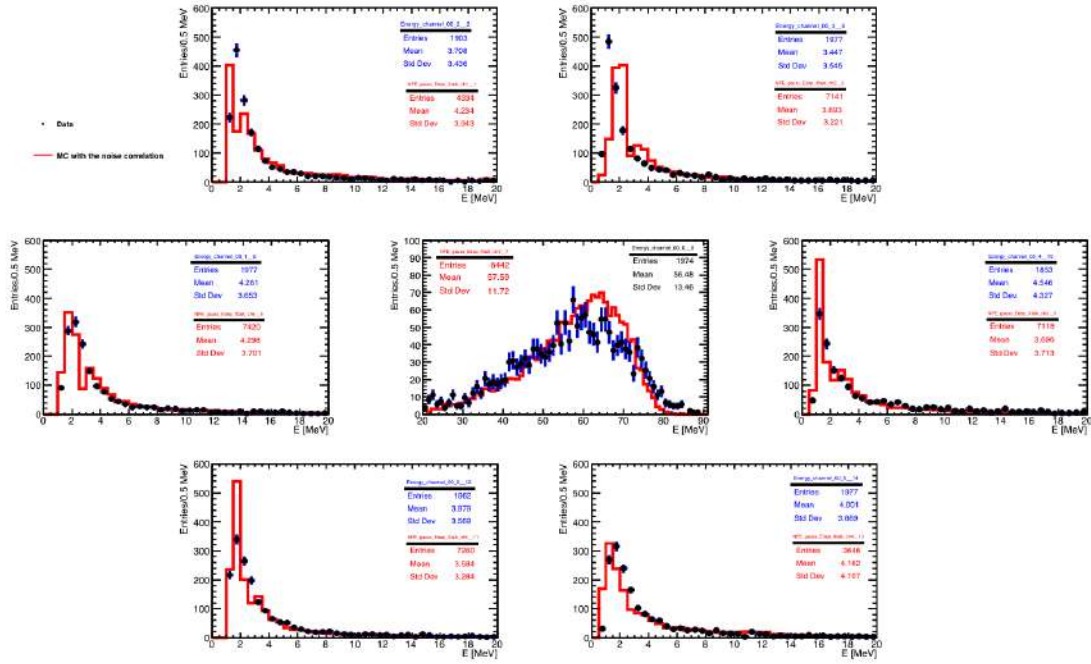
**Figure 6.24:** Orthogonal configuration: Data (black dots) -MC (red line) comparison of the energy deposit in the crystals of the first Ring.
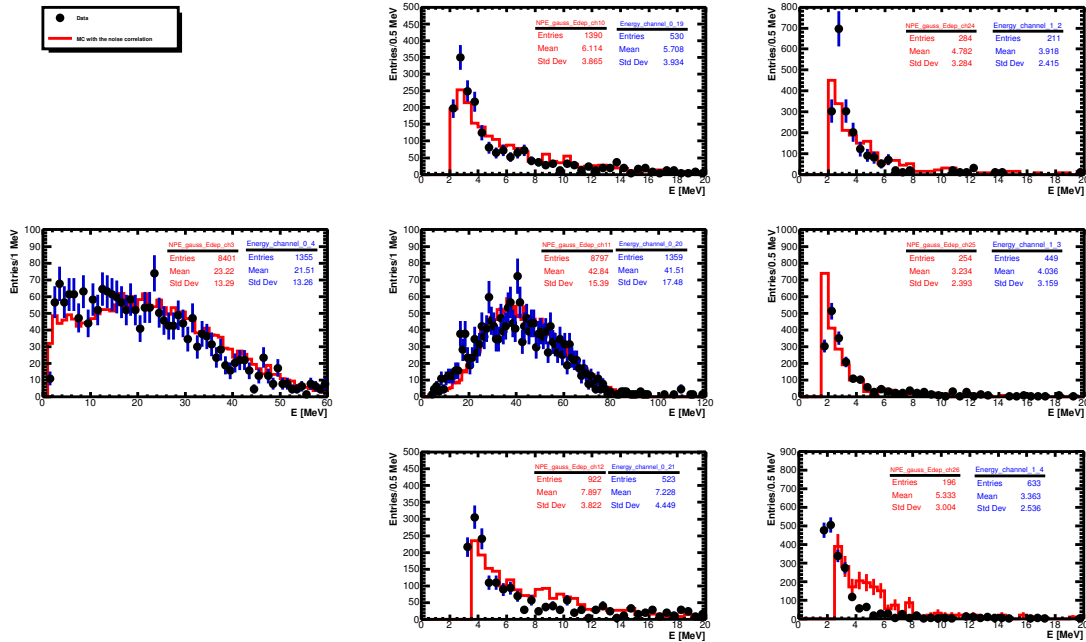


**Figure 6.25:** Tilted configuration: Data (black dots) -MC (red line) comparison of the energy deposit in the crystal fired by the beam and its neighboring crystals .

### 6.6.1.3 Data-MC comparison as a function of the Module-0 rings

The data-MC comparison of the energy distributions and of the energy resolution as a function of the Module-0 rings, for a 100 MeV orthogonal run fired in the central crystal, is shown in Figure 6.26. Figure 6.17 depicts how the rings are organised. As clearly indicated in Figure 6.26 and already mentioned before, most of the energy deposition is contained in the first two rings. The energy resolution variation from Ring 2 to Ring 4 is lower than 1%.
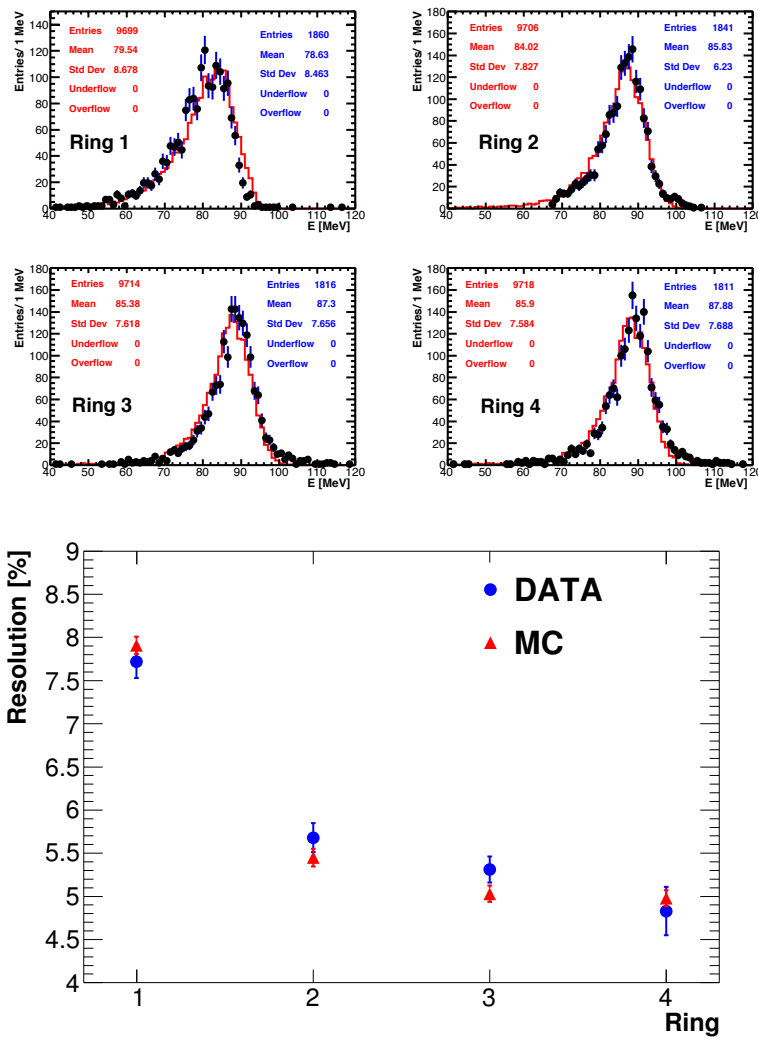


**Figure 6.26:** Top: energy distribution in the different ring for Data (black dots) and MC (red line). Bottom: data (blue dots) - MC (red triangles) comparison of the energy resolution as a function of the Ring number.

## 6.6.2   Energy distribution in orthogonal and tilted configuration

The energy distributions for different beam energies are reported in Figure 6.27 (Figure 6.28 ) for the orthogonal (tilted) configuration. The non Gaussian shape of the distributions is mainly due to the leakage (the crystals radiation length is $X_0 = 10$) and to the presence of the two finger scintillators used as beam trigger.

Since the energy of a conversion electron in Al is $\sim 100$ MeV particular care was
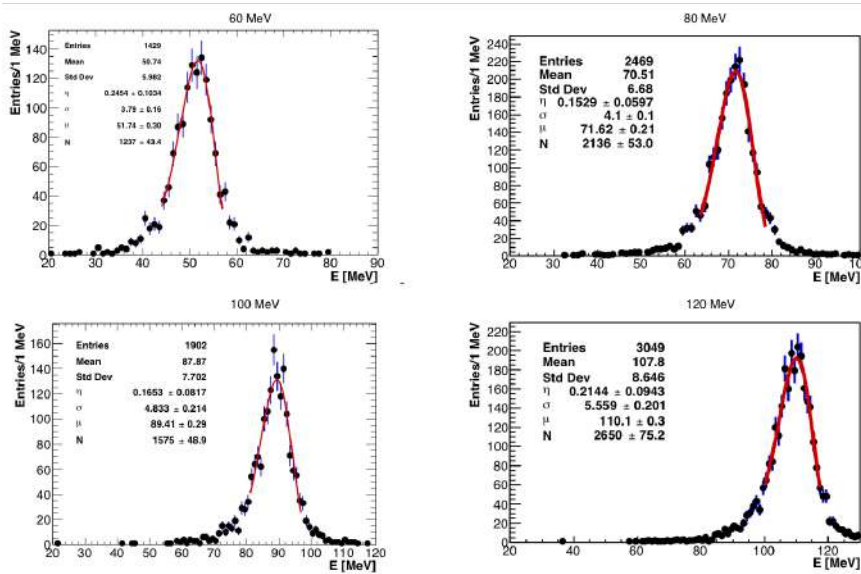


**Figure 6.27:**  Energy deposit in the whole Module-0 with an orthogonal run at different beam energies.

reserved for the 100 MeV runs to study the performances of the calorimeter. In Figure 6.29 (Figure 6.30) the comparison between Data and Monta Carlo energy distribution in the whole calorimeter for the orthogonal (tilted) configuration with a 100 MeV electron beam is reported.
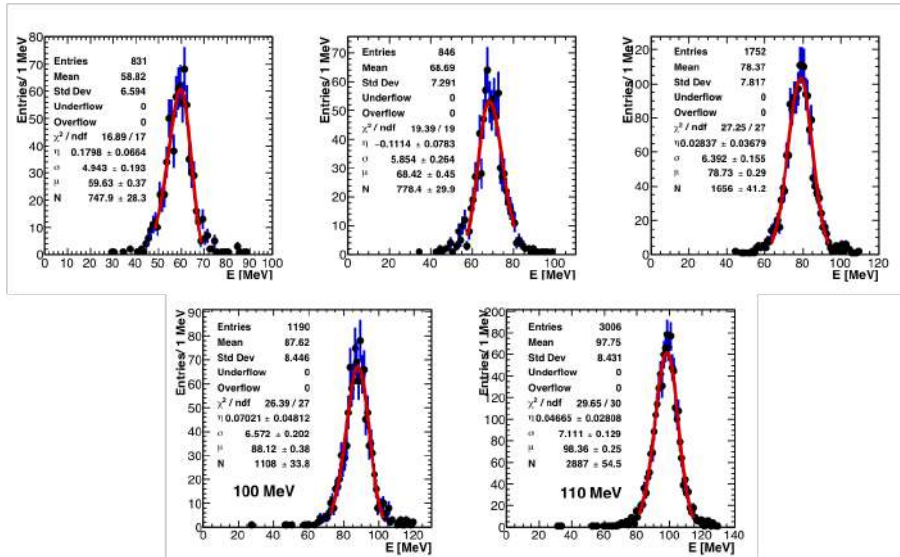
**Figure 6.28:** Energy deposit in the whole Module-0 with a tilted run at different beam energies.
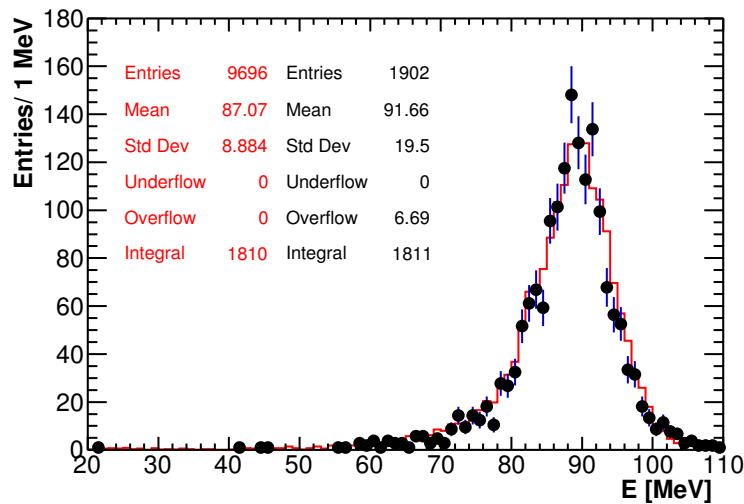


**Figure 6.29:** Data (black dots) - MC (red line) comparison of the energy deposit in the whole Module-0 with an orthogonal 100 MeV beam.
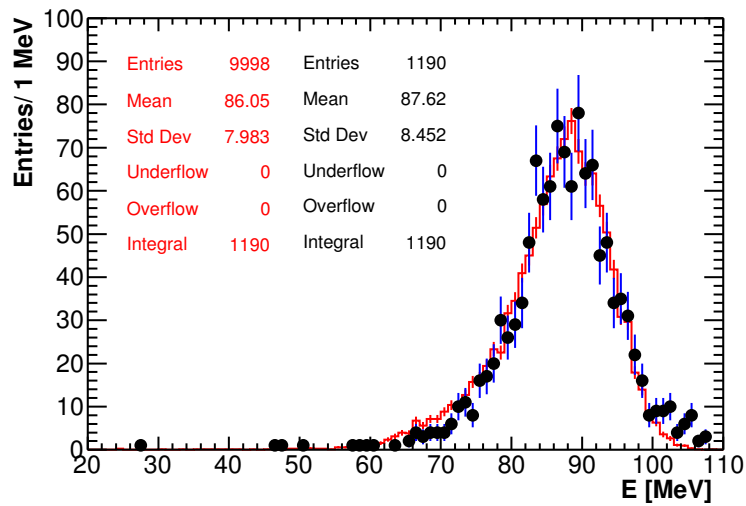
**Figure 6.30:** Data (black dots) - MC (red line) comparison of the energy deposit in the whole Module-0 with a tilted 100 MeV beam.

### 6.6.3 Energy resolution in the whole calorimeter prototype

The energy resolution, evaluated as the ratio of the sigma and the mean value of the energy distribution, obtained in the orthogonal (tilted) run was $\sim 5\%$ ($\sim 7\%$), these results are in good agreement with the Mu2e requirements.

Figure 6.31 shows the measured energy resolution as a function of the total energy reconstructed in the Module-0 for the orthogonal and tilted configuration of the beam.

The fit function used is:
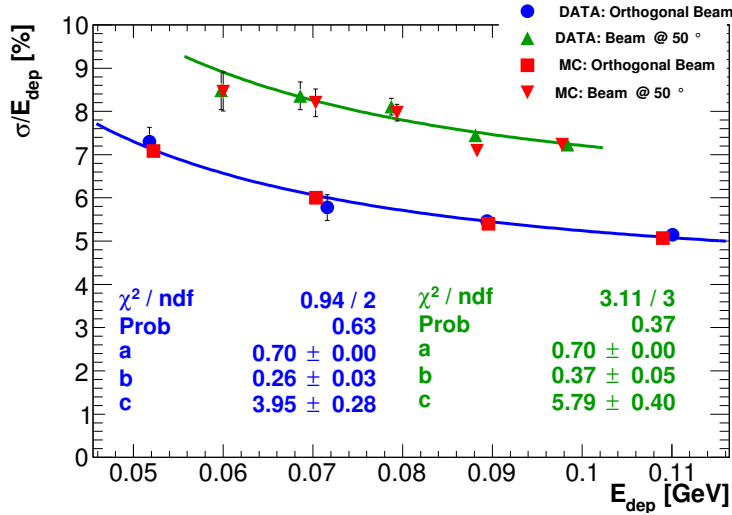


**Figure 6.31:** Energy resolution as a function of the energy deposit in the Module-0 in the orthogonal (blue) and tilted (green) configuration and comparison with the MC expectation.

.

$$\frac{\sigma_E}{E} = \frac{a}{\sqrt{E[GeV]}} \oplus \frac{b}{E[GeV]} \oplus c, \tag{6.5}$$

where the coefficient $a$ represents the stochastic term, $b$ the noise term and $c$ the constant term. Since the fit was insensitive to the stochastic therm, $a$ was fixed to 0.7%, as evaluated by a light yield contribution of 20 photoelectrons /MeV. The energy resolution deteriorated in the tilted run because of the increasing of fluctuation in the leakage term.

## 6.7 Time Reconstruction

The SiPM signal time is determined by fitting the leading edge of the waveform with an analytic function. The best accuracy is achieved by setting the signal time at a constant fraction (CF) of the pulse height. This is possible because the pulse shape is independent on the deposited energy in the crystals and similar for all photosensors used. Three components have to be fixed

- the waveforms fit function;

- the range where to perform the fit;

- the CF of the pulse height where to evaluate the time.

After the study of several different functions, the best result was obtained using an asymmetric log-Normal function:

$$f(t) = \exp\left(-\frac{\ln^2\left[1 - \eta\left(t - t_p\right)/\sigma\right]}{2s_0^2} - \frac{s_0^2}{2}\right)\frac{\eta}{\sqrt{2\pi}\sigma s_0},\tag{6.6}$$

where $t_p$ is the position of the peak. The three components optimisation have been performed on signals from Hamamatsu SiPMs reading out the central crystal, by varying the fit range and the constant fraction threshold. Results on parameter scans are reported in Figure 6.32.
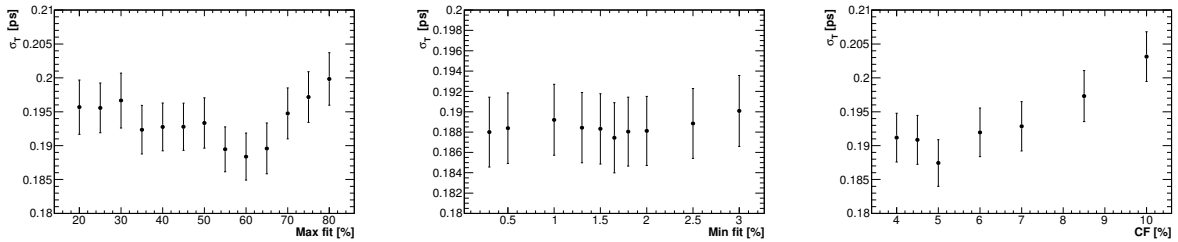


**Figure 6.32:** Optimisation scans of the time resolution as a function of the upper (lower) limit of the fit range on left (middle) and as a function of the Constant Fraction used to evaluate the time itself (right).

The time-fit upper and lower limits have been set to 1.65% and 60% of the pulse maximum height respectively. Figure 6.33 (left) shows an example of a waveform

fit by a log-Normal function in this range. Figure 6.32 shows the constant fraction scan results. The optimized threshold is set at 5% of the pulse height. Figure 6.33 (left) shows an example of a waveform fit by a log-Normal function in this range.

In the Mu2e experiment the sampling frequency of the calorimeter waveform digitizer boards will be 200 Msps while during the test beam it was 1GSPS, so that to evaluate the performance in this configuration, each waveform was re-sampled offline in 5 ns bins. Also at this sampling, we have enough points in the leading edge to allow a stable fit procedure. Figure 6.33 (right) shows an example of the fit performed on a re-sampled waveform at 200 Msps.

## 6.8 Time Resolution

The time resolution was measured using the time difference between the signals of two SiPMs connected to the same crystal. For each event passing the single electron selection cuts, the crystal with the largest energy deposit was used to compute the time difference between the two SiPMs, $\Delta T = T_{left} - T_{right}$. Figure 6.34 shows the resulting distributions at 1 Gsps and 200 Msps sampling frequency for electrons impinging at 0° on the central crystal. The time resolution was deduced by applying a Gaussian fit on the distributions and dividing the $\sigma$ by $\sqrt{2}$ to take into account the contribution of the two sensors. The resolution resulted for each single sensor to be $\sigma_t \sim 132$ ps for 1 Gsps sampling frequency and $\sigma_t \sim 195$ ps for 200 Msps.
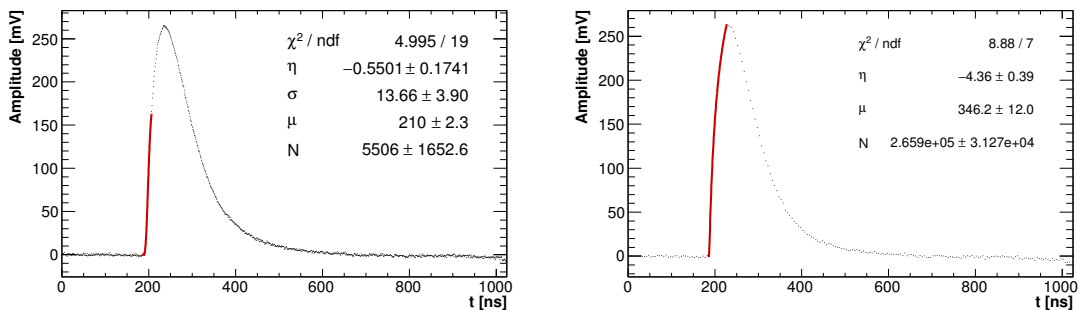


**Figure 6.33:** Example of the outcome of the optimized fit to a waveform at 1 Ghz sampling rate (left) and 200 MHz (right).
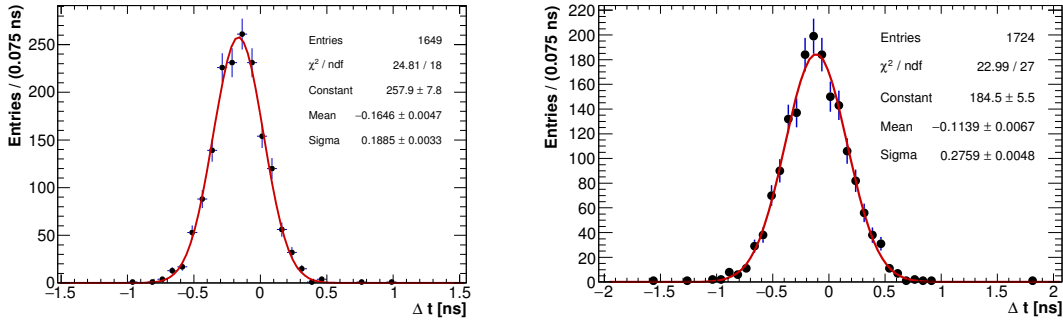
**Figure 6.34:** Time resolution of the central crystal readout by two Hamamatsu SiPM with a beam energy of 100 MeV. On left the sampling rate is at 1 GHz, on right the waveform has been resampled offline at 200 MHz. The red lines represent the Gaussian fit performed.

### 6.8.1   Time resolution as function of the energy

An energy scan has been performed from 60 MeV up to 120 MeV. In the tilted configuration, the channel with the highest energy deposit resulted to be the one readout by SensL SiPMs. Figure 6.35 shows the time resolution as a function of the deposited energy in the highest energetic crystal. The time resolution obtained with MIPs both with Hamamatsu and SensL SiPMs was also added to this plot.
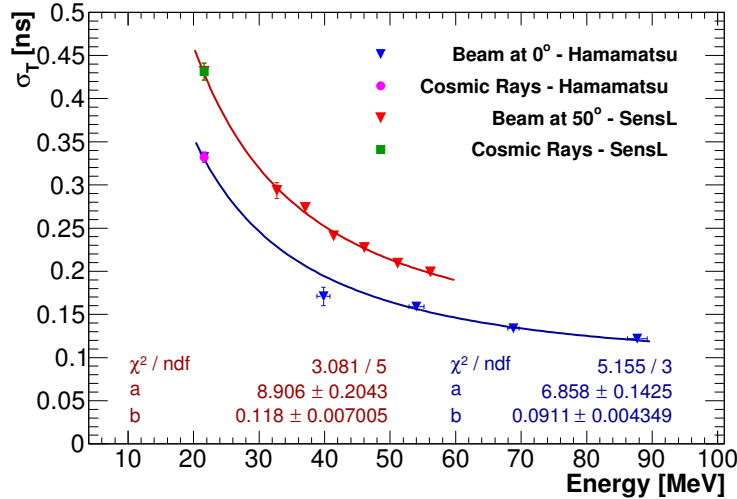


**Figure 6.35:** Time resolution as a function of the deposited energy in the highest energetic crystal.

The dependence of the single sensor time resolution $\sigma_T$ as a function of the
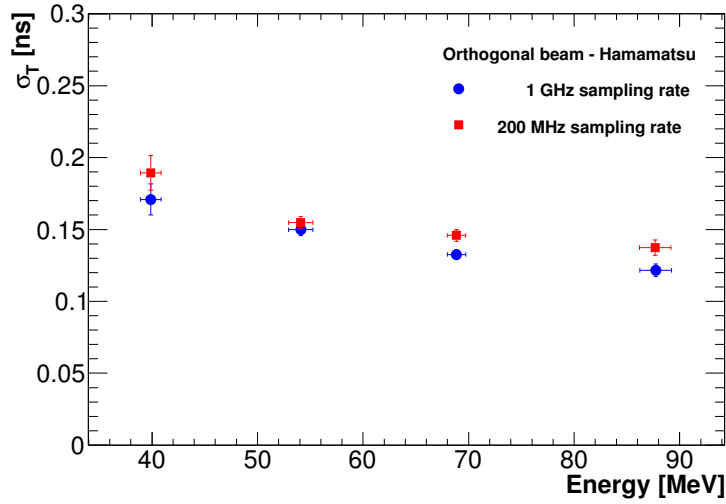
**Figure 6.36:** Time resolution as a function of the deposited energy in the highest energetic crystal.

deposited energy $E_{dep}$ was parametrized by the function:

$$\sigma_T = \frac{a}{E[GeV]} \oplus b, \tag{6.7}$$

where $a$ is proportional to the emission time constant of the undoped CsI and $b$ represents the additional contribution due to the readout electronics.

Figure 6.36 shows the time resolution at 1 Gsps and 200 Msps sampling rate obtained with Hamamatsu SiPMs as a function the deposited energy. A deterioration lower than 30% is observed. This demonstrates that the experiment timing requirement is well satisfied at the Mu2e sampling rate too.

# Chapter 7

# Kinematics, reconstruction and background sources for $\mu^- - e^+$ conversion

An introduction on the relevance of the LNV process $\mu^- + N(A, Z) \to e^+ + N(A, Z - 2)$, and on the results obtained on this search with the previous experiments can be found in Section 1.4. In this chapter, the kinematics of the process as well as the capability of the Mu2e experiment in reconstructing the $e^+$ mono-energetic line for ground state transitions are described. We also summarise the list of considered backgrounds with an emphasis on the nowadays knowledge of the Radiative Muon Capture photon spectrum. The related $e^+$ background is considered one of the most dangerous and it will be fully described and estimated in Chapter 8.

In Mu2e, the $\mu^- - e^+$ conversion mediated through Giant Dipole Resonance will strongly suffer from RMC background, and will be reduced by tracking acceptance. Therefore, in this thesis, only the ground state transitions are considered.

## 7.1    Evaluation on the positron conversion energy

The positron energy in:

$$\mu^- + Al(27, 13) \to e^+ + Na(27, 11), \tag{7.1}$$

is calculated down an accuracy of 10 keV, using an approach consistent with the calculation of the electron energy in $\mu^- Al \to e^- Al$ conversion reported in Ref. [114]. Assuming the daughter nucleus produced in the ground state, the energy conservation for the process of double-charge exchange conversion can be written as

$$M(^{27}\text{Al}) + m_\mu - B_\mu = M(^{27}\text{Na}) + E_{\text{recoil}} + E_{e^+}, \tag{7.2}$$

from which the positron energy can be evaluated as:

$$E_{e^+} = m_\mu - B_\mu - E_{\text{recoil}} - \Delta_{Z-2}, \tag{7.3}$$

where $m_\mu$ is the muon mass, $B_\mu$ is the muon binding energy in the muonic atom, $E_{\text{recoil}}$ is the kinetic energy of the recoiling nucleus in the final state, and $\Delta_{Z-2}$ is the difference between the two nuclear masses. Since the radius of the muon orbit is 200 times smaller than the one of the electron orbit ($r_e \sim 1/m_e$), the electrons do not effectively participate in the muon capture process. For this reason, the kinematical calculations should use the nuclear and not the atomic mass: $M_N = M_A - Z \cdot m_e$, where $M_A = A_r \cdot u$, $A_r$ is the relative atomic mass, **u** is the unified atomic mass unit in MeV/c$^2$, and $\mathbf{m_e}$ is the electron mass.

**Muon binding energy**

To evaluate the muon binding energy in an aluminum nucleus the following expression is used:

$$B_\mu = \frac{Z^2 \alpha^2 M_i}{2} = 0.4734 \text{ MeV}, \tag{7.4}$$

where $Z = 13$ is the nucleus atomic number, $\alpha$ is the fine-structure constant, and $M_i$ is the reduced mass of the initial state:

$$M_i = \frac{m_\mu M(^{27}Al)}{m_\mu + M(^{27}Al)}. \tag{7.5}$$

In Ref. [114], the muon binding energy in muonic aluminum has been calculated by solving the Dirac equation with $m_e = 0$ and taking into account the finite nuclear size. The calculated value is $B_\mu^{\text{art}} = 0.4644$ MeV.

Comparison of the two results $\Delta B_\mu = B_\mu - B_\mu^{\text{art}}$ shows that the correction for the nuclear size in Al is close to 9 keV.

To maintain consistency with Ref. [114], in the following the value of $B_\mu^{\text{art}}$ is used.

### $^{27}$Na recoil kinetic energy

The energy of the recoiling $^{27}$Na nucleus can be calculated by solving the equation of a two body decay:

$$E_1 = \frac{M^2 + m_1^2 - m_2^2}{2M}, \tag{7.6}$$

the quantities reported in Eq. 7.6 are evaluated as:

$$M = M(^{27}\text{Al}) + m_\mu - B_\mu = 25231.695 \text{ MeV/c}^2, \tag{7.7}$$

$$m_1 = M(^{27}\text{Na}) = 25139.202 \text{ MeV/c}^2, \tag{7.8}$$

$$m_2 = m_e, \tag{7.9}$$

and the kinetic energy of the recoiling $^{27}$Na nucleus is:

$$E_{\text{recoil}} = E_1 - M(^{27}\text{Na}) = 0.16952 \text{ MeV}. \tag{7.10}$$

### Determination of the positron energy

Finally inserting in Eq. 7.3 all the numerical values calculated in the previous paragraphs, we can estimate the $e^+$ energy as:

$$E_{e^+} = 92.32 \text{ MeV}. \tag{7.11}$$

## 7.2 Positron generated in leading logarithmic approximation

When detecting $e^+$ from $\mu^- \to e^+$ conversion process, the monochromatic $e^+$ spectrum is modified by the radiative photon emissions and fluctuations of energy loss in the target. While the interactions in the target are taken into account in the Mu2e simulation, the effect of photon emission, described in [117], has to be manually inserted in the generator. Radiation of real photons reduces the positron energy and modifies the leading order conversion spectrum:

$$\frac{1}{\Gamma_0} \frac{d\Gamma}{dE_e} = \frac{1}{E_{max}} \left[ \left( \ln \frac{4E_e^2}{m_e^2} - 2 \right) \frac{E_e^2 + E_{max}}{E_{max}(E_{max} - E_e)} + P(E_e) \right], \tag{7.12}$$

where $E_e$ is the positron energy and $E_{max} = 92.32$ MeV is its endpoint. This probability function is composed of two terms: a universal part, that accounts for the photon emission by a free positron and a model dependent part $P(E_e)$, that corresponds to a very small contribution due to the positrons not being free. This latter term has been neglected in the following.

In Figure 7.1 the spectra obtained from Leading Logarithmic (LL) and Leading Order (LO) generators are reported. Thus, as described in the following, the in-
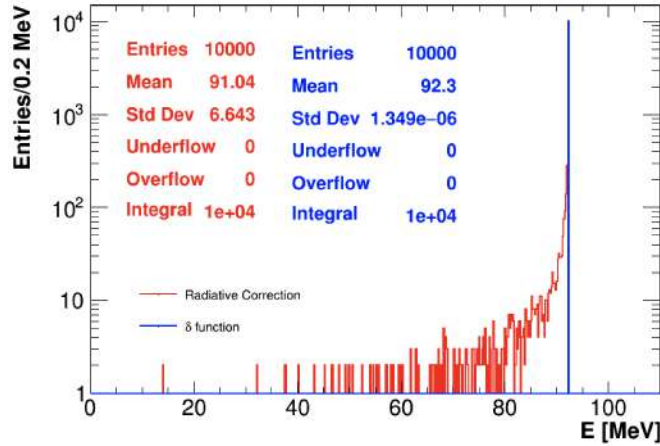


**Figure 7.1:** Comparison of the spectra obtained with the LO (blue) and the LL (red) generator.

troduction of radiative corrections reduces the number of positrons expected within the experimental signal window by several percent.

The Mu2e experiment is optimized for the search of electrons with $\approx 105$ MeV/c momentum; since the $\mu^- \rightarrow e^+$ conversion signal peaks at lower energies (92.3 MeV), to reduce the background particles entering in the signal window, it is necessary to optimize the reconstruction with a specific set of cuts.

The quality cuts applied have been chosen in order to minimise the fraction of tracks with $\Delta P = P - P_{MC} > 2$ MeV at $\sim$90 MeV. The quantity $\Delta P$ represents the difference between the reconstructed momentum and the one provided by the simulation at the tracker entrance. The effect of the applied cuts on the $P - P_{MC}$ can be observed in Figure 7.2, where a comparison of the resolution before and after the cumulative cut applied is reported. For further information see Appendix A.1. The presented results concern only reconstruction efficiencies that have been evaluated using positron generated with the Leading Logarithmic (LL) and Leading Order (LO) approximation in absence and presence of pileup background (in the following
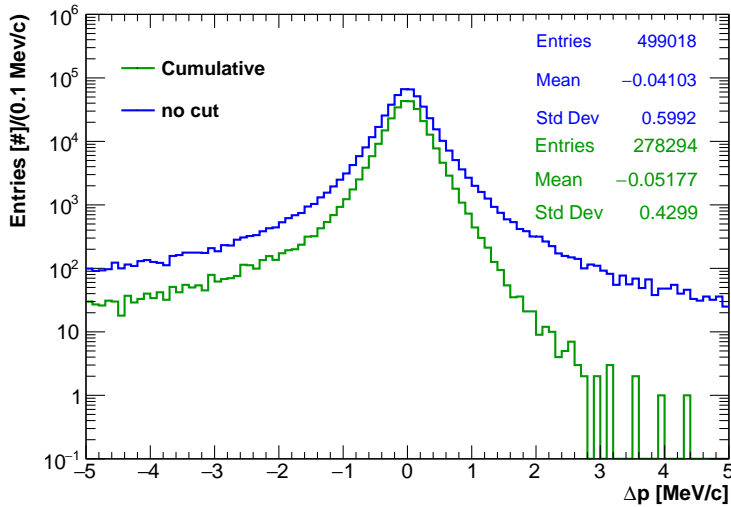
**Figure 7.2:** $P - P_{MC}$ reported in absence of cuts (blue line) and when the cumulative cut is applied (green line).

referred as mixed background).

At the moment of writing, no dataset with mixed background included has been generated in LL approximation, the cut efficiencies have been extrapolated also to this case as: $\epsilon_{LLmix} = \epsilon_{LL} \frac{\epsilon_{LOmix}}{\epsilon_{LO}}$ .

for positrons generated in LL approximation in presence of backgrounds, following :

After the application of these cuts, the overall acceptance, evaluated as the ratio of the reconstructed tracks and the generated tracks, is 17 % for the LL dataset and 18 % for the LO dataset. In Figure 7.3 the reconstructed momentum distribution obtained from the LL and LO datasets is shown. The effect of the radiative corrections in the LL distribution is evident in the increase of the lower momentum tail.

To evaluate the fraction of signal particles outside the momentum signal window, it is necessary to take into account that a further reduction in the acceptance is due to the combination of the radiative corrections and the track reconstruction. In Figure 7.4 (left) this acceptance reduction is reported up to a 10 MeV wide signal window. Both reductions at generation and reconstruction level are reported.

To minimize the background events coming from the high energy tail of the RMC, a signal window between 90.5 MeV and 92.5 MeV have been defined (see Figure 7.4
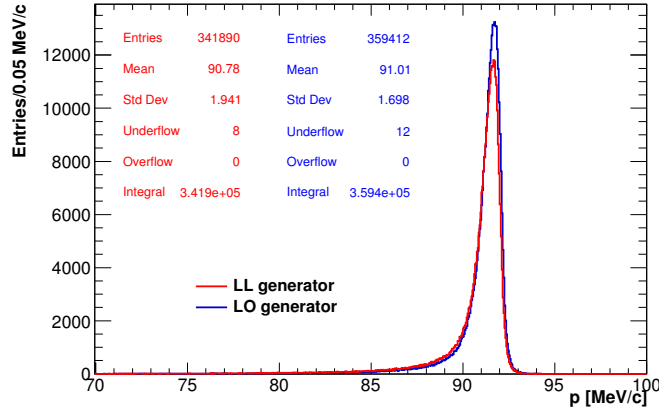
**Figure 7.3:** Comparison of the reconstructed momentum distribution obtained with the LO (blue) and the LL (red) generators.
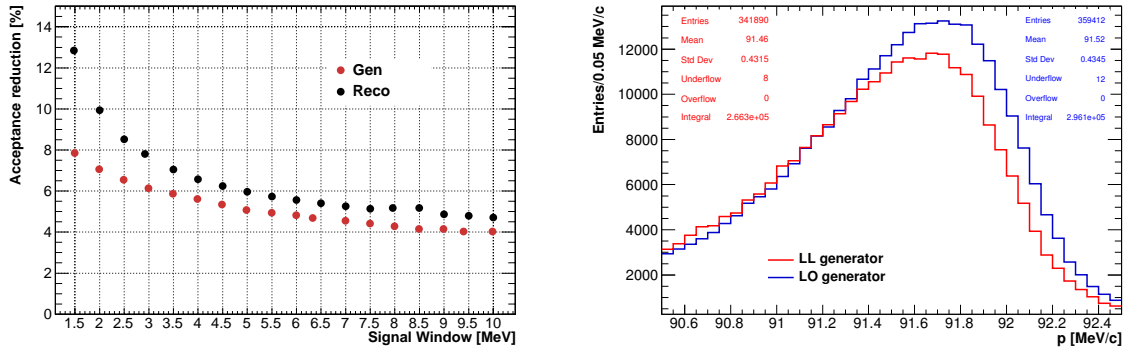


**Figure 7.4:** Acceptance reduction as a function of the selected signal window.

(right)) In this region the expected acceptance reduction is 9% for the dataset generated in LL approximation and 7% for the LO dataset.

## 7.3 Backgrounds

### 7.3.1 Radiative Muon Capture

The most potentially dangerous source of background in a $\mu^- - e^+$ conversion experiment is the RMC, given by the reaction:

$$\mu + N(Z, A) \rightarrow \gamma + \nu_\mu + N(Z - 1, A). \tag{7.13}$$

The produced photon can convert internally or externally, potentially yielding a positron with an energy consistent with that of a conversion positron. Assuming a massless neutrino, the kinematic limit of the photon in this process is evaluated:

$$k_{max} = m_\mu^2 - |B_\mu| - E_{recoil} - \Delta M c^2 \approx k_{DIO}^{max} - \Delta M c^2 = 101.853 \text{ MeV}, \qquad (7.14)$$

where $\Delta M c^2 = M(A, Z-1) - M(A, Z)$, $B_\mu$ is the binding energy of the muon on the parent nucleus, $E_{recoil}$ is the recoil energy of the daughter nucleus and $k_{DIO}^{max}$ is the kinematic endpoint of a DIO electron.

An important consideration in the design of the stopping target is thus to choose a material that exhibits a large value of $\Delta M c^2$ in order to separate the kinematic endpoints of the RMC and DIO processes. The choice of the aluminum was optimized for the $\mu^- - e^-$ conversion search while silicon or titanium would have represented a better solution for this search.

The RMC process has been modeled using the closure approximation [118],[119], which suggests a photon-energy dependence of the form:

$$\frac{d\Lambda_\gamma (E_\gamma)}{dE_\gamma} = N \left( 1 - 2x + 2x^2 \right) x(1-x)^2, \qquad (7.15)$$

where $N$ is a normalization constant and $x = E_\gamma/k_{max}$. In this approximation $k_{max}$ does not necessarily correspond to the value of 101.853 MeV. Rather it is treated as a parameter that can be fit using experimental data. During the '90s the TRIUMF experiment measured the rate of the RMC on different materials. In [120] and in [135] the value of the endpoint for the RMC spectrum on an aluminum target is reported. The collaboration stated respectively $k_{max}^{'98} = 90.1 \pm 2$ MeV and $k_{max}^{'98} = 91 \pm 1.8$ MeV.

A detailed study performed on the evaluation of the best fit for the $k_{\max}$, reported in Appendix B.1, showed that the '98 results used a detector response function not in agreement with the calibration data. We therefore excluded this $k_{\max}$ value. We also re-analyzed the TRIUMF '92 data obtaining the same central value but a better uncertainty $k_{\max Mu2e} = 90.1 \pm 0.5$. This is the reference value used in the following. Other values of interest are $k_{\max} = 91.6$ MeV ( $k_{\max}$ plus $3\sigma_{Mu2e}$) and $k_{\max} = 92.1$ MeV( $k_{\max}$ plus $\sigma_{92}$). In Figure 7.5 the energy spectrum reconstructed by the TRIUMF experiment, as well as three curves, including also the detector response, obtained with different $k_{max}$ are reported.
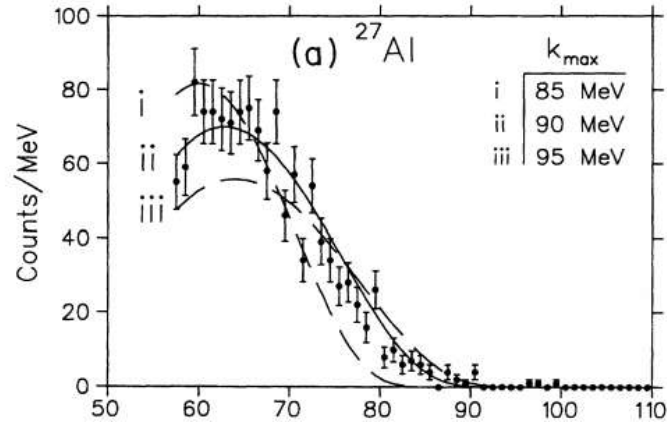
**Figure 7.5:** RMC spectrum on Al with the convolution of the TRIUMF detector response and the closure approximation. The solid line is one giving the best fit on $k_{max}$.

The difference between the $k_{max}$ values obtained from calculation and the experiments is due to the assumption that all the transition strength leads to a single nuclear excitation energy. A detailed description of the procedure used to evaluate the RMC background is reported in Chapter 8.

To account for the internal RMC, the ratio between positron tracks coming from internal and external RMC is considered ([122], [123]). From Figure 7.6, the in-
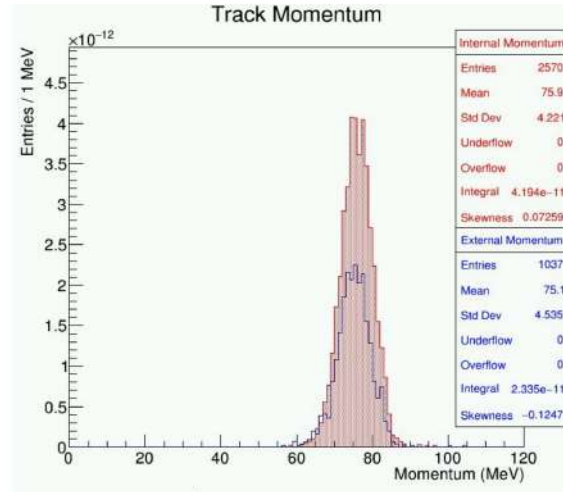


**Figure 7.6:** Internal (red) and external (blue) positron track obtained per photon.

ternal conversions double the external, however there is not enough statistic in the region around 90 MeV. So internal and external conversion are generated for 90 MeV photons. Only conversions being enough asymmetric are considered to be near the

signal region, and the number of highly asymmetric internal conversions is, as shown in Figure 7.7, $\sim 1.5$.
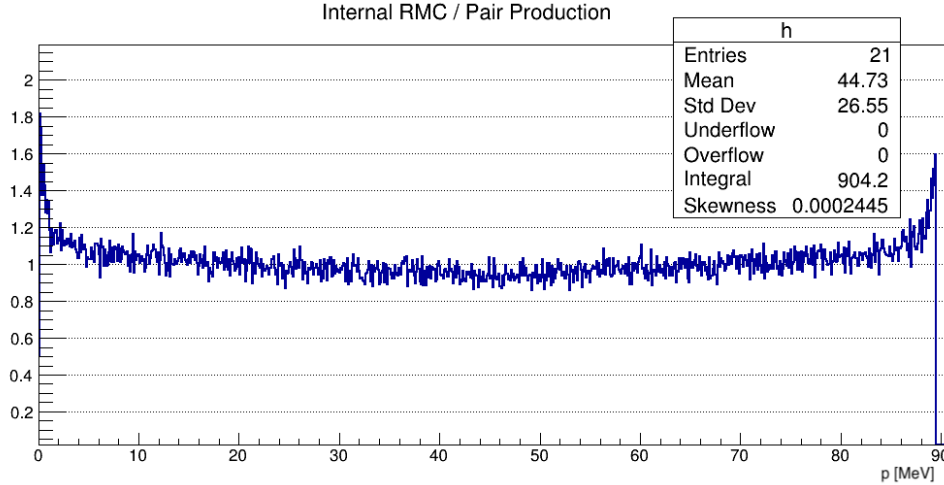


**Figure 7.7:** Ratio of the internal tracks and pair production obtained with 90 MeV photons.

Multiplying these two factors, the ratio of internal/external conversion is $\mathcal{R} = \sim 3$. So that, the expected number of positrons from internal conversion in the signal region has be evaluated as:

$$N_{e^+}^{int} = 3 * N_{e^+}^{ext} \tag{7.16}$$

## 7.3.2 Positron or Muons from Cosmic Rays

As already stated in Chapter 1, the cosmic rays represent another prominent background for $\mu^- - e^\pm$ processes. In absence of the CRV, the Mu2e experiment would observe an $e^\pm$ candidate each day. At the moment of writing two different generators have been used: Daya-Bay [124] and CRY [125]. The primary particles of the first one are only muons while the second assumes only galactic protons and derives tables of particles with the general-purpose Monte Carlo N-Particle (MCNP) [126] code that can be used for neutron, photon, electron, or coupled neutron/photon/-electron transport. Since the large production of cosmic events has not yet finished, the collaboration is also studying another generator named CORSIKA [127]. It contains some interesting features such as the possibility to specify any elevation and value of geomagnetic field and to choose different primary particles, not available in

the other generators. From [128] a relevant difference in the fluxes reproduced by CRY and CORSIKA is observed.In Figure 7.8 an event started from a cosmic ray mimicking a $\mu^- - e^+$ signal is reported. In the following, the procedure developed
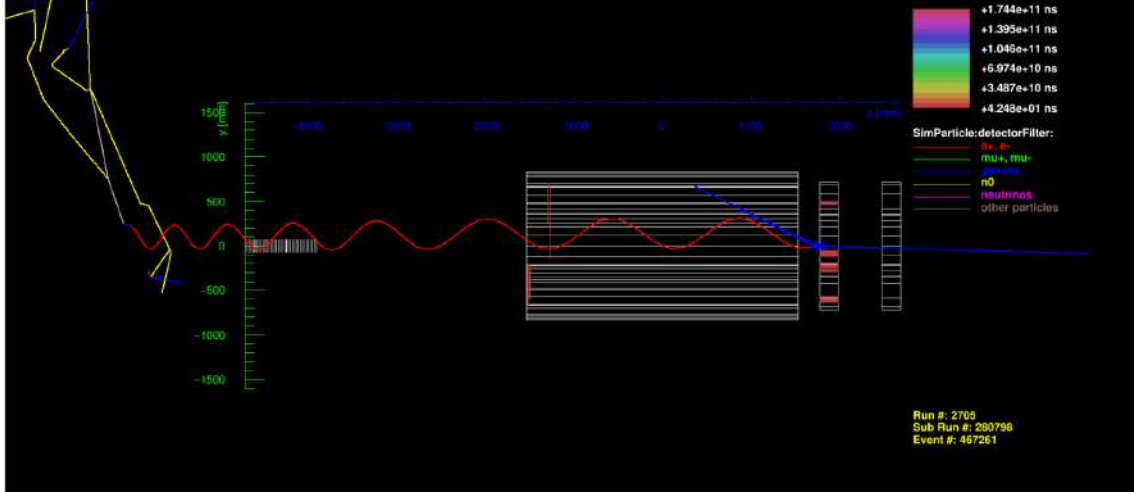


**Figure 7.8:** Example of a cosmic ray event producing $e^+$ from $n \to \pi^+ \to \gamma \to ? \to e^+$.

to estimate the number of positron from cosmic background is reported. In [129] the CR background for the $\mu^- - e^-$ conversion processes considering a signal region ranging between 103.75 MeV and 105 MeV is evaluated as $N_{CR} = 0.209 \pm 0.06$ . This result has been obtained combining the contribution due to CRV inefficiencies and the one due to CR event passing through small holes in the different sections of the CRV.

The majority of the cosmic events (70%) come from muon ionization and the final products are electrons in 90% of the case. Moreover the ratio of produced $e^+/e^-$ is smaller than ‰.

To scale the result to the signal region of the $\mu^- - e^+$ conversion first of all the the ratio $R_{\mu^+/\mu^-}$ is taken into account. From [130] it results to be $R_{\mu^+/\mu^-} = 1.12 \pm 0.13$ . In the following the production processes for $\mu^+$ and $\mu^-$ will be considered completely symmetric. The positive cosmic muon background in the signal region of the $\mu^- - e^-$ conversion is then evaluated as $N_{CR}^{\mu^+} = R_{\mu^+/\mu^-} N_{CR}^{\mu^-} = 0.130 \pm 0.032$. However, the acceptance lowers as the energy of the particles decreases .This acceptance reduction is evaluated integrating the distribution of the cosmic event momentum (see Figure 7.9 in 2 MeV signal region centered at the energies of the

conversion positron (106.3 events) and electron (141.2[1]).
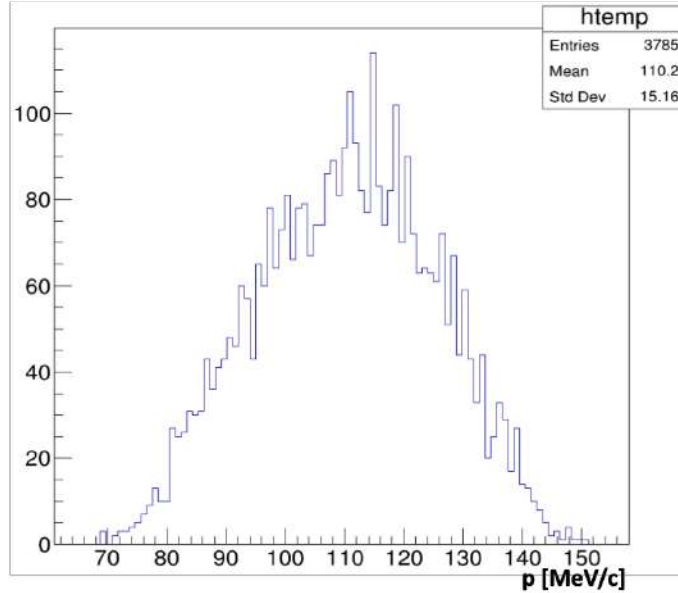


**Figure 7.9:** Reconstructed momentum from the cosmic ray events.

Knowing the acceptance reduction and scaling also for the different signal region width ( 2 MeV for $e^+$ against 1.25 MeV for $e^-$), the expected cosmic background in the signal region is $N_{CR} = 0.28 \pm 0.05$.

### 7.3.3 Other backgrounds

In the following a brief description of other processes that can influence the $\mu^- - e^+$ conversion is reported.

- **Antiprotons:** since the primary 8 GeV proton beam is above the threshold of antiproton production, it is possible that these particles do not interact in the TS and propagate through it arriving late in the stopping target, where they can produce positron the signal window. To limit the number of antiproton reaching the stopping target, absorbers are placed in different sections of the TS;

---

[1]These numbers are not scaled to the Mu2e lifetime

- **RPC:** Pions that survive and arrive at the stopping target during the delayed live gate can potentially give rise to a large background from the $\pi^- + Al \rightarrow \gamma^{(*)} + X$ process. Since the endpoint of this spectrum is at $\sim 135$ MeV the photon can internally or externally convert producing an electron-positron pair with the positron energy in the $\mu^- - e^+$ conversion signal region.

  Differently from the muon lifetime in Al, the pion lifetime is short, so that this process occurs promptly as the pions stop in the target. This background is suppressed by delivering a pulsed proton beam, minimizing the tails of the proton bunch and eliminating out-of-time protons (extinction).

# Chapter 8

# Evaluation of the $e^+$ background from RMC process

In this chapter the Mu2e simulation and a toy Monte Carlo are used to achieve two important goals: (i) evaluate, as a function of the $k_{\max}$, the rate of reconstructed $e^+$ tracks in the 2 MeV wide signal window defined in Chapter 7 and (ii) estimate the capability of determining the RMC photon spectrum and $k_{\max}$ with the Mu2e calorimeter, thus addressing the questions raised on the TRIUMF determination of $k_{\max}$ expressed in Appendix B.1.

## 8.1 Simulating the RMC positron spectrum from external conversion

Assuming to know the value of the RMC endpoint, it is possible to estimate the expected number of positrons produced in RMC events. In the following, only positrons coming from external conversion, i.e. those produced by photons interacting with the stopping target with or without the detector materials, are considered. With the full Monte Carlo simulation and reconstruction, a sample of $9.77 \times 10^8$ photons, with pileup beam related background hits in the event, has been produced. The photon spectrum has been generated flat in $(80 - 111)$ MeV. After the generation stage, only the particles interacting in the detectors are stored and then passed

through the reconstruction. At the end of the reconstruction stage, the statistic is $\sim 0.5 \times 10^5$. In Figure 8.1 the photon energy distribution before and after having applied the RMC weights (described in the following) are shown.
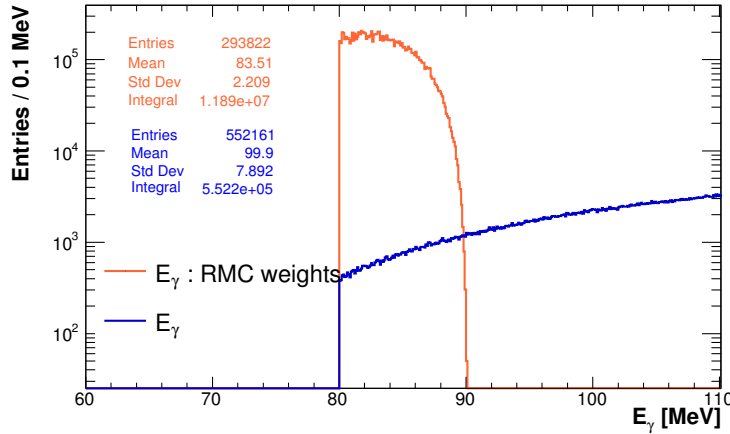


**Figure 8.1:** Photon energy distributions before (blue) and after (orange) having applied the RMC weights for a $k_{\mathrm{max}} = 90.1$ MeV.

The momentum distribution of the positron coming from the photons previously generated, and detected by the Mu2e tracker, is shown in Figure 8.2 before and after the quality cuts described in 7.2. After the quality cuts application no event survives in the signal window.
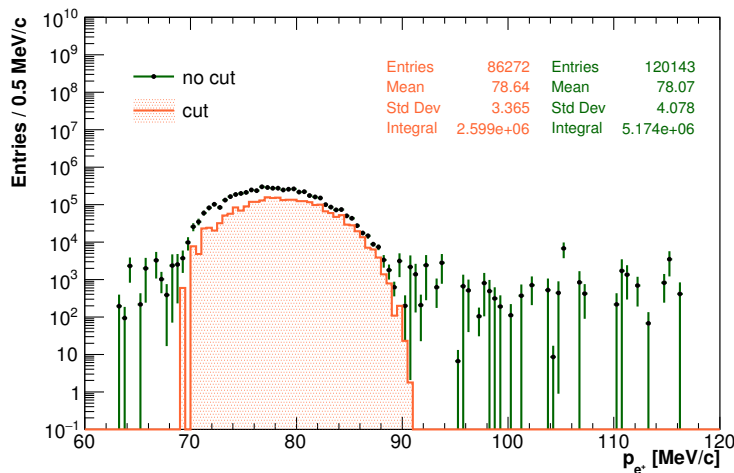


**Figure 8.2:** Positron momentum distributions before (green) and after (orange) having applied the quality cuts previously described.

The generated photon statistics is not sufficient to evaluate with precision the expected number of background events from the RMC process. Since the dataset with larger statistics is under production, a toy Monte Carlo has been implemented. The "building-block" of this toy is the 2D histogram that describes the dependence of the positron track momentum from the energy of the generated photon, see Figure 8.3. The Y projections of each bin are used to extract a track momentum starting from a given simulated photon energy. As previously mentioned, the saved photon energies
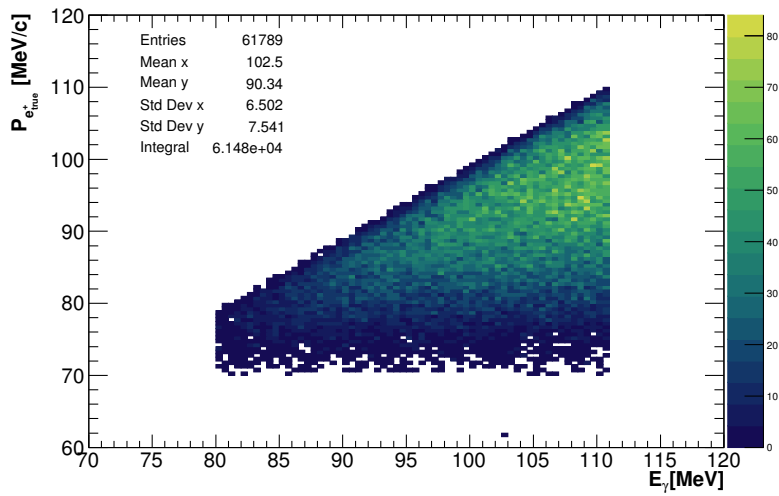


**Figure 8.3:** Histogram describing the dependence of the positron track momentum from the energy of the photons.

are not flat in $E_\gamma$ but show an energy dependence due to the tracker acceptance. In the toy Monte Carlo the tracker acceptance has been evaluated in each energy bin as the ratio between the number of photons converting externally and producing a detected $e^+e^-$ pair and the number of generated photons:

$$\mathcal{A}_i = \frac{N_i^{reco}}{N_i^{theo}} \tag{8.1}$$

The distribution obtained is fit with a polynomial function. The result is reported in Figure 8.4.

To obtain the positron spectrum, the photon energy is randomly extracted from a flat distribution ranging between 80 MeV and the selected $k_{\mathrm{max}}$ and the positron momentum is obtained from the corresponding bin of the 2D distribution. Each
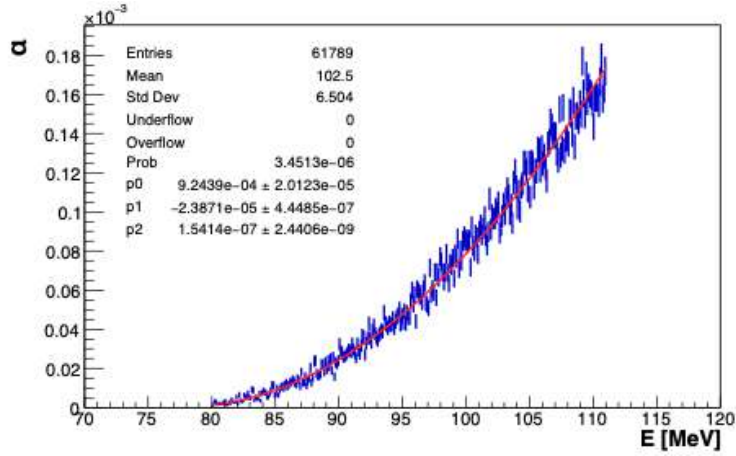
**Figure 8.4:** Acceptance value calculated in each bin, with size 0.1 MeV. The red line is the polynomial fit applied.

positron track is then weighted for the tracker acceptance. As a cross-check the resultant 2D distribution is shown in Figure 8.5.
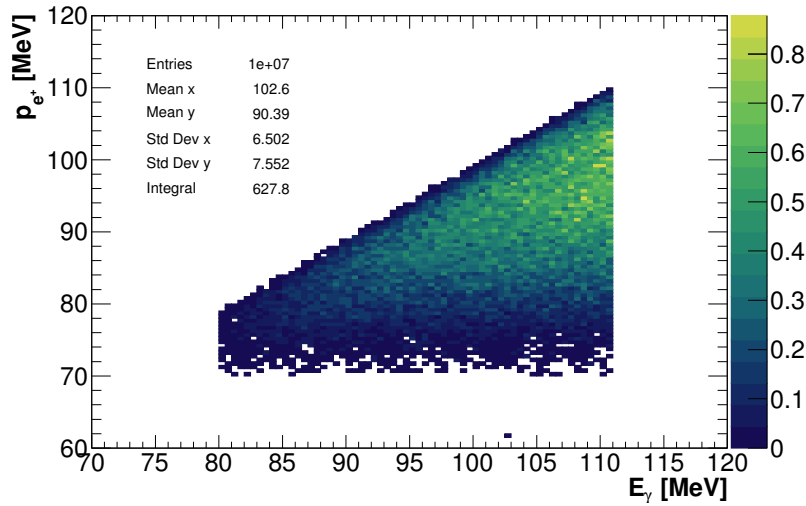


**Figure 8.5:** Dependence of the positron track momentum from the energy of the photons obtained from the Monte Carlo toy.

The histogram obtained with the toy Monte Carlo is in agreement with the one obtained from the official simulation and reconstruction. Indeed considering $9.77 \times 10^8$ generated photons only $6.15 \times 10^4$ positrons have been detected. Thus, the expected number of detected positrons simulating $10^7$ photon is 627.3. This

number has to be compared with the 627.8 tracks obtained from the toy Monte Carlo. As a final step, to obtain the correct positron spectrum from RMC, the photon momentum distribution needs to be weighted for the Closure Approximation function. The different weights applied to the toy Monte Carlo are reported in Figure 8.6 considering a $k_{\max} = 90.1$ MeV.
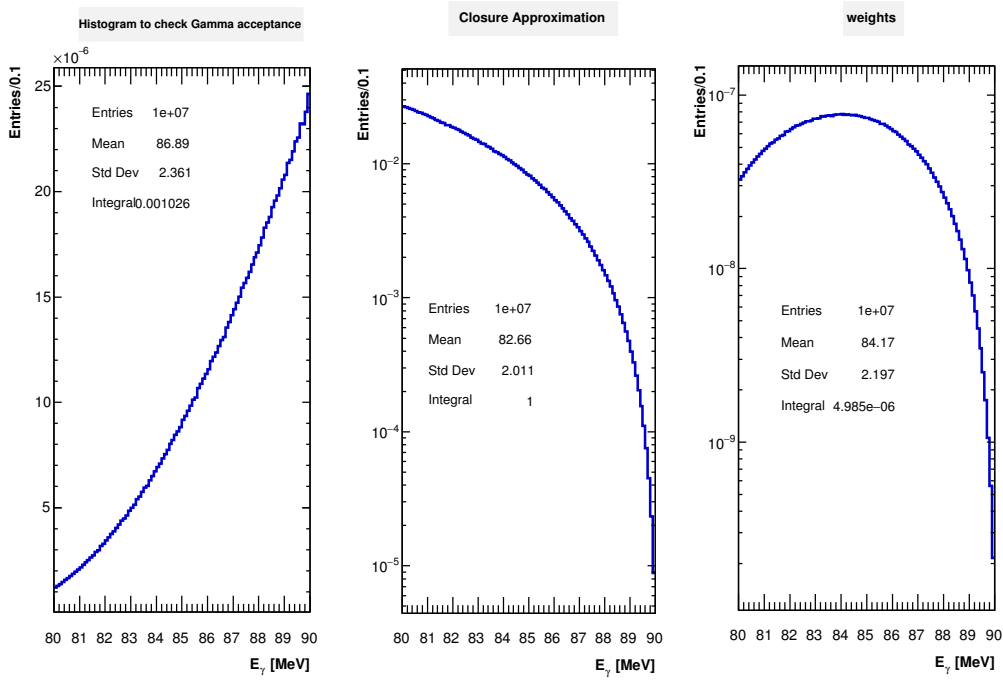


**Figure 8.6:** Distribution of tracker acceptance (left), closure approximation (center) and product of the previous two (right) values as a function of the photon energy. The selected $k_{\max}$ is 90.1 MeV.

To scale the distributions to the experiment lifetime, we apply the overall normalization of the muon capture and probability to obtain an RMC photon in each energy bin as follows:

$$SF = N_{POT} \times \mathcal{P}_{\mu \text{ stop}} \times \mathcal{P}_{\mu \text{ capt}} \times \mathcal{P}_{\text{RMC}}, \tag{8.2}$$

where $N_{POT} = 3.6 \times 10^{20}$ is the number of protons on target collected in three years of runs, $\mathcal{P}_{\mu \text{ stop}} = 1.5 \times 10^{-3}$ is the number of stopped muons per POT (it depends on the tungsten target configuration), $\mathcal{P}_{\mu \text{ capt}}$ is the probability of having a muon capture, and $\mathcal{P}_{\text{RMC}}$ is the number of RMC photons in the photon energy bin

considered. The latter number is evaluated as :

$$\mathcal{P}_{RMC} = \mathcal{P}_{\mathrm{P}} \times \frac{\int_{E_i/k_{\max}}^{E_{i+1}/k_{\max}} (1 - 2x + 2x^2)x(1-x)^2 dx}{\int_{E>57}(1 - 2x + 2x^2)x(1-x)^2 dx} \tag{8.3}$$

where $\mathcal{P}_{\mathrm{P}} = 1.43 \times 10^{-5}$ is the probability of having a RMC photon with energy between 57 MeV and $k_{\max}$ measured experimentally at TRIUMF.

As already anticipated in Chapter 7 tree the results from three different $k_{\max}$ are shown:

- 90.1 MeV: this value has been selected since is the measured endpoint in [120];

- 91.6 MeV: as reported in Appendix B.1 the data published by the TRIUMF experiment have been re-analyzed following the procedure explained. While the $k_{\max}$ obtained is similar to the one published, the uncertainty is $\sim 0.5$ MeV. The selected value correspond to $k_{\max TRIUMF} + 3\sigma_{Mu2e}$.

- 92.1 MeV: the selected value correspond to $k_{\max TRIUMF} + \sigma_{TRIUMF}^{1992}$.

In Figure 8.7 the RMC energy distributions are reported for the three selected $k_{\max}$ values.
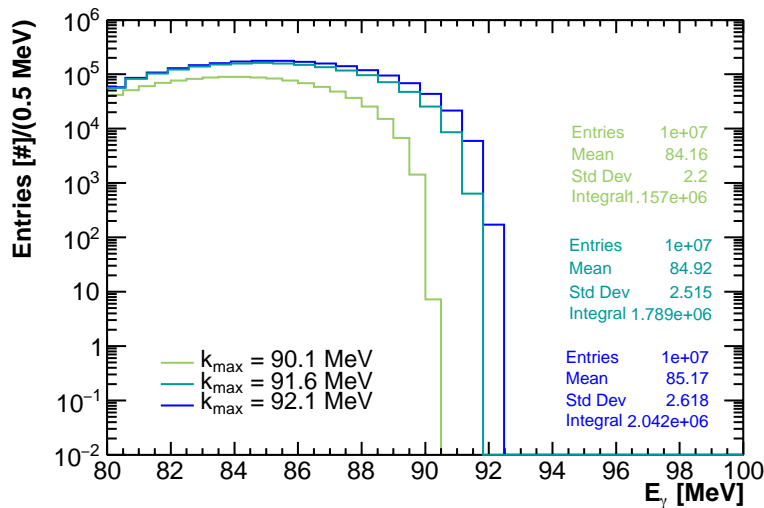


**Figure 8.7:** RMC photon energy obtained from the toy Monte Carlo choosing different $k_{\max}$ values.

Table 8.2 is a summary table containing the ratio of the closure approximation between 80 and 57 MeV starting point, the value of the scale factors applied and the integrals of the photon energy distributions obtained with the official and toy Monte Carlo simulation.

| $k_{max}$ | 90.1 MeV | 91.6 MeV | 92.1 MeV |
|---|---|---|---|
| $\frac{\mathcal{R}(E>80\textbf{ MeV})}{\mathcal{R}(E>57\textbf{ MeV})})$ | 4.93 % | 6.46 % | 6.99% |
| **SF** | $2.35 \times 10^{11}$ | $3.08 \times 10^{11}$ | $3.29 \times 10^{11}$ |
| **MC Integral** | $1.168 \times 10^{6}$ | $1.806 \times 10^{6}$ | $2.063 \times 10^{6}$ |
| **toy Integral** | $1.157 \times 10^{6}$ | $1.79 \times 10^{6}$ | $2.04 \times 10^{6}$ |

**Table 8.1:** Summary table of used parameters and statistics obtained in the generation of the photon energy spectrum for full simulation and our toy MC.

The scale factors are also applied to the distribution of the positron track momentum. To make them as similar as possible to what is expected for the experiment a correction due to the resolution effect has been taken into account. Since, at the moment of writing, a full-sized RMC dataset is not available, the resolution effect has been modeled using the $\mu^{-} - e^{+}$ dataset as shown in Figure 8.8. The red curves, superimposed to the resolution distribution, have used to randomly extract the resolution values to add to the true momentum.
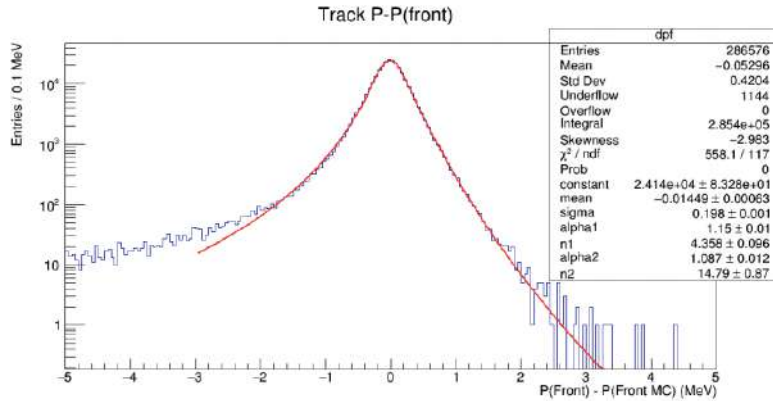


**Figure 8.8:** Momentum resolution used in the toy Monte Carlo as obtained from the $\mu^{-} - e^{+}$ dataset as the difference between the momentum reconstructed and the expected positron momentum (92.32 MeV).

The positron momentum distributions obtained from the toy Monte Carlo, for

the different $k_{\mathrm{max}}$ are reported in Figure 8.9 as well as the one obtained from the official simulation.

In Table 8.2, the expected number of external RMC events in the signal region obtained from the official Mu2e simulation and the from toy Monte Carlo is reported.

| $k_{\mathrm{max}}$ | 90.1 MeV | 91.6 MeV | 92.1 MeV |
|---|---|---|---|
| **Official Simulation** | 0 | 2 | 5 |
| **Official Simulation Scaled** | 0 | $1.80 \pm 1.27$ | $25.11 \pm 0.34$ |
| **Conversion positron resolution** | $(5.13 \pm 5.13) \times 10^{-3}$ | $2.583 \pm 0.073$ | $24.56 \pm 10.98$ |

**Table 8.2:** Expected number of RMC events at different $k_{\mathrm{max}}$ evaluated with different simulations in the 2 MeV signal window.

As an additional check, the integral of the positron distribution is evaluated in two different integration ranges, as reported in Table 8.3.

| $k_{\mathrm{max}} = 90.1$ MeV | all range | 80-100 |
|---|---|---|
| **Official Simulation Scaled** | $1.167 \times 10^6$ | $3.294 \times 10^5$ |
| **Conversion positron resolution** | $1.173 \times 10^6$ | $3.31 \times 10^5$ |
| $k_{\mathrm{max}} = 91.6$ MeV | all range | 80-100 |
| **Official Simulation Scaled** | $1.806 \times 10^6$ | $6.257 \times 10^5$ |
| **Conversion positron resolution** | $1.815 \times 10^6$ | $6.286 \times 10^5$ |
| $k_{\mathrm{max}} = 92.1$ MeV | all range | 80-100 |
| **Official Simulation Scaled** | $1.957 \times 10^6$ | $7.025 \times 10^5$ |
| **Conversion positron resolution** | $2.04 \times 10^6$ | $7.58 \times 10^5$ |

**Table 8.3:** Integral of the positron from RMC momentum distribution evaluated in different ranges for $k_{\mathrm{max}}$ =90.1 MeV (top), $k_{\mathrm{max}}$ =91.6 MeV (middle), $k_{\mathrm{max}}$ =92.1 MeV (bottom).
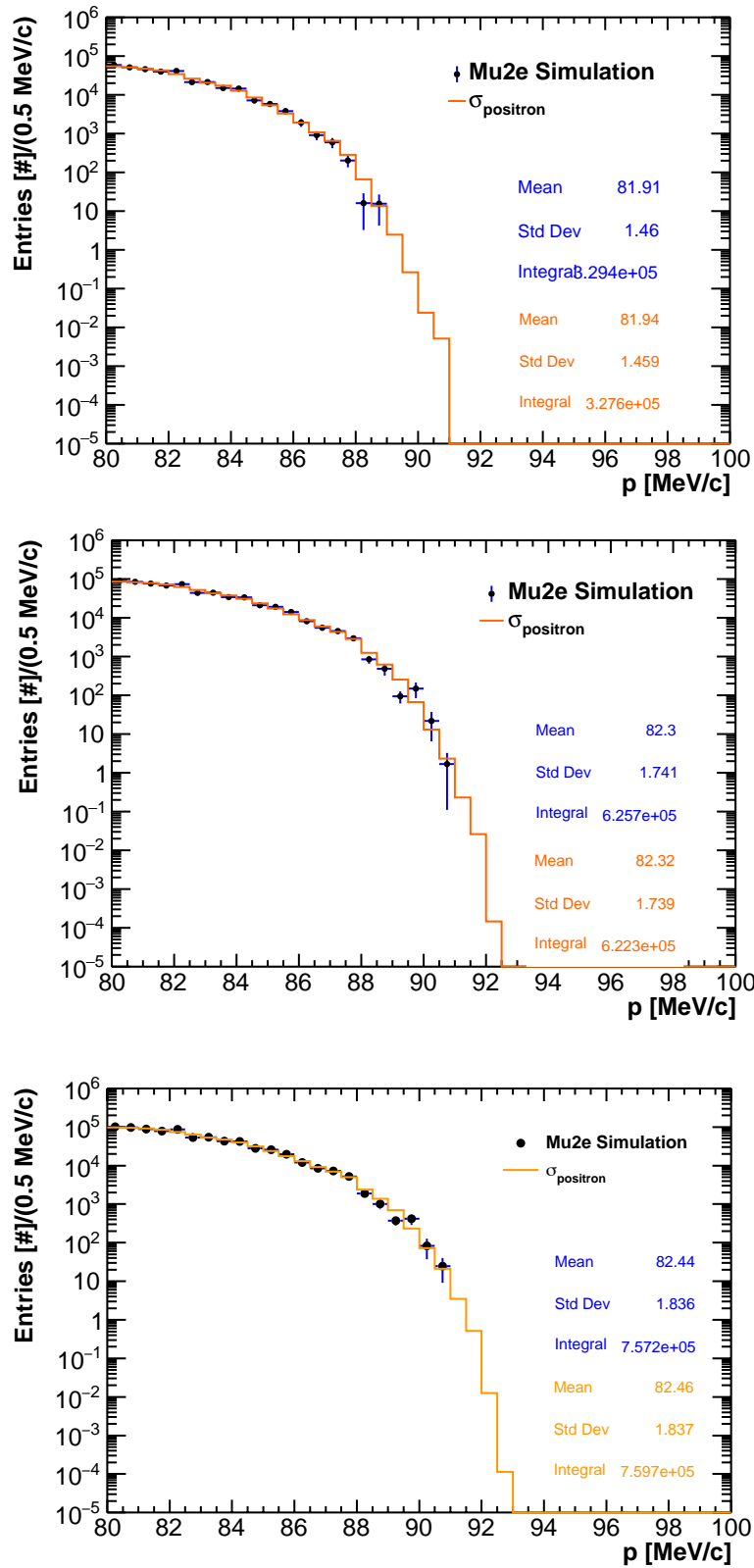
**Figure 8.9:** Positron track momentum distribution obtained from the official simulation (black dot) and the toy Monte Carlo (Orange).

## 8.2 Estimate of the RMC photon spectrum with Mu2e calorimeter

As a byproduct of the RMC background study, we realized that a new determination of the RMC photon spectrum is extremely important since it can both allow a precise evaluation of $k_{\max}$ and provide an independent normalization to $R_{\mu e}$ with respect to the stopping target monitor detector.

A preliminary study was performed using the implemented Monte Carlo simulation: a procedure similar to the one used by the TRIUMF experiment in Chapter 7 has been applied to extract $k_{max}$. The detector response function used is obtained by the MC tuned with the test beam data (Chapter 6). Figure 8.10 shows the comparison
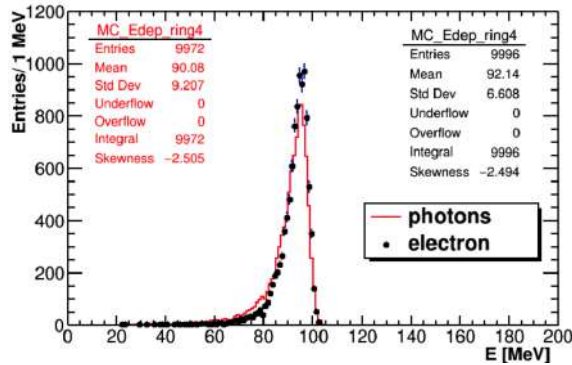


**Figure 8.10:** Photon (red line) and electron (black dot) energy deposition in the whole Module-0 calorimeter.

between the response for electron and photons impinging straight on the calorimeter surface without any material in front except the front panel. The two distributions present a similar energy scale although the one from photons show a higher left tail due to the larger energy leakage which results in a slightly worse energy resolution. The photon energy distributions, simulated between 15 and 130 MeV, are fit with an asymmetric Log-Normal [111]. The resolution dependence on the true photon energy was then fit with a polynomial function.

**Figure 8.11:** Top: energy distribution obtained with a simulated 100 MeV photon. The red line is the best fit obtained and the cyan line is the function extension in the whole energy range. Bottom: Log-N parameters as a function of the photon energy. The red lines are the performed linear fit.

In Figure 8.11, an example of the obtained fits is reported together with the energy dependence of the Log-Normal parameters. At this point, it is possible to convolute the calorimeter detector response, with the Closure Approximation fuction of a given $k_{max}$. The results obtained generating 10000 events with $k_{max} = 90.1$ MeV are reported in Figure 8.12 (top). We tested two cases changing the starting point of
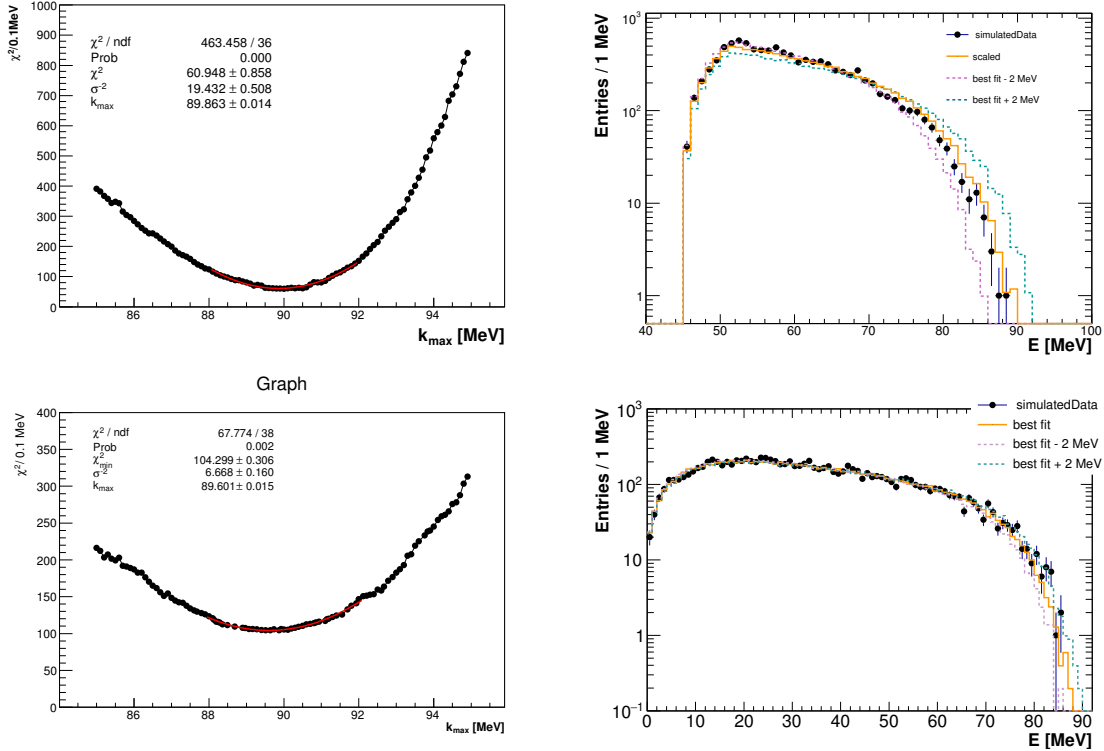


**Figure 8.12:** Left: Scan in $k_{max}$ value of the $\chi^2$ to obtain the best fit to the simulated data using the Closure approximation spectrum from 57 MeV (top) or the whole (bottom) spectrum. Right: Simulated data (dot),distributions corresponding to the best fit (solid orange), best fit + 2 MeV (dashed green) and best fit - 2 MeV (dashed pink). These distributions are reported in logarithmic scale to appreciate the differences.

the Closure approximation: 57 MeV or few MeV. The results obtained are reported in Figure 8.12 (bottom). The $k_{max}$ found are respectively $(89.64 \pm 0.22)$ MeV and $(89.60 \pm 0.38)$ MeV . The two results are well in agreement with each other and with respect to the generated value of 90 MeV within a shift of 500 keV. At the moment of writing, we plan to run this procedure also using the official MC simulation in order to take into account the pileup background . In addition, the resolution shape has been modeled using the results of the test beam performed with electrons both

in the orthogonal and the tilted configuration. A small Data-MC difference in the distributions is still present and this could introduce a fit bias that needs to be better studied and included.

Hence, it will be fundamental to deeply understand both resolution and response functions using the 6 MeV photons and the MIPs to obtain the correct energy scale and the right fit to the experimental data. A measurement of the energy scale could reduce the shift error smaller than 1 MeV.

# Photon rate as normalization source

As shown in Figure 8.13 in Mu2e we expect to have a flat acceptance for RMC photons in the first calorimeter disk. Starting from $2 \times 10^6$ generated events the
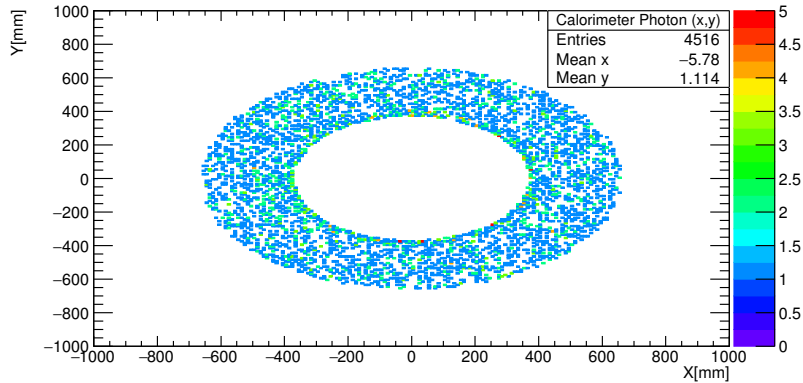


**Figure 8.13:** Photon simulated from the stopping target and impinging the first disk of the calorimeter.

geometrical efficiency resulted to be $2.2 \times 10^{-3}$. This number can slightly reduce if a "safe" acceptance region ($R_{min}$+2 ring, $R_{max}$ -2 rings) is selected. Moreover, as shown before, the calorimeter ensures a very high reconstruction efficiency. On the other side, with respect to the TRIUMF experiment Mu2e has a wider resolution and a slightly higher response loss. The rate of the RMC photons in $\mu$bunch can be estimate following the equation:

$$\frac{\mathcal{R}_{RMC}}{\mu B} = \frac{N_{POT}}{\mu B} \times \frac{N_\mu^{stop}}{POT} \times F_{capt} \times P(RMC) \times \mathcal{R}(T_{gate}), \qquad (8.4)$$

where $\frac{N_{POT}}{\mu B} = 3 \times 10^7$ is the number of proton contained in each microbunch, $\frac{N_\mu^{stop}}{POT} = 1.5 \times 10^{-3}$ is the number of mun stopped per proton on target, $F_{capt}$ is the fraction of muon that undergoes to capture, $P(RMC)$ is the number of RMC photon in a selected signal window and $\mathcal{R}(T_{gate},700\text{-}1650 \text{ ns}) = 0.5$, indicates the probability to reconstruct a prompt RPC photon in the TDAQ gate. Depending on the starting point used, we expect the number of reconstructed RMC photons in a micro bunch to be:

$$0.24 \text{ photons}/\mu B \text{ for E>57 MeV}, \tag{8.5}$$

$$2.00 \text{ photons}/\mu B \text{ for E>few MeV}. \tag{8.6}$$

Including also acceptance and reconstruction efficiency, the rate of reconstructed RMC is:

$$\frac{\mathcal{R}_{RMC}^{acc}}{\mu B} = \mathcal{R}_{RMC} \times \text{Acc}_{RMC} \times \varepsilon = 0.006 \text{ photon}/\mu B, \tag{8.7}$$

In other words, for each beam spill period (of 400 msec) the expected number of reconstructed RMC photon is estimated to be 1500.

There are two possibilities we are studying to perform the normalization:

- as an online monitor: for a spill of $\sim 400$ ms, we estimate 350 RMC photons each 100 ms;

- looking to triggered data. A data reduction factor of $\sim 200$ is expected, so that we estimate 7.5 photons per spill.

In conclusion, the measurement of the RMC spectrum can be used without dedicated triggering by looking at the photons in pileup with the events, providing an unbiased technique for monitoring purposes. Each 100 msec (2 minutes), this technique will give the Mu2e experiment the capability to measure the rate with a precision of 5%, when performed online (on triggered data).

# Chapter 9

# Upper limit sensitivity to $\mu^- - e^+$ conversion

The figure of merit used to optimize experiments searching for a single or new phenomena is the sensitivity. It is defined as the average upper limit one would get from an ensemble of experiments with the expected background and no true signal. The Mu2e experiment is close to be considered a "background free" case and among the possible approaches [131]-[133] to evaluate the sensitivity, the $CL_s$ method [133] is chosen. In $CL_s$ data are compared against two models at one time: a null hypothesis ("$b$"), which asserts that data can be understood with existing physics explanations, and a the signal+background ("s+b") hypothesis, which asserts that the data are modeled by SM physics and one or more new processes .

The confidence level for excluding the "s+b" hypothesis can be written as:

$$CL_{s+b} = P_{s+b}(Q \le Q_{obs}) = \int_{-\inf}^{Q_{obs}} \frac{dP_{s+b}}{dQ} dQ, \tag{9.1}$$

where $dP_{s+b}/dQ$ is the PDF of the test-statistic for signal+ background experiments. This correspond to the probability that $Q$ is less than that obtained in the data. Small values of $CL_{s+b}$ indicate poor compatibility with the "s+b" hypothesis. Similarly, the confidence in the background hypothesis is given by the probability that the test-statistic is less than or equal to the value observed in the experiment, $Q_{obs}$:

$$CL_b = P_b(Q \le Q_{obs}) = \int_{-\inf}^{Q_{obs}} \frac{dP_b}{dQ} dQ, , \tag{9.2}$$

The quantity:

$$CL_s = CL_{s+b}/CL_b. \tag{9.3}$$

represents a normalization of the confidence level observed for the "s+b" hypothesis ( $CL_{s+b}$) to the confidence level observed for the background-only hypothesis, $CL_b$. $CL_s$ cannot be used to exclude a hypothesis to which there is no experimental sensitivity, while in the case of $CL_{s+b}$, 5% of those hypotheses for which there is no sensitivity will be excluded at the 95% CL.

## 9.1   Evaluation of the Upper Limit

A scan on the possible observed data ($N_{obs}$) is performed in the interval (0,20). Then, for each $N_{obs}$ 1000 signal values are randomly extracted from a uniform distribution ranging from 0 to 30. The background considered for this first estimate of the upper limit are the RMC conversions, both internal and external, and cosmic rays. Per each value of selected signal and background, 1000 pseudo-experiments are performed. The evaluation of the background is described in Section 7.3. Considering the 2 MeV signal region, the expected number of background is evaluated as:

$$N_{bckg} = N_{RMC}^{ext} + N_{RMC}^{int} + N_{CR} = 4N_{RMC}^{ext} + 0.28, \tag{9.4}$$

In Figure 9.1 the number of background events obtained for different $k_{\max}$ values are reported. This distribution is fit using a function composed of an exponential and a constant term, which accounts for the cosmic ray events.

In the following, the upper limit on the signal for the $\mu^- - e^+$ conversion will be quoted as function of the number of observed events in the signal region. As stated in Chapter 8, the endpoint of the RMC distribution is not well known. For this reason, different background models have been used to check the sensitivity dependence on the different cases:

- a flat background model, where we extract uniformly in a 2 MeV range centered at $k_{\max} = 90.1$ MeV;

- a Gaussian background distribution peaked at $k_{\max} = 90.1$ MeV, with a $\sigma = 0.5$ MeV;
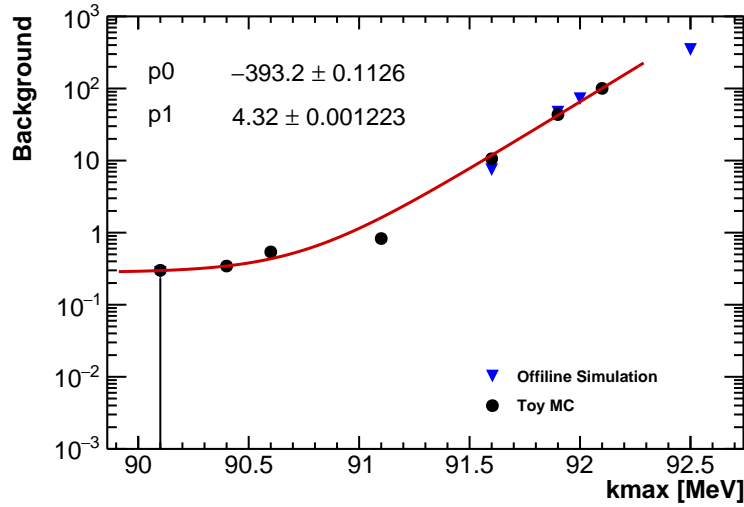
**Figure 9.1:** Expected number of background events as function of the $k_{\max}$ extracted from the Toy Monte Carlo (black dots) described in Chapter8 and from the Official Simulation (blue triangles).

- a Gaussian background distribution peaked at $k_{\max} = 90.1$ MeV, with a $\sigma = 1$ MeV;

- a fixed $k_{\max} = 90.1$ MeV.

Figure 9.2 (top) shows the estimate of the upper limit as a function of the possible number of events observed. Figure 9.2 (bottom) shows instead the probability of observe $N_{obs}$ for each given background model and no signal. The last column of Table 9.1 reports a "conservative upper limit" that has been evaluated convoluting the probability of having a given $N_{obs}$ with a given background model. To validate the code written to evaluate the upper limit, its results have been compared to a "well-certified" code derived from [134]. The momentum distributions of the simulated conversion positron and the backgrounds have been used also as PDFs. The background components have been factorized into two separate PDFs: one for the RMC positrons and the second ine for the cosmic ray events, simulated so that integral in the signal region is exactly the one reported in Chapter 7.

**Figure 9.2:** Top: upper limit at 95% CL of the number of signal event as a function of the number of observed events for different background models. Bottom: probability of having a particular $N_{obs}$ with a given background model depicted for different external RMC background modeling.

Figure 9.3 shows all the PDFs used as input for the sensitivity calculation performed with the validated macro The different upper limits obtained with the dif-
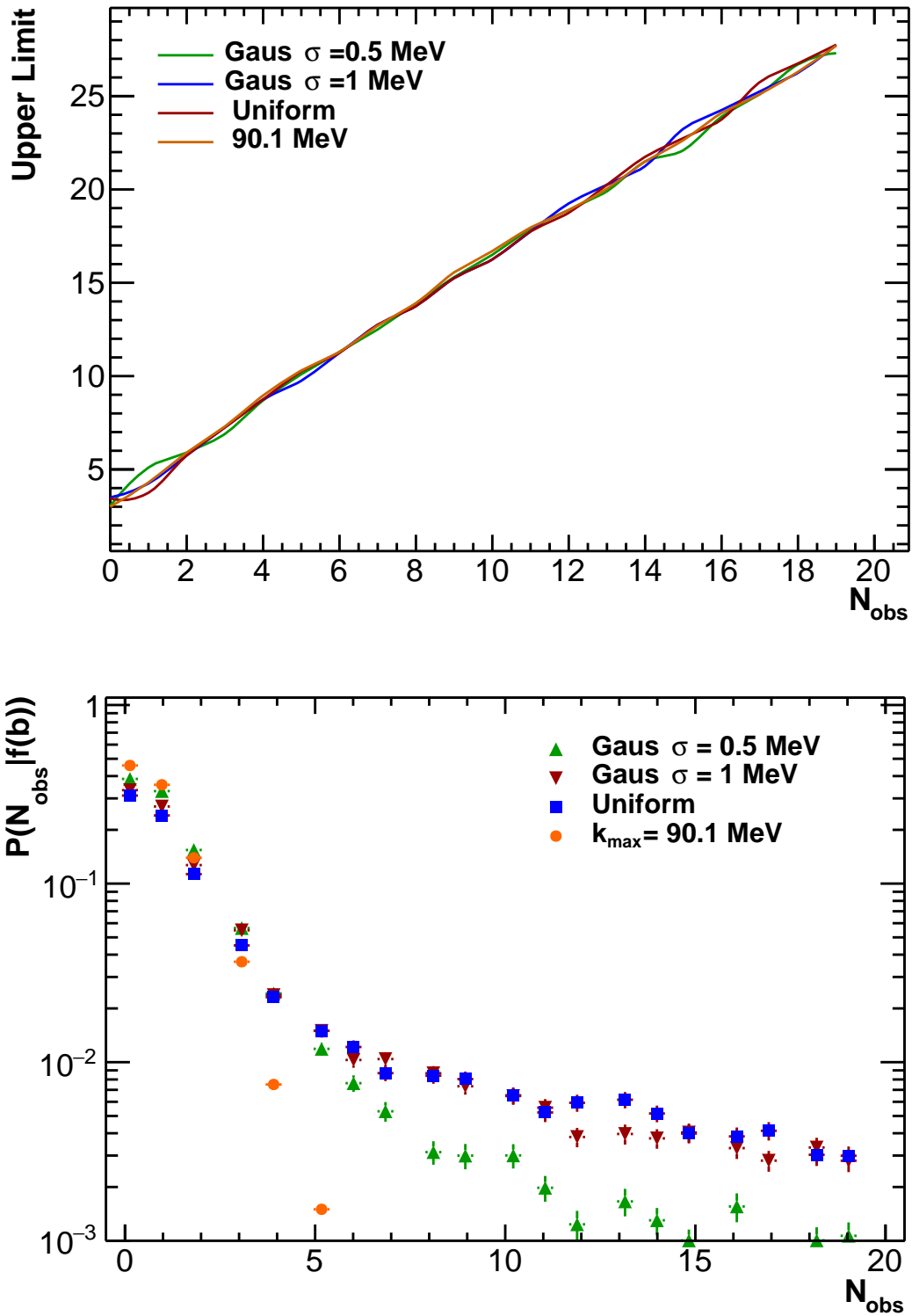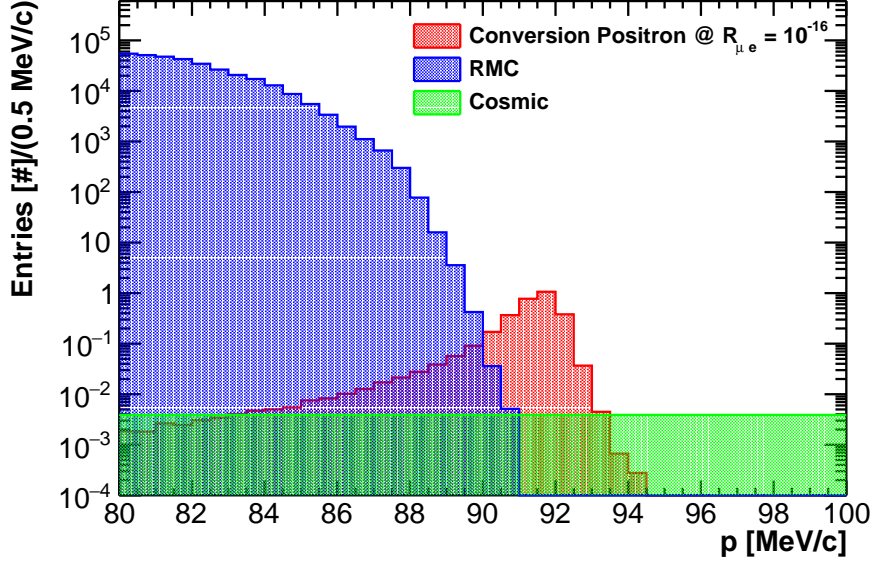


**Figure 9.3:** Momentum distribution for background and Conversion Positron, assuming $R_{\mu e} = 10^{-16}$. Distributions are normalized to the Mu2e expected number of protons on target in 3 years of running, $N_{POT} = 3.6 \times 10^{20}$.

ferent modeling of the $k_{\max}$ are reported in Table 9.1. The sensitivity on $R_{\mu e+}$ has been evaluated as:

$$R_{\mu e+} = \frac{N_{UL}}{N_{e+}^{expected}} = \frac{N_{UL}}{N_{stop}^{\mu} * (1 - P_{Capt}) * \alpha} = \frac{N_{UL}}{1.89 \times 10^{16}} \, , \qquad (9.5)$$

where $N_{UL}$ is the evaluated upper limit for a given background model, $N_{stop}^{\mu}$ is the expected number of muon stopped, for a $N_{POT} = 3.6 \times 10^{20}$, $(1 - P_{Capt}) = 0.39$ is the probability of having the muon decaying and $\alpha = 9\%$ accounts for signal efficiency and acceptance, as described in Section 7.2. As shown in Table 9.1, a good agreement between the validated macro and the other results, it is shown.

## 9.2 Evaluation of the discovery sensitivity

The discovery sensitivity has been evaluated for three fixed value of $k_{\max}$ (90.1 MeV, 91.6 MeV and 91.9 MeV). To quote the discovery sensitivity, the first step is

| Model | $N_{UL}$ @95% | $R_{\mu e^+}$@95% | Conservative $N_{UL}$ |
|---|---|---|---|
| Uniform | 3.5 | $1.85 \times 10^{-16}$ | 6.85 |
| Gaussian $\sigma = 1$ MeV | 3.3 | $1.74 \times 10^{-16}$ | 6.17 |
| Gaussian $\sigma = 0.5$ MeV | 3.1 | $1.64 \times 10^{-16}$ | 6.04 |
| $k_{\max} = 90.1$MeV | 3 | $1.58 \times 10^{-16}$ | 5.3 |
| validated macro $k_{\max} = 90.1$ | 2.99 | $1.58 \times 10^{-16}$ | - |

**Table 9.1:** Upper limit, evaluated when $N_{obs} = 0$, $R_{\mu e^+}$ and "conservative" upper limit evaluated for different background models.

to evaluate the probability of obtaining $N_{obs}$ for a given background:

$$\mathcal{P}(n \geq n_{obs}|b) = \sum_{n \geq n_{obs}} \frac{b^n e^{-b}}{n!}, \tag{9.6}$$

At this point the $N_{obs}$ corresponding to a $\mathcal{P}(n \geq n_{obs}|b) = 5.7 \times 10^{-7}$ ($5\sigma$) represents the number of event corresponding to a discovery.

The probability curves are reported in Figure 9.4 and the discovery sensitivity in Table 9.2. For what have been previously showed, the contribution of the different

| $k_{\max}$ [MeV] | $N_{bckg}$ | $N_{Disc}$ | BR |
|---|---|---|---|
| 90.1 | 0.29 | 6.1 | $3.22 \times 10^{-16}$ |
| 91.6 | 12.60 | 33.76 | $1.78 \times 10^{-15}$ |
| 92.1 | 45.34 | 150.89 | $7.89 \times 10^{-15}$ |

**Table 9.2:** Number of event necessary to have to a discovery and corresponding sensitivity for to the three investigated $k_{\max}$

modeling, for a given value of $k_{\max}$ can, in a first approximation, be neglected. What will effectively change the upper limit and discovery sensitivity is the energy scale of the $k_{\max}$: Table 9.2 shows how a 2 MeV shift in $k_{\max}$ can worsen the discovery sensitivity by a factor 20.
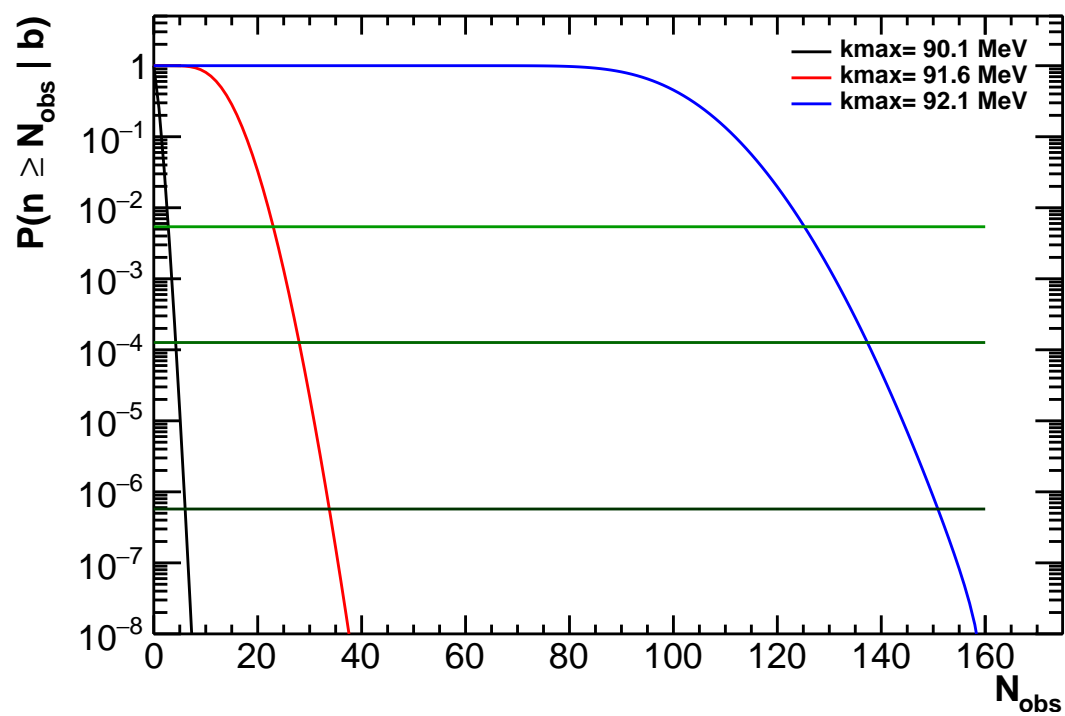
**Figure 9.4:** Probability curves $\mathcal{P}(n \geq n_{obs}|b)$ used to evaluate the discovery sensitivity.

# Conclusions

The work and results of this thesis can be divided into two sections: a first one that focuses on the Mu2e calorimeter R&D phase and on the experimental tests needed to check that the Mu2e crystal calorimeter requirements are satisfied, and a second one on the simulation carried out for the search of the $\mu^-$ - $e^+$ conversion.

Several years of R&D study for the calorimeter system culminated with the construction of a large size prototype (Module-0), made of 51 crystals, each one read out by two custom SiPMs arrays. The Module-0 was tested with an electron beam, with energies ranging between 60 and 120 MeV, delivered at the Beam Test Facility of the National Laboratories of Frascati. This test demonstrated that this detector satisfies the Mu2e requirements both for energy and timing response and resolution ($\sigma_E/E = \mathcal{O}(10\%)$ and $\sigma_T < 500$ ps, at 100 MeV). The obtained results have been compared with a dedicated Monte Carlo simulation, accurately tuned to accounts for all the additional effects observed during the test beam. After completing the Module-0 test beam analysis, I worked on the construction of the QC stations for crystals and sensors and I was responsible for the Mean Time to Failure (MTTF) test of the SiPMs. The calorimeter production phase started on March 2018 and the results found for the CsI crystals and SiPMs properties are excellent. The end of the QC phase is planned for the beginning of 2020 and the detector assembly for middle 2020.

The second part of this thesis focuses on the study of the $\mu^- - e^+$ conversion, an LNV and CLFV process that can be searched for in Mu2e. I have been one of the first PhD students joining the working group on this search channel. After having implemented the effect of radiative corrections to conversion signals in the official simulation, I focused on the study of one of the most prominent background for this

search: the Radiative Muon Capture (RMC) $\mu + N(Z, A) \rightarrow \gamma + \nu_\mu + N(Z - 1, A)$. The importance of a precise modeling of this background resides in the proximity of the photon spectrum endpoint to the conversion positron signal region.

Since, at the moment of writing, a full RMC simulation was not available, a toy Monte Carlo has been written to accounts for the effect of the RMC background in the proximity of the conversion positron signal region. For this kind of measurement is fundamental to know the exact RMC distribution endpoint. Variations of $k_{\mathrm{max}}$ within 2 MeV could, indeed, worsen the sensitivity of the Mu2e experiment to $\mu^- - e^+$ conversion of a factor 10. My work has also demonstrated that the Mu2e calorimeter will have a central role in this measurement by performing a precise determination of the RMC photon spectrum.

The estimated discovery sensitivity, considering a $k_{\mathrm{max}} = 90.1$ MeV is $4.4 \times 10^{-16}$. Even in the worst-case scenario of a $k_{\mathrm{max}} = 91.9$, the Mu2e experiment will improve the latest results from SINDRUM-II by three orders of magnitude.

# Bibliography

[1] G. Altarelli. *The standard model of particle physics*, arXiv preprint hep-ph/0510281 (2005).

[2] G. Aad, et al. *Observation of a new particle in the search for the Standard Model Higgs boson with the ATLAS detector at the LHC*, Physics Letters B 716.1 (2012): 1-29.

[3] S. Chatrchyan, et al. *Observation of a new boson at a mass of 125 GeV with the CMS experiment at the LHC*, Physics Letters B 716.1 (2012): 30-61.

[4] Fukuda, Y., et al. *Evidence for oscillation of atmospheric neutrinos*, Physical Review Letters 81.8 (1998): 1562.

[5] A.M. Baldini et al., *Search for the lepton flavour violating decay $\mu^+ \rightarrow e^+\gamma$ with the full dataset of the MEG experiment*, Eur. Phys. J. C, 76 (2016) 434

[6] U. Bellgardt et al., *Search for the Decay $\mu^+ \rightarrow e^+e^+e^-$* , Nucl. Phys. B299, 1 (1988), doi:10.1016/0550-3213(88)90462-2.

[7] W. Bertl et al., *A search for $\mu \rightarrow e conversion in muonic gold$*, EPJ C, 47(2):337:346 - 2006.

[8] L. Willmann et al., *New bounds from searching for muonium to anti-muonium conversion,*Phys. Rev. Lett. 82 (1999) 49 [hep-ex/9807011].

[9] B. Aubert et al., *Searches for Lepton Flavor Violation in the Decays $\tau^\pm \rightarrow e^\pm\gamma$ and $\tau^\pm \rightarrow \mu^\pm\gamma$*, Phys. Rev. Lett. 104 (2010) 021802

[10] K. Hayasaka et al., *Search for lepton-flavor-violating $\tau$ decays into three leptons with 719 million produced pairs*, Physics Letters B 687 (2010) 139 -143, ISSN: 0370-2693

[11] E. Abouzaid et al. [KTeV Collaboration], *Search for lepton flavor violating decays of the neutral kaon,* Phys. Rev. Lett. 100 (2008) 131803 [arXiv:0711.3472 [hepex]].

[12] D. Ambrose et al. [BNL Collaboration], *New limit on muon and electron lepton number violation from $K_L^0 \to \mu^{\mp} e^{\pm}$ decay,* Phys. Rev. Lett. 81 (1998) 5734 [hepex/9811038].

[13] A. Sher et al., *An Improved upper limit on the decay $K^+ \to \pi^+ \mu^+ e^-$* , Phys. Rev. D 72 (2005) 012005 [hep-ex/0502020]

[14] G. Aad et al. [ATLAS Collaboration], *Search for the lepton flavor violating decay $Z \to e\mu$ in pp collisions at sqrts = 8 TeV with the ATLAS detector,* Phys. Rev. D 90 (2014) no.7, 072010 [arXiv:1408.5774 [hep-ex]].

[15] R. Akers et al. [OPAL Collaboration], *A Search for lepton flavor violating $Z^0$ decays,* Z. Phys. C 67 (1995) 555

[16] A. de Gouvea, and P. Vogel. *Lepton flavor and number conservation, and physics beyond the standard model,* Progress in Particle and Nuclear Physics 71 (2013): 75-92.

[17] Fermilab,*Proton Improvement Plan-II (PIP-II)*, https://pip2.fnal.gov - 2015.

[18] Calibbi, L., et al. "Status of supersymmetric type-I seesaw in SO (10) inspired models." Journal of High Energy Physics 1211 (2012). JHEP, 1211:040, 2012.

[19] Harnik, R., Kopp, J., Zupan, J. "Flavor violating Higgs decays". arXiv preprint arXiv:1209.1397 (2012).

[20] Blanke, M., et al. "FCNC processes in the littlest Higgs model with T-parity: an update." arXiv preprint arXiv:0906.5454 (2009).

[21] Arnold, J. M., Bartosz, F., and Wise, M.B. "Phenomenology of scalar leptoquarks." Physical Review D 88.3 (2013): 035009.

[22] Lee, C. H., Dev, P. B., Mohapatra, R. N. ." Natural TeV-scale left-right seesaw mechanism for neutrinos and experimental tests". Physical Review D, 88(9), 093010.

[23] E. P. Hincks and B. Pontecorvo, *Search for Gamma-Radiation in the 2.2-Microsecond Meson Decay Process*, Phys. Rev. 73 (1948) 257

[24] A.M. Baldini et al., *The design of the MEG II experiment*, Eur. Phys. J. C 78 (380) (2018).

[25] A. K. Perrevoort, *The rare and forbidden: Testing physics beyond the standard model with Mu3e*, SciPost Physics Proceedings 1 (2019): 052.

[26] Honecker, W. et al., *Improved limit on the branching ratio of $\mu - e$ conversion on lead*, Phys. Rev. Lett. 76, 200-203 (1996).

[27] Kaulard, J. et al., *Improved limit on the branching ratio of $\mu$ - e conversion on titanium*, Phys. Lett. B422, 334-338 (1998).

[28] R. Abramishvili, et al. (COMET Collaboration),`http://comet.kek.jp/Documentsfiles/PAC-TDR-2016/COMET-TDR-2016v2.pdf`

[29] N. Teshima, *$\mu$-e conversion experiments at J-PARC*, SciPost Physics Proceedings 1 (2019): 039.

[30] European Particle Physics Strategy Update 2018-2020 : Charged Lepton Flavour Violation using Intense Muon Beams at Future Facilities. `https://indico.cern.ch/event/765096/contributions/3295551/attachments/1785134/2906066/CLFV_Muons.pdf`

[31] A. Czarnecki, X. Garcia i Tormo, W. Marciano, *Muon decay in orbit: Spectrum of high-energy electrons*,Phys. Rev. D 84, 013006 (1 2011).

[32] D. Measday, *The Physics of Muon Capture*, Physics Reports 354, 243-409 (2001).

[33] G. 't Hooft, *Symmetry Breaking through Bell-Jackiw Anomalies*, Phys. Rev. Lett., 37 (1976), p. 8.

[34] M. Agostini et al. *Probing Majorana neutrinos with double-$\beta$ decay.* Science, 27 Sep 2019 1445-1448. Vol. 365, Issue 6460, pp. 1445-1448. DOI: 10.1126/science.aav8613

[35] D. A. Bryman et al., *Search for the Reaction $\mu^- + Cu \rightarrow e^+ + Co$.*Phys. Rev. Lett. 28, 1469 (1972).

[36] A. Badertscher et al., *Search for $\mu^- \rightarrow e^+$ conversion on sulfur* .Phys. Lett. B 79, 371 (1978).

[37] R. Abela et al., *New upper limit for $\mu^- \rightarrow e^+$ conversion.* Phys. Lett. B 95, 318 (1980).

[38] A. Badertscher et al.,*A search for muon-electron and muon-positron conversion in sulfur*, Nucl. Phys. A 377, 406 (1982).

[39] S. Ahmad et al., *Search for muon-electron and muon-positron conversion.* Phys. Rev. D 38, 2102 (1988).

[40] C. Dohmen et al., *Test of lepton-flavour conservation in $\mu \rightarrow e$ conversion on titanium*Phys. Lett. B 317, 631 (1993)

[41] R. Appel et al., *Search for Lepton Flavor Violation in Decays into a Charged Pion and Two Leptons.* Phys. Rev. Lett. 85, 2877 (2000).

[42] J. Batley et al., *New measurement of the $K^{\pm} \rightarrow \pi^{\pm} \mu^+ \mu$âĹŠ decay* . Phys. Lett. B 697, 107 (2011).

[43] J. Batley et al., *Searches for lepton number violation and resonances in $K^{\pm} \rightarrow \pi\mu$ mu decays.* Phys. Lett. B 769, 67 (2017).

[44] K Zuber, *New limits on effective Majorana neutrino masses from rare kaon decays.* Phys. Lett. B 479, 33 (2000).

[45] J. M. Berryman, A. de Gouvêa, K. J. Kelly, andA. Kobach, *Lepton-number-violating searches for muon to positron conversion* .Phys. Rev. D 95, 115010 (2017).

[46] T. Geib, A. Merle, and K. Zuber, $\mu^- \rightarrow e^+$ *conversion from short-range operators* Phys. Lett. B 764,157 (2017).

[47] N. Otuka, et al. *Towards a more complete and accurate experimental nuclear reaction data library (EXFOR): international collaboration between nuclear reaction data centres (NRDC).* Nuclear Data Sheets 120 (2014): 272-276.

[48] P. C. Divari, et al. *Exotic muon-to-positron conversion in nuclei: partial transition sum evaluation by using shell model.* No. JINR–1-104-2001. Joint Institute for Nuclear Research, 2001.

[49] R.M. Dzhilkibaev, *The solenoid muon capture system for the MELC experiment* - 1995. Beam Dynamics and Technology Issues for mu+ mu Colliders: Proceedings of the 9th ICFA Advanced Beam Dynamics Workshop, Oct. 15âĂŞ20 1995, Montauk, New York, 1995

[50] J. L. Popp, (2001). *The MECO experiment: a search for lepton flavor violation in muonic atoms.* Nuclear Instruments and Methods in Physics Research Section A: Accelerators, Spectrometers, Detectors and Associated Equipment, 472(3), 354-358.

[51] Brookheaven National Laboratory web site `https://www.bnl.gov/world/`

[52] F. A. Berg. *Development of a Next generation High-intensity Muon Beam at the Paul Scherrer Institut*

[53] L. Bartoszek, et al. *Mu2e technical design report.* arXiv preprint arXiv:1501.05241 (2015).

[54] P. Derwent, *Accelerators for Intensity Frontier Research*, Conf.Proc. C1205201 (2012) 4185-4189

[55] E. Prebys, S. Werkema, *Out-of-Time Beam Extinction in the MU2E Experiment* tech. rep. (Fermi National Accelerator Laboratory (FNAL), Batavia, IL (United States), 2015).

[56] IPAC, Proc. 2nd International Particle Accelerator Conference, IPAC 2011, San Sebastian, Spain - 2011.

[57] M.J. Lee on behalf of the Mu2e collaboration, *The Straw-tube Tracker for the Mu2e Experiment*, Nuclear and Particle Physics Proceedings Vol. 273-275 (2016) Pag. 2530-2532 [DOI:10.1016/j.nuclphysbps.2015.09.448]

[58] General Atomics website http://www.ga.com/

[59] ASG website https://www.asgsuperconductors.com/

[60] G. Pezzullo, P. Murat. *The calorimeter-seeded track reconstruction for the Mu2e experiment at Fermilab.* 2015 IEEE Nuclear Science Symposium and Medical Imaging Conference (NSS/MIC). IEEE, 2015.

[61] R.Donghia, *Performance studies for the electromagnetic calorimeter of the Mu2e experiment at Fermilab*, Master Thesis (2015)

[62] O.Atanova et al., *Measurement of the energy and time resolution of a undoped CsI + MPPC array for the Mu2e experiment*, JINST 12 (2017) no.05, P05007 [DOI:10.1088/1748-0221/12/05/P05007, arXiv:1702.03720]

[63] N. Atanov et al., *Measurement of time resolution of the Mu2e LYSO calorimeter prototype*, NIM A 812 (2016) 104-111 [DOI: 10.1016/j.nima.2015.12.055, arXiv:1509.04468]

[64] N. Atanov et al., *Design and status of the Mu2e electromagnetic calorimeter*, NIM A 824 (2015), ISSN:0168-9002

[65] L. Bartoszek et al., *Mu2e Conceptual Design Report* physics.ins-det (2012) [arXiv: 1211.7019]

[66] R. Donghia on behalf of the Mu2e calorimeter group, *Design, R&D and status of the crystal calorimeter for the Mu2e experiment*, YRW 2016, Frascati Physics Series, Vol. LXIII, pag. 37 (2016) [arXiv:1607.01301]

[67] R. Donghia on behalf of the Mu2e calorimeter group, *Performance study of single undoped CsI crystals for the Mu2e experiment*, Nuovo Cimento 39 C 276 (2016) [arXiv:1602.02983, DOI: 10.1393/ncc/i2016-16276-y]

[68] R. Donghia on behalf of the Mu2e calorimeter group, *Performance study of single undoped CsI crystals for the Mu2e experiment*, Nuovo Cimento 39 C 276 (2016) [arXiv:1602.02983, DOI: 10.1393/ncc/i2016-16276-y]

[69] R. Donghia et al., *Longitudinal uniformity, time performance and irradiation test of pure CsI crystals*, NIM A824, 678-680, ISSN 0168-9002 (2015) [arxiv:1606.07110, DOI: 10.1016/j.nima.2015.11.042]

[70] Saint Gobain web page, `www.crystals.saint-gobain.com`

[71] V. Saveliev, `Advancesinopticalandphotonicdevices`, InTech (2010)

[72] Hamamatsu, *TSV MPPC array*, production flyer 2015.05 KSX-I50080-E-S13361-3050xx-04

[73] N. Yahlali et al., *Imaging with SiPMs in noble-gas detectors*, physics.ins-det (2012) [arXiv: 1501. 05241]

[74] S. Di Falco et al., *Components Qualification for a Possible use in the Mu2e Calorimeter Waveform Digitizers*, JINST 12 (2017) no.03, C03088 [DOI:10.1088/1748-0221/12/03/C03088, arXiv:1710.01981]

[75] K. Terada and T. Okano, *Conductance modulation method for the measurement of the pumping speed and outgassing rate of pumps in ultra-high vacuum*, Journal of Vacuum Science & Technology A 7 (1998) 2397 [doi.org/10.1116/1.575907]

[76] ENSDF Decay Data In the MIRD Formt, `www.orau.org/ptp/PTPLibrary/library/DOE/bnl/nuclidedata/MIRN16.htm`(1999).

[77] G. Pezzullo et al., *Progress status for the Mu2e calorimeter system*, Journal of Physics: Conference Series 587, 012047 (2015)

[78] S. Agostinelli et al., *Geant4-a simulation toolkit*, NIM A 506, 250 303 (2003) ISSN: 0168-9002

[79] R.Y. Zhu, *Radiation damage in scintillating crystals*, NIM A Vol. 413 (1998) Issues 2-3 [DOI:10.1016/S0168-9002(98)00498-7]

[80] Z.Y. Wei and R.Y. Zhu, *A study on undoped CsI crystals*, NIM A 326 (1993) 508

[81] G.Pezzullo et al., *Status report on dose estimates and future plan*, Mu2e-doc-18417 - 2018

[82] C. Leroy and P.G. Rancoita, *Particle interaction and displacement damage in silicon devices operated in radiation environments*, Reports on Progress in Physics 70, (2007) 493

[83] Y. Qiang et al., *Radiation hardness tests of SiPMs for the JLab Hall D Barrel calorimeter*, NIM A 698, 234 241 (2013) ISSN: 0168-9002

[84] R. Ehrlich, *Update on the cosmic background simulation*-doc-4184 - 2014.

[85] F. Cervelli et al., *Study of the DIO rate for a calorimeter based trigger*, Mu2e-doc-3456-v1 - 2013

[86] D. Brown, *Tracker Selection Cut-set C* Mu2e-doc-3996-v3 - 2014

[87] P. Murat, *Particle Identification with the Mu2e Detector and Rejection of the Cosmics-Induced Background*, Mu2e-doc-2992 - 2013

[88] S. Di Falco et al., *Mu2e standalone calorimeter trigger studies*, Mu2e-doc-12272 - 2017

[89] A. Hoecker et al., *TMVA-Toolkit for multivariate data analysis*, (2007) [arXiv: physics/0703039]

[90] N. Atanov et al., *The Mu2e Calorimeter Final Technical Design Report*, arXiv:1802.06341 [physics.ins-det]

[91] Amcrys official page, http://www.amcrys.com/

[92] Saint Gobain official page https://www.crystals.saint-gobain.com/

[93] Siccas official page http://www.siccas.com/

[94] M. Cordelli et al. Internal note *QA of 72 pre-production un-doped CsI crystals from SICCAS, Amcrys and Saint Gobain.* Mu2e-Doc-20074.

[95] https://home.fnal.gov/ aria/WebsitesInProgress/SiDet/

[96] `https://www.dupont.com/content/dam/dupont/products-and-services/membranes-and-` `Tedlar_ Composite_ Release_ Film_ Applications.pdf`

[97] Z.Y. Wei and R.Y. Zhu, *A study on undoped CsI crystals*, NIM A 326 (1993) 508-512

[98] S. Baccare et al., *Radiation hardness test of un-doped CsI crystals and Silicon Photomultipliers for the Mu2e calorimeter*, CALOR 2016, J.Phys Conf. Ser. 928, conference 1, (2016) 928 012041 [arxiv:1606.07255, DOI: 10.1088/1742-6596/928/1/012041].

[99] Advansid official page, http://advansid.com/home

[100] SensL official pagehttps://sensl.com/

[101] N. Atanov et al., *The Mu2e calorimeter: Quality assurance of production crystals and SiPMs.* NIM A 936 (2019) 154. arXiv:1812.07921

[102] F. Nagy et al., *A model based DC analysis of SiPM break-down voltages*, NIM A 849 (2017) [DOI: 10.1016/j.nima.2017.01.002, arXiv:1606.07805]

[103] http://www.enea.it/it/laboratori-impianti/schede-laboratori/CALLIOPE.pdf

[104] `http://www.ti.com/lit/ds/symlink/tl1963a.pdf`

[105] `http://www.fusione.enea.it/LABORATORIES/Tec/FNG.html.it`

[106] S. Baccaro et al., *Irradiation study of UV Silicon Photomultipliers for the Mu2e calorimeter*, Journal of Instrumentation 12.02 (2017): C02022.

[107] https://www.hzdr.de

[108] Atanov, N. et al. (2017). "Quality Assurance on Un-Doped CsI Crystals for the Mu2e Experiment", IEEE TNS 65 752-757

[109] Cordelli, M. et al.(2017). "Pre-production and quality assurance of the Mu2e calorimeter Silicon Photomultipliers|". Submitted to NIM A

[110] L. W. Nagel. *SPICE2: A Computer Program to Simulate Semiconductor Circuits.* Memorandum No. ERL-M520, University of California, Berkeley, May 1975

[111] C. Grupen, *Particle detectors*, Cambridge Monographs on Particle Physics, Nuclear Physics and Cosmology, 239-240, 1996

[112] Miller, J. P. *Muon Atomic Binding Energies and Endpoint Energies by Isotope*, Mu2e-doc-277-v4

[113] Jenkins, M. *A First Look at $\mu^-$ N(A,Z) to $e^+$ N(A,Z-2) in the Mu2e Experiment*, Mu2e-doc-15078-v3

[114] Czarnecki, A., i Tormo, X. G., Marciano, W. J. (2011). *Muon decay in orbit: spectrum of high-energy electrons.* Physical Review D, 84(1), 013006.

[115] http://pdg.lbl.gov/2018/reviews/rpp2018-rev-phys-constants.pdf

[116] https://physics.nist.gov/cgi-bin/Compositions/stand_alone.pl?ele=&ascii=ascii2&isotype=all

[117] R. Szafron,*Radiative Corrections in Bound States.* Acta Phys. Polon. (2017), 48, 2183.

[118] H. Primakoff. *Theory of the muon capture*, Rev. Mod. Phys. 31, 802 (1959).

[119] P. Christillin, M. Rosa-Clot, S. Servadio. *Radiative muon capture in medium-heavy nuclei* Nucl Phys. A345, 331 (1980).

[120] D.S. Armstrong et al.,*Radiative muon capture on Al, Si, Ca, Mo, Sn and Pb* Phys. Rev. C 46, 1094 (1992).

[121] T. P. Gorringe,et al., *Isotope dependence of radiative muon capture on the $^{58,60,62}Ni$ isotopes.* Phys. Rev. C, 58:1767âĂŞ1776, Sep 1998.

[122] M. MacKenzie, *Comparing Internal and External RMC.* Internal presentation, Mu2e-DocDB 28104.

[123] M. MacKenzie, *Feasibility of Measuring the Fraction of Internal RMC Conversions.* Internal presentation, Mu2e-DocDB 21036

[124] M. Guan, J. Cao, C. Yang, Y. Sun, K.B. Luk. *Muon simulation at the Daya Bay site.* Lawrence Berkeley National Laboratory Paper LBNL-4262E. (2006)

[125] C. Hagmann et al. *Cosmic-ray shower library (CRY).* Lawrence Livermore National Laboratory document UCRL-TM-229453 (2012).

[126] MCNP web site `https://mcnp.lanl.gov/`

[127] CORSIKA an Air Shower Simulation Program `https://web.ikp.kit.edu/corsika/usersguide/usersguide.pdf`

[128] MicroBoon Public Note 1005 *Cosmic Shielding Studies at MicroBooNE* `https://microboone.fnal.gov/wp-content/uploads/MICROBOONE-NOTE-1005-PUB.pdf`

[129] A. Gaponenko*Summary of backgrounds for CD3.* Mu2e-DocDB 7464

[130] J. Kremer, M. Boezio, M. E. Ambriola, G. Barbiellini, S. Bartalucci, R, Bellotti et al. *Measurements of ground-level muons at two geomagnetic locations.* Physical Review Letters, 83(21), 4241 (1999).

[131] Kempthorne, O. Journal of the American Statistical Association 65, 455-456. (1970).

[132] G.J. Feldman, R.D. Cousins. *Unified approach to the classical statistical analysis of small signals.* Phys. Rev. D 57, 3873âĂŞ3889 (7 1998).

[133] A. L. Read. *Modified frequentist analysis of the search results (the $CL_s$ method)* No. CERN-OPEN-2000-205. Cern, 2000.

[134] T. Junk, *Sensitivity, Exclusion and Discovery with Small Signals, Large Backgrounds, and Large Systematic Uncertainties.* CDF/DOC/STATISTICS/PUBLIC/8128 (2007).

[135] P.C. Bergbusch et al.,*Radiative muon capture on O, Al, Si, Ti, Zr, and Ag.* Physical Review C 59.5, 2853 (1999)

[136] P.C. Bergbusch, MS Thesis, Univ of British Columbia, 1995, `https://open.library.ubc.ca/media/download/pdf/831/1.0085569/2.`

# Appendix A

## A.1 Reconstruction cuts applied to the $\mu^- - e^+$ dataset

Table A.1 reports the cumulative efficiencies for the LO, LO mix, LL and extrapolated LL mix datasets. In the following a description of the cuts applied to the $\mu^- - e^+$ dataset, as well as their effect to the momentum distribution, are reported.

| Cut | Min ($\geq$) | Max ($\leq$) | LO | LL | $LO_{mix}$ | $LL_{mix}^{expected}$ |
|---|---|---|---|---|---|---|
| no Cut | | | 0.2195 | 0.2102 | 0.2044 | 0.1957 |
| $N_{active}$ | 18 | 200 | 0.2130 | 0.2038 | 0.2004 | 0.1918 |
| $N_{hits}$-$N_{active}$ | 0 | 6 | 0.2124 | 0.2032 | 0.1977 | 0.1892 |
| $N_{active}/N_{hist}$ | 0.87 | 1 | 0.2124 | 0.2032 | 0.1977 | 0.1892 |
| p Err [MeV/c] | 0 | 0.27 | 0.1919 | 0.1829 | 0.1781 | 0.1698 |
| T0 Err [ns] | 0 | 1.2 | 0.1867 | 0.1779 | 0.1714 | 0.1633 |
| Tan(Dip) | 0.5 | 1.5 | 0.1867 | 0.1778 | 0.1714 | 0.1633 |
| -D0*Q [mm] | -50 | 150 | 0.1857 | 0.1769 | 0.1706 | 0.1626 |
| $\chi^2$/NDoF | 0 | 3.5 | 0.1857 | 0.1769 | 0.1706 | 0.1626 |
| $R_{max}$ [mm] | 400 | 680 | 0.1797 | 0.1709 | 0.1649 | 0.1568 |

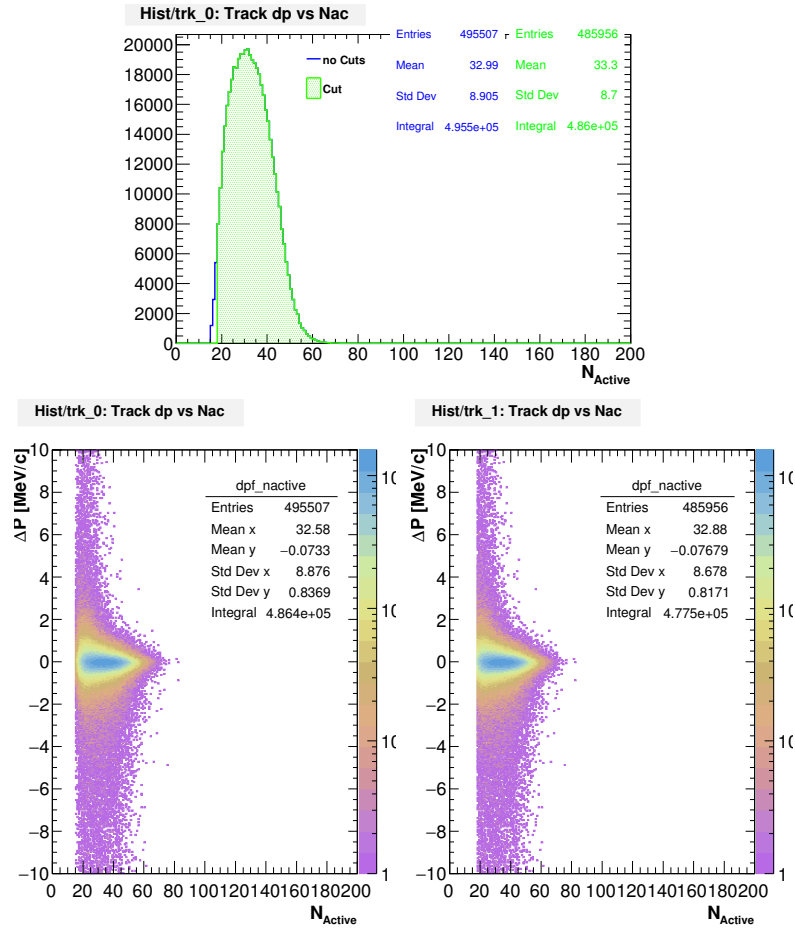**Table A.1:** Cumulative efficiency obtained from the different datasets studied.

**Figure A.1:** First cut applied: $N_{active}$ is the number of hits used in the fit to reconstruct the track. Top: $N_{active}$ distribution before (blue) and after (green) the cut. Bottom: $P - P_{MC}$ plot versus $N_{active}$ before (left) and after (right)the cut.
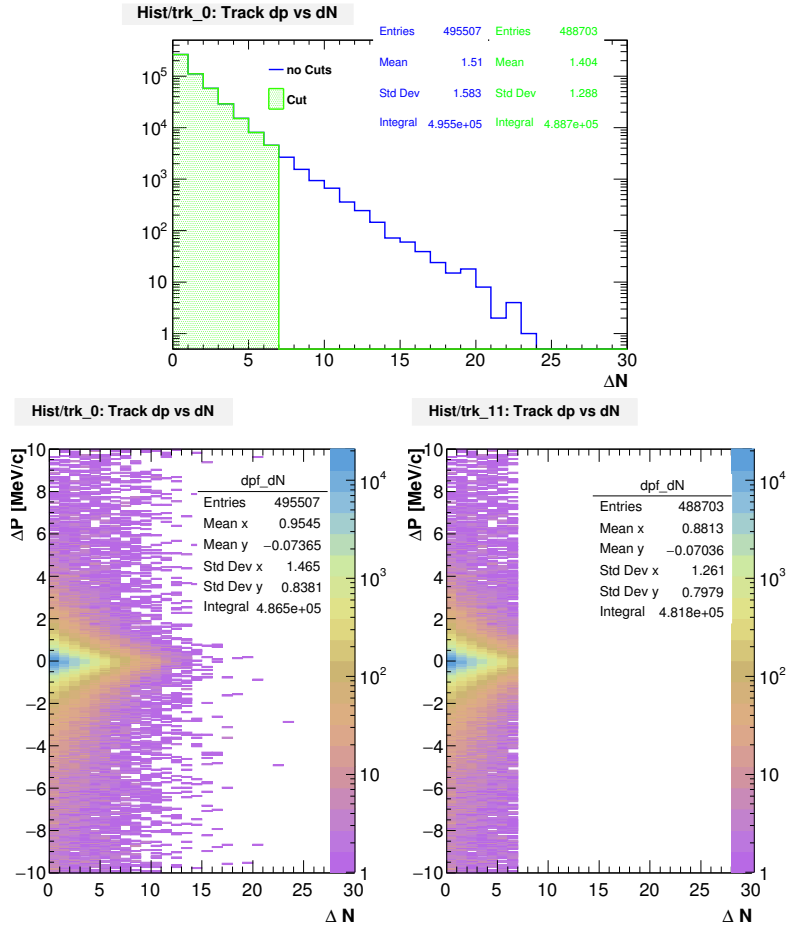
**Figure A.2:** Second cut applied: $\Delta N = N_{hits} - N_{active}$ is the difference t between the number of hits on the track and the number of hits used to fit the track. Top: $\Delta N = N_{hits} - N_{active}$ distribution before (blue) and after (green) the cut. Bottom: $P - P_{MC}$ plot versus $\Delta N = N_{hits} - N_{active}$ before (left) and after (right) the cut.
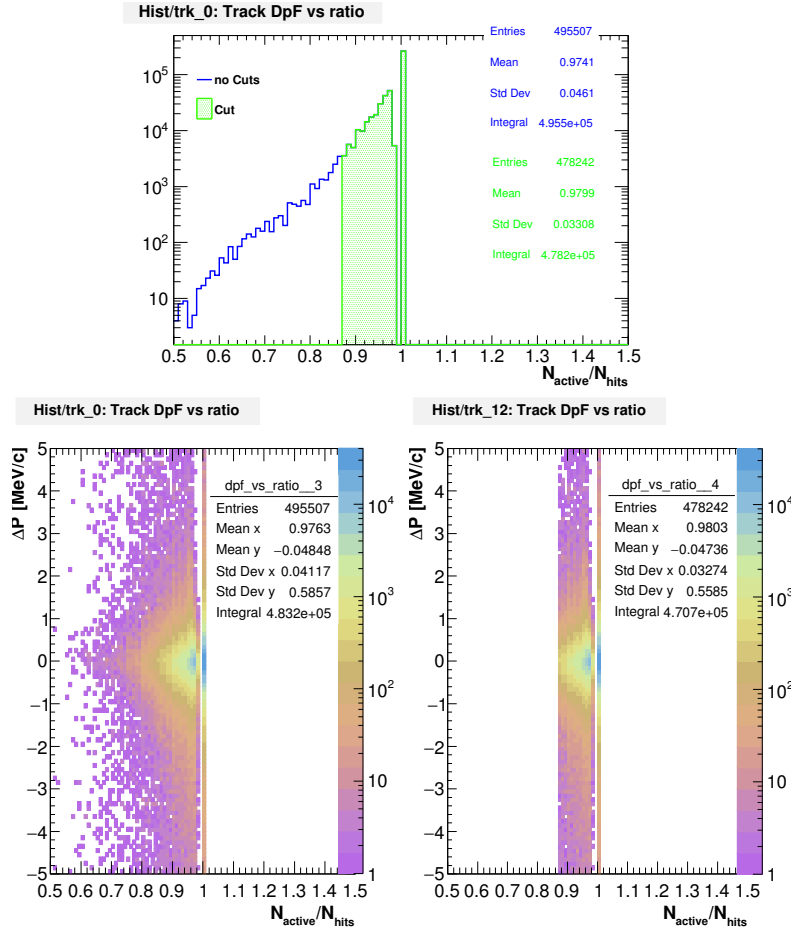
**Figure A.3:** Third cut applied: $\mathcal{R}N = N_{active}/N_{hits}$ is the ratio of the number of hits on the track and the number of hits used to fit the track. Top: $\mathcal{R}N = N_{active}/N_{hits}$ distribution before (blue) and after (green) the cut. Bottom: $P - P_{MC}$ plot versus $\mathcal{R}N = N_{active}/N_{hits}$ before (left) and after (right) the cut.
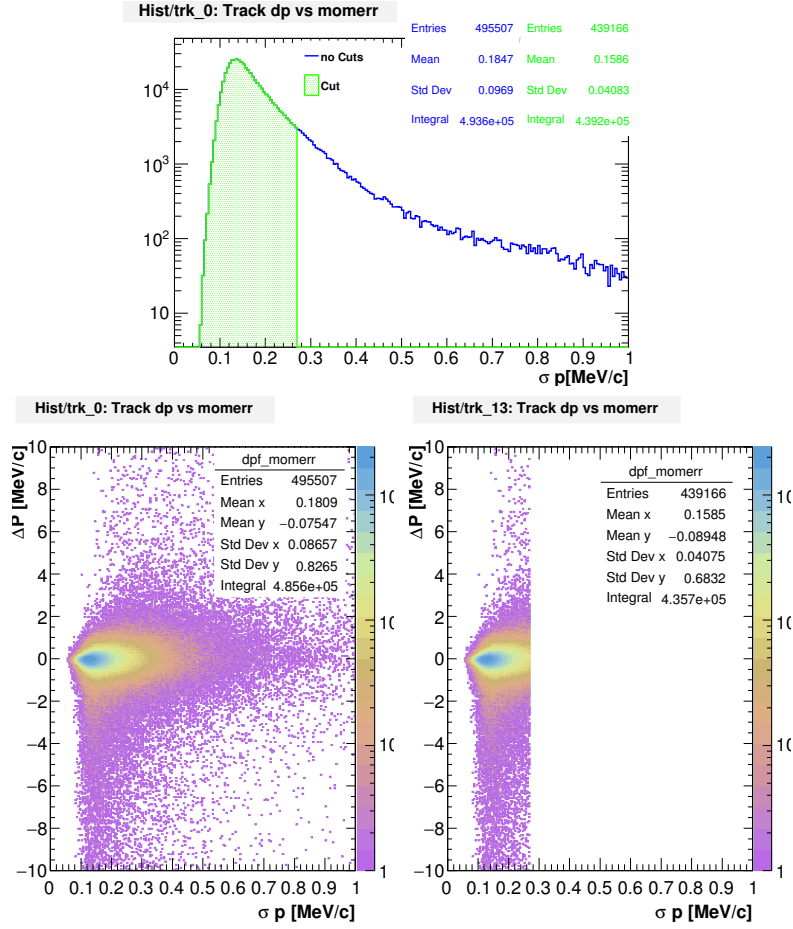
**Figure A.4:** Fourth cut applied: $\sigma$p is the error on the momentum evaluation. Top: $\sigma$p distribution before (blue) and after (green) the cut. Bottom: $P - P_{MC}$ plot versus $\sigma$p before (left) and after (right) the cut.
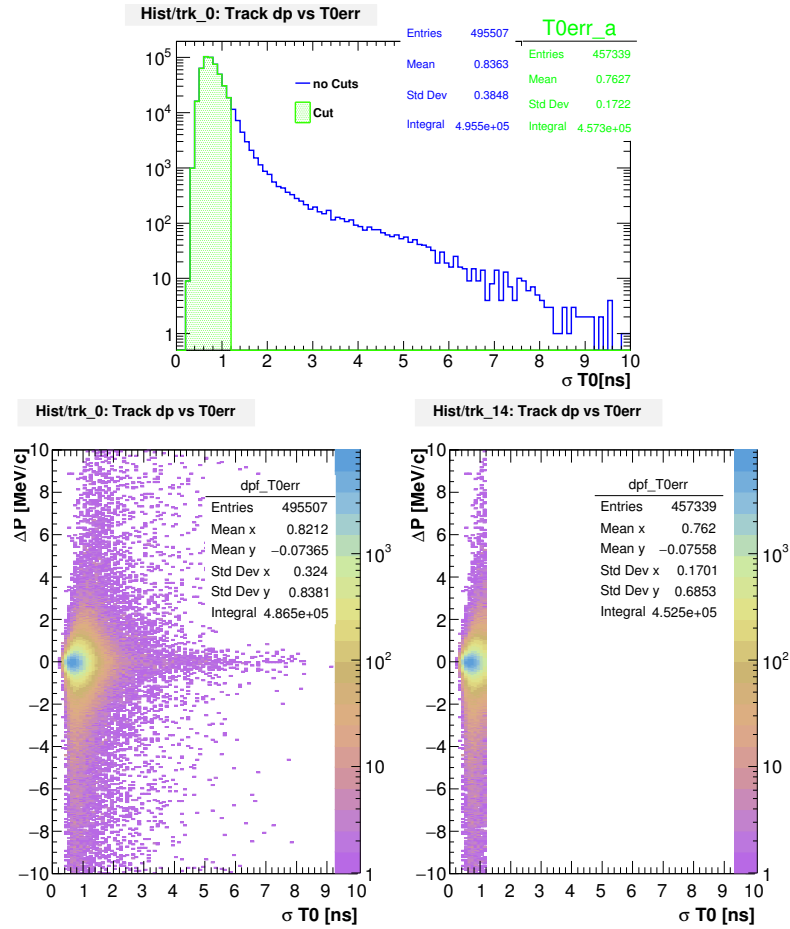
**Figure A.5:** Fifth cut applied: $\sigma T0$ is the error on the termination of $T0$, when the track pass in the middle of the tracker. Top: $\sigma T0$ distribution before (blue) and after (green) the cut. Bottom: $P - P_{MC}$ plot versus $\sigma T0$ before (left) and after (right) the cut.
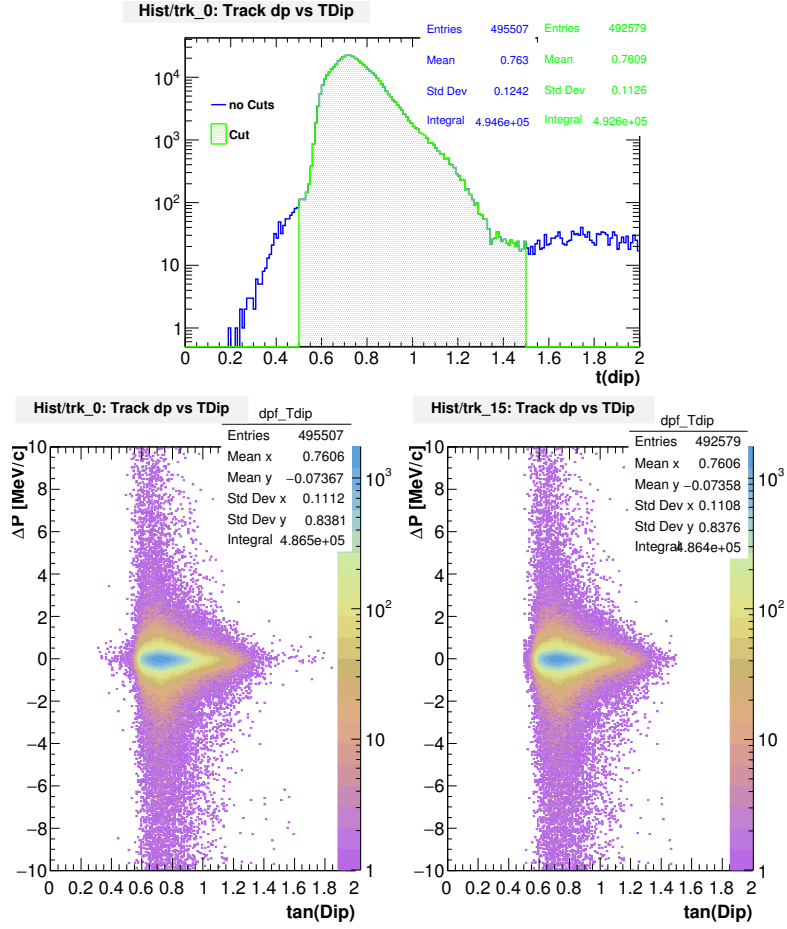
**Figure A.6:** Sixth cut applied: tdip is the tangent of the dip angle.Top: tdip distribution before (blue) and after (green) the cut. Bottom: $P - P_{MC}$ plot versus tdip before (left) and after (right) the cut.
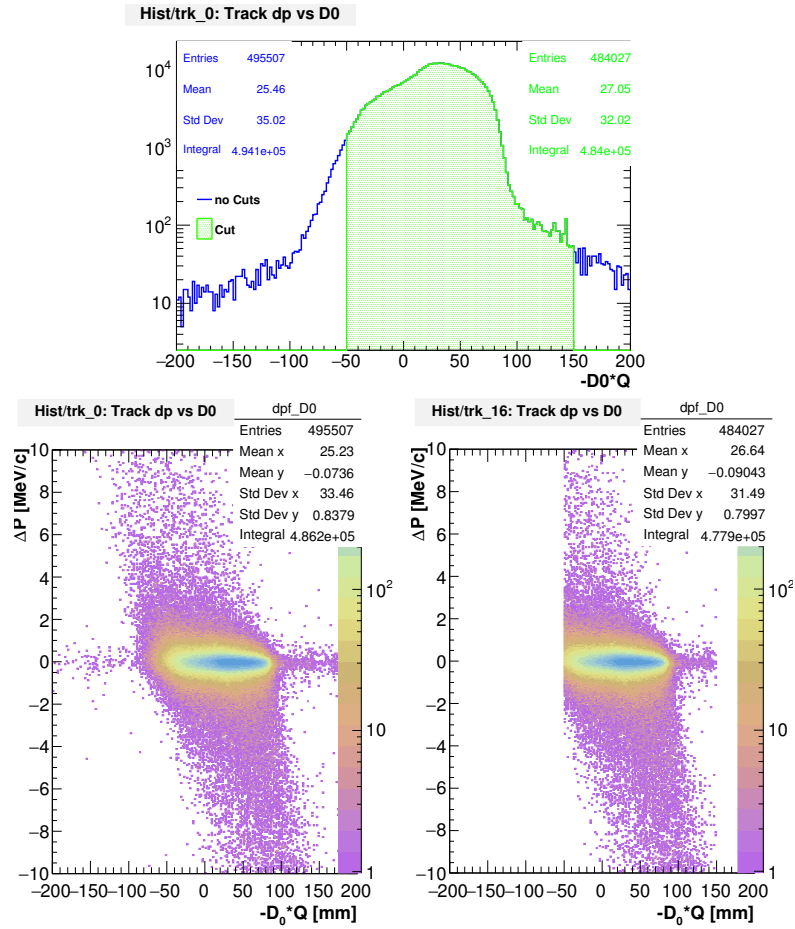
**Figure A.7:** Seventh cut applied: D0 is the impact parameter of the track.Top: D0 distribution before (blue) and after (green) the cut. Bottom: $P - P_{MC}$ plot versus D0 before (left) and after (right) the cut.
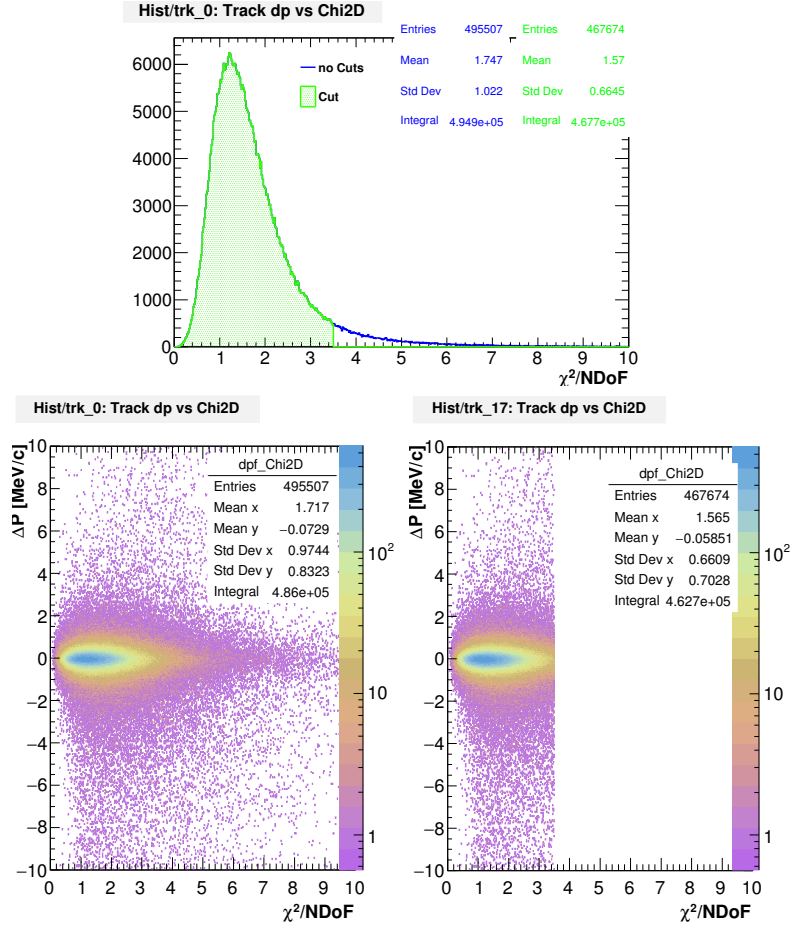
**Figure A.8:** Eighth cut applied: $\chi^2$/NDoF is the $\chi^2$ over the degree of freedom of the track fit.Top: $\chi^2$/NDoF distribution before (blue) and after (green) the cut. Bottom: $P - P_{MC}$ plot versus $\chi^2$/NDoF before (left) and after (right) the cut.
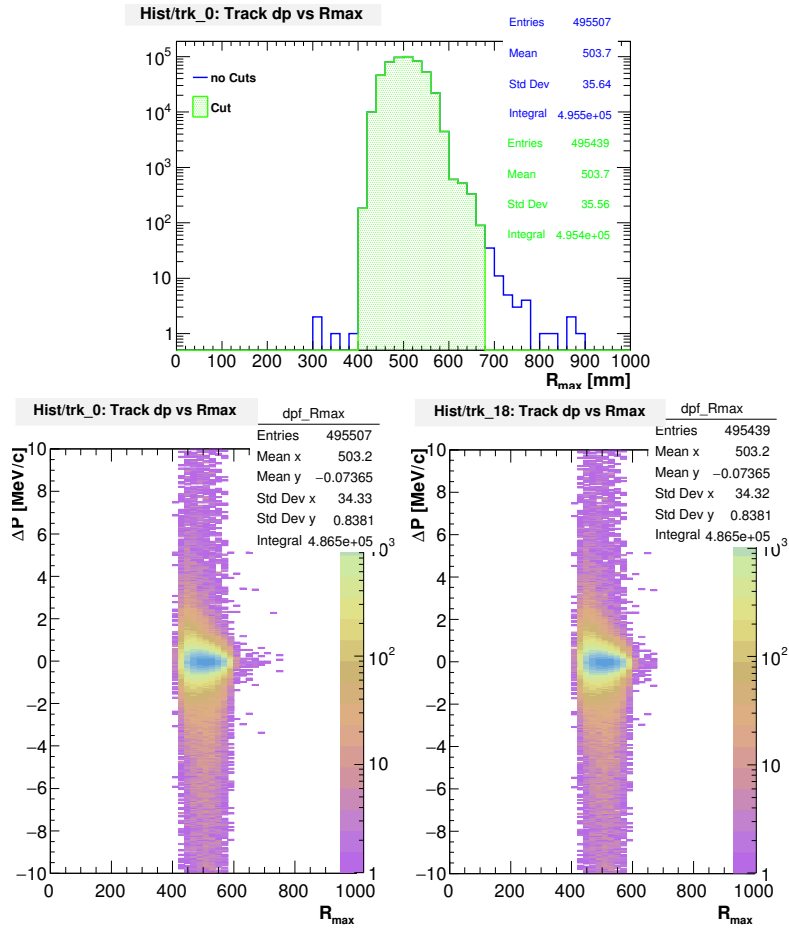
**Figure A.9:** Nineth cut applied: $R_{max}$ is the maximum radius of the track .Top: $R_{max}$ distribution before (blue) and after (green) the cut. Bottom: $P - P_{MC}$ plot versus $R_{max}$ before (left) and after (right) the cut.
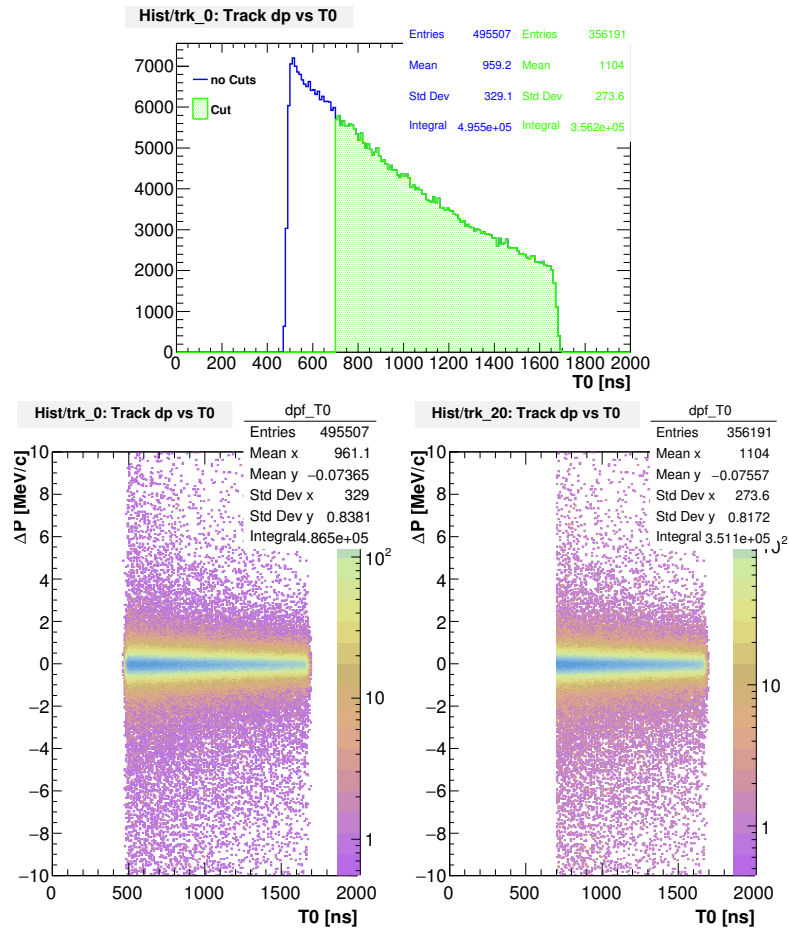
**Figure A.10:** Tenth cut applied: $T0$ is the moment when the track is in the middle of the tracker .Top: $T0$ distribution before (blue) and after (green) the cut. Bottom: $P - P_{MC}$ plot versus $T0$ before (left) and after (right) the cut.

# Appendix B

## B.1  Study of the RMC photon spectrum

As shown in Chapter 7, the expected energy of a positron coming from the $\mu^- \rightarrow e^+$ process is 92.32 MeV. This value is close enough to the endpoint of the RMC photon spectrum on aluminum, so that variations of the endpoint energy within the experimental errors could result in significant changes in the RMC background values. Considering the RMC endpoint reported by the TRIUMF collaboration in [135] $k_{\max} = 90 \pm 1.8$ MeV, the difference between these two energies corresponds to 1.5 $\sigma$, therefore it results extremely important to fully understand the experimental uncertainty on $k_{max}$. The TRIUMF collaboration, in [120] and [121] published the detector response, giving the possibility to reproduce the published photon spectrum endpoints.

The detector response D(E,E') is defined as the probability for a photon with energy E to be reconstructed in the detector with energy E'. As follows from the definition, D(E,E') includes both resolution and acceptance - the integral of D(E,E')dE' gives the total acceptance for a given energy E.

In both [120] and [121], the detector response is determined using a GEANT3-based simulation using monoenergetic photons in a energy range of 50-140 MeV, and it is parameterized analytically. The parameterizations of [120] and [121] are significantly different, the source of the difference is not understood, neither explained.

## 1992 Detector response parametrization

The response of the TRIUMF RMC spectrometer published in [120] is described as a Gaussian function with exponential low- and high-energy tails. In order to reproduce the low-energy resolution tail for high-energy photons, a second Gaussian is added for photon energies above 60 MeV. The functional form is as follows:

$$
D(E,E') = \begin{cases} A \exp\left[-\frac{1}{2\sigma_0^2}(E'-E_o)^2\right] + F \exp\left[-\frac{1}{2\sigma_3^2}(E'-E_3)^2\right] & E_1 < E' < E_2 \\ B \exp\left[-\frac{1}{\sigma_1}(E_1-E')\right] + F \exp\left[-\frac{1}{2\sigma_3^2}(E'-E_3)^2\right] & E' < E_1 \\ C \exp\left[-\frac{1}{\sigma_2}(E'-E_2)\right] + F \exp\left[-\frac{1}{2\sigma_3^2}(E'-E_3)^2\right] & E' > E2 \end{cases}
$$
(B.1)

where $E_1 = E_0 - \frac{\sigma_0^2}{\sigma_1}$, $E_2 = E_0 + \frac{\sigma_0^2}{\sigma_2}$, $B = A \exp\left[-\frac{\sigma_0^2}{2\sigma_1^2}\right]$, $C = A \exp\left[\frac{\sigma_0^2}{2\sigma_2^2}\right]$.

The parameters $A, B, C, F, \sigma_i$, etc. are fitted as polynomials in the photon energy:

$$
f(E) = P_0 + P_1 E + P_2 E^2 + P_3 E^3
$$
(B.2)

The coefficients are reported in Tables B.1 and B.2 .

| Parameter | $P_0$ (MeV) | $P_1$ | $P_2$ (MeV)$^{-1}$ |
|---|---|---|---|
| $\sigma_0$ | -0.5836 | 0.0352 | |
| $\sigma_1$ | -5.879 | 0.1653 | -5.149×10$^{-4}$ |
| $\sigma_2$ | 1.596 | -0.03859 | 3.883×10$^{-4}$ |
| $\sigma_3$ | -47.80 | 1.010 | -4.406×10$^{-3}$ |
| $E_3$ | 1.068 | 0.7507 | |
| $E_0$ (E>60) | -1.161 | 0.9481 | 1.724×10$^{-3}$ |
| $E_0$ (E<60) | 22.73 | 0.1995 | 5.993×10$^{-3}$ |

**Table B.1:** Polynomial parameterization of the coefficiencts in B.1

The energy dependence of the coefficients used to parameterize the response function is shown in Figure B.1.

| Parameter | $P_0$ | $P_1$ $(MeV)^{-1}$ | $P_2$ $(MeV)^{-2}$ | $P_3$ $(MeV)^{-3}$ |
|-----------|-------|-------------------|--------------------|--------------------|
| A | $3.259\times10^{-4}$ | $-4.120\times10^{-4}$ | $1.015\times10^{-5}$ | $-4.05\times10^{-8}$ |
| F/A | $-0.1337$ | $2.828\times10^{-3}$ | $-9.701\times10^{-6}$ | |

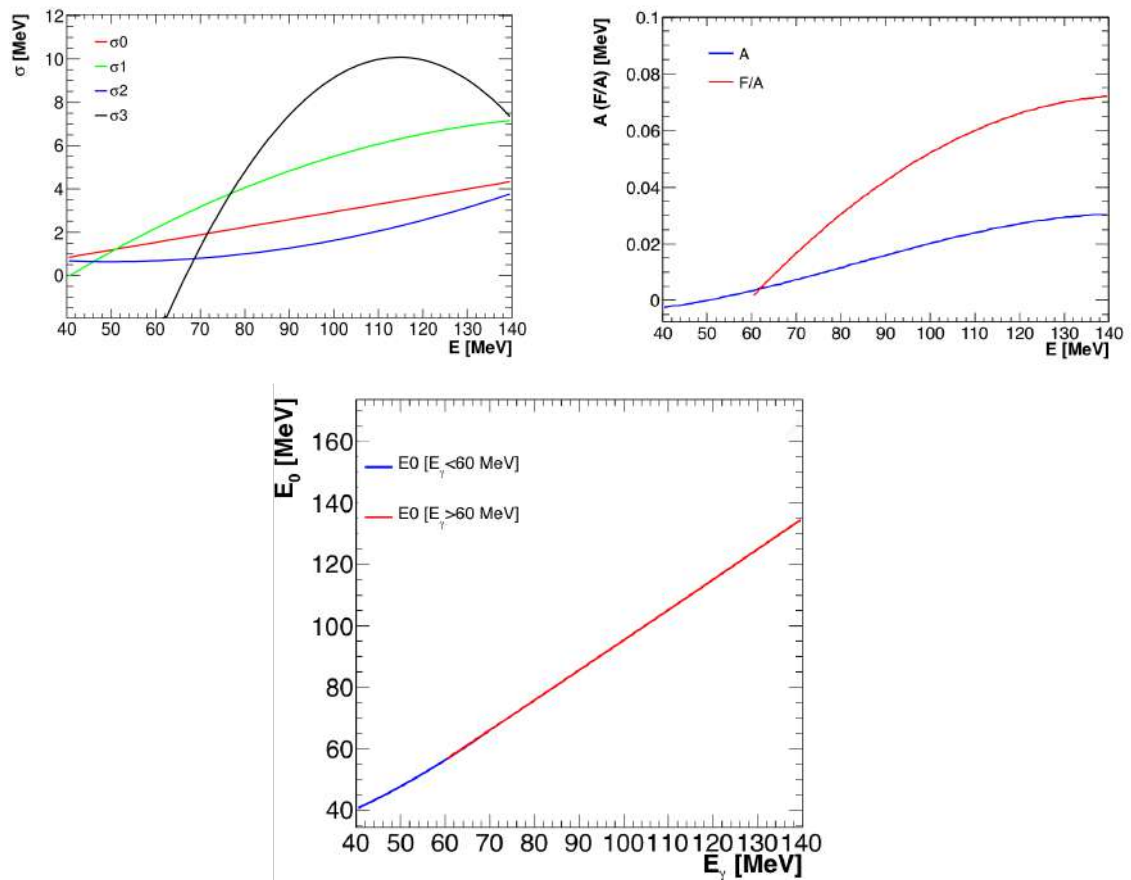**Table B.2:** Polynomial parameterization of coefficients in B.2



**Figure B.1:** Energy dependence of parameters defining the TRIUMF RMC spectrometer response [120]

Examples of the detector response at different energies, namely, 50 MeV, 70 MeV, 90 MeV, and 110 MeV, are shown in Figure B.2. As previously described, for photon energies above 60 MeV, the low-energy tails are well evident.
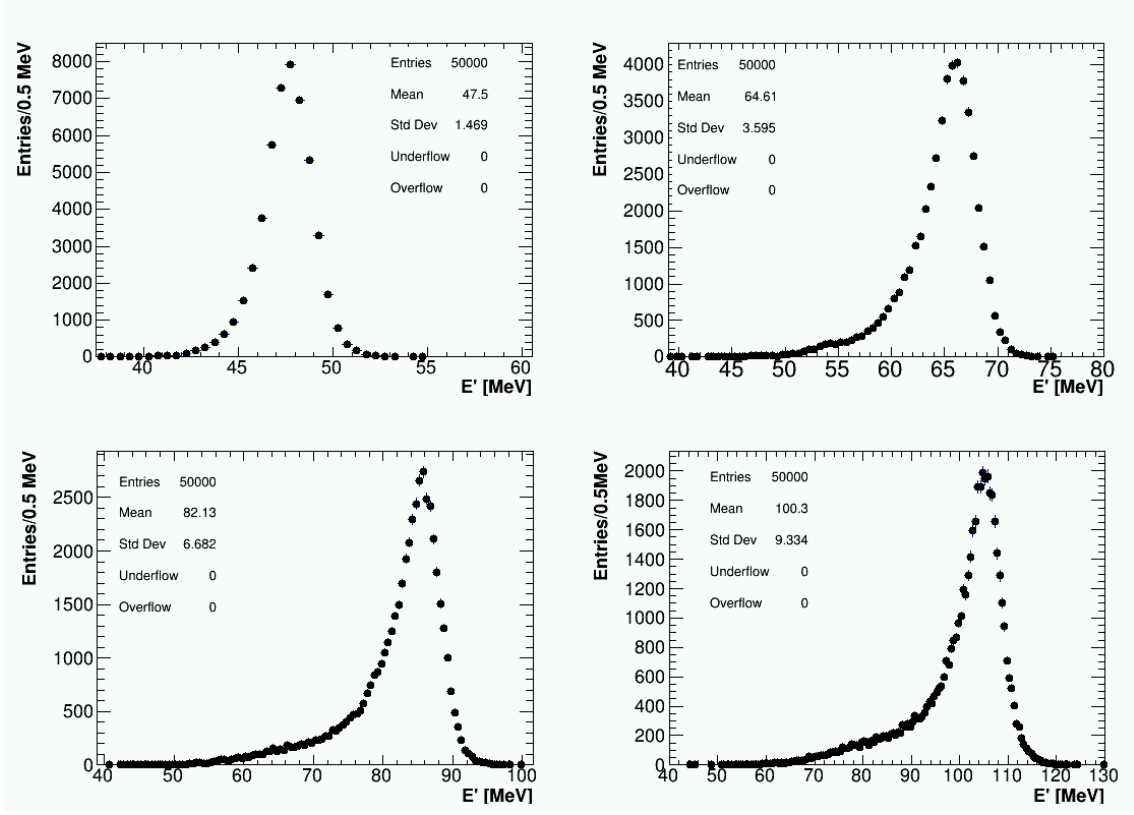
**Figure B.2:** 1992 detector response parametrization for different photon energies: 50 MeV (top left), 70 MeV (top right), 90 MeV (bottom left) and 110 MeV (bottom right).

## 1998 Detector Response

The TRIUMF RMC spectrometer response, published in 1998 ([121]) is significantly different from its 1992 version. The 1998 parameterization is a Gaussian with logaritmic low-energy and exponential high-energy tails:

$$
D(E, E') = \left\{
\begin{array}{ll}
\beta \cdot ln(x)/x & E' \leq (E_0 - \sigma_0) \\
A e^{-(E'-E_0)^2/2\sigma_0^2} & E_0 - \sigma_0 < E' < (E_0 - \sigma_0^2/\sigma^2) \\
A e^{-(E'-E_0)/2\sigma_2} & E' \geq (E_0 + \sigma_0^2/\sigma_2)
\end{array}
\right\}
\tag{B.3}
$$

The parameter $\beta$ allows matching of the low-side and the Gaussian core of the distribution at E'=$E_0 - \sigma_0$.
$x$ is defined as:

$$
x = \frac{\alpha - E'}{\alpha - 37},
$$

with E' in MeV. Dependence of the coefficients $\alpha, A, E_0, \sigma_0, \sigma_2$ on the photon energy is parameterized with the 3-rd order polinomials:

$$\alpha = a_0 + a_1 y + a_2 y^2 + a_3 y^3 \tag{B.4}$$

where $y = (E - 60)/60$, with E in MeV.

Polinomial coefficients, which parameterize the energy dependence of $\alpha, A, E_0, \sigma_0, \sigma_2$, are presented in Table B.3 .

| Parameter | $a_0$ | $a_1$ | $a_2$ | $a_3$ |
|-----------|-------|-------|-------|-------|
| $\alpha$ | 56.1 | 62.5 | -0.826 | 0.0 |
| A | $9.41 \cdot 10^{-4}$ | $2.61 \times 10^{-3}$ | $0.27 \times 10^{-2}$ | $0.835 \times 10^{-3}$ |
| $E_0$ | 54.4 | 57.7 | -0.315 | 0.0 |
| $\sigma_0$ | 2.03 | 10.4 | 1.25 | -0.428 |
| $\sigma_2$ | 0.786 | 0.508 | 0.425 | -0.164 |

**Table B.3:** Coefficients used to parameterize the energy dependence of the response function parameters

Figure B.3 shows the energy dependence of the coefficients used in the detector response function parameterization.
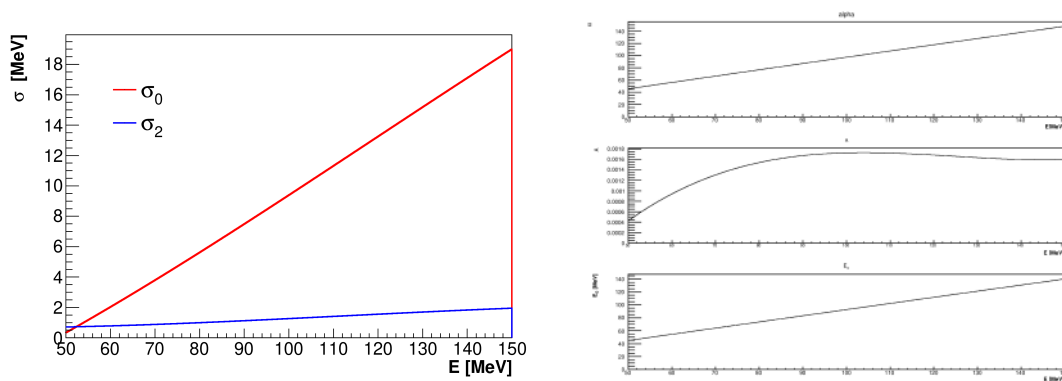


**Figure B.3:** Energy dependence of the different parameter defining the detector response

Figure B.4 reports the 1998 detector response for the same four photon energies shown in Figure B.2. The distributions in Figure B.4 are significantly wider than

similar one shown in Figure B.2. Given that there were no big reported changes in the TRIUMF RMC spectrometer configuration, one can conclude that the understanding of the detector response has significantly evolved in between 1992 and 1998. However, there is no corresponding discussion in the 1998 paper.
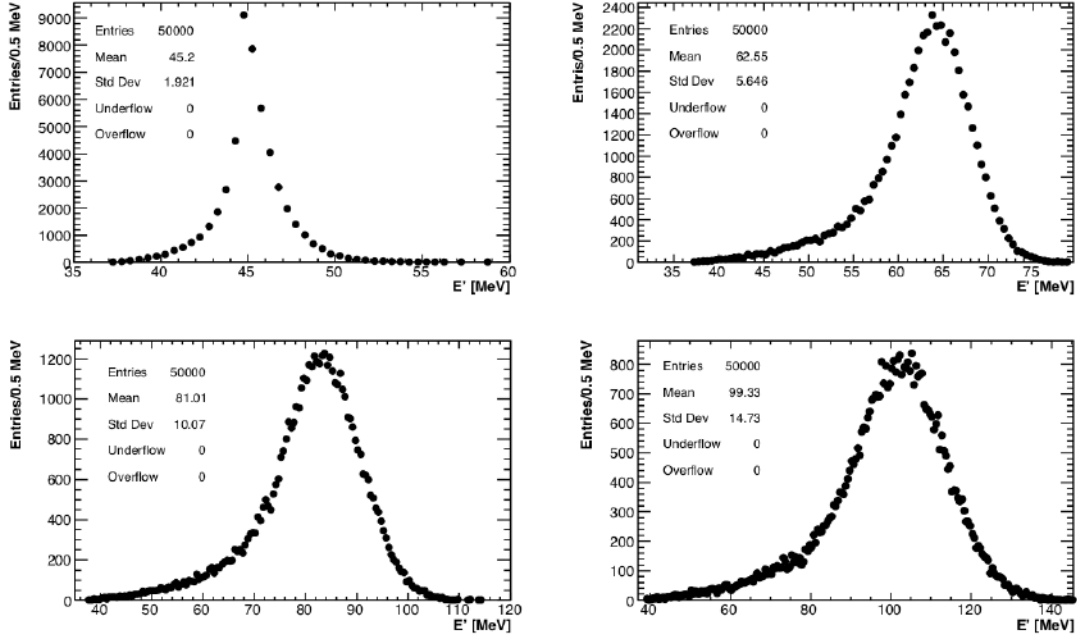


**Figure B.4:** 1998 detector response parametrization for different photon energies

Figure B.5 compares the 1992 and 1998 versions of the TRIUMF RMC spectrometer response at E = 90 MeV (left) and the linearity of the detector response for 1992 and 1998 version as a function of the photon energy (right). Figure B.6 shows how well the 1992 and 1998 parameterizations of the detector response describe the radiative pion capture (RPC) peak on hydrogen at E = 129.4 MeV from $\pi^- p \to \gamma n$ on LH$_2$ reaction reported in the 1992 paper. Figure B.6 demonstrates that the modeled 1992 detector response is consistent with the 1992 data, and the difference between the two parameterizations cannot be interpreted in terms of an improved understanding of the detector response from 1992 to 1998.

The 1998 article validates in a different way the detector response, showing the MC description of the photon spectrum from RPC on $^{12}$Ca. However, this distribution is so wide that the data-to-MC comparison is much less sensitive to the
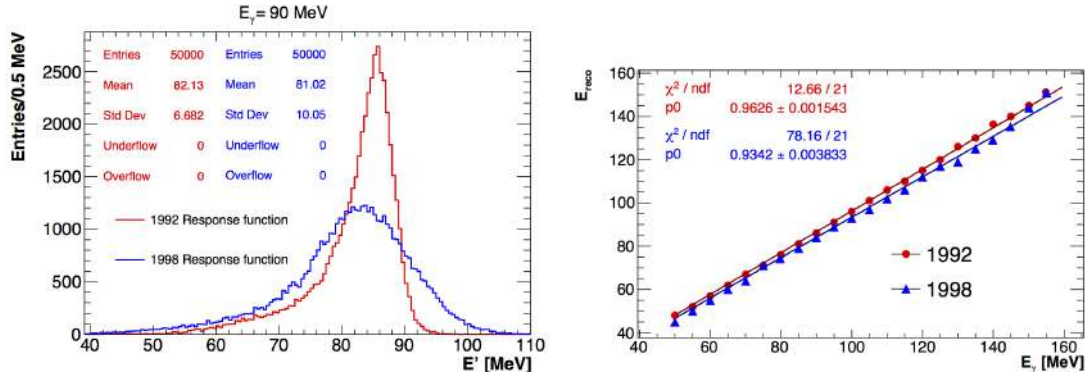
**Figure B.5:** Left: 1992 and 1998 detector response at $E_\gamma = 90$ MeV. Right: dependence of the peak of the detector response function on $E_\gamma$ for 1992 and 1998 response parameterizations.
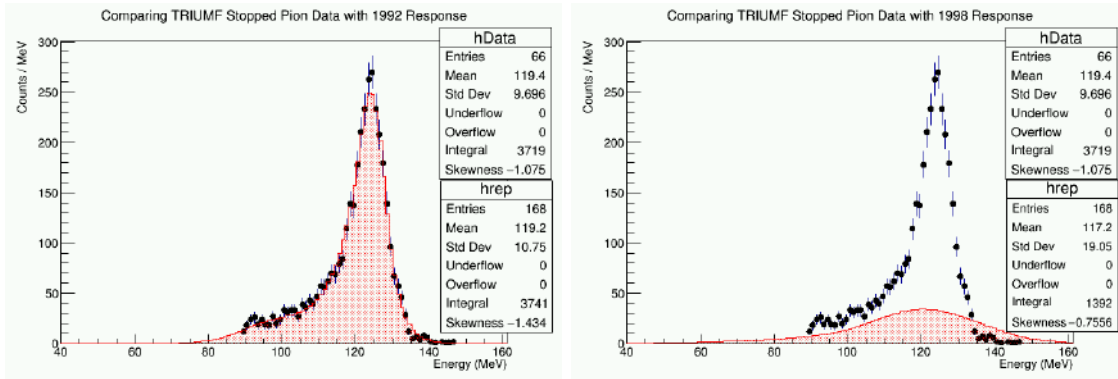


**Figure B.6:** Response function of the 1992 article (left) and 1998 article (right) compared with the 129.4 MeV line from RPC on $LH_2$

modeled detector resolution than the 1992 comparison.

## Fits to the experimental TRIUMF data

In the following the repeated fit to the TRIUMF experimental data as well as a comparison with their results are reported.

To fit the endpoint energy for a given data spectrum, closure approximation spectra were convolved with a detector response function using $k_{max}$ values between 80 MeV and 100 MeV. Each spectrum was scaled to minimize the $\chi^2$. The scale factors to
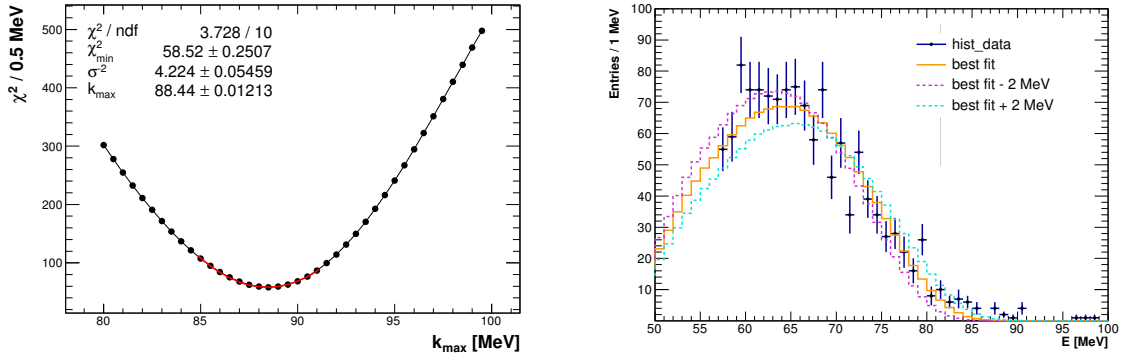
**Figure B.7:** Technique used to evaluate $k_{\max}$. Left: $\chi^2/\text{NDOF}$ as a function of $k_{\max}$. Right: Comparison between the results obtained at the TRIUMF experiment (black dots), our best fit (orange line) and best fit corresponding to a shift in $k_{\max} = 2$ MeV (dashed lines).

minimize the $\chi^2$ and fits were derived by:

$$\chi^2 = \sum_{i=1}^{N}\left(\frac{A*x_i - y_i}{\sigma_i}\right)^2; \quad \frac{\partial\chi^2}{\partial A} = 0 \rightarrow A_{\chi^2} = \frac{\sum_{i=1}^{N}\frac{x_i*y_i}{\sigma_i^2}}{\sum_{i=1}^{N}\frac{x_i^2}{\sigma_i^2}}, \qquad (\text{B.5})$$

where $x_i$ is the predicted value corresponding to data $y_i$ for a given endpoint value.

Then the distributions of $\chi^2$ as a function of the endpoint were fit with a parabola near the minimum to find the best fit endpoint energy:

$$f(k) = \chi^2 + \sigma^{-2}(k - k_{max})^2 \qquad (\text{B.6})$$

The estimated uncertainty is then defined by $\Delta\chi^2 = 1$. This was done using both published detector response functions, an example fit using the 1992 detector response function and the 1992 aluminum data is shown in Figure B.7 The fit $k_{max}$ values for all datasets and both detector response functions are shown in Figures B.8. At the end of this study several interesting results have been obtained although questions have been raised: The fit performed resulted in significantly smaller errors on $k_{\max}$ than the published ones. It seems very likely that the TRIUMF RMC spectrometer collaboration used the wrong definition of the fit errors. To validate this hypothesis [136] indicates that the fit error has been defined as the change in the parameter value corresponding to the change in the fit $\chi^2/\text{DOF}$ by one, rather than the change by one in the total fit $\chi^2$. Moreover, the 1998 parametrisation of the
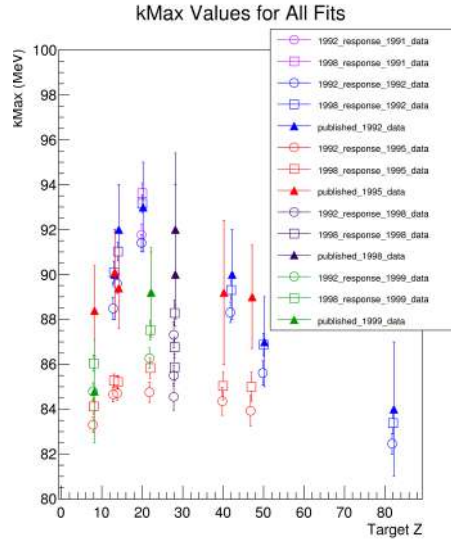
**Figure B.8:** Fit results vs target Z using (a) $\chi^2$ minimization a The 1992 detector response function data points (circles) are offset by -0.2 in z and the published data points (triangles) are offset by +0.2 in z.

detector response gave better fit results for each spectrum fitted, including also the previous results of 1992 and 1995. However, the 1992 detector response is consistent with the positron and the width of the RPC peak published in 1992, while 1998 response is not. This confirms internal inconsistency in the 1992 publication. Lastly, fit $k_{max}$ values for the same target in different years vary on a scale large compared to the fit errors. This shows inconsistencies between the different publication years despite no change in the detector are reported in the published works.